

# **SPECTRAL METHODS FOR KINETIC THEORY MODELS OF VISCOELASTIC FLUIDS**

THÈSE N° 2860 (2003)

PRÉSENTÉE À LA FACULTÉ DES SCIENCES ET TECHNIQUES DE L'INGÉNIEUR

Institut des sciences de l'énergie

SECTION DE GÉNIE MÉCANIQUE

ÉCOLE POLYTECHNIQUE FÉDÉRALE DE LAUSANNE

POUR L'OBTENTION DU GRADE DE DOCTEUR ÈS SCIENCES

PAR

**Alexei LOZINSKI**

M.Sc. in Mathematics, Institut de physique et technologie de Moscou, Russie  
et de nationalité russe

acceptée sur proposition du jury:

Prof. R. G. Owens, directeur de thèse  
Dr M. Gerritsma, rapporteur  
Prof. H.C. Öttinger, rapporteur  
Prof. T. Phillips, rapporteur

Lausanne, EPFL  
2003



# Acknowledgements

First, I would like to thank my thesis supervisor Prof. Robert G. Owens for giving me the opportunity to discover the fascinating world of numerical methods for polymeric fluids and to perform some research in this area. His broad knowledge of the subject, stimulating ideas, wise guidance of my work, Christian tolerance of my imperfections and excellent sense of humour have made my stay at EPFL a most enjoyable experience. I acknowledge with gratitude his efforts in reading and correcting this manuscript.

I am indebted also to my second thesis supervisor Prof. Alfio Quarteroni. His great expertise in numerical mathematics and his amiability have made our discussions most beneficial for me.

This work would certainly not have been possible without collaboration with Cédric Chauvière and Jiannong Fang. I would like to thank them most cordially for sharing with me their knowledge, ideas and computer codes.

Drs. Frank Peters and Martien Hulsen are gratefully acknowledged for making available data from their paper [114].

I am very grateful to Tony Lelièvre, Dr. Frank Peters and Dr. Marco Picasso for some interesting and stimulating discussions.

I would also like to acknowledge gratefully my colleagues from the Laboratory of Fluid Mechanics and the Laboratory of Computational Engineering of EPFL, mentioning especially Mehmet Sahin, Nicolas Fiétier and Emmanuel Leriche, for help and assistance during the course of my PhD. Emmanuel has also kindly accepted to check the French version of the abstract of this thesis.

Many thanks also go to Professors Alain Curnier, Marc Gerritsma, Hans Christian Öttinger and Timothy Phillips who honoured me by being members of my thesis committee.

The Ecole Polytechnique Fédérale de Lausanne and the Swiss National Science Foundation (grant numbers 2100-55543 and 2100-57119) are gratefully acknowledged for financial support over the last three years.

Finally, I would like to express my deepest gratitude to my wife Alla for her constant encouragement and support.



# Abstract

This work is dedicated to the construction of numerical techniques for the models of viscoelastic fluids that result from polymer kinetic theory. Our main contributions are as follows:

1. Inspired by the interpretation of the Oldroyd B model of dilute polymer solutions as a suspension of Hookean dumbbells in a Newtonian solvent, we have constructed new numerical methods for this model that respect some important properties of the underlying differential equations, namely the positive definiteness of the conformation tensor and an energy estimate. These methods have been implemented on the basis of a spectral discretization for simple Couette and Poiseuille planar flows as well as flow past a cylinder in a channel. Numerical experiments confirm the enhanced stability of our approach.
2. Spectral methods have been designed and implemented for the simulation of mesoscopic models of polymeric liquids that do not possess closed-form constitutive equations. The methods are based on the Fokker-Planck equations rather than on the equivalent stochastic differential equations. We have considered the FENE dumbbell model of dilute polymer solutions and the Öttinger reptation model [100] of concentrated polymer solutions. The comparison with stochastic simulation techniques has been performed in the cases of both homogeneous flows and the flow past a cylinder in a channel. Our method turned out to be more efficient in most cases.



# Version Abrégée

L'objectif de ce travail est de contribuer à la construction des méthodes numériques pour la simulation des écoulements des fluides viscoélastiques en utilisant les modèles délivrés par la théorie cinétique des polymères. Nos contributions principales sont les suivantes :

1. Inspirés de l'interprétation cinétique du modèle Oldroyd B – une suspension des « haltères » de Hook dans un solvant Newtonien – nous avons proposé des nouvelles méthodes pour ce modèle qui respectent certaines propriétés importantes des équations différentielles concernées : la définition positive du tenseur de conformation et l'estimation d'énergie. Ces méthodes ont été implémentées à l'aide de discrétisations spectrales pour les écoulements planes de Couette et Poiseuille ainsi que l'écoulement bidimensionnel autour d'un cylindre placé dans un canal. Des expériences numériques démontrent que nos méthodes sont plus stables que celles utilisant l'équation constitutive.

2. Nous avons développé et implémenté des méthodes spectrales pour la discretization des modèles mésoscopiques des fluides polymériques qui ne possèdent pas d'équations constitutives. Nos méthodes sont basées sur les équations de Fokker-Planck plutôt que sur les équations stochastiques différentielles équivalentes. Nous avons choisi le modèle des « haltères » FENE pour les solutions polymériques diluées et le modèle de reptation d'Öttinger [100] pour les solutions polymériques concentrées. La comparaison avec les techniques stochastiques de simulation a été faite pour les écoulements homogènes ainsi que pour l'écoulement bidimensionnel autour d'un cylindre placé dans un canal. Il s'est avéré que nos méthodes sont plus efficaces dans la plupart des situations.





# Contents

<b>Introduction</b>	<b>1</b>
<b>1 Modelling polymeric liquids</b>	<b>5</b>
1.1 Dumbbell models for dilute polymer solutions . . . . .	5
1.1.1 The Fokker-Planck equation . . . . .	5
1.1.2 Stress tensor . . . . .	7
1.1.3 Homogeneous flows . . . . .	8
1.1.4 Local homogeneity assumption . . . . .	11
1.1.5 Constitutive equations . . . . .	13
1.2 Concentrated polymer solutions and melts . . . . .	14
1.3 Stochastic simulations . . . . .	16
<b>2 Spectral methods</b>	<b>21</b>
2.1 Orthogonal polynomials and quadrature formulas . . . . .	21
2.2 Spectral element discretization . . . . .	23
2.3 Numerical example: time-dependent Couette flow of an Oldroyd B fluid . . . . .	26
2.3.1 Problem description . . . . .	26
2.3.2 Numerical schemes . . . . .	26
2.3.3 Stabilization techniques . . . . .	30
2.4 The element-by-element method . . . . .	33
<b>3 On the use of kinetic theory in the construction of numerical methods to simulate flows of an Oldroyd B fluid</b>	<b>37</b>
3.1 Noise-free realizations of the Brownian configuration fields method . . . . .	37
3.1.1 Model description . . . . .	37
3.1.2 The Brownian configuration fields method (Oldroyd B fluid) . . . . .	38
3.1.3 A noise-free implementation of the Brownian configuration fields method by Chauvière . . . . .	39
3.1.4 A new noise-free implementation of the Brownian configuration fields method . . . . .	39
3.1.5 Computational procedure . . . . .	43
3.1.6 Numerical results for the flow past a confined cylinder . . . . .	45
3.1.7 Extension of the method to the FENE-P model . . . . .	48
3.2 An energy estimate for the Oldroyd B model and a numerical scheme respecting it	52
3.2.1 An a priori estimate for an Oldroyd B fluid . . . . .	52
3.2.2 Numerical scheme . . . . .	57
3.2.3 Example: planar channel flow . . . . .	59

3.2.4	Numerical results . . . . .	61
<b>4</b>	<b>Simulations of flows of dilute polymer solutions using a Fokker-Planck equation for the FENE dumbbell model</b>	<b>69</b>
4.1	Discretization of the Fokker-Planck equation for simple flows . . . . .	69
4.1.1	Two-dimensional FENE dumbbells . . . . .	69
4.1.2	Three-dimensional FENE dumbbells . . . . .	73
4.2	Numerical results for simple flows . . . . .	77
4.3	Algorithms for complex flow simulations . . . . .	82
4.3.1	Brownian configuration fields method for FENE dumbbells . . . . .	82
4.3.2	A “slow” FP solver . . . . .	83
4.3.3	A “fast” FP solver . . . . .	84
4.4	Numerical results for the flow past a confined cylinder. . . . .	87
4.4.1	Numerical results for the 2D FENE model . . . . .	88
4.4.2	Numerical results for the 3D FENE model . . . . .	92
4.5	A Fokker-Planck-based numerical method for modelling strongly non-homogeneous flows of dilute polymeric solutions . . . . .	97
4.5.1	Boundary conditions and weak problem statement. . . . .	98
4.5.2	Discretization and solution algorithm . . . . .	100
4.5.3	Numerical results . . . . .	105
<b>5</b>	<b>Fokker-Planck simulations of fast flows of melts and concentrated polymer solutions</b>	<b>113</b>
5.1	Description of the models . . . . .	113
5.1.1	Doi-Edwards model . . . . .	113
5.1.2	Mead-Larson-Doi (MLD) model . . . . .	114
5.1.3	Simplified Uniform (SU) model . . . . .	115
5.1.4	Modified SU model . . . . .	116
5.2	Numerical method . . . . .	117
5.2.1	Time-splitting scheme . . . . .	118
5.2.2	Discretization in configuration space . . . . .	119
5.2.3	Discretization in physical space . . . . .	120
5.3	Results . . . . .	121
5.3.1	Homogeneous flows of the SU model: Stochastic simulations [49] vs. the Fokker-Planck method . . . . .	121
5.3.2	SU and modified SU models: comparison with experimental data . . .	128
5.3.3	Two-dimensional flow past a confined cylinder. . . . .	129
<b>6</b>	<b>Conclusions and future perspectives</b>	<b>137</b>
<b>A</b>	<b>Expression of some operators through spherical harmonics</b>	<b>139</b>
A.1	Discretization of the operator $\mathcal{L}(\boldsymbol{\kappa})$ . . . . .	139
A.2	Discretization of the operator $\boldsymbol{\kappa} : \mathbf{u}\mathbf{u}$ . . . . .	142
<b>B</b>	<b>Equilibrium solution for a FENE fluid in a tube with the account of non-homogeneous effects</b>	<b>145</b>

<b>C Weak approximation of stochastic differential equations with reflecting boundary conditions</b>	<b>149</b>
<b>Bibliography</b>	<b>153</b>
<b>Curriculum Vitae</b>	<b>157</b>



# Introduction

The main goal of this work is to design more efficient and more robust numerical techniques for simulating the flows of polymeric fluids. The latter belong to the class of viscoelastic fluids, i.e. fluids possessing a memory of past deformation, which are present in a wide range of applications e.g. multigrade oils, food processing, biological fluids such as blood. Comprehensive reviews of the state of the art in modelling polymeric fluids are given in the two volumes of the textbook *Dynamics of Polymeric Liquids* by Bird *et al.* [17, 18], and the recent book by Owens and Phillips [108] provides an excellent introduction to the numerical techniques used for the simulation of these models.

Viscoelastic fluids belong to the broad class of non-Newtonian fluids. To be more specific about what we mean by Newtonian and non-Newtonian fluids, let us recall first some basic equations that are valid for any incompressible and isothermal fluid (only such fluids will be considered in this work). The equations of continuity and linear momentum conservation read

$$\nabla \cdot \mathbf{v} = 0, \tag{1}$$

and

$$\rho \left( \frac{\partial \mathbf{v}}{\partial t} + \mathbf{v} \cdot \nabla \mathbf{v} \right) = \nabla \cdot \boldsymbol{\sigma} + \rho \mathbf{f}, \tag{2}$$

where  $\mathbf{v}$  and  $\boldsymbol{\sigma}$  denote, respectively, the velocity and Cauchy stress fields,  $\rho$  is the density of the fluid and  $\mathbf{f}$  is an external force (per unit mass) e.g. gravity. The system (1)-(2) is incomplete and we need an extra equation for the Cauchy stress. The simplest relation for the stress and the velocity is provided by Newton's hypothesis

$$\boldsymbol{\sigma} = -p\mathbf{I} + \eta_s(\nabla \mathbf{v} + \nabla \mathbf{v}^T), \tag{3}$$

where  $\eta_s$  is a constant viscosity and  $p$  is the pressure. Substituting (3) into (2) one obtains the famous Navier-Stokes equations

$$\rho \left( \frac{\partial \mathbf{v}}{\partial t} + \mathbf{v} \cdot \nabla \mathbf{v} \right) + \nabla p - \eta_s \Delta \mathbf{v} = \mathbf{f}. \tag{4}$$

The fluids for which (3) is valid are called Newtonian and water (under normal conditions) is the most important example of these. However, fluids with more complex microstructure (e.g. polymer solutions and melts) can exhibit specific features such as shear-thinning, non-zero normal stress differences in shear flows and memory effects, that cannot be explained by the Newtonian theory. One must then abandon the hypothesis (3) and use instead some other constitutive relation for the stress tensor that is usually much more complicated.

Constitutive models for polymeric fluids can be constructed on two different levels: continuum mechanics [17] and kinetic theory [18]. Continuum mechanics attempts to provide

macroscopic equations of state (usually referred to as constitutive equations) that are founded empirically or microscopically. The simplest examples of constitutive equations are generalizations of the Newtonian law (3) with a viscosity dependent on the velocity gradient. More involved constitutive equations for viscoelastic fluids are usually differential equations or integral equations along the particle paths. Some of the best known examples are the class of Oldroyd models [97] with the special case of Maxwell models. The first numerical simulations for non-trivial geometries using closed-form constitutive equations were performed at the end of the 1970's. Then the so-called *High Weissenberg Numerical Problem* made its first appearance. This problem consists in the breakdown of any numerical method as the Weissenberg number, which is a non-dimensional measure of elasticity of the fluid, is increased and is probably related to the ill-posedness of the governing equations under high Weissenberg numbers. Indeed, existence and uniqueness results are usually known only for sufficiently low Weissenberg numbers (see, for example, [7] for a review).

Polymer kinetic theory attempts to understand the polymer dynamics by starting from a coarse-grained description of polymer chains by representing them as e.g. chains of springs or rods. Statistical mechanics then provides a partial differential equation (PDE) known as the diffusion equation or the Fokker-Planck (FP) equation for the probability density of the microstructural quantities and the stress is obtained as the mean of some function of these quantities. In comparison with the continuum mechanics approach, the kinetic theory gives researchers more freedom and flexibility in incorporating their knowledge and intuition into the models, and this in turn should give rise to better predictions of complex behavior of polymeric fluids.

In some cases, one can derive a macroscopic constitutive equations for the stress starting from the kinetic theory model. The best known example is the interpretation of the Oldroyd B model as a suspension of Hookean dumbbells, i.e. two beads connected by a linear spring. In the present thesis (Chapter 3) we use this equivalence to construct some new numerical methods that are proved to be more stable than the traditional methods, which discretize directly the macroscopic constitutive equation.

In general, however, it is impossible to derive a closed-form constitutive equation for the stress, which is equivalent to a kinetic theory model, and this fact may make kinetic models very complicated for analytical and numerical investigation. One is therefore led to construct efficient numerical techniques to simulate flows using models for which no constitutive equation exists. The most popular way is to use the equivalence existing between FP equations and stochastic differential equations. One can then start from the stochastic differential equation, introduce a large number of pseudo-random realizations of microstructural quantities and solve a PDE for each of them that can be discretized by finite elements or any other numerical technique (micro-macro or CONNFESSIT approach [99]). All this must be coupled with the momentum and continuity equations for the velocity and pressure. It is easy to see that such a technique is extremely expensive, even in one of its most efficient versions, the Brownian configuration fields method [64].

One can try to alleviate the three main disadvantages of the Brownian configuration fields method, which are large CPU cost, huge memory requirements and the presence of statistical noise in the computed elastic extra-stress, by solving directly the FP equation for the probability density instead of the stochastic differential equation. A review of the literature reveals that very little has been done in order to advocate this approach, mainly due to the lack of efficient numerical techniques to solve the FP equation. In the pioneering work of Warner in 1972

[132] the FP equation was used to solve the steady-state shearing flow and small-amplitude oscillatory shearing flow of a FENE fluid. It was only thirteen years later, in 1985, that Fan [43] improved the original idea of Warner by requiring that the probability density function be smooth at the origin, leading to more accurate results. In [44] the method was extended to encapsulated dumbbells. The dilute multibead-rod model was the model of choice of Fan in 1989 in a series of two papers [45, 46]. The second paper is, to our knowledge, the first attempt in the published literature to use the FP equation for flows in complex geometries. In recent work by a group in MIT [2], the start-up of steady shear flow for dilute solutions of rigid rod-like macromolecules was also treated with the FP equation using Daubechies wavelets for the discretization in configuration space. In [96], this method was used to simulate the dynamics of both the rigid dumbbell model and the Doi model for liquid crystalline polymers in a complex flow environment (see also [125]). In the present thesis, we introduce some fast numerical methods for the FP equations for some models of dilute (Chapter 4) and concentrated (Chapter 5) polymer solutions and compare them with stochastic simulations. It turns out that FP-based methods can be significantly more efficient than their stochastic counterparts for models with low-dimensional configuration space.

To date, most numerical simulations of viscoelastic flows have been performed using finite difference, finite volume and finite element methods for the discretization in physical space. However, spectral and pseudospectral methods have, since 1987, also enjoyed extensive (and largely successful) use in solving smooth viscoelastic flow problems, most notably through the efforts of research groups at Delaware [4, 5, 10, 11, 13, 117, 118, 119, 127] and Aberystwyth [35, 55, 104, 105, 107, 121, 122]. In this thesis, we use a variant of pseudospectral methods called the *spectral element method* as implemented by Chauvière and Owens in [33] including a special treatment of the hyperbolic constitutive equation (a combination of streamline upwind Petrov/Galerkin method and element-by-element approach).

The outline of this thesis is as follows:

- In Chapter 1, we present the models for polymeric liquids used in this work. We start with a description of dumbbell models for dilute polymer solutions and related constitutive equations. We then present briefly some models suitable for describing concentrated polymer solutions and conclude the chapter with an introduction to stochastic simulation techniques. All the material of this chapter is well-known and we follow in its presentation the textbooks [18], [99] and [108]. However, in contrast to [18] and following [42, 15, 16, 116], special attention is paid here to the proper formulation of the model in non-homogeneous flows.
- Chapter 2 is also of introductory character. We introduce spectral methods; these being our principal numerical tools. The basic facts about orthogonal polynomials and quadrature formulas are borrowed from [26]. We also give some details about the implementation of a spectral element method for the Oldroyd B model with the special treatment of the constitutive equation, following [33], and some numerical examples for the start-up Couette flow of an Oldroyd B fluid from [84].
- The presentation of our main results begins in Chapter 3. We consider models of dilute polymer solutions (Oldroyd B [97] and FENE-P [112]) having constitutive equations but regarded from the viewpoint of kinetic theory. This viewpoint enables us to construct some new numerical methods that are more robust than their conventional counterparts

and prove some theoretical results. The results of this chapter have been published in [29] and [82].

- In Chapter 4 we turn our attention to the models that do not possess the closed-form constitutive equations. We consider here the FENE dumbbell model for the dilute polymer solutions and give a description of FP-based numerical methods for its simulation. We compare FP-based simulation with the stochastic ones in terms of CPU cost and accuracy. The last section of this chapter is devoted to numerical simulations of a strongly non-homogeneous flow of a FENE fluid in a narrow channel. The results of this chapter have been published in [30], [31], [80] and submitted for publication in [83].
- Chapter 5 contains results of a similar nature to those of the preceding chapter, but concentrated polymer solutions and melts are considered here. We have chosen a reptation model by Öttinger [100] for our numerical simulations and we present some modifications of this model that allow us to achieve better agreement with the experimental data. The results of this chapter have been published for the most part in [81]. The modification of the Öttinger model is a part of the submitted article [50].

Finally, we conclude with a summary of our results and a description of some outstanding issues.



# Chapter 1

## Modelling polymeric liquids

### 1.1 Dumbbell models for dilute polymer solutions

#### 1.1.1 The Fokker-Planck equation

Many of the interesting properties of dilute polymer solutions can be understood by modelling them as suspensions of simple coarse-grained objects (e.g. dumbbells<sup>1</sup>) in a Newtonian liquid. A schematic diagram of a dumbbell is given in Fig. 1.1 and shows two beads, each of mass

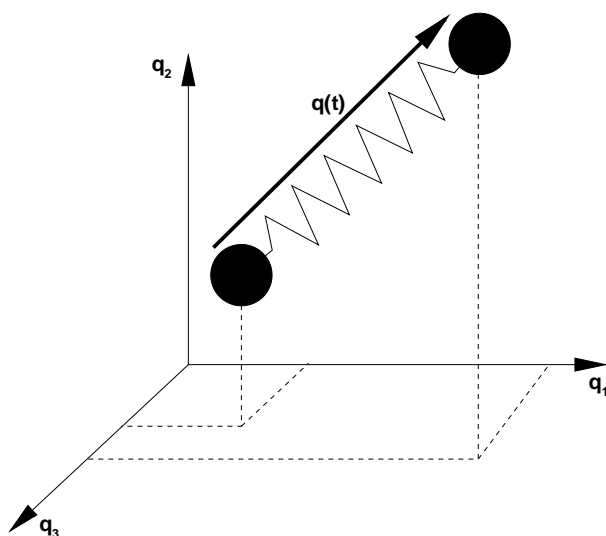


Figure 1.1: Representation of polymer molecules by dumbbells.

$m$  joined by a massless nonlinear spring. We denote the position vectors of the two beads relative to some fixed origin by  $\mathbf{r}_1$  and  $\mathbf{r}_2$ , and  $\mathbf{q} = \mathbf{r}_2 - \mathbf{r}_1$  and  $\mathbf{x} = \frac{1}{2}(\mathbf{r}_1 + \mathbf{r}_2)$  therefore denote, respectively, a dumbbell end-to-end vector and the position vector of the dumbbell's centre of mass. Neglecting acceleration terms, and in the absence of external forces, a force balance

---

<sup>1</sup>Much more complicated objects, e.g. chains of springs or rods, can be used to render the model more realistic, see [18].

equation for the beads yields

$$\zeta \left( \frac{d\mathbf{r}_1}{dt} - \mathbf{v}(\mathbf{r}_1) \right) = \mathbf{B}_1 - \mathbf{F}(\mathbf{r}_1 - \mathbf{r}_2), \quad (1.1)$$

$$\zeta \left( \frac{d\mathbf{r}_2}{dt} - \mathbf{v}(\mathbf{r}_2) \right) = \mathbf{B}_2 - \mathbf{F}(\mathbf{r}_2 - \mathbf{r}_1), \quad (1.2)$$

where  $\zeta$  is a friction coefficient and  $\mathbf{v}(\mathbf{r}_i)$  ( $i = 1, 2$ ) denotes the solvent velocity at the point with position vector  $\mathbf{r}_i$ . In (1.1) and (1.2)  $\mathbf{B}_i$  denotes the Brownian force acting on bead  $i$  and  $\mathbf{F}$  the intermolecular spring force.

The simplest law for the spring force used in the polymer science is the Hookean one:

$$\mathbf{F}(\mathbf{q}) = H\mathbf{q} \quad (1.3)$$

where  $H$  is a spring constant. This law is very attractive mathematically since it allows one to develop a closed-form constitutive equation for the elastic extra-stress (see Section 1.1.5 below) and it is suitable for modelling certain classes of polymeric fluids (Boger fluids). However, it is limited essentially to slow to moderately fast flows since at high flow rate and in extensional flow the dumbbells can extend in length unboundedly, which is certainly not physical. This problem can be cured by incorporating a maximum extensibility into the force law. This is done in another popular model introduced by Warner [132] and known as the Finitely Extensible Non-linear Elastic (FENE) model:

$$\mathbf{F}(\mathbf{q}) = \frac{H\mathbf{q}}{1 - |\mathbf{q}|^2/Q_{\max}^2}, \quad (1.4)$$

where  $Q_{\max}$  is the maximum length of the spring .

Let us introduce the phase-space distribution function  $f(\mathbf{r}_1, \mathbf{r}_2, \dot{\mathbf{r}}_1, \dot{\mathbf{r}}_2, t)$ , defined to be such that  $f(\mathbf{r}_1, \mathbf{r}_2, \dot{\mathbf{r}}_1, \dot{\mathbf{r}}_2, t) d\mathbf{r}_1 d\mathbf{r}_2 d\dot{\mathbf{r}}_1 d\dot{\mathbf{r}}_2$  is the expected number of dumbbells at time  $t$  having bead positions and velocities in the differential boxes  $[\mathbf{r}_i, \mathbf{r}_i + d\mathbf{r}_i]$  and  $[\dot{\mathbf{r}}_i, \dot{\mathbf{r}}_i + d\dot{\mathbf{r}}_i]$  ( $i = 1, 2$ ), respectively. Then, defining a configuration distribution function  $\psi^{12}(t, \mathbf{r}_1, \mathbf{r}_2)$  as the marginal distribution

$$\psi^{12}(t, \mathbf{r}_1, \mathbf{r}_2) = \int_{\dot{\mathbf{r}}_1, \dot{\mathbf{r}}_2} f(\mathbf{r}_1, \mathbf{r}_2, \dot{\mathbf{r}}_1, \dot{\mathbf{r}}_2, t) d\dot{\mathbf{r}}_1 d\dot{\mathbf{r}}_2, \quad (1.5)$$

it may be shown (see [18], for example), that the equation of continuity for  $\psi$  is

$$\frac{\partial \psi^{12}}{\partial t} = -\frac{\partial}{\partial \mathbf{r}_1} \cdot [\ll \dot{\mathbf{r}}_1 \gg \psi] - \frac{\partial}{\partial \mathbf{r}_2} \cdot [\ll \dot{\mathbf{r}}_2 \gg \psi], \quad (1.6)$$

where the average  $\ll \cdot \gg$  over velocity space for a quantity  $A$  is defined by

$$\ll A \gg = \frac{1}{\psi} \int_{\dot{\mathbf{r}}_1, \dot{\mathbf{r}}_2} A f(\mathbf{r}_1, \mathbf{r}_2, \dot{\mathbf{r}}_1, \dot{\mathbf{r}}_2, t) d\dot{\mathbf{r}}_1 d\dot{\mathbf{r}}_2. \quad (1.7)$$

By taking the velocity-space average of (1.1)-(1.2) throughout we get

$$\zeta \left( \ll \frac{d\mathbf{r}_1}{dt} \gg - \mathbf{v}(\mathbf{r}_1) \right) = \ll \mathbf{B}_1 \gg - \mathbf{F}(\mathbf{r}_1 - \mathbf{r}_2), \quad (1.8)$$

$$\zeta \left( \ll \frac{d\mathbf{r}_2}{dt} \gg - \mathbf{v}(\mathbf{r}_2) \right) = \ll \mathbf{B}_2 \gg - \mathbf{F}(\mathbf{r}_2 - \mathbf{r}_1), \quad (1.9)$$

and, assuming equilibration in momentum space (Maxwellian velocity distribution), the statistically averaged Brownian force  $\ll \mathbf{B}_i \gg$  ( $i = 1, 2$ ) may be written

$$\ll \mathbf{B}_i \gg = -\frac{1}{\psi} \frac{\partial}{\partial \mathbf{r}_i} \cdot [\ll m(\dot{\mathbf{r}}_i - \mathbf{v})(\dot{\mathbf{r}}_i - \mathbf{v}) \gg \psi] = -kT \frac{\partial}{\partial \mathbf{r}_i} \ln \psi. \quad (1.10)$$

Thus, from (1.6) and (1.8)-(1.9) we may write down the non-homogeneous FP equation

$$\begin{aligned} \frac{\partial \psi^{12}}{\partial t} = & -\frac{\partial}{\partial \mathbf{r}_1} \cdot \left[ \mathbf{v}(\mathbf{r}_1) \psi^{12} - \frac{1}{\zeta} \mathbf{F}(\mathbf{r}_1 - \mathbf{r}_2) \psi^{12} \right] \\ & -\frac{\partial}{\partial \mathbf{r}_2} \cdot \left[ \mathbf{v}(\mathbf{r}_2) \psi^{12} - \frac{1}{\zeta} \mathbf{F}(\mathbf{r}_2 - \mathbf{r}_1) \psi^{12} \right] + \frac{kT}{\zeta} \frac{\partial^2 \psi^{12}}{\partial \mathbf{r}_1^2} + \frac{kT}{\zeta} \frac{\partial^2 \psi^{12}}{\partial \mathbf{r}_2^2}, \end{aligned} \quad (1.11)$$

or, in terms of the independent variables  $\mathbf{x}$  and  $\mathbf{q}$ , and defining

$$\psi^c(t, \mathbf{x}, \mathbf{q}) = \psi^{12}(t, \mathbf{x} - \mathbf{q}/2, \mathbf{x} + \mathbf{q}/2) :$$

$$\begin{aligned} \frac{\partial \psi^c}{\partial t} = & \frac{\partial}{\partial \mathbf{q}} \cdot \left( \frac{2kT}{\zeta} \frac{\partial \psi^c}{\partial \mathbf{q}} + \frac{2\psi^c \mathbf{F}(\mathbf{q})}{\zeta} - [\mathbf{v}(\mathbf{x} + \mathbf{q}/2) - \mathbf{v}(\mathbf{x} - \mathbf{q}/2)] \psi^c \right) \\ & + \frac{\partial}{\partial \mathbf{x}} \cdot \left( \frac{kT}{2\zeta} \frac{\partial \psi^c}{\partial \mathbf{x}} - \frac{\mathbf{v}(\mathbf{x} - \mathbf{q}/2) + \mathbf{v}(\mathbf{x} + \mathbf{q}/2)}{2} \psi^c \right). \end{aligned} \quad (1.12)$$

### 1.1.2 Stress tensor

Taking an arbitrary surface in the dumbbell solution we consider the contribution to the elastic stress tensor at a point  $P$  with position vector  $\mathbf{r}$  due to (a) the spring tension in dumbbells straddling the surface at  $P$  and (b) changes in momentum brought about by beads passing through the surface at  $P$ . Thus, denoting the total Cauchy stress tensor at  $P$  at time  $t$  by  $\boldsymbol{\sigma}(\mathbf{r}, t)$  we decompose  $\boldsymbol{\sigma}$  into the sum

$$\boldsymbol{\sigma} = \boldsymbol{\sigma}^S + \boldsymbol{\sigma}^C + \boldsymbol{\sigma}^K, \quad (1.13)$$

where  $\boldsymbol{\sigma}^S$  denotes the solvent contribution,  $\boldsymbol{\sigma}^C$  the spring tension contribution and  $\boldsymbol{\sigma}^K$  the bead motion contribution. The expressions for all these contributions in the homogeneous flow case can be found in the book of Bird et al. [18]. We use their extensions to the non-homogeneous flow case developed by Biller and Petruccione [16, 116]:

$$\boldsymbol{\sigma}^S = -p\mathbf{I} + \eta_s(\nabla \mathbf{v} + \nabla \mathbf{v}^T), \quad (1.14)$$

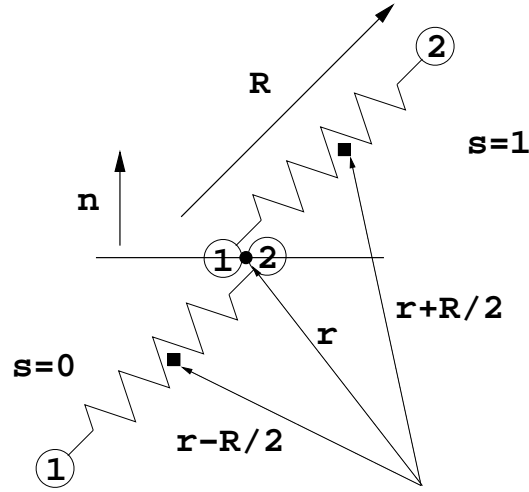
$$\boldsymbol{\sigma}^C(t, \mathbf{r}) = \int \int_{s=0}^1 \mathbf{q} \mathbf{F}(\mathbf{q}) \psi^c(t, \mathbf{r} + (s - 1/2)\mathbf{q}, \mathbf{q}) ds d\mathbf{q}, \quad (1.15)$$

and

$$\boldsymbol{\sigma}^K(t, \mathbf{r}) = -2n(t, \mathbf{r})kT\mathbf{I}, \quad (1.16)$$

where

$$n(t, \mathbf{r}) = \int \psi^c(t, \mathbf{r} + \mathbf{q}/2, \mathbf{q}) d\mathbf{q} \quad (1.17)$$

Figure 1.2: Computation of  $\sigma^C$ .

is the polymer number density. In writing the integrals appearing in (1.15) and (1.17) we assume that  $\psi^c$  is set to zero for “forbidden” configurations i.e., those that mean that a bead leaves the flow domain. The integration with respect to  $\mathbf{q}$  can be thus performed over the whole of  $\mathbb{R}^d$ .

In (1.14)  $p$  is a pressure contribution from the solvent,  $\eta_s$  is the solvent viscosity and  $\dot{\boldsymbol{\gamma}}$  is the rate-of-strain tensor  $\nabla \mathbf{v} + \nabla \mathbf{v}^T$ . (1.17) takes into account our assumption that the mass is concentrated at the beads of the dumbbells. (1.15) is slightly different from the equivalent formula of Bird et al. (see Eq.(13.3-5) of [18]) and takes account of the fact that  $\psi^c$  depends upon  $\mathbf{x}$ . As shown in Fig. 1.2, as the parameter  $s$  varies from 0 to 1 all dumbbells having end-to-end vector  $\mathbf{q}$  and straddling the line at the point with position vector  $\mathbf{r}$  are accounted for: from those with bead “2” having position vector  $\mathbf{r}$  ( $s = 0$ ) to those with bead “1” lying on the line ( $s = 1$ ). If  $\mathbf{n}$  is a unit normal vector to the line then  $\mathbf{q} \cdot \mathbf{n} \psi(\mathbf{r} + (s - 1/2)\mathbf{q}, \mathbf{q}, t) ds$  is the expected number of dumbbells with end-to-end vector  $\mathbf{q}$  whose centres of mass lie in a parallelogram of unit length, of height  $\mathbf{q} \cdot \mathbf{n} ds$  and located at a distance  $(s - 1/2)\mathbf{q} \cdot \mathbf{n}$  from the line.

As in [18] the bead motion contribution  $\sigma^K$  gives rise to an extra pressure term where equilibration in momentum space has been assumed in the derivation of (1.16).

### 1.1.3 Homogeneous flows

Let us consider homogeneous flows, i.e. flows with prescribed velocity field of the form

$$\mathbf{v}(\mathbf{x}) = \boldsymbol{\kappa}(\mathbf{x} - \mathbf{x}_0) + \mathbf{v}_0 \quad (1.18)$$

where  $\boldsymbol{\kappa}$  is a traceless matrix that can depend on time but does not depend on  $\mathbf{x}$  and  $\mathbf{x}_0$  is some reference point. In such a flow, the FP equation (1.12) reduces to

$$\frac{\partial \psi^c}{\partial t} = \frac{\partial}{\partial \mathbf{q}} \cdot \left( -\boldsymbol{\kappa} \mathbf{q} \psi^c + \frac{2kT}{\zeta} \frac{\partial \psi^c}{\partial \mathbf{q}} + \frac{2\psi^c \mathbf{F}(\mathbf{q})}{\zeta} \right) \quad (1.19)$$

and has a solution  $\psi^c(t, \mathbf{q})$  independent of  $\mathbf{x}$ . It is easy to see by integrating (1.19) over configuration space that the integral  $\int \psi^c(t, \mathbf{q}) d\mathbf{q}$  is conserved. In view of (1.17), it means that the polymer number density is constant. The polymer number density will be denoted from now on by  $n_p$ .

In order to rewrite the FP equation in a more conventional and convenient form, we non-dimensionalize  $\mathbf{q}$  as  $\mathbf{q}/l_0$ , where  $l_0 = \sqrt{kT/H}$  is a characteristic microscopic length scale (characteristic dumbbell size<sup>2</sup>) and introduce a characteristic relaxation time  $\lambda = \zeta/4H$ . The non-dimensional force laws looks like:

$$\mathbf{F}(\mathbf{q}) = \mathbf{q}, \quad (1.20)$$

for Hookean dumbbells and

$$\mathbf{F}(\mathbf{q}) = \frac{\mathbf{q}}{1 - |\mathbf{q}|^2/b}, \quad (1.21)$$

for FENE dumbbells with the non-dimensional extensibility parameter  $b = Q_{\max}^2/l_0^2$ . We also normalize the configuration distribution function  $\psi^c$  by  $n_p$  in order to obtain the probability density function (pdf)  $\psi$ , for which we have

$$\int \psi(t, \mathbf{q}) d\mathbf{q} = 1. \quad (1.22)$$

In this notation, the FP equation (1.19) takes the form

$$\frac{\partial \psi}{\partial t} = \frac{\partial}{\partial \mathbf{q}} \cdot \left( -\boldsymbol{\kappa} \mathbf{q} \psi + \frac{1}{2\lambda} \frac{\partial \psi}{\partial \mathbf{q}} + \frac{1}{2\lambda} \mathbf{F}(\mathbf{q}) \psi \right) \quad (1.23)$$

and (1.15) can be rewritten as

$$\boldsymbol{\sigma}^C(t) = n_p kT \int \mathbf{q} \mathbf{F}(\mathbf{q}) \psi(t, \mathbf{q}) d\mathbf{q}. \quad (1.24)$$

The bead motion contribution to the stress  $\boldsymbol{\sigma}^K$  is constant and equal to  $-2n_p kT \mathbf{I}$ .

Let us consider now several important special cases.

## 1. Equilibrium solution

We put  $\boldsymbol{\kappa} = \mathbf{0}$  so that the velocity is constant everywhere. The FP equation (1.23) then has the steady-state equilibrium solution  $\psi_{eq}$ , which satisfies for any isotropic force law, the equation

$$\frac{\partial \psi_{eq}}{\partial \mathbf{q}} + \mathbf{F}(\mathbf{q}) \psi_{eq} = \mathbf{0}. \quad (1.25)$$

In particular, we have for Hookean dumbbells

$$\psi_{eq} = C \exp\left(-\frac{|\mathbf{q}|^2}{2}\right),$$

---

<sup>2</sup>Strictly speaking,  $l_0^2 d$  is the expectation of  $|\mathbf{q}|^2$  for zero velocity equilibrium distribution in the  $d$ -dimensional Hookean dumbbell model, since the corresponding configuration distribution function is given by  $\psi = C \exp(-|\mathbf{q}|^2/2l_0^2)$ .

and for FENE dumbbells

$$\psi_{eq} = C \left( 1 - \frac{|\mathbf{q}|^2}{b} \right)^{b/2},$$

where  $C$  are some normalization constants. By substituting  $\psi = \psi_{eq}$  into (1.25) and using (1.24), we obtain that  $\boldsymbol{\sigma}^C + \boldsymbol{\sigma}^K = -n_p k T \mathbf{I}$  at equilibrium.

In general situation of non-zero velocity it is customary to incorporate the equilibrium polymeric contribution to the stress ( $-n_p k T \mathbf{I}$ ) to the pressure term (adding a constant to the pressure does not change the dynamics of an incompressible fluid) and to combine the rest of  $\boldsymbol{\sigma}^K$  and  $\boldsymbol{\sigma}^C$  into the tensor  $\boldsymbol{\tau}$ :

$$\boldsymbol{\tau}(t) = n_p k T \left( -\mathbf{I} + \int \mathbf{q} \mathbf{F}(\mathbf{q}) \psi(t, \mathbf{q}) d\mathbf{q} \right), \quad (1.26)$$

which can be called the elastic extra-stress. Equation (1.26) is known as the Kramers expression.

## 2. Steady state shear flow

Let the velocity gradient  $\boldsymbol{\kappa}$  be set to

$$\boldsymbol{\kappa} = \dot{\gamma} \mathbf{A}_s \text{ with } \mathbf{A}_s = \begin{pmatrix} 0 & 1 & 0 \\ 0 & 0 & 0 \\ 0 & 0 & 0 \end{pmatrix}.$$

Such a flow is known as steady-state shear flow and  $\dot{\gamma}$  is called the shear rate. The stationary solution of (1.23) cannot be found analytically for a general force law in this case, but it is relatively easy to construct a first-order approximation in the limit of small  $\dot{\gamma}$  (§13.5 of [18]). To see this, we represent the pdf as  $\psi = \psi_{eq}(1 + \lambda \dot{\gamma} \psi_1 + O((\lambda \dot{\gamma})^2))$ , substitute it into (1.23) and take into account (1.25) to obtain the equation for  $\psi_1$

$$\frac{\partial}{\partial \mathbf{q}} \cdot \left( \psi_{eq} \frac{\partial \psi_1}{\partial \mathbf{q}} \right) = 2 \frac{\partial}{\partial \mathbf{q}} \cdot (\mathbf{A}_s \mathbf{q} \psi_{eq})$$

that has solutions  $\psi_1 = \mathbf{A}_s : \mathbf{q} \mathbf{q}$ . By substituting  $\psi = \psi_{eq}(1 + \lambda \dot{\gamma} \psi_1 + O((\lambda \dot{\gamma})^2))$  into (1.26), we obtain the expression for the shear stress<sup>3</sup>

$$\tau_{xy} = \lambda \dot{\gamma} \begin{cases} n_p k T, & \text{for Hookean dumbbells,} \\ n_p k T \frac{b}{b+d+2} + O((\lambda \dot{\gamma})^3), & \text{for } d\text{-dimensional FENE dumbbells.} \end{cases}$$

We recall that the coefficient of proportionality between the viscous shear stress and the shear rate in the Newtonian fluids is called the viscosity of the fluid. By analogy, we term the coefficient of proportionality between the elastic extra-stress and the shear-rate in polymeric liquids at small shear rates as the polymeric viscosity and denote it by  $\eta_p$ . Using this notation, the formula for  $\boldsymbol{\tau}$  can be rewritten for Hookean dumbbells as

$$\boldsymbol{\tau}(t) = \frac{\eta_p}{\lambda} \left( -\mathbf{I} + \int \mathbf{q} \mathbf{q} \psi(t, \mathbf{q}) d\mathbf{q} \right) \quad (1.27)$$

<sup>3</sup>Note that this expression is exact for Hookean dumbbells as it can be most easily seen from the equivalent Oldroyd B constitutive equation in Section 1.1.5 below.

and for FENE dumbbells as

$$\boldsymbol{\tau}(t) = \frac{\eta_p}{\lambda} \left( \frac{b+d+2}{b} \right) \left( -\mathbf{I} + \int \frac{\mathbf{q}\mathbf{q}}{1-|\mathbf{q}|^2/b} \psi(t, \mathbf{q}) d\mathbf{q} \right).$$

Taking into account the second term in the expansion of  $\psi$  in powers of  $\lambda\dot{\gamma}$ , one can show that there are non-zero normal stress differences  $\tau_{xx} - \tau_{yy}$  and  $\tau_{yy} - \tau_{zz}$ . This phenomenon is one of characteristic features of non-linear viscoelastic fluids.

### 3. Extensional flows

Two other important special cases are planar extensional flow with the velocity gradient

$$\boldsymbol{\kappa} = \dot{\boldsymbol{\varepsilon}} \begin{pmatrix} 1 & 0 & 0 \\ 0 & -1 & 0 \\ 0 & 0 & 0 \end{pmatrix}. \quad (1.28)$$

and uniaxial extensional flow with the velocity gradient

$$\boldsymbol{\kappa} = \dot{\boldsymbol{\varepsilon}} \begin{pmatrix} -\frac{1}{2} & 0 & 0 \\ 0 & -\frac{1}{2} & 0 \\ 0 & 0 & 1 \end{pmatrix}. \quad (1.29)$$

In both cases,  $\dot{\boldsymbol{\varepsilon}}$  is called the extensional rate. The FP equation (1.23) has a steady-state analytical solution for both types of extensional flows (and more generally for any symmetric matrix  $\boldsymbol{\kappa}$ ). This solution is given by formula (13.2-14) in [18] and has the form

$$\psi = C \left( 1 - \frac{|\mathbf{q}|^2}{b} \right)^{b/2} \exp(\lambda \boldsymbol{\kappa} : \mathbf{q}\mathbf{q}) \quad (1.30)$$

where  $C$  is some normalization constant.

#### 1.1.4 Local homogeneity assumption

Let us return to the general situation of a non-homogeneous velocity field and adopt the local homogeneity assumption: the velocity  $\mathbf{v}$  and the configuration density  $\psi^c$  are linear on the length scale of the dumbbell. More precisely,  $l_0^2[\partial^2 \mathbf{v}/\partial \mathbf{x}^2] \ll [\mathbf{v}]$  and  $l_0^2[\partial^2 \psi^c/\partial \mathbf{x}^2] \ll [\psi^c]$  where the brackets  $[\cdot]$  denote the characteristic value of the corresponding quantity. After the non-dimensionalization of  $\mathbf{q}$  and the introduction of the relaxation time  $\lambda$ , as in the preceding section, the FP equation (1.12) takes the form

$$\begin{aligned} \frac{\partial \psi^c}{\partial t} + \frac{\mathbf{v}(\mathbf{x} - \mathbf{q}/2) + \mathbf{v}(\mathbf{x} + \mathbf{q}/2)}{2} \cdot \frac{\partial \psi^c}{\partial \mathbf{x}} = \\ \frac{\partial}{\partial \mathbf{q}} \cdot \left( \frac{1}{2\lambda} \frac{\partial \psi^c}{\partial \mathbf{q}} + \frac{1}{2\lambda} \mathbf{F}(\mathbf{q}) \psi^c - [\mathbf{v}(\mathbf{x} + \mathbf{q}/2) - \mathbf{v}(\mathbf{x} - \mathbf{q}/2)] \psi^c \right) + \frac{l_0^2}{8\lambda} \frac{\partial}{\partial \mathbf{x}} \cdot \frac{\partial \psi^c}{\partial \mathbf{x}}. \end{aligned} \quad (1.31)$$

Using the Taylor expansion of the velocity in the vicinity of  $\mathbf{x}$  and neglecting the second-order derivatives of  $\mathbf{v}$  and  $\psi^c$  multiplied by  $l_0^2$  in accordance with the local homogeneity assumption, we can simplify (1.31) as

$$\frac{D\psi}{Dt} = \frac{\partial}{\partial \mathbf{q}} \cdot \left( -\nabla \mathbf{v} \cdot \mathbf{q} \psi + \frac{1}{2\lambda} \frac{\partial \psi}{\partial \mathbf{q}} + \frac{1}{2\lambda} \mathbf{F}(\mathbf{q}) \psi \right) \quad (1.32)$$

where

$$\frac{D}{Dt} = \frac{\partial}{\partial t} + \mathbf{v}(\mathbf{x}) \cdot \frac{\partial}{\partial \mathbf{x}}$$

is the material derivative and  $\nabla \mathbf{v}$  is the velocity gradient:  $\nabla v_{ij} = \partial v_i / \partial x_j$ . From now on, we drop the superscript  $c$  in  $\psi^c$  for the reasons explained in the next paragraph.

The formulas for the stress and the polymer number density can be also simplified under the local homogeneity assumption. Indeed, expanding (1.17) as a Taylor series, we get

$$n(t, \mathbf{r}) = \int \psi(t, \mathbf{r}, \mathbf{q}) d\mathbf{q} + \int l_0 \frac{\partial \psi}{\partial \mathbf{x}}(t, \mathbf{r}, \mathbf{q}) \cdot \frac{\mathbf{q}}{2} d\mathbf{q} + \int l_0^2 \frac{\partial}{\partial \mathbf{x}} \frac{\partial}{\partial \mathbf{x}} \psi(t, \mathbf{r} + \theta \mathbf{q}, \mathbf{q}) : \frac{\mathbf{q} \mathbf{q}}{2} d\mathbf{q}$$

( $\theta \in [0, 1]$ ). The first-order term here is zero due to the symmetry of  $\psi$  if the boundary effects are not taken into account. The second-order term can be neglected by the local homogeneity assumption. Hence, we obtain

$$n(t, \mathbf{r}) = \int \psi(t, \mathbf{r}, \mathbf{q}) d\mathbf{q}$$

and we can see from (1.32) that the polymer number density is conserved. As in the homogeneous flow case, we denote the constant polymer number density by  $n_p$ , normalize  $\psi$  by (1.22) and term it the probability density function. By simplifying in the analogous way, the formulas for the stress, we can recover the Kramers expression (1.26) for the elastic extra-stress. The FP equation (1.32) can be now regarded as an equation for the pdf. It is the same as the FP equation (1.19) of the homogeneous flow case, but the derivative in time is now understood as the material derivative.

To evaluate the validity of the local homogeneity assumption, we consider the characteristic macroscopic length  $L$ . The quantities  $l_0^2[\partial^2 \mathbf{v} / \partial \mathbf{x}^2] / [\mathbf{v}]$  and  $l_0^2[\partial^2 \psi^c / \partial \mathbf{x}^2] / [\psi^c]$  can be estimated in the bulk as  $l_0^2 / L^2$ . In common situations this ratio is indeed negligibly small. For example, it has been estimated interpreted by Bhave et al. [15] to be from  $\mathcal{O}(10^{-9})$  to  $\mathcal{O}(10^{-7})$  when  $L \approx 1$  cm. Therefore, the principal difference between stress and number density predictions based on the solution to (1.31) and (1.32) are to be seen in thin boundary layers. This is unsurprising since it is precisely near physical boundaries that a dumbbell is restricted in the configurations that it may adopt and the usual homogeneous flow assumption is most easily seen to be violated. The local homogeneity assumption can thus be advocated for most polymer flows, where macroscopic length scale is much greater than the typical molecule length. We recall that El-Kareh and Leal [42] expressed the hope that introducing diffusion in physical space could increase the stability of numerical methods, however small the diffusivity coefficient was. However, numerical experiments [127] reveal that for stabilization one needs much larger diffusivity coefficients than those predicted by the kinetic theory. In the last section of Chapter 4 we shall describe a simulation of a flow in a very narrow channel, in which  $(l_0/L)^2$  is not negligible.

Let us summarize the mathematical model under the local homogeneity assumption. The total Cauchy stress is  $\boldsymbol{\sigma} = -p\mathbf{I} + \eta_s(\nabla \mathbf{v} + \nabla \mathbf{v}^T) + \boldsymbol{\tau}$  where  $\boldsymbol{\tau}$  should be calculated by (1.26). Substituting this expression for  $\boldsymbol{\sigma}$  into (2) we obtain the equation for the velocity and pressure

$$\rho \left( \frac{\partial \mathbf{v}}{\partial t} + \mathbf{v} \cdot \nabla \mathbf{v} \right) - \eta_s \Delta \mathbf{v} + \nabla p = \nabla \cdot \boldsymbol{\tau} + \mathbf{f}. \quad (1.33)$$



Equations (1), (1.33) and (1.32) form a complete system that should be supplied by the boundary and initial conditions. We choose Dirichlet boundary condition for the velocity

$$\mathbf{v}|_{\Gamma} = \mathbf{g}, \quad (1.34)$$

where  $\Gamma$  is the boundary of  $\Omega$ . Due to the hyperbolic nature (in physical space) of the FP equation (1.32), the pdf  $\psi$  should be prescribed only on the inflow part of the boundary

$$\Gamma_{in} = \{\mathbf{x} \in \Gamma : \mathbf{v}(\mathbf{x}) \cdot \mathbf{n}(\mathbf{x}) < 0\}, \quad (1.35)$$

where  $\mathbf{n}$  is the outward normal unit vector, so that

$$\psi|_{\Gamma_{in}} = \psi_{in}. \quad (1.36)$$

The initial conditions for  $\psi$  are

$$\psi(0, \mathbf{x}) = \psi_0(\mathbf{x}). \quad (1.37)$$

If  $\rho > 0$  we should additionally supply the initial condition for the velocity

$$\mathbf{v}(0, \mathbf{x}) = \mathbf{v}_0(\mathbf{x}). \quad (1.38)$$

### 1.1.5 Constitutive equations

As already mentioned, the Hookean dumbbell model (under the local homogeneity assumption) allows one to develop a closed form constitutive equation for the elastic extra-stress. To see this we multiply (1.32) by  $q_i q_j$  and integrate it over configuration space

$$\frac{D}{Dt} \int q_i q_j \psi d\mathbf{q} = \int q_i q_j \frac{\partial}{\partial q_k} \left( -\frac{\partial v_k}{\partial q_l} q_l \psi + \frac{1}{2\lambda} \frac{\partial \psi}{\partial q_k} + \frac{1}{2\lambda} q_k \psi \right) d\mathbf{q}$$

where summation is assumed over repeated indices. We then use integration by parts to obtain

$$\frac{D}{Dt} \int q_i q_j \psi d\mathbf{q} - \frac{\partial v_i}{\partial q_l} \int q_l q_j \psi d\mathbf{q} - \frac{\partial v_j}{\partial q_l} \int q_i q_l \psi d\mathbf{q} + \frac{1}{\lambda} \int q_i q_j \psi d\mathbf{q} = -\frac{1}{2\lambda} \int \left( \frac{\partial \psi}{\partial q_i} q_j + \frac{\partial \psi}{\partial q_j} q_i \right) d\mathbf{q}.$$

Integrating by parts again on the right-hand side and using the normalization (1.22), we get

$$\frac{D}{Dt} \int q_i q_j \psi d\mathbf{q} - \frac{\partial v_i}{\partial q_l} \int q_l q_j \psi d\mathbf{q} - \frac{\partial v_j}{\partial q_l} \int q_i q_l \psi d\mathbf{q} + \frac{1}{\lambda} \int q_i q_j \psi d\mathbf{q} = \frac{1}{\lambda} \delta_{ij}.$$

Denoting

$$\boldsymbol{\tau}' = \frac{\eta_p}{\lambda} \int \mathbf{q} \mathbf{q} \psi d\mathbf{q} \quad (1.39)$$

( $\boldsymbol{\tau}'$  is known as the conformation tensor), we can rewrite the last equation in the compact tensor notation as

$$\boldsymbol{\tau}' + \lambda \overset{\nabla}{\boldsymbol{\tau}'} = \frac{\eta_p}{\lambda} \mathbf{I}, \quad (1.40)$$

where the notation  $\overset{\nabla}{\cdot}$  stands for the upper-convected derivative defined by

$$\overset{\nabla}{\boldsymbol{\tau}'} = \frac{D\boldsymbol{\tau}'}{Dt} - \nabla \mathbf{v} \boldsymbol{\tau}' - \boldsymbol{\tau}' \nabla \mathbf{v}^T.$$

We see from (1.27) that  $\boldsymbol{\tau} = \boldsymbol{\tau}' - \frac{\eta_p}{\lambda} \mathbf{I}$  and note that  $\overset{\nabla}{\mathbf{I}} = -(\nabla \mathbf{v} + \nabla \mathbf{v}^T)$  to obtain the equation for  $\boldsymbol{\tau}$ :

$$\boldsymbol{\tau} + \lambda \overset{\nabla}{\boldsymbol{\tau}} = \eta_p (\nabla \mathbf{v} + \nabla \mathbf{v}^T). \quad (1.41)$$

Equation (1.41) is known as the Oldroyd B equation. It was derived originally from continuum mechanics considerations [97].

The Oldroyd B model can be thus summarized as follows: it consists of 3 equations (1), (1.33) and (1.41) forming a complete system that should be supplied with boundary and initial conditions. We choose Dirichlet boundary condition for the velocity (1.34) and initial condition (1.38) if  $\rho > 0$ . Due to the hyperbolic nature of (1.41), the elastic extra-stress  $\boldsymbol{\tau}$  should be prescribed only on the inflow part of the boundary (1.35) so that

$$\boldsymbol{\tau}|_{\Gamma_{in}} = \boldsymbol{\varphi}. \quad (1.42)$$

The initial conditions for  $\boldsymbol{\tau}$  are

$$\boldsymbol{\tau}(0, \mathbf{x}) = \boldsymbol{\tau}_0(\mathbf{x}). \quad (1.43)$$

It is impossible to derive a closed-form equation for FENE dumbbells. There exist, however, several approximations to this law that have such a closure. The most popular among them is the FENE-P model by Peterlin [112] which is based on a pre-averaging of the FENE spring force, so that in non-dimensional form we have

$$\mathbf{F}(\mathbf{q}) = \frac{\mathbf{q}}{1 - \langle |\mathbf{q}|^2 \rangle / b}, \quad (1.44)$$

where  $\langle \cdot \rangle = \int \cdot d\mathbf{q}$ . In the same way as in deriving the Oldroyd B model, we then get the equation for the conformation tensor  $\mathbf{A} = \langle \mathbf{q}\mathbf{q} \rangle$ :

$$\frac{\mathbf{A}}{1 - \text{tr}\mathbf{A}/b} + \lambda \overset{\nabla}{\mathbf{A}} = \mathbf{I}. \quad (1.45)$$

By calculating the first order term of the shear stress in shear flows with small  $\lambda \dot{\gamma}$  one can show that the polymeric viscosity should be defined for the FENE-P model as  $\eta_p = n_p k T \lambda \frac{b}{b+d}$ . Using this notation, the formula (1.26) for the elastic extra-stress  $\boldsymbol{\tau}$  can be written as

$$\boldsymbol{\tau} = \frac{\eta_p}{\lambda} \left( \frac{b+d}{b} \right) \left( -\mathbf{I} + \frac{\mathbf{A}}{1 - \text{tr}\mathbf{A}/b} \right). \quad (1.46)$$

A detailed comparison of the FENE and FENE-P dumbbell models can be found in [60]. Among more recent and more accurate approximations we cite the FENE-L and FENE-LS models introduced in [124, 77] that, unlike the FENE-P approximation, capture properly the hysteretic behaviour of dilute polymer solutions in relaxation following extensional flow.

## 1.2 Concentrated polymer solutions and melts

In this section, we sketch some ideas used to model concentrated solutions and melts of linear polymers. By concentrated polymer solutions we are referring to those solutions of polymers where faithful constitutive modelling requires that interactions between polymers be taken into

account. Such systems are also known as entangled. The best known coarse-grained description of this interaction is provided by so-called reptation models, originally introduced to the field of polymer melts by de Gennes [36] and extended by Doi and Edwards in three landmark papers of the late 1970's [38, 39, 40]. The main physical phenomenon that is captured in this theory is that the motion of a polymer molecule perpendicular to its backbone is strongly reduced by the surrounding polymers, so that one can assume that a polymer molecule moves (reptates) through a tube whose surface is formed by the surrounding polymers. An important feature of such a movement is the separation of time scales for changing the orientation and stretching of polymers. The stretch of polymer chains relaxes quickly after a deformation on a time scale (Rouse time) comparable to that of an unentangled polymer. Changes in orientation are much slower. Indeed, the relaxation of orientation can only proceed via diffusion of the chain out of the tube. When the chain reptates out of the tube, a new tube segment is created at this location. At the other side of the chain a part of the tube disappears. The corresponding time scale is known as the reptation or disengagement time  $\tau_d$ .

Mathematically, the direction of a particular tube segment is described by a unit vector  $\mathbf{u}$ . A parameter  $s \in [0, 1]$  indicates which segment of a polymer chain is in the tube segment with orientation  $\mathbf{u}$ , so that  $s = 0$  and  $s = 1$  correspond to the head and tail, respectively, of the polymer chain. In accordance with the reptation picture, when  $s = 0$  or  $1$ , a new completely random orientation  $\mathbf{u}$  is created. Otherwise the orientation vectors  $\mathbf{u}$  are convected with the flow. To simplify the analytical investigation, the so called Independent Alignment Assumption (IAA), was introduced in the Doi-Edwards (DE) model, according to which each tube segment deforms independently. Furthermore, the polymer molecules in the original DE model are assumed to retract instantaneously back to their equilibrium length after deformation, so that the Rouse time is set effectively to zero. This reptation picture gives rise to the FP equation for the pdf  $\psi(t, \mathbf{u}, s)$ , where  $\psi d\mathbf{u}ds$  is the joint probability that at time  $t$  a tube segment has associated orientation vector in the interval  $[\mathbf{u}, \mathbf{u} + d\mathbf{u}]$  and contains the part of the polymer chain labelled in the interval  $[s, s + ds]$ . In a homogeneous flow with the FP equation is velocity gradient  $\boldsymbol{\kappa}$

$$\frac{\partial \psi}{\partial t} = -\frac{\partial}{\partial \mathbf{u}} \cdot [(\mathbf{I} - \mathbf{u}\mathbf{u}) \cdot \boldsymbol{\kappa} \cdot \mathbf{u}\psi] + \frac{1}{\pi^2 \tau_d} \frac{\partial^2 \psi}{\partial s^2}$$

with the boundary conditions at  $s = 0$  and  $s = 1$

$$\psi(t, \mathbf{u}, s) = \frac{1}{4\pi} \delta(|\mathbf{u}| - 1), \quad s = 0, 1.$$

The elastic extra-stress is then proportional to the average of  $\mathbf{u}\mathbf{u}$ .

Although the predictions of the DE model are in good agreement with experimental data for shear flows at low shear rates, it has some unrealistic features. The best known of these is the prediction of excessive shear-thinning in fast steady shear flows. As explained in numerous papers (see, for example, [92, 49, 114]) this particular weakness is not overcome by building in a non-zero Rouse time and thus allowing tube stretch: the polymers simply end up by orientating themselves along the flow direction and the drag on them is reduced as a consequence. The crucial difference between modern reptation theory and that of Doi and Edwards lies elsewhere: for sufficiently fast flows proper account is taken in these models of a release of constraints by motion of the members of the matrix that forms the tube around a given polymer chain. Thus the polymer is far freer to relax than would be the case by reptation alone. This convective constraint release (CCR) mechanism suppresses the tendency of polymer chains to align with a

shear flow and occurs when polymers of the surrounding matrix move faster than the polymer chain within is able to relax i.e. for shear rates  $\dot{\gamma} > \tau_d^{-1}$ . Modern reptation theories that include these phenomena and avoid IAA are, among others, the models by Marrucci [8], Ianniruberto and Marrucci [66], Hua and Schieber [61, 62, 63], Mead, Larson and Doi [92] and a thermodynamically admissible reptation model by Öttinger [100]. The latter model was proposed in two versions: a “uniform” model where the chain contour labels was uninfluenced by the flow field so that only uniform stretching of the chain could occur, and a “tuned” model where  $s$  was rescaled by the total tube stretching rate. The possibility for anisotropic tube cross sections was also included in the original model. However, following Fang et al. [49], we will consider only the “uniform” variant of the model without anisotropic tube cross sections. Such a model will be termed the simplified uniform (SU) model.

Fang et al. [49] have performed an extensive comparative study of the Hua-Schieber model, the Mead-Larson-Doi (MLD) model and the SU model in various transient and steady shear and extensional flows. The predictions of this model have been by compared with experimental results for a solution of polystyrene in tricresyl phosphate [72]. In shear flows the three reptation models were seen to manifest similar behaviour in many cases and the SU model was able to capture, at least qualitatively, real polymer behaviour. A more detailed description of the DE, MLD and SU reptation models will be given in Chapter 5.

An alternative approach to modelling concentrated solutions is the encapsulated dumbbell model of Bird and Deaguiar [19], which is an extension of the dumbbell model, described in the previous section, and usually used for dilute polymer solutions. Their model includes an anisotropic friction tensor to simulate the restriction on motion in a direction perpendicular to the backbone of a polymer chain. In a recent paper [50] it was shown how CCR and other relaxation mechanisms could be added to this model to produce very good agreement with experimental data both for shear and extensional flows.

### 1.3 Stochastic simulations

As we have seen in the preceding sections, many kinetic theory models for polymeric liquids in homogeneous flows can be mathematically formulated in terms of FP equations for the probability density function  $\psi(t, \mathbf{q})$

$$\frac{\partial \psi}{\partial t} + \frac{\partial}{\partial \mathbf{q}} \cdot (\mathbf{A}(t, \mathbf{q})\psi) = \frac{1}{2} \frac{\partial}{\partial \mathbf{q}} \frac{\partial}{\partial \mathbf{q}} : (\mathbf{D}(t, \mathbf{q})\psi), \quad (1.47)$$

where  $\mathbf{q}$  is a  $d$ -dimensional vector that describes the coarse-grained microstructure,  $\mathbf{A}(t, \mathbf{q})$  is a  $d$ -dimensional vector (the drift term) that defines the deterministic contribution to the model, and  $\mathbf{D}(t, \mathbf{q})$  is a symmetric positive-definite  $d \times d$  matrix known as the diffusion tensor that defines the stochastic contribution to the model.

There is an important equivalence between FP equations and stochastic differential equations of the form

$$d\mathbf{q}(t) = \mathbf{A}(t, \mathbf{q}(t))dt + \mathbf{B}(t, \mathbf{q}(t))d\mathbf{W}(t), \quad (1.48)$$

where  $\mathbf{q}(t)$  is a  $d$ -dimensional stochastic process to be found, and  $\mathbf{W}(t)$  is the Wiener process with the following properties:

- a)  $\mathbf{W}(0) = \mathbf{0}$  with probability 1,

b) For  $0 \leq s < t$ , the random vector  $\mathbf{W}(t) - \mathbf{W}(s)$  has components which are normally distributed with mean zero and variance  $t - s$ , i.e.  $\mathbf{W}(t) - \mathbf{W}(s) \sim \mathbf{N}(0, \sqrt{t - s})$ ,

c) For  $0 \leq s < t < u < v$ ,  $\mathbf{W}(t) - \mathbf{W}(s)$  and  $\mathbf{W}(v) - \mathbf{W}(u)$  are independent random vectors.

It can be shown that if  $\mathbf{A}$  and  $\mathbf{B}$  in (1.48) satisfy the Lipschitz conditions in  $\mathbf{q}$ -space and the linear growth conditions at infinity then (1.48) has a unique solution that is a Markov process with the pdf satisfying (1.47) with

$$\mathbf{D}(t, \mathbf{q}) = \mathbf{B}(t, \mathbf{q})\mathbf{B}^T(t, \mathbf{q}).$$

A rigorous mathematical theory of equations of the form (1.48) was constructed by Itô and is reviewed in [99]. This theory is rather complicated but for our purposes it is sufficient to understand (on an intuitive level) the solution  $\mathbf{q}(t)$  of (1.48) as a limit under  $\Delta t \rightarrow 0$  of the discrete stochastic process  $\mathbf{q}_n = \mathbf{q}(t_n)$ , with  $t_n = n\Delta t$ ,  $n = 1, 2, \dots$ , that satisfies the equation

$$\mathbf{q}_{n+1} = \mathbf{q}_n + \mathbf{A}(t_n, \mathbf{q}_n)\Delta t + \mathbf{B}(t_n, \mathbf{q}_n)\sqrt{\Delta t}\Delta\mathbf{W}_n \quad (1.49)$$

where  $\Delta\mathbf{W}_n$  are mutually independent random  $d$ -dimensional vectors having probability distribution  $\mathbf{N}(0, 1)$ . Strictly speaking, under certain conditions on  $\mathbf{A}$  and  $\mathbf{B}$ , the discrete scheme (1.49), known as the explicit Euler-Maruyama method, converges weakly to the solution of (1.48) with order 1, i.e. for any fixed time  $T > 0$  and  $\Delta t$  such that  $T = n\Delta t$ , for all sufficiently smooth functions  $g : \mathbb{R}_d \rightarrow \mathbb{R}$  with polynomial growth, there exist a constant  $C_g$  independent of  $\Delta t$  such that for sufficiently small  $\Delta t$

$$|\langle g(\mathbf{q}(T)) - g(\mathbf{q}_n) \rangle| \leq C_g \Delta t$$

where the brackets  $\langle \cdot \rangle$  stand for the mathematical expectation. One can also prove the strong convergence of (1.49) that provides information on the accuracy of individual trajectories. In the case when the coefficient  $\mathbf{B}$  does not depend on  $\mathbf{q}$  it is easy to construct an implicit variant of the Euler-Maruyama method by evaluating  $\mathbf{A}$  and  $\mathbf{B}$  at  $t_{n+1}$ ,  $\mathbf{q}_{n+1}$  in (1.49). In the general case, the drift term  $\mathbf{A}$  should be modified in such a scheme to preserve consistency.

The equivalence between FP equations and stochastic differential equations, and the discretizations of the latter of type (1.49) open the way to the construction of stochastic (or Brownian dynamics) simulations of kinetic theory models of polymeric liquids. To achieve this, a large number of pseudo-random realizations  $\mathbf{q}_n^m$ ,  $m = 1, \dots, M$  of the random variables  $\mathbf{q}_n$  at time  $t_n$  are introduced and an equation of type (1.49) should be solved for them with the pseudo-random numbers  $\Delta\mathbf{W}_n^m$ ,  $m = 1, \dots, M$  on the right-hand side. This technique has been successfully applied since 1970's for various models in homogeneous flows (see the book by Öttinger [99] and the references therein) and has turned out to be very flexible and robust. For example, it can be applied even in situations where no FP equation exists so that the physical ideas are incorporated directly into the stochastic numerical scheme, as is the case in the simulations of Hua and Schieber [61, 62, 63].

The 1990's have seen the advent of methods combining Brownian dynamics technique for computing the polymer stress, with a discretization of the conservation equations to simulate the complex flows of fluids described by kinetic theory models. In the case of finite element discretization for the conservation equations Laso and Öttinger [75] termed this hybrid method CONNFFESSIT (Calculation of Non-Newtonian Flow: Finite Elements and Stochastic Simulation Technique). It is known more generally as the micro-macro approach. At each time step the original algorithm of [75] proceeds as follows:

1. Using the current approximation to the polymer stress as a source term in the momentum equation the conservation equations are solved by any standard numerical method to update approximations to the velocity and pressure fields.
2. The new velocity field is then used to convect a sufficiently large number of model polymer ‘molecules’ through the flow domain. This is achieved by integrating the stochastic differential equation associated with the kinetic theory model along particle trajectories (one assumes that the local homogeneity assumption is applicable, so that one can use the homogeneous FP equation with the derivation along the particle paths to update the configurations of the ‘molecules’).
3. The polymer stress within an element is determined from the configurations of the polymer molecules in that element.

This original implementation of the micro-macro approach suffered from several shortcomings. First, the trajectories of a large number of molecules have to be determined. Secondly, to evaluate the local polymer stress the model polymer molecules must be sorted according to elements. Thirdly, the computed stress may be non smooth and this may cause problems when it is differentiated to form the source term in the momentum equation. In subsequent developments of the technique these shortcomings have been overcome to a certain extent.

A means of reducing the statistical error in a stochastic simulation without increasing the number of trajectories is to use variance reduction. Melchior and Öttinger [4, 95] proposed a number of variance reduction methods in the context of the CONNFESSIT methodology based on importance sampling strategies and the idea of control variables. The idea in importance sampling is to introduce a bias that gives greater weight to the realizations that make a substantial contribution to the average. The bias is constructed from an approximate solution of a stochastic differential equation for a modified stochastic process that gives greater weight to the important realizations [94]. In the second approach, based on control variables [95], the idea is to find a random variable that possesses the same fluctuations as the random variable of interest, but with a zero mean. When the control variable is subtracted from the original variable then the mean remains unchanged while the fluctuations are reduced.

The construction of an appropriate control variable to be used in a parallel process simulation is not straightforward in general flow situations. An alternative approach is to use local ensembles of model polymers that are correlated. The idea is that corresponding model polymers in each material element feel the same Brownian force. More precisely, the same initial ensemble of model polymers is defined in each material element and corresponding model polymers in each material element are allowed to evolve using the same sequence of random numbers. This approach leads to strong correlations in the stress fluctuations in neighbouring material elements. The evaluation of the divergence of the stress in the momentum equation involves the difference between stresses and leads to a cancellation of fluctuations and dramatic variance reduction. The Brownian configuration field method of Hulsen et al. [4, 101] and the Lagrangian particle method of Halin et al. [59] are examples of variance reduced stochastic simulation methods based on the idea of correlated local ensembles of model polymers. Not only do these techniques reduce the spatial fluctuations in the computed velocity and stress fields but they also require the generation of fewer random numbers. This greatly reduces the computational cost associated with these stochastic simulation techniques. The cost of achieving variance reduction is that unphysical correlations in the random forces are introduced into

the simulations. For problems in which physical fluctuations are important one must revert to calculations based on uncorrelated Brownian forces even though this is likely to be more expensive.

In the Lagrangian particle method [59], the stochastic differential equation is integrated by placing a large number of dumbbells at each Lagrangian particle. Over each time interval, the configuration of each dumbbell is determined by solving the stochastic differential equation along the particle trajectory using the velocity field obtained from a standard numerical simulation of the conservation equations. The polymer stress associated with each particle is then approximated by taking an ensemble average over its client dumbbells. Variance reduction is achieved through correlated ensembles of dumbbells. The implementation of this idea in the context of the Lagrangian particle method is accomplished by specifying that corresponding dumbbells in each Lagrangian particle have the same initial configuration and evolve using the same sequence of Brownian forces.

Brownian configuration fields method [64] overcomes the problem of having to track particle trajectories, provides efficient variance reduction and may be interpreted as an Eulerian implementation of the idea of correlated local ensembles. This method departs from the standard micro-macro approach in that it is based on the evolution of a number of continuous configuration fields rather than the convection of discrete particles specified by their configuration vector. Dumbbell connectors with the same initial configuration and subject to the same random forces throughout the flow domain are combined to form a configuration field. The polymer dynamics is then described by the evolution of an ensemble of configuration fields instead of the evolution of local ensembles of model polymers. The method also provides a smooth spatial representation of the configuration field that can be differentiated to form the source term in the momentum equation.





# Chapter 2

## Spectral methods

### 2.1 Orthogonal polynomials and quadrature formulas

We review here some standard results concerning the orthogonal polynomials that constitute the basis of spectral methods. More details can be found in the textbooks on spectral methods, for example [14] and [26].

#### Expansion in terms of a system of orthogonal polynomials

Let  $w(x)$  be a positive function on  $(-1, 1)$ . We consider the space  $L_w^2(-1, 1)$  of functions  $v$  such that

$$\|v\|_w = \int_{-1}^1 |v(x)|^2 w(x) dx$$

is finite. The associated inner product is

$$(u, v)_w = \int_{-1}^1 u(x)v(x)w(x)dx.$$

Assume that  $\{p_k\}_{k=0,1,\dots}$  is a system of algebraic polynomials (where the degree of  $p_k$  is equal to  $k$ ) that are mutually orthogonal in  $L_w^2(-1, 1)$ :

$$(p_k, p_l)_w = \delta_{kl} \|p_k\|_w^2.$$

For an integer  $N > 0$ , consider a truncated expansion of a function  $u \in L_w^2(-1, 1)$  in terms of the system  $\{p_k\}$  :

$$P_N u = \sum_{k=0}^N u_k p_k$$

where

$$u_k = \frac{1}{\|p_k\|_w^2} (u, p_k)_w.$$

Due to the orthogonality of  $p_k$ ,  $P_N u$  is the orthogonal projection in  $L_w^2(-1, 1)$  of  $u$  upon the space  $\mathbb{P}_N$  of all polynomials of degree  $\leq N$ , i.e.

$$(P_N u, v)_w = (u, v)_w \quad \text{for all } v \in \mathbb{P}_N.$$

The Weierstrass theorem implies that the system  $\{p_k\}$  is complete in  $L_w^2(-1, 1)$  so that for all  $u \in L_w^2(-1, 1)$  we have

$$\|u - P_N u\|_w \rightarrow 0 \quad \text{as } N \rightarrow \infty.$$

The polynomials orthogonal with respect to the weight  $w(x) = (1-x)^{J_\alpha}(1+x)^{J_\beta}$  with some  $J_\alpha, J_\beta > -1$  are known as Jacobi polynomials. They are usually denoted as  $P_k^{J_\alpha, J_\beta}(x)$  under the normalization  $P_k^{J_\alpha, J_\beta}(1) = \binom{k+J_\alpha}{k}$ . Jacobi polynomials can be alternatively defined as the eigenfunctions of the following singular Sturm-Liouville problem:

$$-((1-x)^{1+J_\alpha}(1+x)^{1+J_\beta}u')' = \lambda_k(1-x)^{J_\alpha}(1+x)^{J_\beta}u$$

with  $\lambda_k = k(k+J_\alpha+J_\beta+1)$ . The importance of Jacobi polynomials for numerical methods lies in the fact that the expansion of infinitely smooth functions in terms of them guarantees the spectral convergence, that is faster than any power of  $N$ . More precisely one can prove for any function  $u(x) \in L_w^2(-1, 1)$  such that its  $m$ -th derivative  $u^{(m)}(x)$  is in the same space that

$$\|u - P_N u\|_w \leq CN^{-m} (\|u^{(m)}\|_w + \|u\|_w),$$

where  $C > 0$  depends only on  $m$ .

In the special case  $w = 1$ , i.e.  $J_\alpha = J_\beta = 0$  the Jacobi polynomials are also known as Legendre polynomials.

## Gauss integration

Let  $x_1, \dots, x_N$  be the roots of the  $N$ -th orthogonal polynomial  $p_N$  and let  $w_1, \dots, w_N$  be the solution of the linear system

$$\sum_{j=1}^N (x_j)^{k-1} w_j = \int_{-1}^1 x^{k-1} w(x) dx, \quad k = 1, \dots, N.$$

Then,  $w_j > 0$  for  $j = 1, \dots, N$  and

$$\sum_{j=1}^N p(x_j) w_j = \int_{-1}^1 p(x) w(x) dx \tag{2.1}$$

for all polynomials  $p(x) \in \mathbb{P}_{2N-1}$ . The positive numbers  $w_j$  are called quadrature weights. The quadrature rule is optimal in the sense that it is not possible to find  $x_j, w_j > 0, j = 1, \dots, N$  such that (2.1) holds for all polynomials  $p(x) \in \mathbb{P}_{2N}$ .

We will use the Gauss integration only in the case of Jacobi polynomials and term it Gauss-Jacobi or Gauss-Legendre (GL) in the special case of Legendre polynomials. It is convenient to introduce Lagrange interpolating polynomials through the points  $x_j$ , i.e.  $h_i(x) \in \mathbb{P}_{N-1}$ ,  $i = 1, \dots, N$  such that  $h_i(x_j) = \delta_{ij}$ ,  $i, j = 1, \dots, N$ , and to define the differentiation matrix  $D_{ij} = h_i'(x_j)$  and the matrix of second derivatives  $D_{ij}^{(2)} = h_i''(x_j)$ . In the case of Jacobi polynomials, the points  $x_j$ , the weights  $w_j$  and the entries of the matrix  $D_{ij}$  can be calculated analytically. The necessary formulas and FORTRAN codes can be found in [6]. In the computations reported in this work we have used their implementation by E. M. Rønquist.

As for the matrix of second derivatives, it is easy to see that  $D^{(2)}$  is the square of  $D$ . Indeed, since  $h'_i(x)$  is a polynomial of degree  $N - 2$  we can expand it in terms of  $h_j(x)$  as

$$h'_i(x) = h'_i(x_j)h_j(x) = D_{ij}h_j(x),$$

where we assume the summation over repeated indices. Differentiating the last equality and applying it once more we obtain

$$h''_i(x) = D_{ij}h'_j(x) = D_{ij}D_{jk}h_k(x).$$

Thus,  $h''_i(x_k) = D_{ij}D_{jk}$ .

### Gauss-Lobatto integration

Let  $-1 = x_0, x_2, \dots, x_N = 1$  be the roots of polynomial  $q(x) = p_{N+1} + ap_N + bp_{N-1}$  where the numbers  $a$  and  $b$  are chosen so that  $q(\pm 1) = 0$  and let  $w_0, \dots, w_N$  be the solution of the linear system

$$\sum_{j=0}^N (x_j)^k w_j = \int_{-1}^1 x^k w(x) dx, \quad k = 0, \dots, N.$$

Then,

$$\sum_{j=0}^N p(x_j) w_j = \int_{-1}^1 p(x) w(x) dx \tag{2.2}$$

for all polynomials  $p(x) \in \mathbb{P}_{2N-1}$ .

We shall use Gauss-Lobatto integration only for  $w = 1$ , i.e. with Legendre polynomials, and term it Gauss-Lobatto-Legendre (GLL). As in the case of GL integration, one can introduce Lagrange interpolating polynomials, i.e.  $h_i(x) \in \mathbb{P}_N$ ,  $i = 0, \dots, N$  such that  $h_i(x_j) = \delta_{ij}$ ,  $i, j = 0, \dots, N$ , and the differentiation matrix  $D_{ij} = h'_i(x_j)$ . The formulas and FORTRAN codes to compute  $x_j$ ,  $w_j$  and  $D_{ij}$  corresponding to Legendre polynomials can be found in [26]. In the computations reported in this work we have used their implementation by E. M. Rønquist.

## 2.2 Spectral element discretization

Spectral element methods [85, 109] are high-order weighted residual methods for partial differential equations enjoying exponential rates of convergence for smooth problems and involving, as do finite element methods, a decomposition of the problem domain into subdomains. They differ from  $p$ -type finite element methods, however, in the choice of test and trial functions: whereas  $p$  finite element methods use representations in each element for the variables in terms of linear combinations of Legendre polynomials, in spectral element methods tensorized bases are employed, consisting of Lagrange interpolating polynomials based on Gauss-type quadrature points.

A few words are in order here on the history of applications of Legendre spectral element methods to simulations of viscoelastic flows. The first such application in computing creeping flows was by Van Kemenade and Deville [129, 130] in 1994. The authors attempted to deal with the question of whether or not the loss of convergence of standard finite element and

finite difference methods was due to the low-order space discretizations of such methods. The authors concluded that the failure of their spectral element method to converge beyond a limiting Weissenberg number showed that the so-called “high Weissenberg number problem” could not be attributed to the order of the space discretization, either in the case of flows with or without a change of mathematical type. In [129] excellent agreement was obtained by the authors with the results of Pilitsis and Beris [117, 118]. A comparison of the spectral element results with those produced using the  $4 \times 4$  SUPG finite element method of Marchal and Crochet [87] for Weissenberg numbers up to 12 gave not only excellent agreement, but the spectral element method proved cheaper for comparable accuracy in the two methods. Among more recent publications, where spectral element methods have been applied to viscoelastic flows modelled by constitutive equations of differential type, we cite those of Phillips et al. [120], Fiétier [51], Fiétier and Deville [52], Owens [102] and Chauvière and Owens [32, 33]. In the last paper, it was found that enhanced stability and accuracy were possible using consistent streamline upwinding with a Legendre spectral element method (contrary to the opinion of Liu and Beris, expressed in [78]). Further improvement in the quality of the solution was evident by solving the constitutive equations on an element-by-element basis, taking account of upstream velocity and stress information only at each elemental solve. Weissenberg numbers more than double those achieved in [106] were now realizable.

Let us illustrate the spectral element method with the example of the Stokes system

$$\nabla \cdot \mathbf{v} = 0, \quad (2.3)$$

$$-\beta \Delta \mathbf{v} + \nabla p = \mathbf{f}. \quad (2.4)$$

We introduce the following linear spaces over the flow domain  $\Omega \subset \mathbb{R}^2$

$$V = \left\{ \mathbf{v} \in (H^1(\Omega))^2 : \mathbf{v} = \mathbf{0} \text{ on } \Gamma = \partial\Omega \right\}, \quad (2.5)$$

$$Q = L_0^2(\Omega). \quad (2.6)$$

Equipped with these functional spaces, we introduce the following bilinear forms:  $A : V \times V \rightarrow \mathbb{R}$ ,  $B : Q \times V \rightarrow \mathbb{R}$ ,  $C : (L_2(\Omega))^2 \times V \rightarrow \mathbb{R}$ , thus:

$$A(\mathbf{v}, \mathbf{w}) = \beta \int_{\Omega} \nabla \mathbf{v}^T : \nabla \mathbf{w} d\mathbf{x} \quad \forall \mathbf{v}, \mathbf{w} \in V, \quad (2.7)$$

$$B(q, \mathbf{w}) = \int_{\Omega} q \nabla \cdot \mathbf{w} d\mathbf{x} \quad \forall q \in Q, \mathbf{w} \in V, \quad (2.8)$$

$$C(\mathbf{f}, \mathbf{w}) = \int_{\Omega} \mathbf{f} \cdot \mathbf{w} d\mathbf{x} \quad \forall \mathbf{f} \in (L_2(\Omega))^2, \mathbf{w} \in V. \quad (2.9)$$

With these definitions, the Galerkin weak formulation of the governing equations (2.3)-(2.4) may be formally written: find  $(\mathbf{v}, p) \in V \times Q$  such that

$$A(\mathbf{v}, \mathbf{w}) - B(p, \mathbf{w}) = C(\mathbf{f}, \mathbf{w}), \quad \forall \mathbf{w} \in V, \quad (2.10)$$

$$B(q, \mathbf{v}) = 0, \quad \forall q \in Q, \quad (2.11)$$

The Legendre spectral element method [85] may be used for the discretization of the continuous problem (2.10)-(2.11).

The domain  $\Omega$  is partitioned into  $K$  (say) non-overlapping spectral elements  $\{\Omega_k\}_{k=1}^K$  and each of the spectral elements is mapped onto a parent element

$$\widehat{\Omega} = \{(\xi, \eta) : -1 \leq \xi, \eta \leq 1\}.$$

This can be achieved using the transfinite mapping technique of Gordon and Hall [8]. Then, letting  $P_N$  denote the space of functions such that their restrictions to every spectral element  $\Omega_k$  are inverse images of polynomials of degree  $\leq N$  in both  $\xi$  and  $\eta$  under the mapping  $\Omega_k \rightarrow \widehat{\Omega}$ , our choice of finite-dimensional subspace  $V^N \subset V$  for the components of velocity is

$$V^N = V \cap P_N.$$

We may then write down discrete representations  $\mathbf{v}_N$  for the velocity vector, as follows:

$$\mathbf{v}_N|_{\Omega_k} \equiv \mathbf{v}_N^k(\xi, \eta) = \sum_{i=0}^N \sum_{j=0}^N \mathbf{v}_{i,j}^k h_i(\xi) h_j(\eta) \in V_N, \quad (2.12)$$

In (2.12),  $h_i(\xi)$ , are the degree  $N$  Lagrange interpolating polynomials through the Gauss-Lobatto-Legendre points. In order to satisfy the Babuška-Brezzi condition for the velocity/pressure compatibility, a suitable choice for the pressure approximation space is  $Q^N \equiv L^2(\Omega) \cap P_{N-2}$ , see [14]. The spectral representation of the pressure in  $\Omega_k$  is therefore taken as

$$p_N^k(\xi, \eta) = \sum_{i=0}^{N-2} \sum_{j=0}^{N-2} p_{i,j}^k \tilde{h}_i(\xi) \tilde{h}_j(\eta), \quad (2.13)$$

where  $\tilde{h}_i(\xi)$ ,  $0 \leq i \leq N-2$ , are Lagrange interpolating polynomials of degree  $N-2$  based on the interior Gauss-Lobatto-Legendre points. Inserting the discrete spectral representation of  $(\mathbf{v}, p)$  into (2.10)-(2.11), the problem is now: find  $(\mathbf{v}_N, p_N) \in V_N \times Q_N$ , such that

$$\sum_{k=1}^K (A_k(\mathbf{v}_N^k, \mathbf{w}_N^k) - B_k(p_N^k, \mathbf{w}_N^k)) = C_k(\mathbf{f}_N^k, \mathbf{w}_N^k), \quad \forall \mathbf{w}_N^k \in V_N, \quad (2.14)$$

$$\sum_{k=1}^K B_k(q_N^k, \mathbf{v}_N^k) = 0, \quad \forall q_N^k \in Q_N. \quad (2.15)$$

The integrals appearing in (2.14)-(2.15) are determined numerically using Gauss-Lobatto quadrature rules. Equations (2.14)-(2.15) can now be written in the following matrix-vector product form:

$$\begin{aligned} \mathbf{A}_x \mathbf{v}_x - \mathbf{B}_x \mathbf{p} &= \mathbf{C} \mathbf{f}_x, \\ \mathbf{A}_y \mathbf{v}_y - \mathbf{B}_y \mathbf{p} &= \mathbf{C} \mathbf{f}_y, \\ \mathbf{B}_x^T \mathbf{v}_x + \mathbf{B}_y^T \mathbf{v}_y &= \mathbf{0}, \end{aligned}$$

where  $\mathbf{f}_x$ ,  $\mathbf{f}_y$ ,  $\mathbf{v}_x$ ,  $\mathbf{v}_y$  and  $\mathbf{p}$  are vectors containing, in an obvious way, the nodal values of the right-hand side  $\mathbf{f}$  and the velocity and pressure variables.

The discretization of the Stokes system described above will be used in all our simulations of complex creeping flows of polymer fluids since we decouple the solution of the conservation equations for velocity and pressure from the solution to the constitutive relations for the elastic extra-stress at each time step. In the next section, we give a simple example of such a decoupled simulation.

## 2.3 Numerical example: time-dependent Couette flow of an Oldroyd B fluid

### 2.3.1 Problem description

Let us consider the incompressible, isothermal and inertialess (or massless) flow of an Oldroyd B viscoelastic fluid in the absence of body forces. The governing equations for these flows are the conservation of mass (1), conservation of linear momentum (1.33) with  $\rho = 0$  and the constitutive equation, which we take here in the form (1.40) for the positive definite tensor  $\boldsymbol{\tau}'$  defined in (1.39). These three equations can be written in dimensionless form as

$$\nabla \cdot \mathbf{v} = 0, \quad (2.16)$$

$$-\beta \Delta \mathbf{v} + \nabla p = \nabla \cdot \boldsymbol{\tau}', \quad (2.17)$$

$$\boldsymbol{\tau}' + We \left( \frac{\partial \boldsymbol{\tau}'}{\partial t} + \mathbf{v} \cdot \nabla \boldsymbol{\tau}' - \boldsymbol{\tau}'(\nabla \mathbf{v}) - (\nabla \mathbf{v})^T \boldsymbol{\tau}' \right) = \frac{1 - \beta}{We} \mathbf{I}, \quad (2.18)$$

where  $\beta$  is the ratio of the solvent to total viscosity  $\beta = \eta_s/(\eta_s + \eta_p)$  and  $We$  is a Weissenberg number  $We = \lambda U/L$  where  $U$  and  $L$  are the characteristic velocity and length, respectively. For our numerical tests we will attempt to solve a simple benchmark problem – start-up Couette flow in the rectangle  $\Omega = (-1, 1)^2$  (see Fig. 2.1). Cartesian coordinates  $(x, y)$  are chosen with  $x$  in the streamwise direction and  $y$  perpendicular to  $x$  in the plane of the flow. With a velocity field  $\mathbf{v} = (v_x, v_y)$  given by

$$v_x = (y + 1)(1 - e^{-t/We}), \quad v_y = 0 \quad (2.19)$$

the components of  $\boldsymbol{\tau}'$  may be expressed analytically by the formulas

$$\begin{aligned} \tau'_{xx} = & 2(1 - \beta)We \left( 1 + e^{-t/We} \left( 1 - 2\frac{t}{We} - \frac{t^2}{2We^2} \right) - \right. \\ & \left. e^{-2t/We} \left( \frac{t}{We} + 2 \right) \right) + \frac{1 - \beta}{We}, \end{aligned}$$

$$\tau'_{xy} = (1 - \beta) \left( 1 - \left( 1 + \frac{t}{We} \right) e^{-t/We} \right), \quad \tau'_{yy} = \frac{1 - \beta}{We},$$

the pressure  $p$  being an arbitrary constant. The parameter  $\beta$  is set equal to 0.1.

The steady Couette flow of an Oldroyd B fluid at  $Re = 0$  is known to be linearly stable [134]. Nothing is presently known about the linear stability of the start-up Couette problem at  $Re = 0$ . Note that the analytical solution tends to a stationary Couette flow as time tends to infinity.

### 2.3.2 Numerical schemes

We discretize the problem (2.16)–(2.18) in space using the spectral element method. One spectral element is used (the method can be termed hence simply as a pseudospectral one). The discretization of velocity and pressure has been described in Section 2.2. Nothing is presently known about compatibility conditions which may apply to the discrete spaces  $V^N$  and  $\Sigma^N$  for

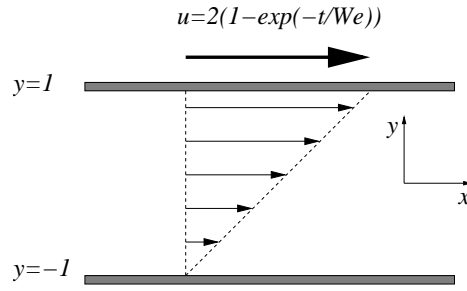


Figure 2.1: Couette flow.

the velocity and the elastic extra-stress, respectively, used in numerical solutions to the full set of non-linear equations (2.16)–(2.18). The partial existing results are as follows: in the mixed Galerkin formulation of the 3 fields Stokes limit of the Upper Convected Maxwell equations ( $We = 0, \beta = 0$ ) a compatibility condition applies between  $V^N$  and  $\Sigma^N$  [53, 54], however no such condition is required for the same limit of the Oldroyd B equations ( $We = 0, \beta \neq 0$ , see [8]). Consistent with the latter result, we approximate the components of the elastic extra-stress by the polynomials of the same degree as the components of the velocity.

For discretization with respect to time we use the uniform grid  $t_i = i\Delta t$  and the system of equations is decoupled at each time step as follows:

1. We solve the Stokes problem (2.16)–(2.17) to obtain  $\mathbf{v}^{i+1}, p^{i+1}$  at time  $t_{i+1}$  using the tensor  $\boldsymbol{\tau}'_i$  from the previous time step  $t_i$  which has already been computed. The discretization of the Stokes problem is described in Section 2.2.
2. The constitutive equation (2.18) for  $\boldsymbol{\tau}'_{i+1}$  is solved afterwards using the velocities from time steps  $t_i$  and  $t_{i+1}$ . The choice of the numerical method for the constitutive equation turns out to be the most important factor for the success of the simulations.

We present first a Galerkin approximation of Eq. (2.18). Let  $\Sigma_N(\Omega)$  be the space of symmetric tensors whose components are arbitrary polynomials from  $P_N(\Omega)$ . Then  $\boldsymbol{\tau}'_{i+1}$  is the unique element of  $\Sigma_N(\Omega)$  satisfying the following equations:

$$\begin{aligned}
 We \left( \frac{\boldsymbol{\tau}'_{i+1} - \boldsymbol{\tau}'_i}{\Delta t} + \mathbf{v}^{i+\alpha} \cdot \nabla \boldsymbol{\tau}'_{i+\alpha}, \mathbf{S} \right) &+ a_{\mathbf{v}^{i+\alpha}}(\boldsymbol{\tau}'_{i+\alpha}, \mathbf{S}) \\
 &= \frac{1 - \beta}{We} (\mathbf{I}, \mathbf{S}), \forall \mathbf{S} \in \Sigma_N^{in}(\Omega), \\
 \boldsymbol{\tau}'_{i+\alpha}|_{\Gamma_{in}} &= \boldsymbol{\varphi}'_{i+\alpha},
 \end{aligned} \tag{2.20}$$

where

$$\begin{aligned}
 \Sigma_N^{in}(\Omega) &= \{\mathbf{S} \in \Sigma_N(\Omega) : \mathbf{S}|_{\Gamma_{in}} = \mathbf{0}\}, \\
 \boldsymbol{\tau}'_{i+\alpha} &= (1 - \alpha)\boldsymbol{\tau}'_i + \alpha\boldsymbol{\tau}'_{i+1}, \quad \mathbf{v}^{i+\alpha} = (1 - \alpha)\mathbf{v}^i + \alpha\mathbf{v}^{i+1}, \\
 a_{\mathbf{v}}(\mathbf{T}, \mathbf{S}) &= (\mathbf{T} - We(\mathbf{T}(\nabla \mathbf{v}) + (\nabla \mathbf{v})^T \mathbf{T}), \mathbf{S}),
 \end{aligned}$$

and  $\boldsymbol{\varphi}'_{i+\alpha}$  is an appropriate approximation of the inflow boundary condition  $\boldsymbol{\varphi}$  at time  $(i+\alpha)\Delta t$ . We have here introduced the parameter  $\alpha \in [0, 1]$  which accounts for different time marching

algorithms; for instance  $\alpha = 1/2$  for a Crank-Nicolson scheme and  $\alpha = 1$  for a backward Euler scheme.

Applying an energy method to Eq. (2.20) one can prove that if  $\alpha \in [1/2, 1]$ ,  $\nabla \cdot \mathbf{v}^i = 0$  and  $a_{\mathbf{u}^{i+\alpha}}(\boldsymbol{\tau}'_{i+\alpha}, \boldsymbol{\tau}'_{i+\alpha}) \geq 0$  for any integer  $i \geq 0$ , then any perturbations to the right-hand side of Eq. (2.20) that are uniformly bounded in time give rise (at worst) to linear growth of the error for  $\boldsymbol{\tau}'$ . More precisely, denoting by  $\tilde{\boldsymbol{\tau}}'_i$  the solution of Eq. (2.20) with the right-hand side modified by adding a term  $(\mathbf{R}^i, \mathbf{S})$  for any  $\mathbf{R}^i \in \Sigma_N(\Omega)$  we have the inequality

$$\|\tilde{\boldsymbol{\tau}}'_n - \boldsymbol{\tau}'_n\|_{L_2(\Omega)} \leq \frac{n\Delta t}{We} \max_{i < n} \|\mathbf{R}^i\|_{L_2(\Omega)}. \quad (2.21)$$

The requirement of a solenoidal velocity can be easily overcome. Indeed, for the scheme

$$\begin{aligned} We \left( \frac{\boldsymbol{\tau}'_{i+1} - \boldsymbol{\tau}'_i}{\Delta t} + \mathbf{v}^{i+\alpha} \cdot \nabla \boldsymbol{\tau}'_{i+\alpha} + \frac{1}{2}(\nabla \cdot \mathbf{v}^{i+\alpha})\boldsymbol{\tau}'_{i+\alpha}, \mathbf{S} \right) \\ + a_{\mathbf{v}^{i+\alpha}}(\boldsymbol{\tau}'_{i+\alpha}, \mathbf{S}) = \frac{1-\beta}{We} (\mathbf{I}, \mathbf{S}), \end{aligned} \quad (2.22)$$

the estimate (2.21) can be established even if  $\nabla \cdot \mathbf{v}^i \neq 0$ . (Note that the method (2.22) is consistent since  $\nabla \cdot \mathbf{v} = 0$  for the exact solution of the differential equation).

However, the issue of positive definiteness of the bilinear form  $a_{\mathbf{v}}$  is crucial and the solution can become unstable if  $a_{\mathbf{v}}$  is too “negative”. There is a simple necessary and sufficient criterion for positive semi-definiteness of the bilinear form  $a_{\mathbf{v}^{i+\alpha}}$ , namely

$$\Lambda_{\max}(\nabla \mathbf{v}^{i+\alpha} + (\nabla \mathbf{v}^{i+\alpha})^T) \leq \frac{1}{We},$$

everywhere in  $\Omega$ ,  $\Lambda_{\max}(\nabla \mathbf{v}^{i+\alpha} + (\nabla \mathbf{v}^{i+\alpha})^T)$  being the largest eigenvalue of the rate-of-strain tensor.

The simplest Galerkin method (2.20) works well for  $We \leq 1$ . For example, Fig. 2.2 shows some results for  $We = 1$ . The method is unconditionally stable, in agreement with the estimate (2.21); refining of the mesh in space does not improve the accuracy (Fig. 2.2(a)) since the exact solution is represented by polynomials of degree at most 1, but the error diminishes when the time step  $\Delta t$  decreases (Fig. 2.2(b)). Moreover, the error decays to zero rapidly as time goes on. Here, and in what follows, we present the plots of the relative error for  $\boldsymbol{\tau}'$  in the maximum norm since the errors for velocity and pressure are always less than that of the tensor  $\boldsymbol{\tau}'$ . The method (2.20) fails already for  $We = 2$  as can be seen in Fig. 2.3(a). However, the instability can be attributed partly (at least) in this case to the influence of the non-zero divergence of the velocity since method (2.22) works much better for the same value of  $We$  (Fig. 2.3(b)). Note, nevertheless, that all is still not well since, as in Fig. 2.2(a), increasing the mesh resolution does nothing to enhance accuracy.

Both methods (2.20) and (2.22) fail for some larger values of  $We$  in the sense that for any sufficiently large  $We$  there exists a critical time  $T_{crit}(We)$  such that the numerical solution for any  $N$  and  $\Delta t$  blows up at some time  $t \in (0, T_{crit})$ . Moreover,  $T_{crit}$  is a decreasing function of  $N$  for any fixed  $We$  (Fig. 2.4(a) shows some examples for  $We = 50$ ).

In order to gain more insight into the reasons for the instability we present in Fig. 2.4(b) some model simplified calculations for the same value of  $We$ . The dashed curve here represents the error in calculations with a simplified constitutive equation

$$\boldsymbol{\tau}' + We \left( \frac{\partial \boldsymbol{\tau}'}{\partial t} + \mathbf{v} \cdot \nabla \boldsymbol{\tau}' \right) = \frac{1-\beta}{We} \mathbf{I}, \quad (2.23)$$



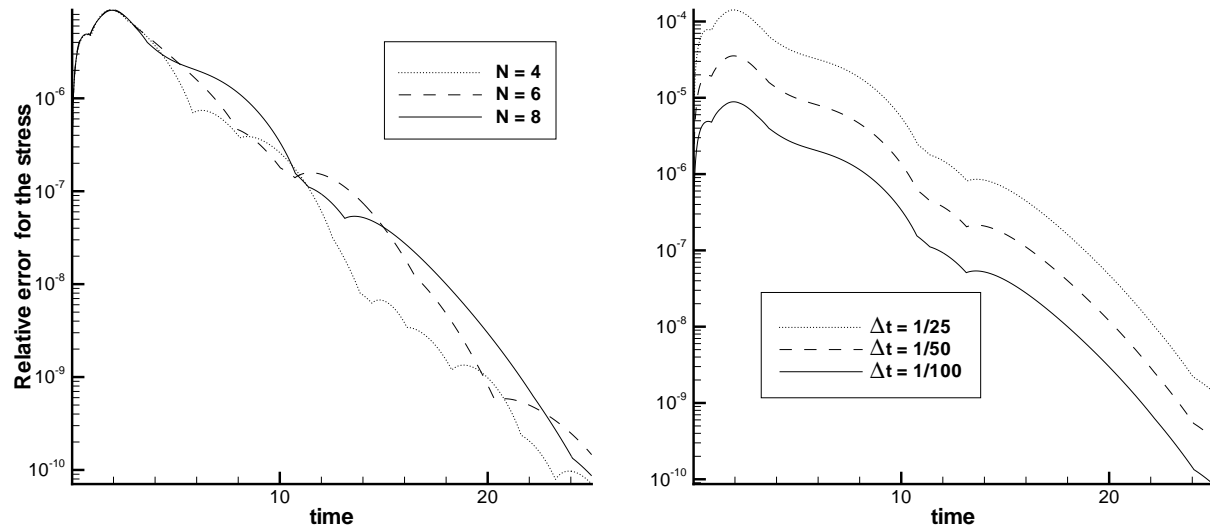


Figure 2.2: Galerkin approximation at  $We = 1$ ; (a)  $\Delta t = 1/100$ , (b)  $N = 8$ .

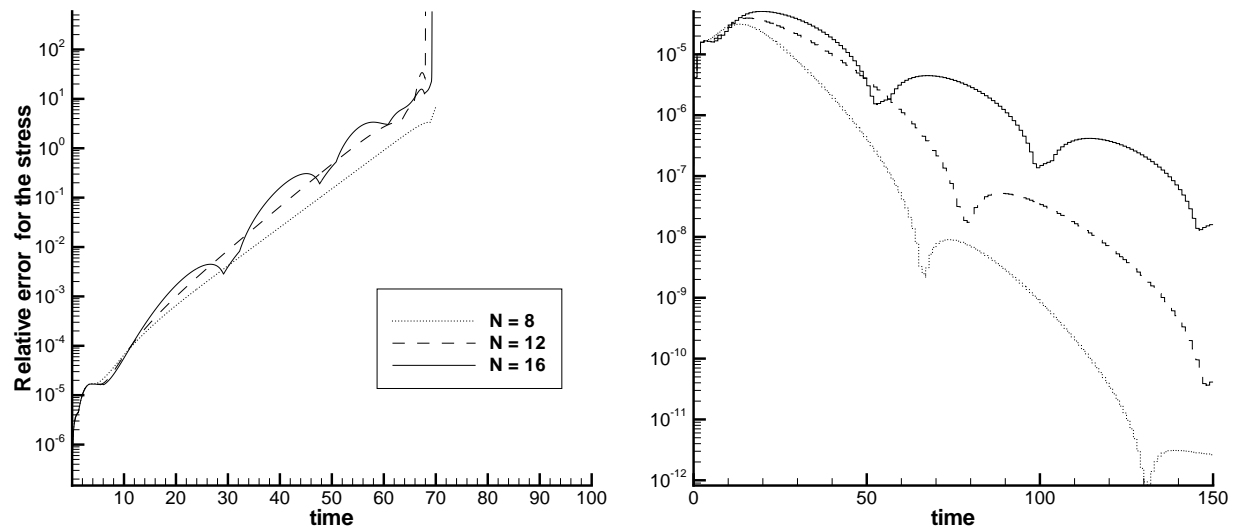


Figure 2.3: Galerkin approximation at  $We = 2$ ; (a) method (2.20), (b) method (2.22).

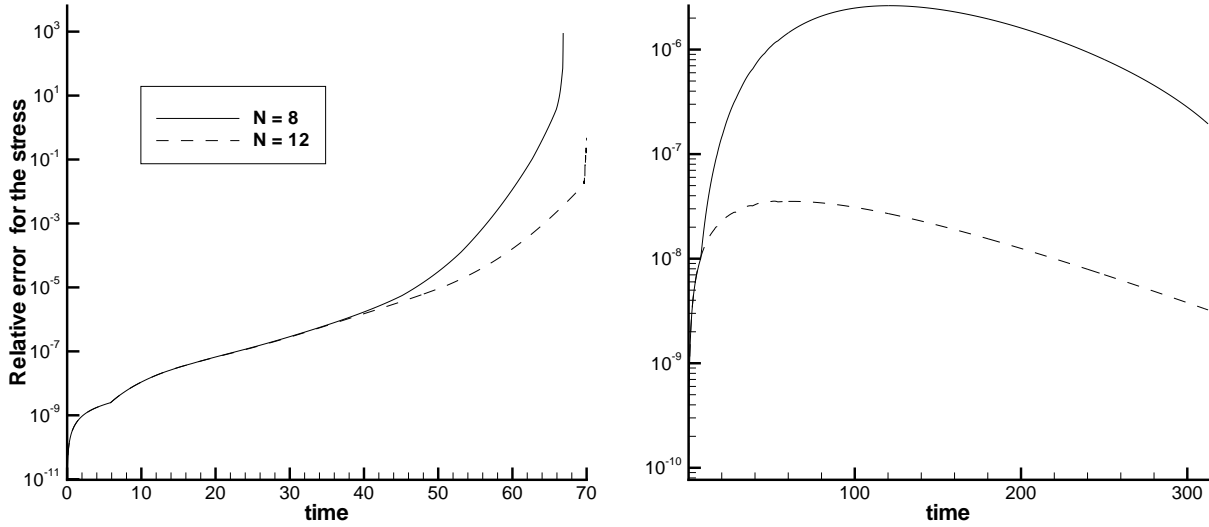


Figure 2.4: Galerkin approximation at  $We = 50$ ; (a) the full Oldroyd B model, (b) simplified model computations.

instead of Eq. (2.18). The absence of instabilities in this case can be easily explained by observing that the Galerkin method for Eq. (2.23) differs from those of Eqs. (2.20) or (2.22) only in that the term  $a_{\mathbf{v}^{i+\alpha}}(\boldsymbol{\tau}'_{i+\alpha}, \mathbf{S})$  is replaced by the inner product  $(\boldsymbol{\tau}'_{i+\alpha}, \mathbf{S})$  which is obviously positive-definite.

Our second simplified example (the solid curve in Fig. 2.4(b)) involves solving the original constitutive equation (2.18) along with the substitution of the exact velocity field (2.19) into it. Here again the Galerkin method works perfectly well which indicates that one of the sources of instabilities can be the very high sensitivity of this numerical method to small errors in the velocity.

### 2.3.3 Stabilization techniques

We first consider two well-known stabilization techniques, namely filtering and the SUPG (streamline upwinded/Petrov-Galerkin) method [23]. Filtering consists of projecting onto the space of polynomials of a lower order. That is, applying a filter to a function  $u_N \in P_N(\Omega)$  gives the function  $u_M \in P_M(\Omega)$  such that

$$(u_M, v_M) = (u_N, v_M), \quad \forall v_M \in P_M(\Omega),$$

for some  $M < N$ . Numerical experiments show that filtering of the elastic extra-stress tensor has a much stronger effect on the stability of the solution than filtering of either the velocity or its gradient. But applying even very crude filters can only postpone the blow-up of the solution. This is the case, for example, for calculations at the rather moderate value of  $We = 6$ , as can be seen from Fig. 2.5.

The SUPG method consists in replacing the test function  $\mathbf{S}$  in Eq. (2.20) by

$$\tilde{\mathbf{S}} = \mathbf{S} + \Theta \left( \frac{\mathbf{v}^{i+\alpha}}{|\mathbf{v}^{i+\alpha}|} \cdot \nabla \right) \mathbf{S}.$$

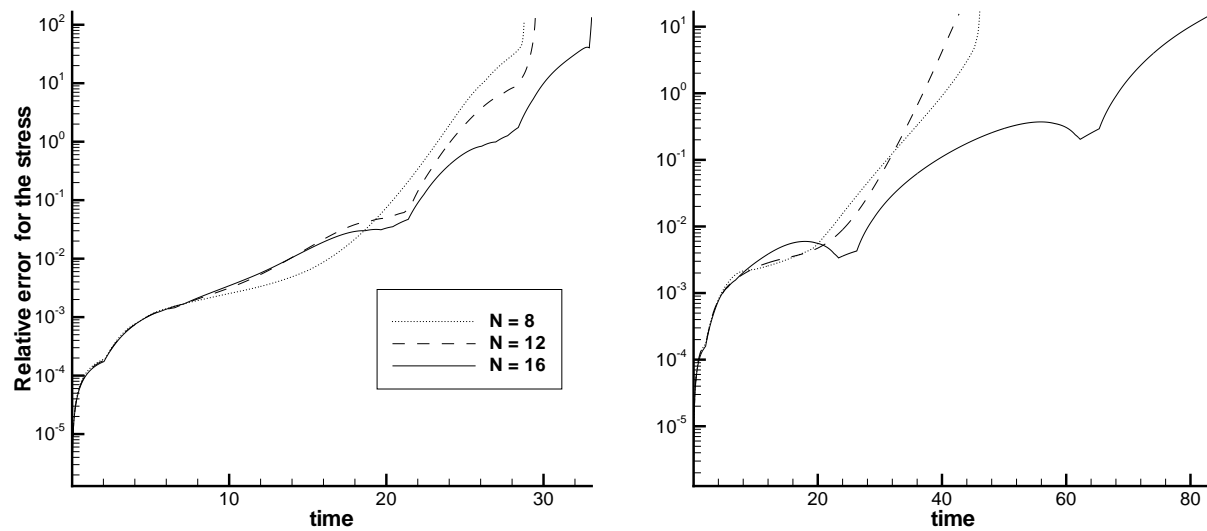


Figure 2.5: Filtering,  $We = 6$ ; (a)  $M = N/2$ , (b)  $M = N/3$ .

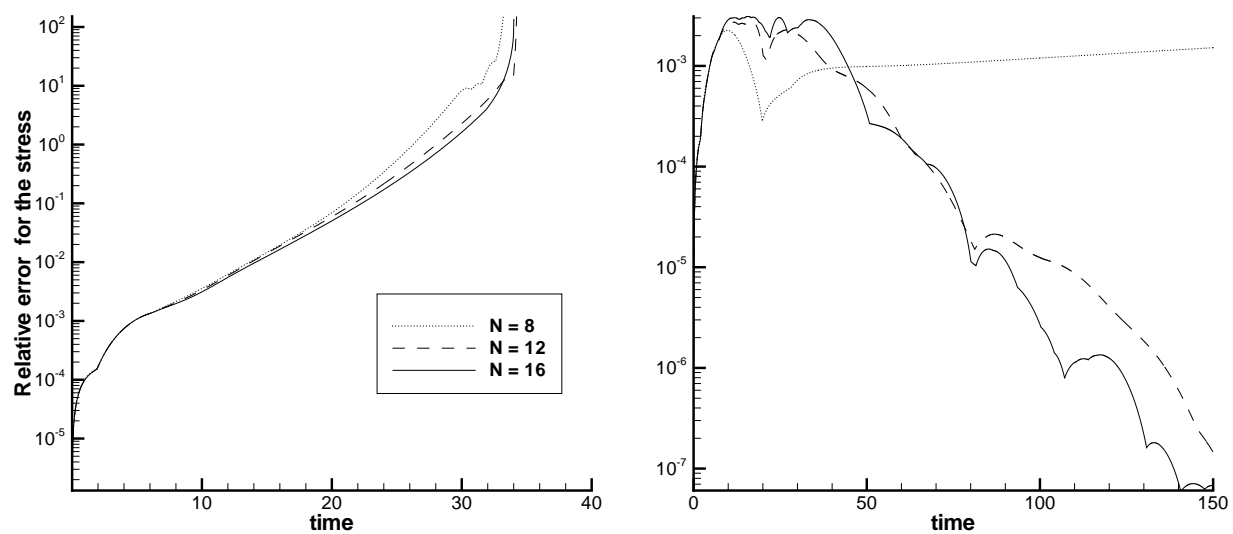


Figure 2.6:  $We = 6$ ; (a) SUPG with  $\Theta = 1/N^2$ , (b) SUPG with  $\Theta = 1$  and filtering  $N/2$ .

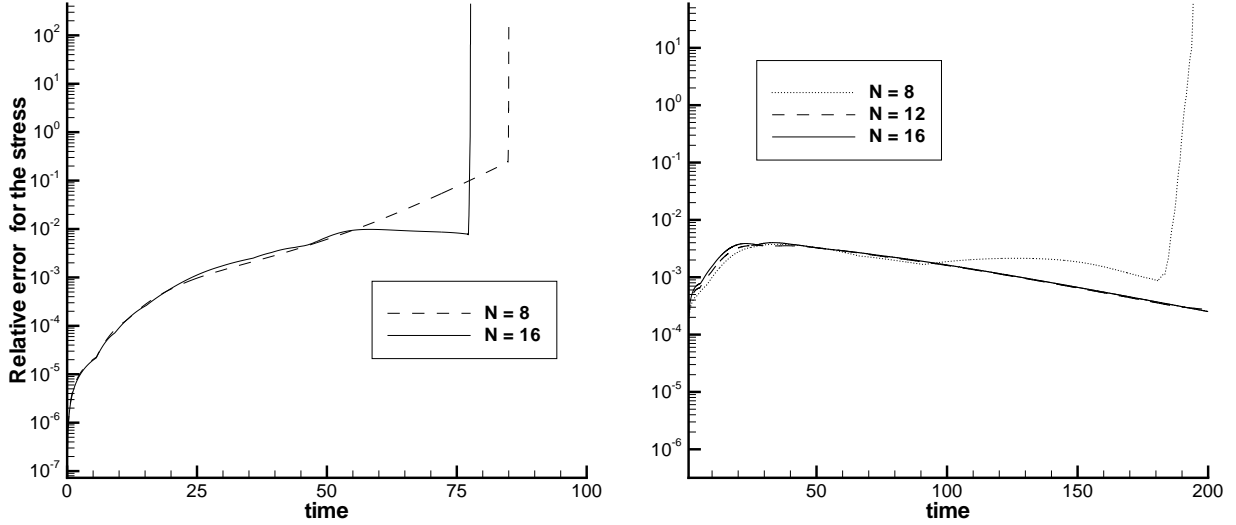


Figure 2.7:  $We = 50$ ; (a) SUPG with  $\Theta = 1$  and filtering  $N/2$ , (b) stabilized method (2.25).

We have thus

$$We \left( \frac{\boldsymbol{\tau}'_{i+1} - \boldsymbol{\tau}'_i}{\Delta t} + \mathbf{v}^{i+1} \cdot \nabla \boldsymbol{\tau}'_{i+\alpha}, \tilde{\mathbf{S}} \right) + a_{\mathbf{v}^{i+\alpha}}(\boldsymbol{\tau}'_{i+\alpha}, \tilde{\mathbf{S}}) = \frac{1-\beta}{We} (\mathbf{I}, \tilde{\mathbf{S}}),$$

instead of Eq. (2.20). Deciding on the proper choice of the upwinding factor  $\Theta$  is not an easy task. For steady-state viscoelastic simulations  $\Theta \sim 1/N^2$  can lead to a significant improvement in terms of stability [33]. However, this seems to be too small for time-dependent simulations (see Fig. 2.6(a)). Only rather large values of the upwinding factor ( $\Theta = 1$ , for example) combined with the crude  $N/2$  filter leads to satisfactory results (Fig. 2.6(b)).

No combination of filtering and SUPG helps to stabilize the solution at larger values of  $We$  (see, for example, Fig. 2.7(a) for  $We = 50$ ). The only thing which we found suitable was to add stabilizing positive-definite terms to the left-hand side of the Galerkin equations. We introduce therefore a Galerkin approximation of Eq. (2.18) with the weak treatment of the inflow conditions:

$$\begin{aligned} We \left( \frac{\boldsymbol{\tau}'_{i+1} - \boldsymbol{\tau}'_i}{\Delta t} + \mathbf{v}^{i+1} \cdot \nabla \boldsymbol{\tau}'_{i+\alpha}, \mathbf{S} \right) + a_{\mathbf{v}^{i+\alpha}}(\boldsymbol{\tau}'_{i+\alpha}, \mathbf{S}) - \frac{We}{2} \int_{\Gamma_{in}} (\mathbf{v}^{i+1}, \mathbf{n}) \mathbf{T}^{i+\alpha} : \mathbf{S} ds \\ = \frac{1-\beta}{We} (I, \mathbf{S}) - \frac{We}{2} \int_{\Gamma_{in}} (\mathbf{v}^{i+1}, \mathbf{n}) \boldsymbol{\varphi}^{i+\alpha} : \mathbf{S} ds, \quad \forall \mathbf{S} \in \Sigma_N(\Omega). \end{aligned} \quad (2.24)$$

The scheme (2.24) has approximately the same properties as (2.20) and the estimate (2.21) can be established for it under the same hypotheses. We then add to the left-hand side (LHS) some positive-definite bilinear form, for example,

$$\text{LHS} := \text{LHS} + \tilde{\Theta}(\nabla \boldsymbol{\tau}', \nabla \mathbf{S}), \quad \tilde{\Theta} = \frac{We}{2N}. \quad (2.25)$$

This method gives a stable solution with the error tending to 0 as the solution approaches the steady state (see Fig. 2.7(b)). Although the term  $\tilde{\Theta}(\nabla \boldsymbol{\tau}', \nabla \mathbf{S})$  is not balanced by anything on the right-hand side, the method (2.25) is still consistent (unlike the stabilized schemes of

Sureshkumar and Beris [127] or Atalık and Keunings [3]) since  $\tilde{\Theta}$  is a decreasing function of  $N$ .

As a summary of this section, we can note that none of the traditional stabilizing techniques has been able to produce a method suitable for spectral element calculations of time-dependent viscoelastic flows for all values of the parameter  $We$ . We note that the instability observed in our computations cannot be attributed to the presence of higher harmonics alone, as is demonstrated by the experiments with filtering. A stabilized method has been developed yielding numerically stable solutions for all  $We$  but at the expense of rather large errors for intermediate times.

## 2.4 The element-by-element method

Many simulations described in the subsequent chapters, will be performed for time-dependent flows of various polymer fluids past a cylinder confined in a channel. Spectral element discretization will be used in physical space. It is easy to see that an efficient method for hyperbolic constitutive equations (or for an FP equation for kinetic theory models) is of special importance in such simulations. Indeed, the Stokes system (for inertialess flows) is a linear system with constant coefficients so that the matrices resulting from its discretization can be constructed and LU-decomposed once for all, and this makes the solution for pressure and velocity relatively inexpensive. On the other hand, all the constitutive relations are non-linear with coefficients depending on the velocity, so that the matrices for their discretization should be constructed and decomposed at every time step.

Fortunately, an efficient method for the discretization of hyperbolic equations encountered in viscoelastic flows simulations, termed the element-by-element method, has been developed in [33]. This method uses continuous approximations of the unknowns in the hyperbolic equation, but allows it to be solved sequentially element-by-element. Thus, the element-by-element method has the advantages of the discontinuous Galerkin method of Lesaint and Raviart [76] but avoids the inconvenience of the latter of having to compute line integrals at the interfaces between adjacent spectral elements. We here provide a description of the element-by-element method borrowed from [33] and using the example of the stationary Oldroyd B constitutive

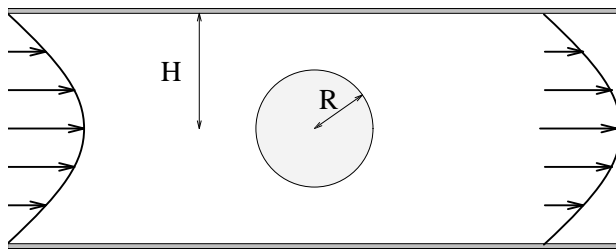


Figure 2.8: Cylinder radius  $R$  placed symmetrically in a 2D channel of half-width  $H$ .



without recirculation. We illustrate this for the flow around a cylinder confined in a channel, see Fig. 2.8. Figure 2.9 shows an example of numbering 22 spectral elements in accordance with the streamlines.

The ordering of the elements is based on the velocity field available at the previous Newton iteration in the case of the stationary flow simulation described here. In a time-dependent simulation, the velocity from the last time step should be used instead. The stress components are required to be continuous across elemental interfaces.  $C^0$  continuity between spectral elements is automatically satisfied by feeding  $\boldsymbol{\tau}_k^-$  on  $\partial\Omega_k^-$  as an inflow condition for any spectral element  $\Omega_k$ . The main difference with the standard Galerkin method lies in the treatment of interfaces between spectral elements. The application of the constitutive equation on the outflow boundary  $\partial\Omega_k^+$  of an element  $\Omega_k$  does not imply a contribution from other elements having boundaries with non-empty intersection with  $\partial\Omega_k^+$  but it only requires contributions from element  $\Omega_k$  itself. To state more precisely what we mean, we consider the simple case of Figure 2.10 where two conforming spectral elements  $\Omega_1$  and  $\Omega_2$  are contiguous and have an interface  $\partial\Omega_{12}$ . Let us assign a numbering  $(p_1, q_1)$  (say) in  $\Omega_1$  to a Gauss-Lobatto point in the interior of  $\partial\Omega_{12}$ . Suppose now that the local numbering for the same point in  $\Omega_2$  is  $(p_2, q_2)$  and take a test tensor  $\mathbf{S}$  such that

$$\mathbf{S}|_{\Omega_1} \equiv \mathbf{S}_N^{(p_1, q_1)} \quad \text{and} \quad \mathbf{S}|_{\Omega_2} \equiv \mathbf{S}_N^{(p_2, q_2)},$$

where  $\mathbf{S}_N^{(i, j)}$  denotes the second-order test tensor both of whose components are polynomials of degree  $N$ , these vanishing at all  $(N+1)^2$  Gauss-Lobatto points except the  $(i, j)$ th. For the standard Galerkin method, the above choice of  $\mathbf{S}$  yields

$$\begin{aligned} & \int_{\Omega_1} (\boldsymbol{\tau} + We \boldsymbol{\nabla} \boldsymbol{\tau}) : \mathbf{S}^{(p_1, q_1)} d\mathbf{x} + \int_{\Omega_2} (\boldsymbol{\tau} + We \boldsymbol{\nabla} \boldsymbol{\tau}) : \mathbf{S}^{(p_2, q_2)} d\mathbf{x} = \\ (1 - \beta) & \int_{\Omega_1} (\boldsymbol{\nabla} \mathbf{v} + \boldsymbol{\nabla} \mathbf{v}^T) : \mathbf{S}^{(p_1, q_1)} d\mathbf{x} + (1 - \beta) \int_{\Omega_2} (\boldsymbol{\nabla} \mathbf{v} + \boldsymbol{\nabla} \mathbf{v}^T) : \mathbf{S}^{(p_2, q_2)} d\mathbf{x}. \end{aligned}$$

When an element-by-element approach is used, instead of summing the contributions from the elements that share a common edge only contributions from the upstream region of  $\partial\Omega_{12}$  are needed. If flow is from left to right in Figure 2.10 and  $\partial\Omega_{12}$  is then the inflow boundary of  $\Omega_2$  we obtain

$$\int_{\Omega_1} (\boldsymbol{\tau} + We \boldsymbol{\nabla} \boldsymbol{\tau}) : \mathbf{S}^{(p_1, q_1)} d\mathbf{x} = (1 - \beta) \int_{\Omega_1} (\boldsymbol{\nabla} \mathbf{v} + \boldsymbol{\nabla} \mathbf{v}^T) : \mathbf{S}^{(p_1, q_1)} d\mathbf{x}.$$

The qualitative improvement of the element-by-element method over the standard Galerkin spectral element method has been shown in [33] (see Figs. 4a-b there). For greater smoothness and higher Weissenberg numbers, this method can also be used in conjunction with the SUPG technique (see Fig. 4c in [33]). Yet higher Weissenberg numbers could be achieved in [103] by allowing the upwinding factor to vary from one test function to another. We recall, however, that no significant improvement has been observed by using SUPG technique in time-dependent simulations (see the preceding section).





# Chapter 3

## On the use of kinetic theory in the construction of numerical methods to simulate flows of an Oldroyd B fluid

### 3.1 Noise-free realizations of the Brownian configuration fields method

#### 3.1.1 Model description

We consider in this section inertialess, isothermal flow of an incompressible Oldroyd B fluid in a bounded domain  $\Omega \subset \mathbb{R}^d$ . The basic conservation equations can be written in this case as (1) and (1.33) with  $\rho = 0$ . As always,  $\mathbf{v}$  denotes the fluid velocity,  $p$  is the pressure,  $\boldsymbol{\tau}$  is the elastic extra-stress tensor, and  $\eta_s$  is the solvent viscosity. As explained in Section 1.1, the stress  $\boldsymbol{\tau}$  can be computed either from the constitutive equation (1.41) or, by interpreting the fluid as a suspension of Hookean dumbbells, by the formula (cf. (1.27))

$$\boldsymbol{\tau} = \frac{\eta_p}{\lambda} (-\mathbf{I} + \langle \mathbf{q}\mathbf{q}^T \rangle) \quad (3.1)$$

where the brackets  $\langle \cdot \rangle$  are used to express the ensemble average of the quantities inside the brackets and  $\mathbf{q}$  is the dumbbells' end-to-end vector. As is explained in Section 1.3, random process  $\mathbf{q}(t, \mathbf{x})$  is the solution to the stochastic differential equation, which takes the following form for Hookean dumbbells:

$$d\mathbf{q} + \left( \mathbf{v} \cdot \nabla \mathbf{q} - \nabla \mathbf{v} \cdot \mathbf{q} + \frac{1}{2\lambda} \mathbf{q} \right) dt = \sqrt{\frac{1}{\lambda}} d\mathbf{W}. \quad (3.2)$$

The kinetic theory interpretation of the Oldroyd B model permits the construction of stochastic simulation techniques for it. In the next section, we give the description of one such technique, which is the Brownian configuration fields (BCF) method.

### 3.1.2 The Brownian configuration fields method (Oldroyd B fluid)

Using a simple implicit Euler-Maruyama scheme for the time discretization of (3.2), we obtain the following stochastic partial differential equation:

$$\begin{aligned} \mathbf{q}(t_i, \mathbf{x}) &+ \left( \mathbf{v}(t_i, \mathbf{x}) \cdot \nabla \mathbf{q}(t_i, \mathbf{x}) - \nabla \mathbf{v}(t_i, \mathbf{x}) \mathbf{q}(t_i, \mathbf{x}) + \frac{1}{2\lambda} \mathbf{q}(t_i, \mathbf{x}) \right) \Delta t \\ &= \mathbf{q}(t_{i-1}, \mathbf{x}) + \sqrt{\frac{\Delta t}{\lambda}} \Phi(t_i) \end{aligned} \quad (3.3)$$

where  $\Phi(t_i)$  are mutually independent random vectors (discrete increments of the Wiener process scaled by a factor of  $1/\sqrt{\Delta t}$ ) having probability distribution  $\mathbf{N}(0, 1)$  so that  $\langle \Phi(t_i) \Phi^T(t_j) \rangle = \delta_{ij} \mathbf{I}$ . Note that the increments of the discrete Wiener process  $\Delta \mathbf{W}_i = \sqrt{\Delta t} \Phi(t_i)$  in (3.3) do not depend on  $\mathbf{x}$  although the original stochastic differential equation (3.2) assumes an independent Wiener process on each particle path. We can afford this simplification since we are interested only in some averages of random vectors  $\mathbf{q}(t_i, \mathbf{x})$ . This idea is the basis of the BCF method [64].

Denoting the linear operator in the first line of (3.3) by  $\mathbf{E}_\mathbf{v}$ , this equation can be rewritten as

$$\mathbf{E}_\mathbf{v} \mathbf{q}(t_i, \mathbf{x}) = \mathbf{q}(t_{i-1}, \mathbf{x}) + \sqrt{\frac{\Delta t}{\lambda}} \Phi(t_i). \quad (3.4)$$

We suppose that the fluid is at equilibrium at time  $t_0 = 0$ , and the system of equations (3.4) is therefore supplied with initial conditions of the form

$$\mathbf{q}(\mathbf{x}, t_0) = \Phi(t_0), \quad (3.5)$$

where  $\Phi(t_0)$  is a Gaussian vector satisfying  $\langle \Phi(t_0) \rangle = \mathbf{0}$  and  $\langle \Phi(t_0) \Phi^T(t_0) \rangle = \mathbf{I}$ .

In the BCF method all the random quantities  $\Phi(t_i)$  are modelled by a large number of pseudo-random vectors  $\Phi_m(t_i)$ ,  $m = 1, \dots, M$ , each of them having approximately Gaussian distribution. This gives rise to  $M$  configuration fields  $\{\mathbf{q}_m(t_i, \mathbf{x})\}_{1 \leq m \leq M}$  which model the random quantities  $\mathbf{q}(t_i, \mathbf{x})$  and therefore satisfy the equations

$$\mathbf{E}_\mathbf{v} \mathbf{q}_m(t_i, \mathbf{x}) = \mathbf{q}_m(t_{i-1}, \mathbf{x}) + \sqrt{\frac{\Delta t}{\lambda}} \Phi_m(t_i). \quad (3.6)$$

Then an approximation of equation (3.1) for the computation of the elastic extra-stress tensor is

$$\boldsymbol{\tau}(t_i, \mathbf{x}) \approx \frac{\eta_p}{\lambda} \left( -\mathbf{I} + \frac{1}{M} \sum_{m=1}^M \mathbf{q}_m(t_i, \mathbf{x}) \mathbf{q}_m^T(t_i, \mathbf{x}) \right). \quad (3.7)$$

Using equation (3.7) leads to elastic extra-stresses suffering from the slow  $O(\frac{1}{\sqrt{M}})$  convergence typical of stochastic methods. In order to get solutions with relatively low noise level, it is usual to solve (3.6) with at least several thousands independent pseudo-random vectors  $\Phi_m(t_i)$  at each time step<sup>1</sup>. The mesoscopic approach is not only CPU intensive but it also requires large amount of memory since all the vectors  $\{\mathbf{q}_m(t_{i-1}, \mathbf{x})\}_{1 \leq m \leq M}$  coming from the previous calculation at time  $t_{i-1}$  must be stored in order to evaluate the right-hand side of (3.6) at time  $t_i$ .

<sup>1</sup>Several hundreds pseudo-random realizations may be enough if variance reduction techniques are used, see [20, 21]

### 3.1.3 A noise-free implementation of the Brownian configuration fields method by Chauvière

Chauvière [28] showed how the linear structure of the equation (3.4) could be used to construct a noise-free implementation of the BCF method. The main idea of his method is the following: instead of performing a stochastic simulation as in (3.6), one can express the random vectors  $\mathbf{q}(t_i, \mathbf{x})$  as linear combinations of Gaussian mutually independent vectors  $\Phi_j(t_j)$ ,  $j \leq i$  and write down the PDEs for the coefficients of these linear combinations. One can then solve these PDEs numerically and obtain the elastic extra-stress as the second moments of sums of Gaussian variables.

Let us describe the method in more detail. It is based on the following result:

**Theorem 3.1 from [28].** *For any  $i \geq 1$ , there exist  $d \times i$  (non-random) vectors denoted by  $\{\mathbf{q}_j^{t_i-l}(t_i, \mathbf{x})\}_{0 \leq l \leq i-1}^{1 \leq j \leq d}$  such that the solution  $\mathbf{q}(t_i, \mathbf{x})$  of (3.4) at time  $t_i$  is given by*

$$\mathbf{q}(t_i, \mathbf{x}) = \sum_{j=1}^d \left\{ \left( \sum_{l=0}^{i-1} \sqrt{\frac{\Delta t}{\lambda}} \mathbf{q}_j^{t_i-l}(t_i, \mathbf{x}) \Phi_j(t_{i-l}) \right) + \mathbf{q}_j^{t_1}(t_i, \mathbf{x}) \Phi_j(t_0) \right\}. \quad (3.8)$$

The proof of this theorem is by induction and gives an explicit expression for the vectors  $\mathbf{q}_j^{t_i-l}(t_i, \mathbf{x})$  which can be obtained with equation

$$\mathbf{q}_j^{t_i}(t_i, \mathbf{x}) = \mathbf{E}_v^{-1}(t_i, \mathbf{x}) \mathbf{e}_j, \quad (3.9)$$

at their time of creation and subsequently updated according to the equation

$$\mathbf{q}_j^{t_i-l}(t_i, \mathbf{x}) = \mathbf{E}_v^{-1}(t_i, \mathbf{x}) \mathbf{q}_j^{t_{i-l}}(t_{i-l}, \mathbf{x}) \text{ for } l = 1, \dots, i-1. \quad (3.10)$$

The notation  $\mathbf{e}_j$  in (3.9) stands for the  $j$ -th Cartesian basis vector. The next theorem shows how the elastic extra-stress can be computed from the vectors  $\{\mathbf{q}_j^{t_i-l}(t_i, \mathbf{x})\}_{0 \leq l \leq i-1}^{1 \leq j \leq d}$ .

**Theorem 3.2 from [28].** *The elastic extra-stress tensor  $\boldsymbol{\tau}(t_i, \mathbf{x})$  at time  $t_i$  can be computed from the vectors  $\{\mathbf{q}_j^{t_i-l}(t_i, \mathbf{x})\}_{0 \leq l \leq i-1}^{1 \leq j \leq d}$  by:*

$$\boldsymbol{\tau}(\mathbf{x}, t_i) = \frac{\eta_p}{\lambda} \left( -\mathbf{I} + \sum_{j=1}^d \left\{ \left( \sum_{l=0}^{i-1} \frac{\Delta t}{\lambda} \mathbf{q}_j^{t_i-l}(t_i, \mathbf{x}) \otimes \mathbf{q}_j^{t_i-l}(t_i, \mathbf{x}) \right) + \mathbf{q}_j^{t_1}(\mathbf{x}, t_i) \otimes \mathbf{q}_j^{t_1}(t_i, \mathbf{x}) \right\} \right). \quad (3.11)$$

The resulting method (3.9)–(3.11) is thus deterministic and noise-free. As can be seen from its description, its computational cost increases linearly with the number of time steps. Although this method was demonstrated to be more efficient than a traditional implementation of the BCF method for the benchmark problem of the flow past a confined cylinder, it is obviously much more expensive than a direct discretization of the constitutive equation. In the next section, we shall follow a slightly different approach in implementing the BCF method, that will result in a numerical method whose computational cost is of the same order as that of traditional methods that solve the constitutive equation.

### 3.1.4 A new noise-free implementation of the Brownian configuration fields method

The idea of this implementation is to represent the solution  $\mathbf{q}(t_i, \mathbf{x})$  of (3.4) (in the sense of probability distributions) as

$$\mathbf{q}(t_i, \mathbf{x}) \sim \mathbf{A}(t_i, \mathbf{x}) \tilde{\Phi}(t_i), \quad (3.12)$$

where by definition  $\tilde{\Phi}(t_i)$  are  $d$ -dimensional Gaussian random vectors satisfying

$$\langle \tilde{\Phi}(t_i) \rangle = \mathbf{0} \text{ and } \langle \tilde{\Phi}(t_i) \tilde{\Phi}^T(t_j) \rangle = \delta_{ij} \mathbf{I}, \quad (3.13)$$

and  $\mathbf{A}(t_i, \mathbf{x})$  are  $d \times d$  (non-random) matrices satisfying recurrence relations specified in the following

**Theorem 1** *Let  $\mathbf{q}(t_i, \mathbf{x})$  be the solution to (3.4)–(3.5) and  $\mathbf{A}(t_i, \mathbf{x})$  for  $i \geq 1$  denote symmetric positive definite  $d \times d$  matrices defined by*

$$\mathbf{A}^2(t_i, \mathbf{x}) = \hat{\mathbf{A}}(t_i, \mathbf{x}) \hat{\mathbf{A}}^T(t_i, \mathbf{x}) + \tilde{\mathbf{A}}(t_i, \mathbf{x}) \tilde{\mathbf{A}}^T(t_i, \mathbf{x}), \quad (3.14)$$

where  $\hat{\mathbf{A}}(t_i, \mathbf{x})$  and  $\tilde{\mathbf{A}}(t_i, \mathbf{x})$  are  $d \times d$  matrices satisfying the following equations<sup>2</sup>

$$\begin{cases} \mathbf{E}_{\mathbf{v}} \tilde{\mathbf{A}}(t_i, \mathbf{x}) = \mathbf{A}(t_{i-1}, \mathbf{x}), \\ \mathbf{E}_{\mathbf{v}} \hat{\mathbf{A}}(t_i, \mathbf{x}) = \sqrt{\frac{\Delta t}{\lambda}} \mathbf{I}, \end{cases} \quad (3.15)$$

and

$$\mathbf{A}(t_0, \mathbf{x}) = \mathbf{I}. \quad (3.16)$$

Then, we have

$$\mathbf{q}(t_i, \mathbf{x}) \sim \mathbf{A}(t_i, \mathbf{x}) \tilde{\Phi}(t_i), \quad (3.17)$$

where  $\tilde{\Phi}(t_i)$  is a  $d$ -dimensional Gaussian random vector satisfying (3.13).

**Proof:** We will prove this statement by induction on  $i$ . We first note that (3.17) is true for  $i = 0$ . Let us suppose then that (3.17) is true at time  $t_{i-1}$ . We can now introduce two  $d \times d$  matrices  $\tilde{\mathbf{A}}(t_i, \mathbf{x})$  and  $\hat{\mathbf{A}}(t_i, \mathbf{x})$  satisfying the relations (3.15). Then, according to Eq. (3.4) and using the inductive hypothesis, we have

$$\mathbf{q}(t_i, \mathbf{x}) \sim \tilde{\mathbf{A}}(t_i, \mathbf{x}) \tilde{\Phi}(t_{i-1}) + \hat{\mathbf{A}}(t_i, \mathbf{x}) \Phi(t_i). \quad (3.18)$$

Since the distribution of a Gaussian vector is uniquely determined by its mean and covariance matrix, in order to prove the relation (3.17), we need to show the two following equalities

1.  $\langle \mathbf{q}(t_i, \mathbf{x}) \rangle = \langle \mathbf{A}(t_i, \mathbf{x}) \tilde{\Phi}(t_i) \rangle,$
2.  $\langle \mathbf{q}(t_i, \mathbf{x}) \mathbf{q}^T(t_i, \mathbf{x}) \rangle = \left\langle \mathbf{A}(t_i, \mathbf{x}) \tilde{\Phi}(t_i) \left( \mathbf{A}(t_i, \mathbf{x}) \tilde{\Phi}(t_i) \right)^T \right\rangle.$

The first equality is trivially satisfied since  $\langle \mathbf{A}(t_i, \mathbf{x}) \tilde{\Phi}(t_i) \rangle = \mathbf{A}(t_i, \mathbf{x}) \langle \tilde{\Phi}(t_i) \rangle = \mathbf{0}$ , according to Eq. (3.13). In order to prove the second equality, we note that  $\tilde{\Phi}(t_{i-1})$  and  $\Phi(t_i)$

---

<sup>2</sup>Note that the operator  $\mathbf{E}_{\mathbf{v}}$  is applied here to matrix fields although it was defined as acting on vectors. This is done in the usual way, namely  $\mathbf{E}_{\mathbf{v}}$  is applied separately to each column of the corresponding matrix.

are independent random variables since  $\Phi(t_i)$  is proportional to the increment in the Wiener process ( $\mathbf{W}(t_i) - \mathbf{W}(t_{i-1})$ ) which does not depend on the history for  $t \leq t_{i-1}$ ; so that we have

$$\left\langle \tilde{\Phi}(t_{i-1}) \Phi^T(t_i) \right\rangle = \left\langle \Phi(t_i) \tilde{\Phi}^T(t_{i-1}) \right\rangle = \mathbf{0}. \quad (3.19)$$

Replacing  $\mathbf{q}(t_i, \mathbf{x})$  by its statistically equivalent expression (3.18) and by using (3.19), we obtain

$$\begin{aligned} \left\langle \mathbf{q}(t_i, \mathbf{x}) \mathbf{q}^T(t_i, \mathbf{x}) \right\rangle &= \left\langle \left( \tilde{\mathbf{A}}(t_i, \mathbf{x}) \tilde{\Phi}(t_{i-1}) + \hat{\mathbf{A}}(t_i, \mathbf{x}) \Phi(t_i) \right) \right. \\ &\quad \left. \left( \tilde{\mathbf{A}}(t_i, \mathbf{x}) \tilde{\Phi}(t_{i-1}) + \hat{\mathbf{A}}(t_i, \mathbf{x}) \Phi(t_i) \right)^T \right\rangle \\ &= \hat{\mathbf{A}}(t_i, \mathbf{x}) \hat{\mathbf{A}}^T(t_i, \mathbf{x}) + \tilde{\mathbf{A}}(t_i, \mathbf{x}) \tilde{\mathbf{A}}^T(t_i, \mathbf{x}). \end{aligned} \quad (3.20)$$

In a similar way we compute  $\left\langle \mathbf{A}(t_i, \mathbf{x}) \tilde{\Phi}(t_i) \left( \mathbf{A}(t_i, \mathbf{x}) \tilde{\Phi}(t_i) \right)^T \right\rangle$  as follows

$$\begin{aligned} \left\langle \mathbf{A}(t_i, \mathbf{x}) \tilde{\Phi}(t_i) \left( \mathbf{A}(t_i, \mathbf{x}) \tilde{\Phi}(t_i) \right)^T \right\rangle &= \left\langle \mathbf{A}(t_i, \mathbf{x}) \tilde{\Phi}(t_i) \tilde{\Phi}^T(t_i) \mathbf{A}^T(t_i, \mathbf{x}) \right\rangle \\ &= \mathbf{A}(t_i, \mathbf{x}) \left\langle \tilde{\Phi}(t_i) \tilde{\Phi}^T(t_i) \right\rangle \mathbf{A}^T(t_i, \mathbf{x}) \\ &= \mathbf{A}(t_i, \mathbf{x}) \mathbf{A}^T(t_i, \mathbf{x}). \end{aligned} \quad (3.21)$$

Comparing the right-hand sides of the equations (3.20) and (3.21) we see that the random vectors  $\mathbf{q}(t_i, \mathbf{x})$  and  $\mathbf{A}(t_i, \mathbf{x}) \tilde{\Phi}(t_i)$  have the same covariance matrices and therefore are equivalent in distribution provided the matrices  $\mathbf{A}(t_i, \mathbf{x})$  are defined at each point  $\mathbf{x}$  by (3.14). Note that Eq. (3.14) has a unique solution for  $\mathbf{A}(t_i, \mathbf{x})$  in the class of symmetric positive definite matrices since its right-hand side is a symmetric and positive definite matrix. The theorem is thus proved by induction.  $\square$

Theorem 5 can be used in order to derive a simple expression for the elastic extra-stress  $\boldsymbol{\tau}(\mathbf{x}, t_i)$  as stated in the theorem below.

**Theorem 2** *The elastic extra-stress  $\boldsymbol{\tau}(t_i, \mathbf{x})$  at time  $t_i = i\Delta t$  is given by*

$$\boldsymbol{\tau}(t_i, \mathbf{x}) = \frac{\eta_p}{\lambda} \left( -\mathbf{I} + \mathbf{A}^2(t_i, \mathbf{x}) \right), \quad (3.22)$$

where  $\mathbf{A}(t_i, \mathbf{x})$  is the  $d \times d$  matrix defined by equation (3.14).

**Proof:** The vector  $\mathbf{q}$  in equation (3.1) at time  $t_i$  and at a position  $\mathbf{x}$  can be replaced by its statistically equivalent expression  $\mathbf{A}(t_i, \mathbf{x}) \tilde{\Phi}(t_i)$  derived in Theorem 5. and the elastic extra-stress becomes

$$\boldsymbol{\tau}(t_i, \mathbf{x}) = \frac{\eta_p}{\lambda} \left( -\mathbf{I} + \left\langle \mathbf{A}(t_i, \mathbf{x}) \tilde{\Phi}(t_i) \left( \mathbf{A}(t_i, \mathbf{x}) \tilde{\Phi}(t_i) \right)^T \right\rangle \right) \quad (3.23)$$

We can now use the relation (3.21) derived in Theorem 5 to get (3.22).  $\square$

Note that expression (3.22) for the elastic extra-stress tensor gives noise-free solutions. In the next theorem, we would like to make the connection between the new way of computing the elastic extra-stress described above and the Oldroyd B constitutive equation (1.41). This theorem is thus a justification of the discretization of stochastic differential equation in the very simple case of Hookean dumbbells.

**Theorem 3** *The elastic extra-stress tensor computed by (3.22) and (3.4)–(3.16) satisfies the equation*

$$\begin{aligned} \frac{\boldsymbol{\tau}(t_i, \mathbf{x}) - \boldsymbol{\tau}(t_{i-1}, \mathbf{x})}{\Delta t} &+ \frac{1}{\lambda} \boldsymbol{\tau}(t_i, \mathbf{x}) + \mathbf{v}(t_i, \mathbf{x}) \cdot \nabla \boldsymbol{\tau}(t_i, \mathbf{x}) \\ &- \nabla \mathbf{v}(t_i, \mathbf{x}) \boldsymbol{\tau}(t_i, \mathbf{x}) - \boldsymbol{\tau}(t_i, \mathbf{x}) \nabla \mathbf{v}^T(t_i, \mathbf{x}) \\ &= \frac{\eta_p}{\lambda} (\nabla \mathbf{v}(t_i, \mathbf{x}) + \nabla \mathbf{v}^T(t_i, \mathbf{x})) + O(\Delta t) \end{aligned} \quad (3.24)$$

which gives the Oldroyd B constitutive equation (1.41) in the limit  $\Delta t \rightarrow 0$ .

**Proof:** Let us start by developing the following tensor product:

$$\begin{aligned} &\left\langle \left( \mathbf{q}(t_{i-1}, \mathbf{x}) + \sqrt{\frac{\Delta t}{\lambda}} \boldsymbol{\Phi}(t_i) \right) \otimes \left( \mathbf{q}(t_{i-1}, \mathbf{x}) + \sqrt{\frac{\Delta t}{\lambda}} \boldsymbol{\Phi}(t_i) \right) \right\rangle \\ &= \langle \mathbf{q}(t_{i-1}, \mathbf{x}) \otimes \mathbf{q}(t_{i-1}, \mathbf{x}) \rangle + \sqrt{\frac{\Delta t}{\lambda}} \langle \mathbf{q}(t_{i-1}, \mathbf{x}) \otimes \boldsymbol{\Phi}(t_i) \rangle \\ &\quad + \sqrt{\frac{\Delta t}{\lambda}} \langle \boldsymbol{\Phi}(t_i) \otimes \mathbf{q}(t_{i-1}, \mathbf{x}) \rangle + \frac{\Delta t}{\lambda} \langle \boldsymbol{\Phi}(t_i) \otimes \boldsymbol{\Phi}(t_i) \rangle. \end{aligned} \quad (3.25)$$

In order to simplify the above expression, we note that the random vectors  $\mathbf{q}(t_{i-1}, \mathbf{x})$  and  $\boldsymbol{\Phi}(t_i)$  are independent, so we have

$$\begin{aligned} &\left\langle \left( \mathbf{q}(t_{i-1}, \mathbf{x}) + \sqrt{\frac{\Delta t}{\lambda}} \boldsymbol{\Phi}(t_i) \right) \otimes \left( \mathbf{q}(t_{i-1}, \mathbf{x}) + \sqrt{\frac{\Delta t}{\lambda}} \boldsymbol{\Phi}(t_i) \right) \right\rangle \\ &= \langle \mathbf{q}(t_{i-1}, \mathbf{x}) \otimes \mathbf{q}(t_{i-1}, \mathbf{x}) \rangle + \frac{\Delta t}{\lambda} \mathbf{I}. \end{aligned} \quad (3.26)$$

We can now substitute  $\mathbf{q}(t_{i-1}, \mathbf{x})$  by its equivalent expression obtained from (3.3) and divide throughout by  $\Delta t$  to obtain

$$\begin{aligned} \frac{1}{\Delta t} \langle \mathbf{q} \otimes \mathbf{q} \rangle_{(t_{i-1}, \mathbf{x})} + \frac{\mathbf{I}}{\lambda} &= \Delta t \left\langle \left( \frac{1}{\Delta t} \mathbf{q} + \mathbf{v} \cdot \nabla \mathbf{q} - (\nabla \mathbf{v}) \mathbf{q} + \frac{1}{2\lambda} \mathbf{q} \right) \otimes \right. \\ &\quad \left. \left( \frac{1}{\Delta t} \mathbf{q} + \mathbf{v} \cdot \nabla \mathbf{q} - (\nabla \mathbf{v}) \mathbf{q} + \frac{1}{2\lambda} \mathbf{q} \right) \right\rangle_{(t_i, \mathbf{x})}. \end{aligned} \quad (3.27)$$

Here we have introduced the notation  $\langle \cdot \rangle_{(t_i, \mathbf{x})}$  to indicate that all variables inside the brackets are evaluated at  $\mathbf{x}$  at time  $t_i$ . By developing the tensor product and neglecting the higher order terms in  $\Delta t$ , we obtain

$$\begin{aligned} \frac{1}{\Delta t} \langle \mathbf{q} \otimes \mathbf{q} \rangle_{(t_{i-1}, \mathbf{x})} + \frac{\mathbf{I}}{\lambda} &= \langle \mathbf{q} \otimes (\mathbf{v} \cdot \nabla \mathbf{q}) \rangle_{(t_i, \mathbf{x})} - \langle \mathbf{q} \otimes (\nabla \mathbf{v}) \mathbf{q} \rangle_{(t_i, \mathbf{x})} \\ &+ \frac{1}{\lambda} \langle \mathbf{q} \otimes \mathbf{q} \rangle_{(t_i, \mathbf{x})} + \langle (\mathbf{v} \cdot \nabla \mathbf{q}) \otimes \mathbf{q} \rangle_{(t_i, \mathbf{x})} \\ &- \langle (\nabla \mathbf{v}) \mathbf{q} \otimes \mathbf{q} \rangle_{(t_i, \mathbf{x})} + \frac{1}{\Delta t} \langle \mathbf{q} \otimes \mathbf{q} \rangle_{(t_i, \mathbf{x})} + O(\Delta t). \end{aligned} \quad (3.28)$$

We can group some of the terms since

$$\mathbf{q} \otimes (\mathbf{v} \cdot \nabla \mathbf{q}) + (\mathbf{v} \cdot \nabla \mathbf{q}) \otimes \mathbf{q} = \mathbf{v} \cdot \nabla (\mathbf{q} \otimes \mathbf{q}), \quad (3.29)$$

and note that

$$\mathbf{q} \otimes \nabla \mathbf{v} \mathbf{Q} = \mathbf{q} \otimes \mathbf{q} (\nabla \mathbf{v})^T, \quad (3.30)$$

to simplify equation (3.28) as follows

$$\begin{aligned} \frac{1}{\Delta t} \langle \mathbf{q} \otimes \mathbf{q} \rangle_{(t_{i-1}, \mathbf{x})} + \frac{\mathbf{I}}{\lambda} &= \frac{1}{\Delta t} \langle \mathbf{q} \otimes \mathbf{q} \rangle_{(t_i, \mathbf{x})} + \frac{1}{\lambda} \langle \mathbf{q} \otimes \mathbf{q} \rangle_{(t_i, \mathbf{x})} \\ &+ \mathbf{v}(t_i, \mathbf{x}) \cdot \nabla \langle \mathbf{q} \otimes \mathbf{q} \rangle_{(t_i, \mathbf{x})} \\ &- \nabla \mathbf{v}(t_i, \mathbf{x}) \langle \mathbf{q} \otimes \mathbf{q} \rangle_{(t_i, \mathbf{x})} \\ &- \langle \mathbf{q} \otimes \mathbf{q} \rangle_{(t_i, \mathbf{x})} \nabla \mathbf{v}^T(t_i, \mathbf{x}) + O(\Delta t). \end{aligned} \quad (3.31)$$

We have according to equation (3.22)

$$\langle \mathbf{q} \otimes \mathbf{q} \rangle_{(t_i, \mathbf{x})} = \mathbf{A}(t_i, \mathbf{x}) \mathbf{A}^T(t_i, \mathbf{x}) = \mathbf{I} + \frac{\lambda}{\eta_p} \boldsymbol{\tau}(\mathbf{x}, t_i).$$

Inserting the above expression into equation (3.31), we obtain (3.24).  $\square$

Theorem 3 shows that our method is equivalent to the implicit Euler numerical scheme for the constitutive equation (1.41) if one neglects the terms of order  $\Delta t$ . One can then ask what is the advantage of our method over a straight forward simulations based upon the constitutive equation. We point out two such advantages:

1. The BCF methods are usually more stable than ones based directly upon the macroscopic equations. One should expect the same of our method since it is in fact a version of the BCF method which employs an infinite number of configuration fields. This observation is justified by the numerical results of Section 3.1.6.
2. One can prove that any solution of the Oldroyd B constitutive equation should satisfy the property that the conformation tensor  $\mathbf{I} + \frac{\lambda}{\eta_p} \boldsymbol{\tau}$  is positive definite for all  $\mathbf{x}$  and  $t$ . The violation of this property in numerical simulations can result in Hadamard instabilities [70]. The positive definiteness of the conformation tensor is preserved automatically by our method due to (3.22). On the contrary, it can be violated in traditional numerical simulations using closed-form constitutive equations.

### 3.1.5 Computational procedure

The algorithm introduced in the previous section was discrete only with respect to time. In this section, we will describe how it can be discretized in space as well. The considerations here are quite general and do not suppose a particular type of discretization i.e. methods such as finite element methods, spectral element methods, finite volume methods, etc. may equally well be used.

Let the computational grid consist of points  $\mathbf{x}_l$ ,  $1 \leq l \leq N_c$  and let  $\overline{\mathbf{E}}_{\mathbf{v}}(t_i)$  be the matrix resulting from the discretization of the linear operator  $\mathbf{E}_{\mathbf{v}}$  at time  $t_i$  for a given velocity field  $\mathbf{v}$ . We recall that the operator  $\mathbf{E}_{\mathbf{v}}$  acts on vector fields, which are now defined at each of the

grid nodes  $\{\mathbf{x}_l\}$ , hence the dimensions of the matrix  $\bar{\mathbf{E}}_{\mathbf{v}}(t_i)$  are  $(dN_c) \times (dN_c)$ . We suppose that the problem is well-posed so that  $\bar{\mathbf{E}}_{\mathbf{v}}(t_i)$  has the inverse  $\bar{\mathbf{E}}_{\mathbf{v}}^{-1}(t_i)$ . The unknowns in our approach are  $d \times d$  matrices  $\mathbf{A}(t_i, \mathbf{x}_l)$  defined at all the grid points  $\mathbf{x}_l$ ,  $1 \leq l \leq N_c$  and for all times  $t_i = i\Delta t$ .

At the initial time we set

$$\mathbf{A}(t_0, \mathbf{x}_l) = \mathbf{I}, \quad \boldsymbol{\tau}(t_0, \mathbf{x}_l) = \mathbf{0}, \quad 1 \leq l \leq N_c.$$

The general computational procedure at the  $i$ -th time step ( $i \geq 0$ ) may be summarized as follows:

1. Solve the discrete analogue of the Stokes problem (1), (1.33) to determine the velocity field  $\mathbf{v}(t_{i-1}, \mathbf{x}_l)$  using the elastic extra-stress  $\boldsymbol{\tau}(t_{i-1}, \mathbf{x}_l)$  computed at the previous time step.
2. Compute the matrix  $\bar{\mathbf{E}}_{\mathbf{v}}(t_i)$  based on the velocity  $\mathbf{v}(t_{i-1}, \mathbf{x}_l)$ .
3. Gather all the  $d \times d$  matrices  $\mathbf{A}(t_{i-1}, \mathbf{x}_l)$ ,  $l = 1, \dots, N_c$  into a  $(dN_c) \times d$  matrix  $\mathcal{A}(t_{i-1})$  by stacking them one on top of another and denote by  $\mathcal{I}$  the  $(dN_c) \times d$  matrix composed of  $N_c$  identity  $d \times d$  matrices arranged in the same manner. Compute new  $(dN_c) \times d$  matrices  $\tilde{\mathcal{A}}(t_i)$  and  $\hat{\mathcal{A}}(t_i)$  satisfying (approximately if an iterative technique is used) the equations

$$\begin{aligned} \bar{\mathbf{E}}_{\mathbf{v}}(t_i) \tilde{\mathcal{A}}(t_i) &= \mathcal{A}(t_{i-1}), \\ \bar{\mathbf{E}}_{\mathbf{v}}(t_i) \hat{\mathcal{A}}(t_i) &= \sqrt{\frac{\Delta t}{\lambda}} \mathcal{I}, \end{aligned}$$

which are the discrete analogues of (3.15). Disassemble  $\tilde{\mathcal{A}}(t_i)$  and  $\hat{\mathcal{A}}(t_i)$  back into the matrices  $\tilde{\mathbf{A}}(\mathbf{x}_l, t_i)$  and  $\hat{\mathbf{A}}(\mathbf{x}_l, t_i)$ , respectively, with  $l = 1, \dots, N_c$ .

4. Compute the  $d \times d$  symmetric positive definite matrices  $\mathbf{A}(t_i, \mathbf{x}_l)$  by solving at every grid point  $\mathbf{x}_l$ ,  $1 \leq l \leq N_c$  the equation

$$\mathbf{A}^2(t_i, \mathbf{x}_l) = \hat{\mathbf{A}}(t_i, \mathbf{x}_l) \hat{\mathbf{A}}^T(t_i, \mathbf{x}_l) + \tilde{\mathbf{A}}(t_i, \mathbf{x}_l) \tilde{\mathbf{A}}^T(t_i, \mathbf{x}_l). \quad (3.32)$$

5. Compute the extra stress  $\boldsymbol{\tau}(\mathbf{x}_l, t_i)$  by applying at every grid point  $\mathbf{x}_l$ ,  $1 \leq l \leq N_c$  the formula

$$\boldsymbol{\tau}(t_i, \mathbf{x}_l) = \frac{\eta_p}{\lambda} (-\mathbf{I} + \mathbf{A}^2(t_i, \mathbf{x}_l)). \quad (3.33)$$

6. Increment  $i$  by 1 and go to stage 1 unless the final time has been reached or a stopping criterion is satisfied.

Note that steps 4 and 5 of the algorithm need a number of operations proportional to  $N_c$  so their cost will be very small in comparison with steps 1–3. In step 3 we need to solve the linear system with the matrix  $\bar{\mathbf{E}}_{\mathbf{v}}(t_i)$  with  $2d$  different right-hand sides. This means that our method is equivalent in terms of the cost to a BCF method with  $2d$  configuration fields. It is an important improvement since in the BCF approach the number of configuration fields may



be several thousands. Clearly, our method is also advantageous with respect to the method of Chauvière [28] described in Section 3.1.3 since the linear system with the matrix  $\bar{\mathbf{E}}_{\mathbf{v}}(t_i)$  is solved there with  $2d(i+1)$  right-hand sides. In fact, our method is at least as efficient as the methods based on the constitutive equation and for some implementations it can be even cheaper (see the numerical results in the next section).

### 3.1.6 Numerical results for the flow past a confined cylinder

In order to evaluate the performance of the proposed numerical method, we shall compute solutions for the planar viscoelastic flow of an Oldroyd B fluid past a cylinder placed symmetrically in a channel (see Fig. 2.8). For an extensive review of this benchmark problem, the reader is referred to the recent book by Owens and Phillips [108]. The ratio of the cylinder's radius  $R$  to the half-width of the channel  $H$  is taken equal to 0.5. This benchmark problem is acknowledged to be more difficult than the related sphere problem because for the same aspect ratio  $R/H$ , the planar flow past a cylinder in a channel undergoes stronger contraction and expansion than the axisymmetric flow past a sphere. The Weissenberg number  $We$  for this problem is defined in the usual fashion to be

$$We = \frac{\lambda \bar{U}}{R}, \quad (3.34)$$

where  $\bar{U}$  is the average velocity of the fluid in the channel at entry. The ratio of the solvent viscosity  $\eta_s$  to the total viscosity  $\eta = (\eta_s + \eta_p)$  was taken equal to 0.59, as is usually done in the literature [27, 41, 48, 126] for this benchmark problem.

We implement three approaches: direct discretization of the constitutive equation, the method of Chauvière [28] described in Section 3.1.3 and our new noise free implementation of the BCF method summarized in the preceding section.

#### Discretization of the equations

For discretization in physical space, we use for all three approaches the Legendre spectral element method [85, 109], as described in Section 2.2. The flow domain is divided into 46 conforming spectral elements and polynomial degrees ranging from  $N = 6$  to  $N = 12$  are used in the two spatial directions for velocity and stress or matrix fields  $\mathbf{A}$  (the polynomials for the pressure are always of degree  $N - 2$ ). To discretize the constitutive equation and the operator  $\mathbf{E}_{\mathbf{v}}$  we use the element-by-element method described in Section 2.4 in combination with the SUPG technique with an upwinding factor  $1/N^2$ . The time steps are chosen equal to  $\Delta t = 0.025$  and the iterations are stopped when the following convergence criterion is fulfilled for all collocation points  $\mathbf{x} \in \Omega$  :

$$\frac{|\mathbf{v}(t_{i+1}, \mathbf{x}) - \mathbf{v}(t_i, \mathbf{x})|}{\Delta t} \leq 10^{-4}.$$

#### Filtering

Most of our numerical results would not have been possible without filtering the solutions. This filter takes the form

$$\sigma(\eta) = \exp(-\alpha\eta^{2p}),$$

where  $2p$  is the order of the filter and  $\alpha = -\ln \varepsilon$ ;  $\varepsilon$  being the machine accuracy. An extensive description and detailed properties of this filter can be found in [6, 57] and references therein. For all our numerical experiments, we use the same order for the filter i.e.  $p = 9$ , which was found to give the best compromise between stability and accuracy. For the numerical results of the new method described in this paper, we filter the columns of the matrices  $\tilde{\mathcal{A}}(t_i)$  and  $\tilde{\mathcal{A}}(t_i)$  introduced in the previous section. This was found to give better results (in terms of accuracy and robustness) than filtering the elastic extra-stress. For macroscopic simulations, microscopic quantities are not available and therefore we filter the elastic extra-stress. Although no filter was originally used in [28], the results reported in Table 3.4 make use of the filter in order not to disadvantage any of the tested methods.

## Numerical results

The drag factor  $F^*$  on the cylinder is defined by

$$F^* = \frac{F}{4\pi\eta\bar{U}}, \quad (3.35)$$

where  $F$  is the drag on the cylinder

$$F = \int_0^\pi \left\{ \left( -p + 2\eta_s \frac{\partial u_x}{\partial x} + \tau_{xx} \right) \cos \theta + \left( \eta_s \left( \frac{\partial u_y}{\partial x} + \frac{\partial u_x}{\partial y} \right) + \tau_{xy} \right) \sin \theta \right\} R d\theta.$$

Tables 3.1 and 3.2 give the value of the drag factor for the new mesoscopic approach described in Section 3.1.5 and for the classical Oldroyd B constitutive equation (1.41), respectively, for different level of discretization ( $N = 6, \dots, 12$ ) and different Weissenberg numbers<sup>3</sup>. We see that the mesoscopic simulation is always more stable (Weissenberg numbers up to 0.9 can be reached) than its macroscopic counterpart for which the maximum Weissenberg number achievable was limited to 0.7.

All the values for  $F^*$  obtained by our method are very close to those presented in [41, 48, 126]. Moreover, in Table 3.3 we show that the drag factor on the cylinder converges to that from [48] as the time step is reduced with the exception of the case  $We = 0.9$ .  $\varepsilon_F$  in this table stands for the absolute value of the difference between  $F^*$  computed by our method and that from [48], divided by the latter.

The CPU intensive part of our algorithm is the LU decomposition of the matrix  $\bar{\mathbf{E}}_{\mathbf{v}}$  at each time step. Since we are using an element-by-element method, then for a 2D problem and using a polynomial representation of degree  $N$ , we need to LU decompose matrices of size  $2(N+1)^2$ . The number of operations involved per time step is then proportional to  $8(N+1)^6$ . When a macroscopic approach is used, instead of having two unknowns ( $Q_x, Q_y$ ), we have three unknowns ( $\tau_{xx}, \tau_{xy}, \tau_{yy}$ ) and the size of the matrices to be LU decomposed is now  $3(N+1)^2$ . The cost involved is then proportional to  $27(N+1)^6$ . The gain in using our new approach for the computation of the non-Newtonian part is therefore more than threefold as compared to using a closed-form constitutive equation. The relative CPU time taken to compute both the velocity field and the elastic extra-stress is compared for the three methods in Table 3.4. Note that the overall gain in time is less than threefold since we have to solve on each time step the

---

<sup>3</sup>Omissions in Table 3.2 indicate that the code blows up for the corresponding parameter set. The same behaviour was observed for higher Weissenberg numbers that are therefore not included in the table.

Table 3.1: Drag factor  $F^*$  computed on uniform meshes ( $N = 6, \dots, 12$ ). Mesoscopic simulation.

<b>We</b>	<b>N=6</b>	<b>N=8</b>	<b>N=10</b>	<b>N=12</b>
<b>0.5</b>	9.4464	9.4468	9.4464	9.4462
<b>0.6</b>	9.3696	9.3638	9.3636	9.3638
<b>0.7</b>	9.3446	9.3292	9.3278	9.3274
<b>0.8</b>	9.3649	9.3352	9.3327	9.3291
<b>0.9</b>	9.4218	9.3742	9.3709	9.3615

Table 3.2: Drag factor  $F^*$  computed on uniform meshes ( $N = 6, \dots, 12$ ). Macroscopic simulation.

<b>We</b>	<b>N=6</b>	<b>N=8</b>	<b>N=10</b>	<b>N=12</b>
<b>0.5</b>	9.4621	9.4628	9.4548	9.4560
<b>0.6</b>	-	9.3806	9.3710	9.3726
<b>0.7</b>	-	9.3553	9.3402	9.3365

Table 3.3: Drag factor  $F^*$  computed on uniform mesh ( $N = 10$ ) for different time steps  $\Delta t$ . Mesoscopic simulation.

<b>We</b>	$\Delta t = 2.5 \times 10^{-2}$		$\Delta t = 1.25 \times 10^{-2}$		$\Delta t = 6.25 \times 10^{-3}$	
	$F^*$	$\varepsilon_F$	$F^*$	$\varepsilon_F$	$F^*$	$\varepsilon_F$
<b>0.5</b>	9.4464	$1.0 \cdot 10^{-3}$	9.4509	$5.6 \cdot 10^{-4}$	9.4530	$3.4 \cdot 10^{-4}$
<b>0.6</b>	9.3636	$9.6 \cdot 10^{-4}$	9.3672	$5.7 \cdot 10^{-4}$	9.3682	$4.7 \cdot 10^{-4}$
<b>0.7</b>	9.3278	$8.8 \cdot 10^{-4}$	9.3314	$5.0 \cdot 10^{-4}$	9.3319	$4.4 \cdot 10^{-4}$
<b>0.8</b>	9.3327	$7.0 \cdot 10^{-4}$	9.3374	$1.9 \cdot 10^{-4}$	9.3389	$3.3 \cdot 10^{-5}$
<b>0.9</b>	9.3709	$2.2 \cdot 10^{-3}$	9.3772	$2.8 \cdot 10^{-3}$	9.3824	$3.4 \cdot 10^{-3}$

Table 3.4: Relative CPU time for three different methods on uniform meshes ( $N = 7, \dots, 10$ ) at  $We = 0.6$ .

	<b>N=7</b>	<b>N=8</b>	<b>N=9</b>	<b>N=10</b>
Present method	1.0	1.0	1.0	1.0
Constitutive equation	1.5	1.5	1.6	1.6
Method in [28]	18.7	14.4	16.6	15.9

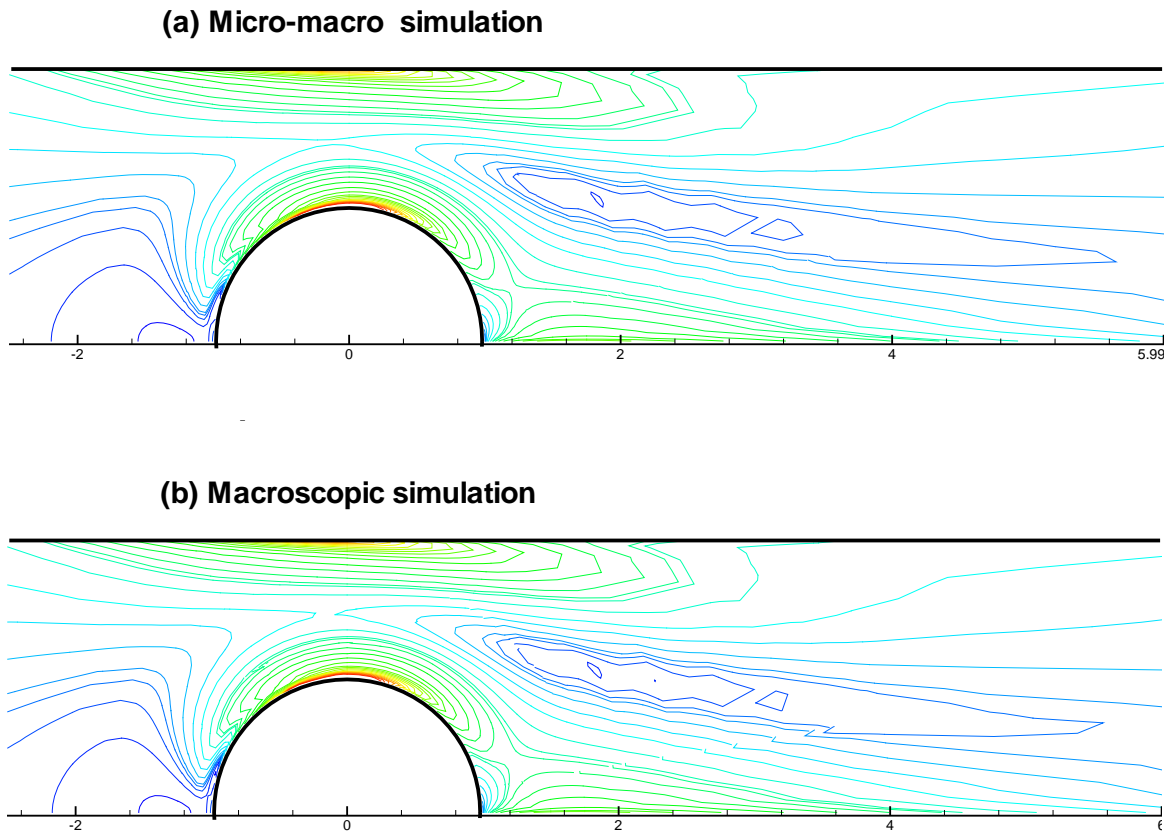


Figure 3.1: Contours of  $\tau_{xx}$  computed with a uniform mesh  $N = 8$  at  $We = 0.7$ . Oldroyd B fluid.

Stokes problem. We can see however, that depending on the mesh used, the present approach is between 1.5 to 1.6 times faster than using a constitutive equation and it is also between 14.4 to 18.7 times faster than using the method presented in [28].

In Fig. 3.1, we have represented the contour plot of  $\tau_{xx}$  with  $N = 8$  and  $We = 0.7$  for the new method introduced in this paper (a) and when a constitutive equation is used (b). We can see that, as expected, the two methods give similar results.

### 3.1.7 Extension of the method to the FENE-P model

The method described in the previous sections may be extended to the FENE-P model, i.e. the dumbbells having spring force law (1.44). The operator  $\mathbf{E}_v$  introduced in Section 3.1.2 may now be replaced by

$$\mathbf{E}_v \mathbf{q}(t_i, \mathbf{x}) = \mathbf{q}(t_i, \mathbf{x}) + \left( \mathbf{v}(t_i, \mathbf{x}) \cdot \nabla \mathbf{q}(t_i, \mathbf{x}) - \nabla \mathbf{v}(t_i, \mathbf{x}) \mathbf{q}(t_i, \mathbf{x}) + \frac{1}{2\lambda} \frac{\mathbf{q}(t_i, \mathbf{x})}{1 - \frac{1}{b} \langle |\mathbf{q}(t_{i-1}, \mathbf{x})|^2 \rangle} \right) \Delta t. \quad (3.36)$$

Note that in the equation above, we have taken the non-linear term  $\langle \mathbf{q}(t_{i-1}, \mathbf{x})^2 \rangle$  explicitly. Then, it can be shown by induction, in the same way as in Theorem 5 that  $\mathbf{q}(\mathbf{x}, t_i) \sim \mathbf{A}(t_i, \mathbf{x}) \tilde{\Phi}(t_i)$ , where  $\mathbf{A}(t_i, \mathbf{x})$  is defined by the same equation (3.14) as in the Oldroyd B case. The only minor modification to the demonstration of Theorem 5 concerns the configuration field at equilibrium which is, for the  $d$ -dimensional FENE-P dumbbells,  $\mathbf{q}(t_0, \mathbf{x}) \sim \sqrt{\frac{b}{b+d}} \tilde{\Phi}(t_0)$ . For the FENE-P model, the elastic extra-stress tensor is given by (1.46). We can replace  $\langle \mathbf{q}(t_i, \mathbf{x}) \mathbf{q}^T(t_i, \mathbf{x}) \rangle$  by  $\mathbf{A}^2(t_i, \mathbf{x})$  and also find an expression for  $\langle |\mathbf{q}(t_i, \mathbf{x})|^2 \rangle$  as a function of  $\mathbf{A}(t_i, \mathbf{x})$  as follows:

$$\begin{aligned} \langle |\mathbf{q}(t_i, \mathbf{x})|^2 \rangle &= tr \langle \mathbf{q}(t_i, \mathbf{x}) \mathbf{q}^T(\mathbf{x}, t_i) \rangle \\ &= tr \left\langle \mathbf{A}(t_i, \mathbf{x}) \tilde{\Phi}(t_i) \left( \mathbf{A}(t_i, \mathbf{x}) \tilde{\Phi}(t_i) \right)^T \right\rangle \\ &= tr \left( \mathbf{A}(t_i, \mathbf{x}) \left\langle \tilde{\Phi}(t_i) \tilde{\Phi}^T(t_i) \right\rangle \mathbf{A}(t_i, \mathbf{x}) \right) \\ &= tr \mathbf{A}^2(t_i, \mathbf{x}). \end{aligned} \tag{3.37}$$

Then the expression for the elastic extra-stress tensor (1.46) may be written

$$\boldsymbol{\tau}(t_i, \mathbf{x}) = \frac{\eta_p}{\lambda} \left( \frac{b+d}{b} \right) \left( -\mathbf{I} + \frac{\mathbf{A}^2(t_i, \mathbf{x})}{1 - tr \mathbf{A}^2(t_i, \mathbf{x})/b} \right). \tag{3.38}$$

Note that when  $b \rightarrow \infty$ , we recover the expression (3.22) of the Oldroyd B model.

## Numerical results

We now present some numerical results for the flow of a FENE-P fluid past a cylinder confined in a channel using the method described above. The flow geometry is shown in Fig. 2.8. The parameters of the domain and the type of discretization in physical space are the same as that of our Oldroyd B flow simulations in the preceding section. We choose the maximum extensibility parameter  $b$  to equal 10. Although the flow is planar, there is no physical reason to suppose that the dumbbells lie in the plane of the flow, and indeed the configuration vector  $\mathbf{q}$  should be three-dimensional (the 3D FENE-P model). However, we will also consider a 2D FENE-P model, in which case  $\mathbf{q}$  is restricted to lie in the plane of the flow<sup>4</sup>. The computational cost of the 2D FENE-P model is only slightly less than that of the 3D FENE-P model, because the latter consists of a problem for a  $2 \times 2$  matrix field (for the components of matrix  $\mathbf{A}$  lying in the upper left corner) and a separate equation for  $A_{33}$ . The non-linear coupling term, which links these two equations, is treated explicitly according to (3.36). On the other hand, an analogous distinction between two-dimensional and three-dimensional dumbbells heavily affects the computational cost for the FENE model (see Chapter 4).

We first demonstrate convergence with mesh refinement by comparing the results on meshes with  $N = 10$  and  $N = 12$ . This is done for the 2D FENE-P model at a Weissenberg number  $We = 1$  in Fig. 3.2 and for the 3D FENE-P model at a Weissenberg number  $We = 2$  in Fig. 3.3. The  $xx$ -component of the elastic extra-stress is plotted in both cases along the axis of

---

<sup>4</sup>A distinction between two-dimensional and three-dimensional dumbbells is not important in the Hookean case since the 3D Oldroyd B equation for planar flows can be decoupled into the 2D Oldroyd B equation for  $\tau_{xx}, \tau_{xy}, \tau_{yy}$  and an independent equation for  $\tau_{zz}$ , which has the solution  $\tau_{zz} = 0$ .

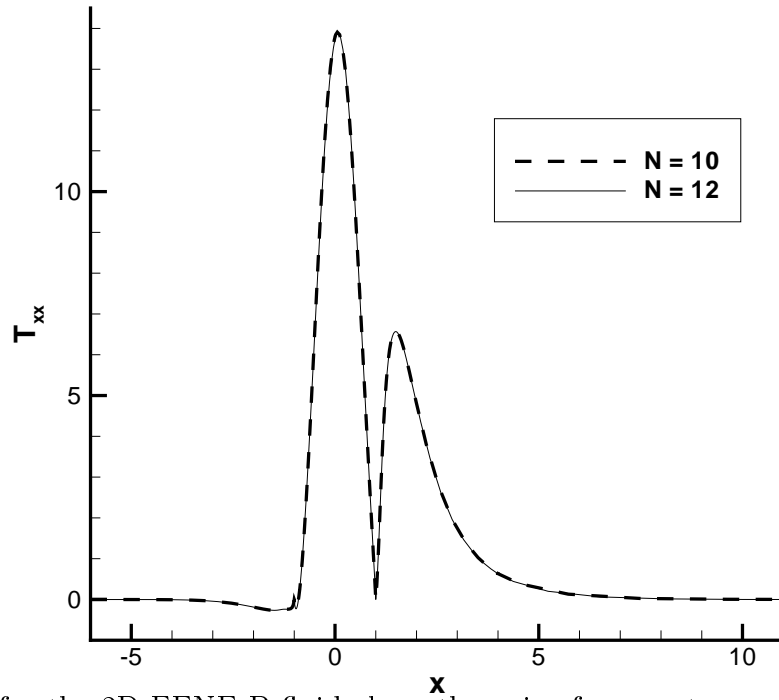


Figure 3.2:  $\tau_{xx}$  for the 2D FENE-P fluid along the axis of symmetry and the cylinder surface computed at  $We = 1$ .  $\Delta t = 0.01$ .

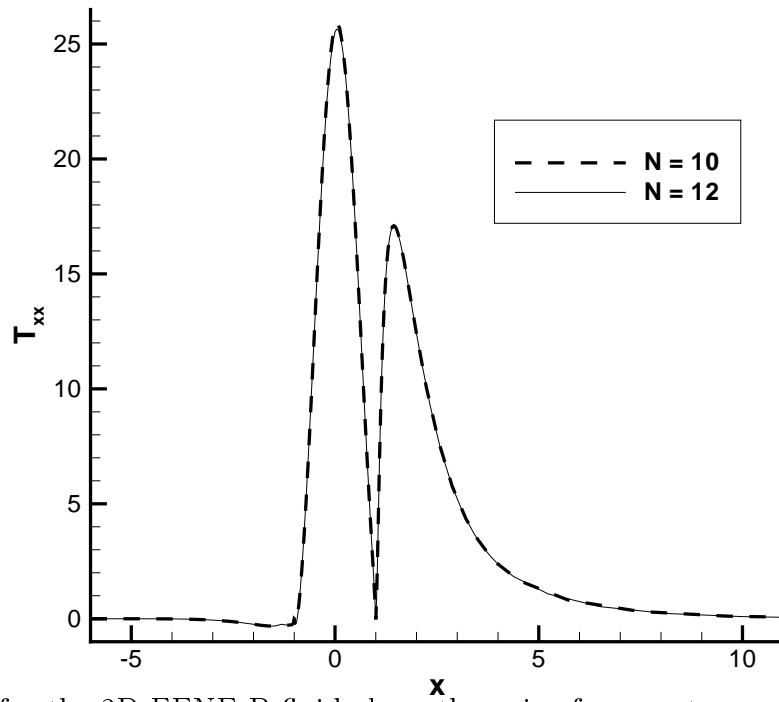


Figure 3.3:  $\tau_{xx}$  for the 3D FENE-P fluid along the axis of symmetry and the cylinder surface computed at  $We = 2$ .  $\Delta t = 0.01$ .

We	2D FENE-P	3D FENE-P
0.6	8.7363	8.8302
0.8	8.5095	8.5932
1.0	8.3641	8.4390
1.2	8.2659	8.3338
1.4	8.1970	8.2594
1.6	8.1473	8.2055
1.8	8.1109	8.1657
2.0	—	8.1360

Table 3.5: Drag factors for the FENE-P fluid computed on a uniform mesh with  $N = 10$ .  $\Delta t = 0.01$ .

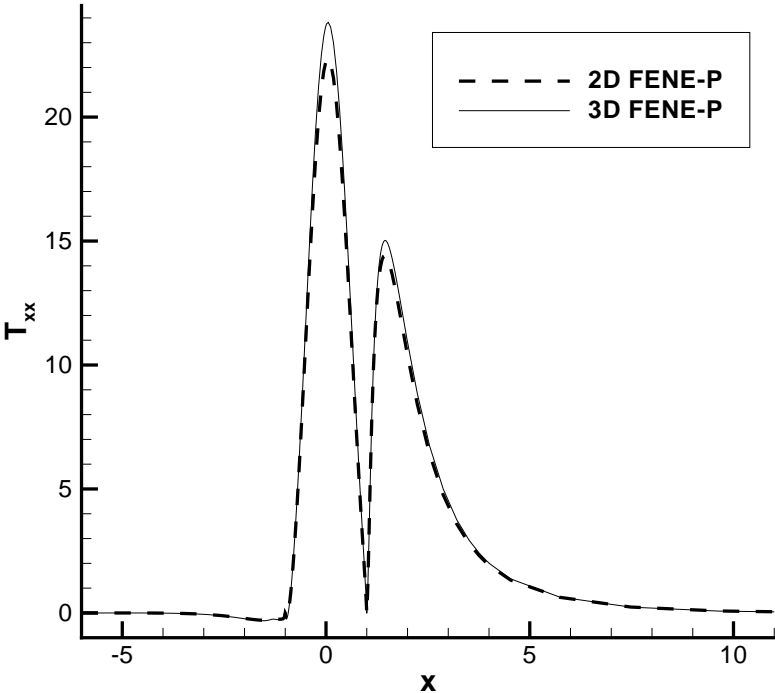


Figure 3.4:  $\tau_{xx}$  for the 2D FENE-P fluid along the axis of symmetry and the cylinder surface computed at  $We = 1.8$  on the uniform mesh with  $N = 10$ .  $\Delta t = 0.01$ .

symmetry and the cylinder surface. We see that convergence is achieved in the “eyeball” norm for both models. The  $N = 10$  mesh is used therefore in presenting the rest of our numerical results.

We were able to reach a Weissenberg number of 1.8 using the 2D FENE-P model and 2.0 using the 3D FENE-P model. The drag factors defined by (3.35) for both models are reported in Table 3.5. We see that they are very close for all the achievable Weissenberg numbers, that of the 2D case being slightly lower (about 0.5-1 percent) than that of the 3D case. However, the difference in the stress pointwise may be more significant, as can be seen from Fig. 3.4. The results of the same kind will be demonstrated for 2D and 3D FENE models in Chapter 4.

## 3.2 An energy estimate for the Oldroyd B model and a numerical scheme respecting it

### 3.2.1 An a priori estimate for an Oldroyd B fluid

In this section we present energy estimates for the stresses and velocity components in a general setting, for both inertial and inertialess flows of an Oldroyd B fluid. Our results apply to flows in bounded domains in any number of dimensions, subject to Dirichlet and possibly inflow boundary conditions. Although the results are obtained from the constitutive equation, their physical meaning is understood from the kinetic theory interpretation of the model. A novel numerical scheme is introduced and shown to be superior to a conventional Galerkin discretization of the Oldroyd B equations.

Let us recall the governing equations for flow of an incompressible, isothermal Oldroyd B fluid in some bounded domain  $\Omega \subset \mathbb{R}^d$ :

$$\nabla \cdot \mathbf{v} = 0, \quad (3.39)$$

$$Re \left( \frac{\partial \mathbf{v}}{\partial t} + (\mathbf{v} \cdot \nabla) \mathbf{v} \right) - \beta \nabla^2 \mathbf{v} + \nabla p = \nabla \cdot \boldsymbol{\tau}' + \mathbf{f}, \quad (3.40)$$

$$\frac{1}{We} \boldsymbol{\tau}' + \left( \frac{\partial \boldsymbol{\tau}'}{\partial t} + (\mathbf{v} \cdot \nabla) \boldsymbol{\tau}' - \nabla \mathbf{v} \boldsymbol{\tau}' - \boldsymbol{\tau}' \nabla \mathbf{v}^T \right) = \frac{(1 - \beta)}{We^2} \mathbf{I}. \quad (3.41)$$

The notation and non-dimensionalization here are the same as in Section 2.3 but we now allow for the possibility of positive Reynolds numbers  $Re = \rho V L / \eta$  where  $V$  and  $L$  are, respectively, characteristic velocity and length.

The system (3.39)–(3.41) is augmented by boundary and initial conditions

$$\mathbf{v}|_{\Gamma} = \mathbf{g}, \quad (3.42)$$

$$\boldsymbol{\tau}'|_{\Gamma_{in}} = \boldsymbol{\varphi}', \quad (3.43)$$

where  $\Gamma$  is the boundary of  $\Omega$  and  $\Gamma_{in}$  the inflow part of  $\Gamma$  (see (1.35)),

$$\boldsymbol{\tau}(0, \mathbf{x}) = \boldsymbol{\tau}_0(\mathbf{x}), \quad (3.44)$$

and, if  $Re > 0$ ,

$$\mathbf{v}(0, \mathbf{x}) = \mathbf{v}_0(\mathbf{x}). \quad (3.45)$$



Interpreting an Oldroyd B fluid as a suspension of Hookean dumbbells, we can rewrite the definition (1.39) of  $\boldsymbol{\tau}'$  under our non-dimensionalization as

$$\boldsymbol{\tau}' = \frac{(1-\beta)}{We} \langle \mathbf{q}\mathbf{q} \rangle, \quad (3.46)$$

where  $\mathbf{q}$  is the end-to-end vector of the dumbbell. We note from (3.46) that  $\boldsymbol{\tau}'$  is a symmetric positive definite tensor. We also note that the space of such tensors does not constitute a vector space and that we are not at liberty, consequently, to define a norm on this space. However, because of the symmetry and positive definiteness of  $\boldsymbol{\tau}'$ ,  $\text{tr}\boldsymbol{\tau}' \geq 0$  and  $\text{tr}\boldsymbol{\tau}' = 0$  iff  $\boldsymbol{\tau}' \equiv \mathbf{0}$ . Thus a non-negative function  $\|\cdot\|_{*,\Omega}$  having domain all  $d \times d$  positive definite real symmetric tensors defined on  $\Omega$  may be defined as follows:

$$\|\boldsymbol{\tau}'\|_{*,\Omega} = \int_{\Omega} \text{tr}\boldsymbol{\tau}' \, d\mathbf{x}. \quad (3.47)$$

From (3.47)

$$\|\boldsymbol{\tau}'\|_{*,\Omega} = \frac{(1-\beta)}{We} \int_{\Omega} \langle Q^2 \rangle \, d\mathbf{x}, \quad (3.48)$$

where  $Q = |\mathbf{q}|$  is the length of the interconnecting spring, and (3.47) thus returns a scaled average over physical and configuration space of  $Q^2$ , which can be interpreted as the potential energy of the dumbbells. We recall, in passing, that there is no physical mechanism in the Oldroyd B fluid to prevent the dumbbell springs from becoming infinitely extended.

We are now in a position to prove an a priori energy estimate.

**Theorem 4** *Let  $\mathbf{f}(t, \cdot) \in (L^2(\Omega))^d$ ,  $t \geq 0$  and  $\mathbf{g}(t, \mathbf{x}) \in (H^{1/2}(\Gamma))^d$ ,  $t \geq 0$ ,  $\mathbf{x} \in \Gamma$  be functions chosen so that there exists a divergence-free vector field  $\mathbf{v}^*(t, \cdot) \in (W^{1,\infty}(\Omega))^d$  satisfying  $\mathbf{v}^*|_{\Gamma} = \mathbf{g}$  and such that the numbers*

$$c_1 = \sup_{t \geq 0} \|\nabla \mathbf{v}^*(t, \cdot)\|_{L^\infty(\Omega)}$$

and

$$\begin{aligned} c_2 = & \sup_{t \geq 0} \left( d \text{Meas}(\Omega) \frac{(1-\beta)}{We^2} + \left| \int_{\Gamma_{in}} (\mathbf{g}(t, \mathbf{x}) \cdot \mathbf{n}(\mathbf{x})) \text{tr}\boldsymbol{\varphi}'(t, \mathbf{x}) \, d\mathbf{x} \right| \right. \\ & \left. + \left\| \left( \mathbf{f} - \text{Re} \left( \frac{\partial \mathbf{v}^*}{\partial t} + \mathbf{v}^* \cdot \nabla \mathbf{v}^* \right) \right) (t, \cdot) \right\|_0^2 + \|\mathbf{v}^*(t, \cdot)\|_1^2 \right), \end{aligned}$$

are finite.

Then there exist positive constants  $\gamma$  and  $C$  depending only on  $\Omega$ ,  $\text{Re}$ ,  $We$ , and  $\beta$  such that any solution to (3.39)-(3.45) satisfies

$$\begin{aligned} \frac{\text{Re}}{2} \|\mathbf{v}(t, \cdot)\|_0^2 + \|\boldsymbol{\tau}'(t, \cdot)\|_{*,\Omega} & \leq (2\text{Re}\|\mathbf{v}_0\|_0^2 + \|\boldsymbol{\tau}'_0\|_{*,\Omega}) \exp(2c_1 d - \gamma) t \\ & \quad + \frac{C c_2}{\gamma - 2c_1 d} (1 - \exp(2c_1 d - \gamma) t) \\ & \quad + 2\text{Re}\|\mathbf{v}_0^*\|_0^2 \exp(2c_1 d - \gamma) t \\ & \quad + \text{Re}\|\mathbf{v}^*(t, \cdot)\|_0^2. \end{aligned} \quad (3.49)$$

Moreover, when  $\mathbf{g} = \mathbf{0}$ , any solution to (3.39)-(3.45) may be shown to satisfy

$$\begin{aligned} Re\|\mathbf{v}(t, \cdot)\|_0^2 + \|\boldsymbol{\tau}'(t, \cdot)\|_{*,\Omega} &\leq (Re\|\mathbf{v}_0\|_0^2 + \|\boldsymbol{\tau}'_0\|_{*,\Omega}) \exp(-\gamma t) \\ &+ \frac{Cc_2}{\gamma} (1 - \exp(-\gamma t)). \end{aligned} \quad (3.50)$$

**Proof.** Let us put  $\mathbf{v} = \mathbf{v}^* + \mathbf{w}$ . We multiply the momentum equation (3.40) by  $\mathbf{w}$ , integrate it over  $\Omega$  and use integration by parts to obtain

$$Re \left( \frac{\partial \mathbf{v}}{\partial t} + \mathbf{v} \cdot \nabla \mathbf{v}, \mathbf{w} \right) + \beta(\nabla \mathbf{v}, \nabla \mathbf{w}) = -(\boldsymbol{\tau}', \nabla \mathbf{w}) + (\mathbf{f}, \mathbf{w}). \quad (3.51)$$

We note that

$$(\mathbf{v} \cdot \nabla \mathbf{w}, \mathbf{w}) = \frac{1}{2} \int_{\Omega} \mathbf{v} \cdot \nabla |\mathbf{w}|^2 dx = \frac{1}{2} \int_{\Gamma} (\mathbf{v} \cdot \mathbf{n}) |\mathbf{w}|^2 dx = 0.$$

Hence

$$(\mathbf{v} \cdot \nabla \mathbf{v}, \mathbf{w}) = (\mathbf{v} \cdot \nabla \mathbf{v}^*, \mathbf{w}) = (\mathbf{v}^* \cdot \nabla \mathbf{v}^*, \mathbf{w}) + (\mathbf{w} \cdot \nabla \mathbf{v}^*, \mathbf{w})$$

and (3.51) can be rewritten as

$$\begin{aligned} \frac{Re}{2} \frac{d}{dt} \|\mathbf{w}\|_0^2 + \beta |\mathbf{w}|_1^2 + Re \left( \frac{\partial \mathbf{v}^*}{\partial t} + \mathbf{v}^* \cdot \nabla \mathbf{v}^*, \mathbf{w} \right) + Re(\mathbf{w} \cdot \nabla \mathbf{v}^*, \mathbf{w}) \\ = -\beta(\nabla \mathbf{v}^*, \nabla \mathbf{w}) - (\boldsymbol{\tau}', \nabla \mathbf{v}) + (\boldsymbol{\tau}', \nabla \mathbf{v}^*) + (\mathbf{f}, \mathbf{w}). \end{aligned} \quad (3.52)$$

Let us now take traces of Eq. (3.41):

$$\frac{1}{We} \operatorname{tr} \boldsymbol{\tau}' + \left( \frac{\partial \operatorname{tr} \boldsymbol{\tau}'}{\partial t} + (\mathbf{v} \cdot \nabla) \operatorname{tr} \boldsymbol{\tau}' - 2\nabla \mathbf{v} : \boldsymbol{\tau}' \right) = d \frac{(1-\beta)}{We^2}. \quad (3.53)$$

Integrating each term in Eqn. (3.53) over the domain  $\Omega$  yields

$$\begin{aligned} \frac{1}{We} \|\boldsymbol{\tau}'\|_{*,\Omega} + \frac{d}{dt} \|\boldsymbol{\tau}'\|_{*,\Omega} + \int_{\Omega} \mathbf{v} \cdot \nabla \operatorname{tr} \boldsymbol{\tau}' dx \\ - 2(\boldsymbol{\tau}', \nabla \mathbf{v}) = d \operatorname{Meas}(\Omega) \frac{(1-\beta)}{We^2}. \end{aligned} \quad (3.54)$$

Using integration by parts and the incompressibility equation  $\nabla \cdot \mathbf{v} = 0$  we can see that

$$\begin{aligned} \int_{\Omega} \mathbf{v} \cdot \nabla \operatorname{tr} \boldsymbol{\tau}' dx &= \int_{\Gamma} (\mathbf{v} \cdot \mathbf{n})(\operatorname{tr} \boldsymbol{\tau}') dx \\ &\geq \int_{\Gamma_{in}} (\mathbf{g} \cdot \mathbf{n}) \operatorname{tr} \boldsymbol{\tau}' dx. \end{aligned} \quad (3.55)$$

The last inequality in (3.55) is valid since  $(\mathbf{g} \cdot \mathbf{n}) \geq 0$  on  $\Gamma \setminus \Gamma_{in}$  and  $\operatorname{tr} \boldsymbol{\tau}' \geq 0$  everywhere.

We multiply Eq. (3.52) by 2, add it to Eq. (3.54) and use (3.55) to obtain

$$\begin{aligned} \frac{1}{We} \|\boldsymbol{\tau}'\|_{*,\Omega} + \frac{d}{dt} \|\boldsymbol{\tau}'\|_{*,\Omega} + Re \frac{d}{dt} \|\mathbf{w}\|_0^2 + 2\beta |\mathbf{w}|_1^2 \\ \leq F(t) + 2(\boldsymbol{\tau}', \nabla \mathbf{v}^*) + 2(\tilde{\mathbf{f}}, \mathbf{w}) - 2\beta(\nabla \mathbf{v}^*, \nabla \mathbf{w}) - 2Re(\mathbf{w} \cdot \nabla \mathbf{v}^*, \mathbf{w}). \end{aligned} \quad (3.56)$$

with

$$F(t) = d\text{Meas}(\Omega) \frac{(1-\beta)}{We^2} - \int_{\Gamma_{in}} (\mathbf{g} \cdot \mathbf{n}) \text{tr} \varphi' \, d\mathbf{x}$$

and

$$\tilde{\mathbf{f}} = \mathbf{f} - Re \left( \frac{\partial \mathbf{v}^*}{\partial t} + \mathbf{v}^* \cdot \nabla \mathbf{v}^* \right).$$

We are now going to prove some auxiliary inequalities. First of all note that at any point in space and time we have

$$|\boldsymbol{\tau}' : \nabla \mathbf{v}^*| \leq \sum_{i,j=1}^d \left| \tau'_{ij} \frac{\partial u_i^*}{\partial x_j} \right| \leq c_1 \sum_{i,j=1}^d |\tau'_{ij}|. \quad (3.57)$$

The tensor  $\boldsymbol{\tau}'$  is symmetric and positive definite everywhere, so that

$$|\tau'_{ij}| \leq \frac{1}{2} (\tau'_{ii} + \tau'_{jj}),$$

pointwise. We now conclude from (3.57) that

$$|\boldsymbol{\tau}' : \nabla \mathbf{v}^*| \leq \frac{c_1}{2} \left( \sum_{i,j=1}^d |\tau'_{ii}| + \sum_{i,j=1}^d |\tau'_{jj}| \right) = c_1 d \text{tr} \boldsymbol{\tau}'.$$

Integrating over  $\Omega$  and using the fact that

$$\int_{\Omega} |f| \, d\mathbf{x} \geq \left| \int_{\Omega} f \, d\mathbf{x} \right|,$$

for any  $f \in L^1(\Omega)$ , gives

$$|(\boldsymbol{\tau}', \nabla \mathbf{v}^*)| \leq c_1 d \|\boldsymbol{\tau}'\|_{*,\Omega}. \quad (3.58)$$

In a similar fashion to (3.58) we may prove that

$$|(\mathbf{w} \cdot \nabla \mathbf{v}^*, \mathbf{w})| = \left| \int_{\Omega} v_i v_j \frac{\partial u_i^*}{\partial x_j} \, d\mathbf{x} \right| \leq c_1 \sum_{i,j=1}^d \int_{\Omega} |v_i v_j| \, d\mathbf{x} \leq c_1 d \|\mathbf{w}\|_0^2. \quad (3.59)$$

Using the Cauchy-Schwarz inequality, the Poincaré-Friedrichs inequality and a Young's-type inequality we may write

$$2|(\tilde{\mathbf{f}}, \mathbf{w})| \leq 2C_1 \|\tilde{\mathbf{f}}\|_0 |\mathbf{w}|_1 \leq \frac{C_1^2}{\beta_1} \|\tilde{\mathbf{f}}\|_0^2 + \beta_1 |\mathbf{w}|_1^2, \quad (3.60)$$

and

$$2\beta |(\nabla \mathbf{v}^*, \nabla \mathbf{w})| \leq \frac{\beta^2}{\beta_2} |\mathbf{v}^*|_1^2 + \beta_2 |\mathbf{w}|_1^2, \quad (3.61)$$

where  $\beta_1$  and  $\beta_2$  are arbitrary positive numbers and  $C_1$  is the constant in the Poincaré-Friedrichs inequality that is dependent only on  $\Omega$ .

We get from the inequalities (3.56)–(3.61):

$$\begin{aligned} & \frac{1}{We} \|\boldsymbol{\tau}'\|_{*,\Omega} + \frac{d}{dt} \|\boldsymbol{\tau}'\|_{*,\Omega} + Re \frac{d}{dt} \|\mathbf{w}\|_0^2 + (2\beta - \beta_1 - \beta_2) |\mathbf{w}|_1^2 \\ & \leq F(t) + 2c_1 d \|\boldsymbol{\tau}'\|_{*,\Omega} + 2c_1 d Re \|\mathbf{w}\|_0^2 + \frac{C_1^2}{\beta_1} \|\tilde{\mathbf{f}}\|_0^2 + \frac{\beta^2}{\beta_2} |\mathbf{v}^*|_1^2 \end{aligned}$$

We can choose  $\beta_1 = \beta_2 = \beta/2$  and obtain, using the Poincaré-Friedrichs inequality, that

$$\begin{aligned} & \frac{1}{We} \|\boldsymbol{\tau}'\|_{*,\Omega} + \frac{d}{dt} \|\boldsymbol{\tau}'\|_{*,\Omega} + Re \frac{d}{dt} \|\mathbf{w}\|_0^2 + \frac{\beta}{C_1^2} \|\mathbf{w}\|_0^2 \\ & \leq F(t) + 2c_1 d \|\boldsymbol{\tau}'\|_{*,\Omega} + 2c_1 d Re \|\mathbf{w}\|_0^2 + 2 \frac{C_1^2}{\beta} \|\tilde{\mathbf{f}}\|_0^2 + 2\beta |\mathbf{u}^*|_1^2 \\ & \leq 2c_1 d \|\boldsymbol{\tau}'\|_{*,\Omega} + 2c_1 d Re \|\mathbf{w}\|_0^2 + Cc_2 \end{aligned} \quad (3.62)$$

with

$$C = \max \left( 1, 2 \frac{C_1^2}{\beta}, 2\beta \right). \quad (3.63)$$

Let us introduce

$$|||\mathbf{w}, \boldsymbol{\tau}'||| \equiv Re \|\mathbf{v}\|_0^2 + \|\boldsymbol{\tau}'\|_{*,\Omega}$$

and

$$\gamma = \min \left( \frac{1}{We}, \frac{\beta}{C_1^2 Re} \right). \quad (3.64)$$

Using this notation, we can derive from (3.62):

$$\frac{d}{dt} |||\mathbf{w}, \boldsymbol{\tau}'||| + \gamma |||\mathbf{w}, \boldsymbol{\tau}'||| \leq 2c_1 d |||\mathbf{w}, \boldsymbol{\tau}'||| + Cc_2. \quad (3.65)$$

An application of Gronwall's lemma to (3.65) gives

$$\begin{aligned} |||\mathbf{w}, \boldsymbol{\tau}'||| & \leq |||\mathbf{w}_0, \boldsymbol{\tau}'_0||| \exp(2c_1 d - \gamma)t \\ & \quad + \frac{Cc_2}{\gamma - 2c_1 d} (1 - \exp(2c_1 d - \gamma)t). \end{aligned} \quad (3.66)$$

If  $\mathbf{g} = \mathbf{0}$  then  $\mathbf{v}^*$  may be taken to be the zero vector and (3.50) follows immediately.

If  $\mathbf{v}^* \neq \mathbf{0}$  we use the triangle inequality

$$\|\mathbf{v}\|_0 \leq \|\mathbf{v}^*\|_0 + \|\mathbf{w}\|_0, \quad (3.67)$$

and square both sides to get

$$\|\mathbf{v}\|_0^2 \leq \|\mathbf{v}^*\|_0^2 + 2\|\mathbf{v}^*\|_0 \|\mathbf{w}\|_0 + \|\mathbf{w}\|_0^2 \leq 2\|\mathbf{v}^*\|_0^2 + 2\|\mathbf{w}\|_0^2, \quad (3.68)$$

so that

$$\frac{1}{2} \|\mathbf{v}\|_0^2 - \|\mathbf{v}^*\|_0^2 \leq \|\mathbf{w}\|_0^2. \quad (3.69)$$

Similarly,

$$\|\mathbf{w}\|_0^2 \leq 2\|\mathbf{v}^*\|_0^2 + 2\|\mathbf{v}\|_0^2. \quad (3.70)$$

The inequality (3.49) then follows from (3.66), (3.69) and (3.70).  $\square$

### 3.2.2 Numerical scheme

We present here a time-discretized algorithm for simulation of unsteady Oldroyd B flows that can be shown to preserve the energy estimate derived in Theorem 4. We fix some  $\Delta t > 0$  and proceed at each time  $t_i = i\Delta t$ ,  $i \geq 1$  as follows: suppose that we know  $(\mathbf{v}_{i-1}, \boldsymbol{\tau}'_{i-1})$  from the previous time step, where  $\boldsymbol{\tau}'_{i-1}$  is symmetric and positive definite everywhere. Then we find a vector field  $\mathbf{v}_i(\mathbf{x})$ , a scalar field  $p_i(\mathbf{x})$  and a  $d \times d$  tensor field  $\mathbf{A}_i(\mathbf{x})$  such that

$$Re \left( \frac{\mathbf{v}_i - \mathbf{v}_{i-1}}{\Delta t} + \mathbf{v}_i \cdot \nabla \mathbf{v}_i \right) - \beta \nabla^2 \mathbf{v}_i + \nabla p_i = \nabla \cdot (\mathbf{A}_i \mathbf{A}_i^T) + \mathbf{f}_i, \quad (3.71)$$

$$\nabla \cdot \mathbf{v}_i = 0, \quad (3.72)$$

$$\mathbf{A}_i + \Delta t \left[ \frac{1}{2We} \mathbf{A}_i + (\mathbf{v}_i \cdot \nabla) \mathbf{A}_i - \nabla \mathbf{v}_i \mathbf{A}_i \right] = \sqrt{\boldsymbol{\tau}'_{i-1}}, \quad (3.73)$$

$$\mathbf{v}_i|_{\Gamma} = \mathbf{g}_i, \quad \mathbf{A}_i|_{\Gamma_{in}} = \sqrt{\boldsymbol{\varphi}'_i}, \quad (3.74)$$

where  $\mathbf{f}_i$ ,  $\mathbf{g}_i$  and  $\boldsymbol{\varphi}'_i$  are the values of  $\mathbf{f}$ ,  $\mathbf{g}$  and  $\boldsymbol{\varphi}'$  at time  $t = t_i$ . We then set at every point  $\mathbf{x} \in \Omega$

$$\boldsymbol{\tau}'_i = \mathbf{A}_i \mathbf{A}_i^T + \frac{(1 - \beta)\Delta t}{We^2} \mathbf{I}. \quad (3.75)$$

Note that the square root in (3.74) is taken of symmetric and positive definite matrices and that the result of this operation is assumed to be symmetric and positive definite as well. The positive definiteness of  $\boldsymbol{\tau}'_i$  is preserved automatically by (3.75).

The numerical scheme proposed above bears similarities to that described in Sections 3.1.4–3.1.5, the essential difference being that nonlinear coupling between the momentum equation (3.71) and Eq. (3.73) is introduced here.

**Lemma 5**  $\mathbf{v}_i$ ,  $p_i$  and  $\boldsymbol{\tau}'_i$  defined by (3.71)–(3.75) satisfy the Oldroyd B equation system (3.39)–(3.41) as  $\Delta t \rightarrow 0$ .

**Proof.** The equivalence of (3.39) and (3.71) is clear since we have from (3.75)

$$\nabla \cdot (\mathbf{A}_i \mathbf{A}_i^T) = \nabla \cdot \boldsymbol{\tau}'_i.$$

From (3.73) we have, on multiplying the equation by its transpose that

$$\begin{aligned} \mathbf{A}_i \mathbf{A}_i^T + \Delta t \left( \frac{1}{We} \mathbf{A}_i \mathbf{A}_i^T + (\mathbf{v}_i \cdot \nabla) \mathbf{A}_i \mathbf{A}_i^T - \nabla \mathbf{v}_i \mathbf{A}_i \mathbf{A}_i^T - \mathbf{A}_i \mathbf{A}_i^T (\nabla \mathbf{v}_i)^T \right) \\ = \boldsymbol{\tau}'_{i-1} + O(\Delta t)^2. \end{aligned} \quad (3.76)$$

By substituting (3.75) into (3.76) we see that  $\boldsymbol{\tau}'_i$  satisfies

$$\begin{aligned} \boldsymbol{\tau}'_i + \Delta t \left( \frac{1}{We} \boldsymbol{\tau}'_i + (\mathbf{v}_i \cdot \nabla) \boldsymbol{\tau}'_i - \nabla \mathbf{v}_i \boldsymbol{\tau}'_i - \boldsymbol{\tau}'_i \nabla \mathbf{v}_i^T \right) \\ = \boldsymbol{\tau}'_{i-1} + \frac{(1 - \beta)\Delta t}{We^2} \mathbf{I} + O(\Delta t)^2, \end{aligned} \quad (3.77)$$

which is equivalent to (3.41).  $\square$

We now prove that the weak Galerkin solution to the scheme (3.71)–(3.75) satisfies the bound (3.50) in the case of zero Dirichlet boundary conditions on the velocity. The result can be extended easily to the case of general boundary conditions.

**Lemma 6** *Let  $\mathbf{g} = \mathbf{0}$ . The weak Galerkin solution of (3.71)–(3.75) satisfies the bound (3.50) as  $\Delta t \rightarrow 0$ .*

**Proof.** Introducing a solenoidal test vector  $\mathbf{w}$  that vanishes on  $\Gamma$  and a test tensor  $\mathbf{S}$ , weak forms of (3.71) and (3.73) may be written down, respectively, in the form

$$\begin{aligned} \frac{Re}{\Delta t} (\mathbf{v}_i - \mathbf{v}_{i-1}, \mathbf{w}) + Re (\mathbf{v}_i \cdot \nabla \mathbf{v}_i, \mathbf{w}) + \beta (\nabla \mathbf{v}_i, \nabla \mathbf{w}) \\ = -(\mathbf{A}_i \mathbf{A}_i^T, \nabla \mathbf{w}) + (\mathbf{f}_i, \mathbf{w}), \end{aligned} \quad (3.78)$$

and

$$\begin{aligned} \frac{1}{\Delta t} (\mathbf{A}_i, \mathbf{S}) + \left[ \frac{1}{2We} (\mathbf{A}_i, \mathbf{S}) + (\mathbf{v}_i \cdot \nabla \mathbf{A}_i, \mathbf{S}) - (\nabla \mathbf{v}_i \mathbf{A}_i, \mathbf{S}) \right] \\ = \frac{1}{\Delta t} \left( \sqrt{\boldsymbol{\tau}'_{i-1}}, \mathbf{S} \right). \end{aligned} \quad (3.79)$$

We begin the proof by choosing  $\mathbf{w} = \mathbf{v}_i$  in (3.78), multiplying throughout by 2 and using (3.60) with  $\beta_1 = \beta$ . This yields the inequality

$$\frac{2Re}{\Delta t} (\mathbf{v}_i - \mathbf{v}_{i-1}, \mathbf{v}_i) + \beta (\nabla \mathbf{v}_i, \nabla \mathbf{v}_i) + 2 (\nabla \mathbf{v}_i \mathbf{A}_i, \mathbf{A}_i) \leq \frac{C_1^2}{\beta} \|\mathbf{f}_i\|_0^2. \quad (3.80)$$

In the weak form (3.79) we now choose  $\mathbf{S} = \mathbf{A}_i$ , and use a Young's inequality on the right-hand side to get

$$\left( \frac{1}{We} + \frac{1}{\Delta t} \right) (\mathbf{A}_i, \mathbf{A}_i) - 2 (\nabla \mathbf{v}_i \mathbf{A}_i, \mathbf{A}_i) \leq \frac{1}{\Delta t} \left( \sqrt{\boldsymbol{\tau}'_{i-1}}, \sqrt{\boldsymbol{\tau}'_{i-1}} \right). \quad (3.81)$$

Summing up (3.80) and (3.81), using the Poincaré-Friedrichs inequality and noting that

$$\left( \sqrt{\boldsymbol{\tau}'_{i-1}}, \sqrt{\boldsymbol{\tau}'_{i-1}} \right) = \int_{\Omega} \text{tr} \left( \sqrt{\boldsymbol{\tau}'_{i-1}} \right)^2 dx = \|\boldsymbol{\tau}'_{i-1}\|_{*,\Omega},$$

allows us to write

$$\begin{aligned} \frac{2Re}{\Delta t} (\mathbf{v}_i - \mathbf{v}_{i-1}, \mathbf{v}_i) + \frac{\beta}{C_1^2} (\mathbf{v}_i, \mathbf{v}_i) + \left( \frac{1}{We} + \frac{1}{\Delta t} \right) (\mathbf{A}_i, \mathbf{A}_i) \\ \leq \frac{1}{\Delta t} \|\boldsymbol{\tau}'_{i-1}\|_{*,\Omega} + \frac{C_1^2}{\beta} \|\mathbf{f}_i\|_0^2. \end{aligned} \quad (3.82)$$

Referring to Eqn. (3.75) we see that

$$(\mathbf{A}_i, \mathbf{A}_i) = \int_{\Omega} \text{tr} (\mathbf{A}_i \mathbf{A}_i^T) dx = \|\boldsymbol{\tau}'_i\|_{*,\Omega} - \frac{d(1-\beta)\Delta t}{We^2} \text{Meas}(\Omega), \quad (3.83)$$

so that, using a Young's inequality to treat the product of  $\mathbf{v}_i$  and  $\mathbf{v}_{i-1}$  in the inertial term in (3.82), we get

$$\begin{aligned} \frac{Re}{\Delta t} (\mathbf{v}_i, \mathbf{v}_i) + \frac{\beta}{C_1^2} (\mathbf{v}_i, \mathbf{v}_i) + \left( \frac{1}{We} + \frac{1}{\Delta t} \right) \|\boldsymbol{\tau}'_i\|_{*,\Omega} - \frac{1}{\Delta t} \|\boldsymbol{\tau}'_{i-1}\|_{*,\Omega} \\ \leq \frac{Re}{\Delta t} (\mathbf{v}_{i-1}, \mathbf{v}_{i-1}) + \frac{C_1^2}{\beta} \|\mathbf{f}_i\|_0^2 \\ + \frac{(1-\beta)d\Delta t \text{Meas}(\Omega)}{We^2} \left( \frac{1}{We} + \frac{1}{\Delta t} \right). \end{aligned} \quad (3.84)$$

Let us now rearrange (3.84) and recall, as in (3.64), that

$$\gamma = \min \left( \frac{1}{We}, \frac{\beta}{C_1^2 Re} \right).$$

Then from (3.84) we may conclude that

$$\begin{aligned} & \left( \gamma + \frac{1}{\Delta t} \right) \|\mathbf{v}_i, \boldsymbol{\tau}'_i\| - \frac{1}{\Delta t} \|\mathbf{v}_{i-1}, \boldsymbol{\tau}'_{i-1}\| \\ & \leq \frac{C_1^2}{\beta} \sup_{i \geq 1} \|\mathbf{f}_i\|_0^2 + \frac{d(1-\beta)\text{Meas}(\Omega)}{We^2} \left( 1 + \frac{\Delta t}{We} \right). \end{aligned} \quad (3.85)$$

Define

$$s_i = \|\mathbf{v}_i, \boldsymbol{\tau}'_i\| - \frac{C_1^2}{\beta\gamma} \sup_{i \geq 1} \|\mathbf{f}_i\|_0^2 - \frac{d(1-\beta)\text{Meas}(\Omega)}{\gamma We^2} \left( 1 + \frac{\Delta t}{We} \right). \quad (3.86)$$

Then from (3.85) we see that

$$\left( \gamma + \frac{1}{\Delta t} \right) s_i \leq \frac{s_{i-1}}{\Delta t},$$

and hence that

$$s_i \leq (1 + \gamma\Delta t)^{-i} s_0.$$

Substituting for  $s_i$  from (3.86) we then get

$$\begin{aligned} \|\mathbf{v}_i, \boldsymbol{\tau}'_i\| & \leq \|\mathbf{v}_0, \boldsymbol{\tau}'_0\| (1 + \gamma\Delta t)^{-i} \\ & + \frac{C}{\gamma} \text{Meas}(\Omega) \left[ \sup_{i \geq 1} \|\mathbf{f}_i\|_0^2 + \frac{d(1-\beta)}{We^2} \left( 1 + \frac{\Delta t}{We} \right) \right] (1 - (1 + \gamma\Delta t)^{-i}), \end{aligned} \quad (3.87)$$

with  $C = C_1^2/\beta$ , which is smaller than  $C$  defined in (3.63). At any fixed time  $t = i\Delta t$  as  $\Delta t \rightarrow 0$  and  $i \rightarrow \infty$ ,  $(1 + \gamma\Delta t)^{-i} \rightarrow \exp(-\gamma t)$  and the bound (3.50) may therefore be seen to be respected by the numerical scheme.  $\square$

### 3.2.3 Example: planar channel flow

The results of the previous two sections apply to all bounded flows of an Oldroyd B fluid where we supply Dirichlet boundary conditions for the components of velocity and prescribe inflow conditions for the components of the elastic tensor  $\boldsymbol{\tau}'$ . The results equally well apply to periodic flows of an Oldroyd B fluid, where the pressure (minus, possibly, a pressure gradient), velocity and stress are considered periodic in at least one coordinate direction and Dirichlet velocity conditions are imposed on the boundary.

In this section we present the derived a priori bounds (3.49)-(3.50) for planar channel flow of an Oldroyd B fluid. Similar results would apply for circular Poiseuille flows of such a fluid. The boundary of the domain  $\Omega = \{(x_1, x_2) \in (0, L) \times (0, 1)\}$  is denoted by  $\Gamma$  and the inflow and outflow boundaries for the Dirichlet problem by  $\Gamma^{in}$  and  $\Gamma^{out}$ , respectively. We proceed to describe firstly the periodic problem and follow this up with the results of the analysis when inflow conditions on  $\boldsymbol{\tau}'$  are imposed.

### Periodic boundary conditions

In this case periodicity in the flow variables  $(\mathbf{v}, \boldsymbol{\tau}')$  is assumed in the  $x_1$  direction over some length  $L$ . The pressure may be expressed as the sum of a steady base flow pressure  $-Px_1 + c$  ( $P \geq 0$  and  $c$ , constants) and an  $L$ -periodic part  $\tilde{p}$ . We now drop the tilde on the periodic part of the pressure and simply put the body force  $\mathbf{f} = (P, 0)$  in (3.40). The divergence-free velocity field  $\mathbf{v}^*$  may be taken to be zero. Consequently  $c_1 = 0$ .

With  $\mathbf{f} = (P, 0)$  in (3.40) and  $\mathbf{g} = \mathbf{0}$  on  $x_2 = 0$  and  $1$ ,  $c_2$  is given by

$$c_2 = \text{Meas}(\Omega) \left[ \frac{2(1-\beta)}{We^2} + P^2 \right]. \quad (3.88)$$

When  $Re = 0$  and with  $c_1$  and  $c_2$  as given above, Eqn. (3.49) leads to the following bound on  $\|\boldsymbol{\tau}'\|_{*,\Omega}$ :

$$\begin{aligned} \|\boldsymbol{\tau}'\|_{*,\Omega} &\leq \|\boldsymbol{\tau}'_0\|_{*,\Omega} \exp\left(-\frac{t}{We}\right) \\ &\quad + CWe \text{Meas}(\Omega) \left[ \frac{2(1-\beta)}{We^2} + P^2 \right] \left(1 - \exp\left(-\frac{t}{We}\right)\right). \end{aligned} \quad (3.89)$$

For  $Re \neq 0$  and noting that  $\mathbf{w} = \mathbf{v}$ , the inequality (3.50) reads

$$\begin{aligned} \|\|\mathbf{v}, \boldsymbol{\tau}'\|\| &\leq \|\|\mathbf{v}_0, \boldsymbol{\tau}'_0\|\| \exp(-\gamma t) \\ &\quad + \frac{C}{\gamma} \text{Meas}(\Omega) \left[ \frac{2(1-\beta)}{We^2} + P^2 \right] (1 - \exp(-\gamma t)). \end{aligned} \quad (3.90)$$

### Inflow boundary conditions

A steady state solution  $(\mathbf{v}, p, \boldsymbol{\tau}')$  of plane Poiseuille flow of an Oldroyd B fluid between two plates  $x_2 = 0$  and  $x_2 = 1$  in the absence of body forces ( $\mathbf{f} = \mathbf{0}$ ) may be written in the form

$$p = -Px_1 + c, \quad (3.91)$$

$$\mathbf{v} = (v_1, v_2) = (Px_2(1-x_2)/2, 0), \quad (3.92)$$

$$\tau'_{11} = \frac{(1-\beta)}{We} + 2We(1-\beta) \left(\frac{dv_1}{dx_2}\right)^2, \quad (3.93)$$

$$\tau'_{12} = (1-\beta) \frac{dv_1}{dx_2}, \quad (3.94)$$

$$\tau'_{22} = \frac{(1-\beta)}{We}, \quad (3.95)$$

where  $-P$  is a constant pressure gradient. The solution (3.91)-(3.95) has led us to choose the boundary conditions (see (3.42))  $\mathbf{g} = Px_2(1-x_2)/2$  and  $\boldsymbol{\varphi}'$  as in (3.93)-(3.95). Thus a suitable choice of  $\mathbf{v}^*$  is  $\mathbf{v}^* = \mathbf{g}$  throughout  $\Omega$ . With this choice  $c_1 = P/2$ . In order to calculate  $c_2$  we compute

$$|\mathbf{v}^*|_1^2 = \int_{\Omega} \left(\frac{P}{2} - Px_2\right)^2 dx_1 dx_2 = \text{Meas}(\Omega) \frac{P^2}{12}, \quad (3.96)$$



and

$$\begin{aligned} \left| \int_{\Gamma^{in}} \mathbf{g} \cdot \mathbf{n} \operatorname{tr} \boldsymbol{\varphi}' \right| &= \int_{x_2=0}^1 \frac{P}{2} x_2 (1-x_2) \left[ \frac{2(1-\beta)}{We} + We(1-\beta)(1-2x_2)^2 \frac{P^2}{2} \right] dx_2 \\ &= \frac{P(1-\beta)}{6We} + \frac{P^3(1-\beta)We}{120}. \end{aligned} \quad (3.97)$$

Thus

$$c_2 = \left( 2 \frac{(1-\beta)}{We^2} + \frac{P^2}{12} \right) \operatorname{Meas}(\Omega) + \frac{P(1-\beta)}{6We} + \frac{P^3(1-\beta)We}{120}. \quad (3.98)$$

Let us now consider the cases of zero and non-zero Reynolds number flows. When  $Re = 0$  the analysis of Theorem 4 indicates that the stress  $\boldsymbol{\tau}'$  is bounded as follows:

$$\begin{aligned} \|\boldsymbol{\tau}'\|_{*,\Omega} &\leq \|\boldsymbol{\tau}'_0\|_{*,\Omega} \exp\left(2P - \frac{1}{We}\right)t \\ &\quad + \frac{Cc_2}{(1/We) - 2P} \left(1 - \exp\left(2P - \frac{1}{We}\right)t\right), \end{aligned} \quad (3.99)$$

with  $c_2$  as given in (3.98). When  $Re > 0$  inequality (3.49) shows that

$$\begin{aligned} \frac{Re}{2} \|\mathbf{v}\|_0^2 + \|\boldsymbol{\tau}'\|_{*,\Omega} &\leq Re \|\mathbf{v}^*\|_0^2 (1 + 2 \exp(2P - \gamma)t) \\ &\quad + (2Re \|\mathbf{v}_0\|_0^2 + \|\boldsymbol{\tau}'_0\|_{*,\Omega}) \exp(2P - \gamma)t \\ &\quad + \frac{Cc_2}{\gamma - 2P} (1 - \exp(2P - \gamma)t), \end{aligned} \quad (3.100)$$

where  $\|\mathbf{v}^*\|_0^2 = \frac{P^2}{120} \operatorname{Meas}(\Omega)$  and  $c_2$  is as given in (3.98).

#### *Remarks*

It should be noted that although  $(\mathbf{v}, p, \boldsymbol{\tau}')$  may be interpreted as being the sum of a base flow and a perturbation, the estimates given in (3.89), (3.90), (3.99) and (3.100) cannot be used to infer whether or not channel flow of an Oldroyd B fluid is stable to infinitesimal or finite amplitude disturbances. However, we are at least able to deduce that for periodic channel flow as  $t \rightarrow \infty$ , finite bounds, proportional to  $\operatorname{Meas}(\Omega) [2(1-\beta)/We^2 + P^2]$ , exist on  $\|\boldsymbol{\tau}'\|_{*,\Omega}$  and  $\|\|\mathbf{v}, \boldsymbol{\tau}'\|\|$  for the inertialess and inertial cases, respectively.

In the event of inflow boundary conditions being specified on the components of the elastic stress, proof of the existence of finite bounds on the velocity and stress fields may be seen from (3.99) and (3.100) to be conditional on the pressure gradient being sufficiently small. The condition on  $P$  in (3.100) is more stringent in this respect than that in (3.99).

### 3.2.4 Numerical results

We report here some numerical results obtained with two different schemes. The first one (referred to as Method 1 in the sequel) is the scheme described in Section 3.2.2. The other one (Method 2) is a direct implicit Euler discretization in time of (3.39)–(3.40) and (3.41) with an implicit treatment of the convective terms in both (3.40) and (3.41). Note that both our methods are thus fully implicit. We consider planar Poiseuille flow with periodic boundary conditions in the  $x_1$ -direction with a wavenumber  $\alpha$ , so that the flow domain is  $\Omega =$

$(0, 2\pi/\alpha) \times (-1, 1)$ . For the discretization in space we use in both approaches a spectral method, employing a Fourier series in the periodic direction and Lagrange interpolating polynomials  $h_l(x_2)$  on the Gauss-Legendre-Lobatto (GLL) grid in the  $x_2$ -direction. Thus the velocity is represented as

$$\mathbf{v}(x_1, x_2, t) = \sum_{k=-N/2}^{N/2} \sum_{l=0}^M \mathbf{v}_{kl}(t) \exp(i\alpha k x_1) h_l(x_2).$$

The same polynomial basis is used for  $\tau'_i$  and  $\mathbf{A}_i$ . The pressure is approximated in the  $x_2$ -direction by polynomials of degree  $M - 2$  instead of  $M$  in order to avoid spurious pressure modes [14]. The integrals in the weak forms of the Galerkin equations are evaluated using a GLL quadrature rule. The resulting nonlinear algebraic problem is solved at each time step using a simple iterative method.

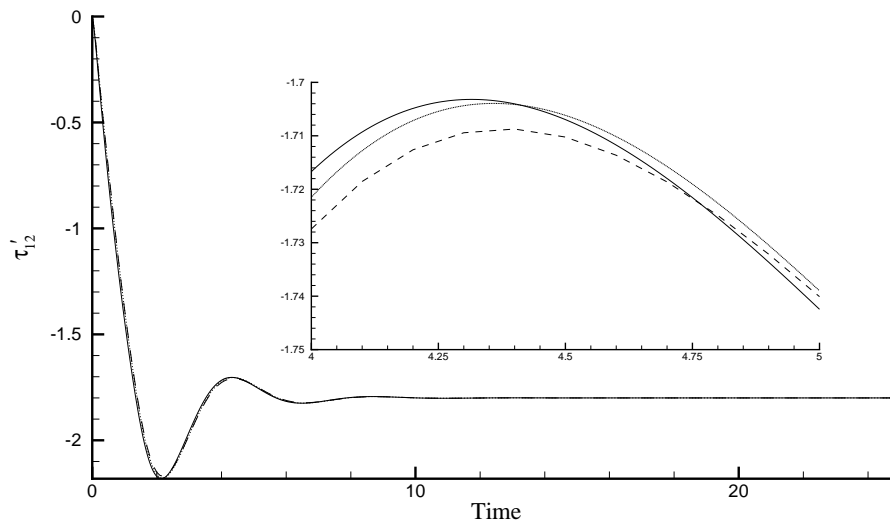


Figure 3.5: Start-up Poiseuille flow.  $\tau'_{12}$  on the wall  $x_2 = 1$ .  $Re = 1$ ,  $We = 1$ . Solid curve – analytical solution; dashed curve – Method 1 with  $M = 8$ ,  $N = 4$  and  $\Delta t = 0.01$ ; dotted curve – Method 1 with  $M = 16$ ,  $N = 4$  and  $\Delta t = 0.001$ .

For all the computations described in this section care had to be taken to ensure that the discretization in the transverse direction  $x_2$  was sufficiently fine for a given value of  $N$  and  $\alpha$ . Keiller [73] observed that artificial numerical instabilities could occur in finite difference simulations of the time-dependent viscoelastic Couette problem and proposed an instability criterion  $We_{crit} = O(\Delta x/\Delta y)$  for the problem, where  $\Delta x$  and  $\Delta y$  are the resolution scales in the streamwise and cross-stream directions, respectively. Keiller [74] also suggested that a similar criterion could apply to steady-state calculations of viscoelastic Poiseuille flow. Interestingly, the necessity of adequate refinement in the streamwise direction relative to the cross-stream direction is also in evidence for simulations of time-dependent shear flows using finite volume methods [123], finite element methods [24] and spectral element methods [51].

In validation of Method 1 we begin by showing in Fig. 3.5 values of  $\tau'_{12}$  computed on the wall  $x_2 = 1$  with two different meshes and time steps for start-up Poiseuille flow, and

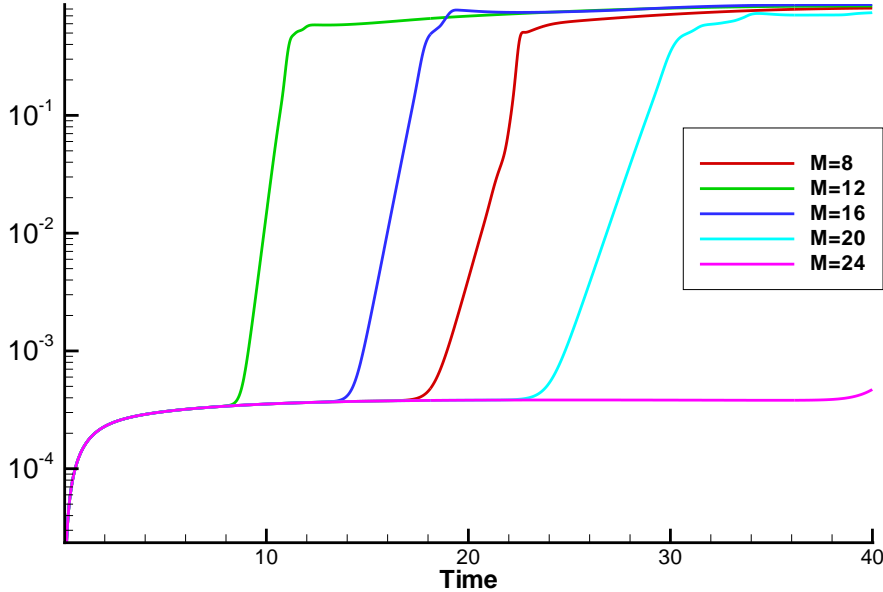


Figure 3.6: Evolution of perturbation in creeping Poiseuille flow.  $L_2$  error in the elastic extra-stress against time. Method 1 with  $We = 10$ ,  $N = 4$ ,  $\Delta t = 0.005$ .

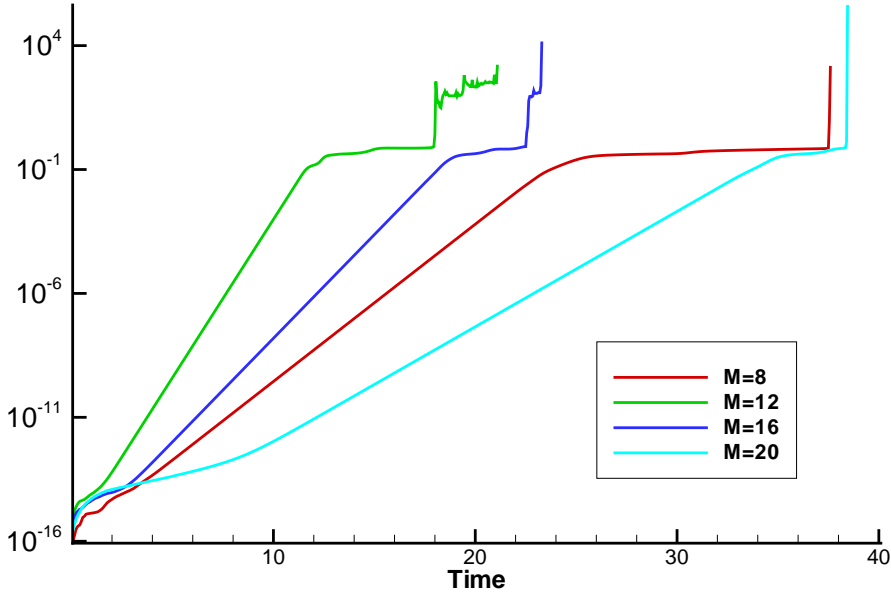


Figure 3.7: Evolution of perturbation in creeping Poiseuille flow.  $L_2$  error in the elastic extra-stress against time. Method 2 with  $We = 10$ ,  $N = 4$ ,  $\Delta t = 0.005$ .

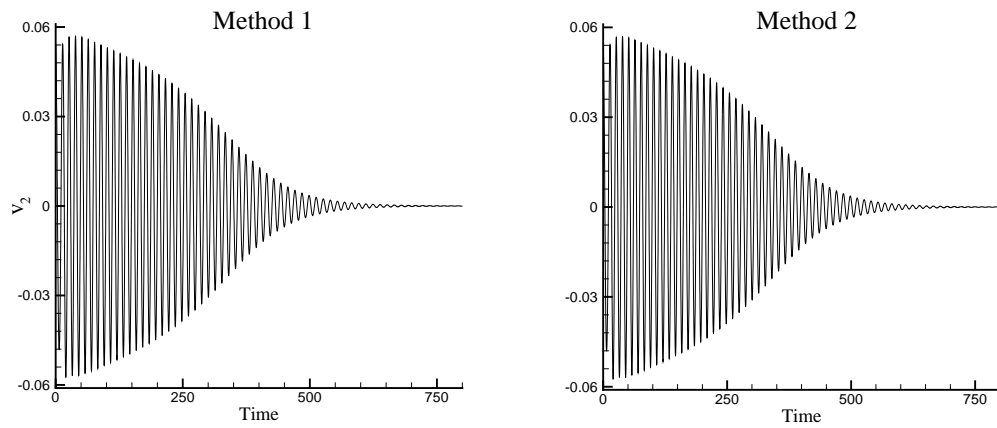


Figure 3.8: Evolution of perturbation in Poiseuille flow.  $v_2$  at  $(0, 0)$ .  $Re = 2400$ ,  $E = 4 \times 10^{-4}$ ,  $\beta = 0.5$ ,  $\alpha = 1.3231$ ,  $M = 24$ ,  $N = 8$  and  $\Delta t = 0.005$ .

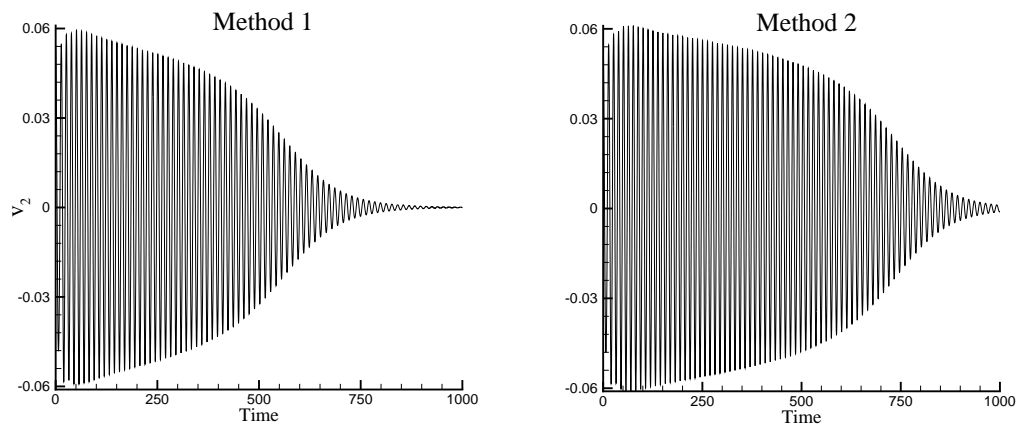


Figure 3.9: Evolution of perturbation in Poiseuille flow.  $v_2$  at  $(0, 0)$ .  $Re = 2400$ ,  $E = 6 \times 10^{-4}$ ,  $\beta = 0.5$ ,  $\alpha = 1.3231$ ,  $M = 24$ ,  $N = 8$  and  $\Delta t = 0.005$ .

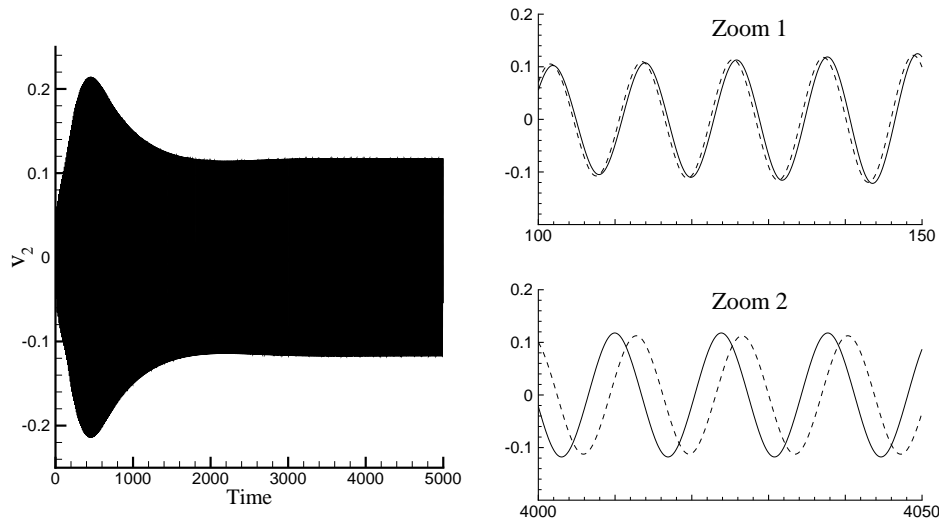


Figure 3.10: Evolution of perturbation in Poiseuille flow computed with Method 1.  $v_2$  at  $(0, 0)$ .  $Re = 3500$ ,  $E = 4.11 \times 10^{-4}$ ,  $\beta = 0.5$ ,  $\alpha = 1.3231$  and  $\Delta t = 0.005$ . In Zoom 1 is shown a magnification of the perturbations for  $100 \leq t \leq 150$  and in Zoom 2 a similar magnification for  $4000 \leq t \leq 4050$ . Solid curve –  $M = 24$ ,  $N = 8$ ; dotted curve –  $M = 28$ ,  $N = 10$ .

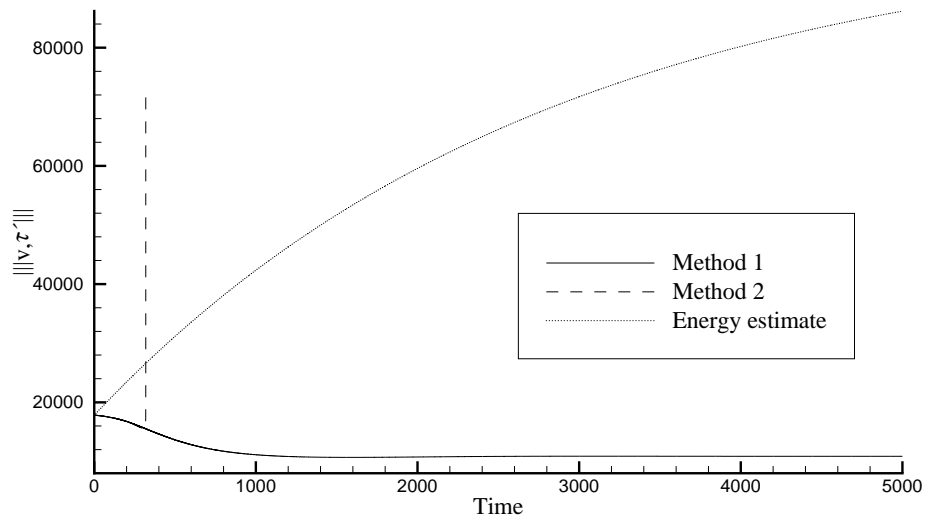


Figure 3.11: Evolution of  $\|\mathbf{v}, \boldsymbol{\tau}'\| = Re\|\mathbf{v}\|_0^2 + \|\boldsymbol{\tau}'\|_{*,\Omega}$  for the same parameters as in Fig. 3.10.

compare these with the exact solution of Waters and King [133]. The Weissenberg number and the Reynolds number are both set to unity. Zero initial conditions were supplied for all components of and elastic stress  $\boldsymbol{\tau}$  and a constant pressure gradient  $\partial p/\partial x_1 = -2$  was applied at all time. As the mesh is refined and the time step reduced increasingly good close agreement with the exact solution may be observed, even near the first stress overshoot. For this problem no limiting Weissenberg number was encountered provided that, for sufficiently small  $N$ ,  $M$  was chosen sufficiently large.

In Figs. 3.6 - 3.10 we show the results of our computations when the steady state solution of the Oldroyd B Poiseuille problem was finitely perturbed at  $t = 0$ . We start with creeping flows ( $Re = 0$ ), see Figs. 3.6 and 3.7. The initial perturbation here was chosen to be very small (of order  $10^{-15}$ ) random but nevertheless the same for the 2 methods. As can be seen from the figures, no distinct advantage has been found in using our new method for these flows. The determining factor seems to be the ratio of discretization steps in two directions. Note, however, that the simulations using Method 1 do not explode in time, as do those using Method 2. This is the manifestation of the fact that the former respect the energy bound (3.50) whereas the latter do not.

However, we are able to prove the superiority of our new method for simulations of flows with inertia. The initial perturbation in this case was constructed from the eigenfunctions of the Newtonian linear stability problem corresponding to the least stable eigenvalue with the aim of comparing our results with those of Atalik and Keunings [3] who considered the evolution of finite perturbations of this type to viscoelastic Poiseuille flow. The maximum norm of the velocity perturbations was set equal to 0.1 in all our numerical experiments and, following one of the choices of Atalik and Keunings, the wavenumber  $\alpha$  was taken as 1.3231. In Figs. 3.8 and 3.9 we show the results of finitely perturbing the Oldroyd B Poiseuille flow at elasticity numbers  $E = We/Re$  of  $4 \times 10^{-4}$  and  $6 \times 10^{-4}$ , respectively. The value of  $v_2$  at  $(0, 0)$  is plotted. According to the study of Atalik and Keunings [3], a periodic non-decaying wave should result in the first case, whereas the second case is borderline, lying on the curve of neutral stability of Fig. 6 of [3]. We see that both Methods 1 and 2 predict that the perturbations die out with time. Agreement in Fig. 3.8 between the two methods is excellent whereas at the higher elasticity number the oscillations are sustained for rather longer using Method 2.

Increasing the Reynolds number to 3500 whilst keeping the same Weissenberg number as in Fig. 3.9 leads to periodic and non-decaying oscillations, as shown in Fig. 3.10. The elasticity number is now equal to  $4.11 \times 10^{-4}$  and the results are consistent with the predictions of Atalik and Keunings. In order to investigate the long term behaviour with mesh refinement, solutions on two different meshes  $(M, N) = (24, 8)$  and  $(28, 10)$  were computed. A small difference in period became apparent for large  $t$  and in Zoom 2 of the figure this shows up as a slight shift between the perturbations in  $v_2$  computed at  $(0, 0)$  using the two meshes. At these large times the amplitude of the oscillations has settled down to a steady state and is computed to be approximately 0.11 on the finer mesh and 0.12 on the coarser mesh. The period of the oscillations is approximately 13.87 on both meshes.

In Fig. 3.11 we demonstrate what happens when Method 2 is applied to the same Poiseuille problem as described in the previous paragraph. In this case the iterative process employed at each time step to solve the nonlinear governing equations fails to converge after 63760 time steps. Even before this point, however, the energy estimate (3.49) has been violated by Method 2. We note that the failure of Method 2 cannot be attributed to the lack of positive definiteness

of  $\boldsymbol{\tau}'$  since it was checked to be positive definite at all collocation points at all points in time. In contrast, and in keeping with the analysis of Section 3, the value of  $\|\|\mathbf{v}, \boldsymbol{\tau}'\|\|$  computed with Method 1 is less than the theoretical bound at all times.





# Chapter 4

## Simulations of flows of dilute polymer solutions using a Fokker-Planck equation for the FENE dumbbell model

In this chapter we report on the results on using the numerical methods based on the FP equation for a dilute polymer solution modelled by FENE dumbbells with the force law (1.4) (or (1.21) in the non-dimensional form). The global or local homogeneity of the flow (see Section 1.1.4) will be assumed in the first 4 sections of this chapter and the simulations, which do not use these assumptions, will be presented in the last Section. Throughout this chapter, we shall be interested mostly in two-dimensional planar flows. However, even in this case, there is no physical reason to suppose that the dumbbells lie in the plane of the flow, hence the configuration vector  $\mathbf{q}$  should be three-dimensional. For simplicity, one can also consider a simplified model where  $\mathbf{q}$  is restricted to lie in the plane of the flow. In the latter case, we will denote the model as 2D FENE, and in the former case as 3D FENE.

### 4.1 Discretization of the Fokker-Planck equation for simple flows

In this section, we restrict ourselves to the case of homogeneous flows, so that the velocity is given by (1.18). Thus, we do not need to solve the momentum and mass conservation equations and we are only seeking a pdf  $\psi(t, \mathbf{q})$  that is independent of spatial position. Let us recall that the FP equation can be written in this case after non-dimensionalization of  $\mathbf{q}$  as

$$\frac{\partial \psi}{\partial t} + \operatorname{div}_{\mathbf{q}} \left( \left( \boldsymbol{\kappa} \mathbf{q} - \frac{1}{2\lambda} \frac{\mathbf{q}}{1 - |\mathbf{q}|^2/b} \right) \psi \right) = \frac{1}{2\lambda} \Delta_{\mathbf{q}} \psi. \quad (4.1)$$

The discretization of this equation for 2D FENE and 3D FENE models is described separately in the following two subsections.

#### 4.1.1 Two-dimensional FENE dumbbells

The magnitude of the configuration vectors for the FENE dumbbells cannot exceed  $\sqrt{b}$ , hence the pdf  $\psi$  for the 2D FENE model should be defined in the disc  $|q| < \sqrt{b}$ . Therefore, it is

natural to use polar coordinates  $(\rho, \varphi)$  to represent  $\mathbf{q}$  as

$$q_1 = \rho \cos \varphi, \quad q_2 = \rho \sin \varphi, \quad \text{with } \rho \in [0, \sqrt{b}] \text{ and } \varphi \in [0, 2\pi]. \quad (4.2)$$

We now give a detailed expression for (4.1) in the variables  $(\rho, \varphi)$  :

$$\begin{aligned} \frac{\partial \psi}{\partial t} = & -\rho b_1(\boldsymbol{\kappa}, \varphi) \frac{\partial \psi}{\partial \rho} - b_2(\boldsymbol{\kappa}, \varphi) \frac{\partial \psi}{\partial \varphi} + \frac{1}{2\lambda} \left( \frac{b\rho}{b-\rho^2} + \frac{1}{\rho} \right) \frac{\partial \psi}{\partial \rho} \\ & + \frac{b^2}{\lambda(b-\rho^2)^2} \psi + \frac{1}{2\lambda} \frac{\partial^2 \psi}{\partial \rho^2} + \frac{1}{2\lambda\rho^2} \frac{\partial^2 \psi}{\partial \varphi^2}, \end{aligned} \quad (4.3)$$

where  $b_1(\boldsymbol{\kappa}, \varphi)$  and  $b_2(\boldsymbol{\kappa}, \varphi)$  are defined by

$$b_1(\boldsymbol{\kappa}, \varphi) = \kappa_{11} \cos 2\varphi + \frac{\kappa_{12} + \kappa_{21}}{2} \sin 2\varphi, \quad (4.4)$$

and

$$b_2(\boldsymbol{\kappa}, \varphi) = -\kappa_{11} \sin 2\varphi + \left( \frac{\kappa_{12} + \kappa_{21}}{2} \right) \cos 2\varphi + \frac{\kappa_{21} - \kappa_{12}}{2}. \quad (4.5)$$

We note that (4.3) possesses two singularities at  $\rho = 0$  and  $\rho = \sqrt{b}$  that require special treatment. Consistent with the fact that the probability density function should be zero at  $\rho = \sqrt{b}$  and satisfy  $\partial\psi/\partial\rho = 0$  at  $\rho = 0$  (the latter condition follows from symmetry of the pdf with respect to  $\mathbf{q}$ ), we introduce a new unknown  $\alpha(t, \eta, \varphi)$  defined by

$$\psi(t, \rho, \varphi) = \left( \frac{1-\eta}{2} \right)^s \alpha(t, \eta, \varphi), \quad (4.6)$$

where

$$\rho^2 = b \frac{1+\eta}{2}, \quad \eta \in [-1, 1], \quad (4.7)$$

and  $s$  is a positive number. The choice of  $s$  will be discussed below. Substituting the expression for  $\psi$  given by (4.6) into (4.3), we get

$$\frac{\partial \alpha}{\partial t} = L_0 \alpha + \kappa_{11} L_1 \alpha + \kappa_{12} L_2 \alpha + \kappa_{21} L_3 \alpha, \quad (4.8)$$

where  $L_0, \dots, L_3$  are linear operators (independent of  $\boldsymbol{\kappa}$ ) defined by

$$\begin{aligned} L_0 = & \frac{2(b-2s)(2-s-s\eta)}{b\lambda(1-\eta)^2} + \frac{2}{b\lambda} \left( \frac{(b-4s)(1+\eta)}{1-\eta} + 2 \right) \frac{\partial}{\partial \eta} \\ & + \frac{4(1+\eta)}{\lambda b} \frac{\partial^2}{\partial \eta^2} + \frac{1}{\lambda b(1+\eta)} \frac{\partial^2}{\partial \varphi^2}, \end{aligned} \quad (4.9)$$

$$L_1 = \frac{2s(1+\eta)}{1-\eta} \cos 2\varphi - 2(1+\eta) \cos 2\varphi \frac{\partial}{\partial \eta} + \sin 2\varphi \frac{\partial}{\partial \varphi}, \quad (4.10)$$

$$L_2 = \frac{s(1+\eta)}{1-\eta} \sin 2\varphi - (1+\eta) \sin 2\varphi \frac{\partial}{\partial \eta} - \frac{1}{2} \cos 2\varphi \frac{\partial}{\partial \varphi} + \frac{1}{2} \frac{\partial}{\partial \varphi}, \quad (4.11)$$

and

$$L_3 = \frac{s(1+\eta)}{1-\eta} \sin 2\varphi - (1+\eta) \sin 2\varphi \frac{\partial}{\partial \eta} - \frac{1}{2} \cos 2\varphi \frac{\partial}{\partial \varphi} - \frac{1}{2} \frac{\partial}{\partial \varphi}. \quad (4.12)$$

### Discretization in configuration space

We shall search for an approximate solution  $\alpha(t, \eta, \varphi)$  to the FP equation (4.8) of the form

$$\alpha_N(t, \eta, \varphi) = \sum_{i=0}^1 \sum_{l=i}^{N_F} \sum_{k=1}^{N_R} \alpha_{kl}^i(t) h_k(\eta) \Phi_{il}(\varphi), \quad (4.13)$$

for some positive integers  $N_F$  and  $N_R$ , with

$$\Phi_{il}(\varphi) = \begin{cases} \cos 2l\varphi, & i = 0 \\ \sin 2l\varphi, & i = 1 \end{cases} = \cos\left(2l\varphi - i\frac{\pi}{2}\right). \quad (4.14)$$

In the above expression,  $\{h_k(\eta)\}_{1 \leq k \leq N_R}$  are Lagrange interpolating polynomials based on the Gauss-Legendre points  $\eta_r$  (see Section 2.1). Note that the set  $\{\eta_r\}$  is chosen so that it does not include the points  $\eta = -1$  and  $\eta = 1$  since the boundary conditions there are already taken into account by (4.6). Only the Fourier modes of even order are kept in (4.14) because of the symmetry of  $\alpha(\eta, \varphi)$ . The integrals with respect to  $\eta$  are evaluated using the Gauss quadrature rule (2.1). The integrals with respect to  $\varphi$  can be computed analytically.

To calculate the components of the matrix  $\mathbf{L}_0$  that is the discretization of the operator  $L_0$  defined by (4.9), we insert (4.13) into (4.9), form its product with a test function  $h_m(\eta)\Phi_{jn}(\varphi)$  and integrate over configuration space, to obtain

$$\mathbf{L}_0 \alpha_N = \sum_{j=0}^1 \sum_{n=j}^{N_F} \sum_{m=1}^{N_R} (L_0 \alpha)_{mn}^j h_m(\eta) \Phi_{jn}(\varphi)$$

with

$$\begin{aligned} (L_0 \alpha)_{mn}^j &= \sum_{k=1}^{N_R} \left( \frac{2}{b\lambda} \left( \frac{(b-4s)(1+\eta_m)}{1-\eta_m} + 2 \right) h'_k(\eta_m) + \frac{4(1+\eta_m)}{\lambda b} h''_k(\eta_m) \right) \alpha_{kn}^j \\ &+ \left( \frac{2(b-2s)(2-s-s\eta_m)}{b\lambda(1-\eta_m)^2} - \frac{4l^2}{\lambda b(1+\eta_m)} \right) \alpha_{mn}^j. \end{aligned} \quad (4.15)$$

Note that the quadrature weights in Gauss integration with respect to  $\eta$  have been cancelled in (4.15) so that this equation is simply an evaluation of the differential operator (4.9) at the quadrature points. This approach is known as the collocation method.

The discretizations  $\mathbf{L}_1, \dots, \mathbf{L}_3$  of operators  $L_1, \dots, L_3$ , defined by (4.10)–(4.12), may be written in similar notation as

$$(L_1 \alpha)_{mn}^j = \sum_{i=0}^1 \sum_{l=i}^{N_F} \sum_{k=1}^{N_R} \left[ \left( \frac{2s(1+\eta_m)}{1-\eta_m} h'_k(\eta_m) - 4 \frac{1+\eta_m}{1-\eta_m} \delta_{km} \right) J_{iljn}^0 + K_{iljn}^1 \delta_{km} \right] \alpha_{kl}^i, \quad (4.16)$$

$$(L_2 \alpha)_{mn}^j = \sum_{i=0}^1 \sum_{l=i}^{N_F} \sum_{k=1}^{N_R} \left[ \left( \frac{s(1+\eta_m)}{1-\eta_m} h'_k(\eta_m) - 2 \frac{1+\eta_m}{1-\eta_m} \delta_{km} \right) J_{iljn}^1 - \frac{1}{2} K_{iljn}^0 \delta_{km} \right] \alpha_{kl}^i + (-1)^j n \alpha_{mn}^{1-j}, \quad (4.17)$$

$$(L_3\alpha)_{mn}^j = \sum_{i=0}^1 \sum_{l=i}^{N_F} \sum_{k=1}^{N_R} \left[ \left( \frac{s(1+\eta_m)}{1-\eta_m} h'_k(\eta_m) - 2 \frac{1+\eta_m}{1-\eta_m} \delta_{km} \right) J_{iljn}^1 - \frac{1}{2} K_{iljn}^0 \delta_{km} \right] \alpha_{kl}^i - (-1)^j n \alpha_{mn}^{1-j}, \quad (4.18)$$

where

$$\begin{aligned} J_{iljn}^p &= \frac{1}{\pi(1+\delta_{n0})} \int_0^{2\pi} \cos\left(2\varphi - p\frac{\pi}{2}\right) \Phi_{il}(\varphi) \Phi_{jn}(\varphi) d\varphi \\ &= \frac{1}{2(1+\delta_{n0})} \left( \delta_{l+n,1} \cos(p-i-j)\frac{\pi}{2} + \delta_{n-l,1} \cos(p+i-j)\frac{\pi}{2} + \delta_{l-n,1} \cos(p-i+j)\frac{\pi}{2} \right), \end{aligned}$$

and

$$K_{iljn}^p = \frac{1}{\pi(1+\delta_{n0})} \int_0^{2\pi} \sin\left(2\varphi - p\frac{\pi}{2}\right) \Phi'_{il}(\varphi) \Phi_{jn}(\varphi) d\varphi = 2l(-1)^{1-i} J_{iljn}^p.$$

Equation (4.8) can be discretized in time using an implicit Euler scheme. Combining it with the discretization in configuration space described above, we arrive at a scheme

$$\bar{\alpha}_N^{n+1} = (\mathbf{I} - \Delta t (\mathbf{L}_0 + \kappa_{11}\mathbf{L}_1 + \kappa_{12}\mathbf{L}_2 + \kappa_{21}\mathbf{L}_3))^{-1} \bar{\alpha}_N^n, \quad (4.19)$$

where  $\bar{\alpha}_N^n$  is the vector of the expansion coefficients  $\alpha_{kl}^i(t)$  at time  $t_n = n\Delta t$ .

If one is only interested in the steady-state solution, one can find directly a non-trivial solution  $\bar{\alpha}_N$  of

$$(\mathbf{L}_0 + \kappa_{11}\mathbf{L}_1 + \kappa_{12}\mathbf{L}_2 + \kappa_{21}\mathbf{L}_3) \bar{\alpha}_N^n = \mathbf{0} \quad (4.20)$$

by changing one of the rows in the singular matrix  $(\mathbf{L}_0 + \kappa_{11}\mathbf{L}_1 + \kappa_{12}\mathbf{L}_2 + \kappa_{21}\mathbf{L}_3)$  by the discretized form of the integral of  $\psi$  over the whole of configuration space (see (4.27)), set equal to unity.

### Computation of the elastic extra-stress

The elastic extra-stress can be written as (see equation (3))

$$\boldsymbol{\tau} = \frac{\eta_p}{\lambda} \left( \frac{b+4}{b} \right) \left( -\mathbf{I} + \int_{|\mathbf{q}| < \sqrt{b}} \mathbf{q} \otimes \mathbf{F}(\mathbf{q}) \psi d\mathbf{q} \right). \quad (4.21)$$

Using (4.2) and (4.7), an expression for  $\mathbf{q} \otimes \mathbf{F}(\mathbf{q})$  is

$$\mathbf{q} \otimes \mathbf{F}(\mathbf{q}) = \frac{r^2}{1 - \frac{r^2}{b}} \mathbf{e} \otimes \mathbf{e} = b \frac{1+\eta}{1-\eta} \mathbf{e} \otimes \mathbf{e}, \quad (4.22)$$

where  $\mathbf{e}$  is the unit vector  $(\cos \varphi, \sin \varphi)$ . With the help of (4.6), the integral appearing in (4.21) can now be rewritten as

$$\int_{|\mathbf{q}| < \sqrt{b}} \mathbf{q} \otimes \mathbf{F}(\mathbf{q}) \psi d\mathbf{q} = \int_{-1}^1 \int_0^{2\pi} \frac{b^2}{16} (1+\eta) \left( \frac{1-\eta}{2} \right)^{s-1} \alpha \mathbf{e} \otimes \mathbf{e} d\varphi d\eta. \quad (4.23)$$

We then replace  $\alpha$  in the above integral by its expression (4.13), evaluate the integral with respect to  $\varphi$  analytically and the integral with respect to  $\eta$  numerically. Most of the terms vanish and we get the following expressions for the three components of the elastic extra-stress

$$\tau_{xx} = \frac{\eta_p b + 4}{\lambda b} \left( -1 + \frac{\pi b^2}{16} \sum_{i=1}^{N_R} \omega_i (1 + \eta_i) \left( \frac{1 - \eta_i}{2} \right)^{s-1} (2\psi_{i0}^0 + \psi_{i1}^0) \right), \quad (4.24)$$

$$\tau_{xy} = \frac{\eta_p b + 4}{\lambda b} \frac{\pi b^2}{16} \sum_{i=1}^{N_R} \omega_i (1 + \eta_i) \left( \frac{1 - \eta_i}{2} \right)^{s-1} \alpha_{i1}^1, \quad (4.25)$$

$$\tau_{yy} = \frac{\eta_p b + 4}{\lambda b} \left( -1 + \frac{\pi b^2}{16} \sum_{i=1}^{N_R} \omega_i (1 + \eta_i) \left( \frac{1 - \eta_i}{2} \right)^{s-1} (2\alpha_{i0}^0 - \alpha_{i1}^0) \right), \quad (4.26)$$

where  $\omega_i$  are the Gauss-Legendre quadrature weights as in (2.1).

Analogously, the formula for computing the integral of  $\psi$  over the whole of configuration space may be written as

$$\int_{|\mathbf{q}| < \sqrt{b}} \psi d\mathbf{q} \approx \frac{\pi b}{2} \sum_{i=1}^{N_R} \omega_i \left( \frac{1 - \eta_i}{2} \right)^s \alpha_{i0}^0. \quad (4.27)$$

### 4.1.2 Three-dimensional FENE dumbbells

For the 3D FENE model, configuration space is a ball of radius  $\sqrt{b}$  and therefore it is natural to represent the vector  $\mathbf{q}$  in spherical coordinates

$$q_1 = \rho \sin \theta \cos \varphi, \quad q_2 = \rho \sin \theta \sin \varphi, \quad q_3 = \rho \cos \theta, \quad (4.28)$$

where  $\rho \in [0, \sqrt{b}]$ ,  $\varphi \in [0, 2\pi]$  and  $\theta \in [0, \pi]$ . We now introduce the unit vector  $\mathbf{u}$  defined by  $\mathbf{q} = \rho \mathbf{u}$  and the following two operators

$$\Lambda = \frac{\partial}{\partial \mathbf{u}} \cdot (\mathbf{I} - \mathbf{u}\mathbf{u}) \frac{\partial}{\partial \mathbf{u}}, \quad (4.29)$$

$$\mathcal{L}(\boldsymbol{\kappa})\psi = \frac{\partial}{\partial \mathbf{u}} \cdot [(\mathbf{I} - \mathbf{u}\mathbf{u}) \cdot \boldsymbol{\kappa} \cdot \mathbf{u}\psi]. \quad (4.30)$$

With these notations, the FP equation (4.1) takes the form:

$$\frac{D\psi}{Dt} + \mathcal{L}(\boldsymbol{\kappa})\psi + \operatorname{div}_{\mathbf{q}} \left( (\rho \boldsymbol{\kappa} : \mathbf{u}\mathbf{u}\mathbf{u} - \frac{1}{2\lambda} \frac{\rho \mathbf{u}}{1 - \rho^2/b}) \psi \right) = \frac{1}{2\lambda} \left( \frac{\partial^2}{\partial \rho^2} + \frac{2}{\rho} \frac{\partial}{\partial \rho} + \frac{1}{\rho^2} \Lambda \right) \psi. \quad (4.31)$$

Expanding the divergence operator, we get

$$\begin{aligned} \frac{\partial \psi}{\partial t} + \mathcal{L}(\boldsymbol{\kappa})\psi + \left( 3\boldsymbol{\kappa} : \mathbf{u}\mathbf{u} - \frac{3 - \rho^2/b}{2\lambda(1 - \rho^2/b)^2} \right) \psi + \left( \boldsymbol{\kappa} : \mathbf{u}\mathbf{u} - \frac{1}{2\lambda(1 - \rho^2/b)} \right) \rho \frac{\partial \psi}{\partial \rho} \\ = \frac{1}{2\lambda} \left( \frac{\partial^2}{\partial \rho^2} + \frac{2}{\rho} \frac{\partial}{\partial \rho} + \frac{1}{\rho^2} \Lambda \right) \psi. \end{aligned} \quad (4.32)$$

To treat the boundary conditions we introduce the transformation of variables as in the 2D case

$$\psi(t, \rho, \theta, \varphi) = \left( \frac{1 - \eta}{2} \right)^s \alpha(t, \eta, \theta, \varphi),$$

where  $\rho$  and  $\eta$  are related by (4.7). The FP equation (4.32) can now be rewritten as

$$\frac{D\alpha}{Dt} = -\mathcal{L}(\boldsymbol{\kappa})\alpha - \boldsymbol{\kappa} : \mathbf{uu} \left( 3 - 2s \frac{1 + \eta}{1 - \eta} \right) \alpha - 2\boldsymbol{\kappa} : \mathbf{uu}(1 + \eta) \frac{\partial \alpha}{\partial \eta} + L_0 \alpha, \quad (4.33)$$

where

$$\begin{aligned} L_0 &= \frac{1}{\lambda b(1 + \eta)} \Lambda + \frac{(5 - \eta - 2s(1 + \eta))(b - 2s)}{b\lambda(1 - \eta)^2} \\ &+ \frac{2}{b\lambda} \left( 3 + (b - 4s) \frac{1 + \eta}{1 - \eta} \right) \frac{\partial}{\partial \eta} + \frac{4(1 + \eta)}{b\lambda} \frac{\partial^2}{\partial \eta^2}, \end{aligned} \quad (4.34)$$

is the part of the FP operator that does not depend on the velocity gradient.

We restrict ourselves to velocity gradients of the form

$$\boldsymbol{\kappa} = \begin{pmatrix} \kappa_{11} & \kappa_{12} & 0 \\ \kappa_{21} & -\kappa_{11} - \kappa_{33} & 0 \\ 0 & 0 & \kappa_{33} \end{pmatrix}. \quad (4.35)$$

We can now rewrite the FP equation (4.33) in the form analogous to that of the 2D FENE model (4.8)

$$\frac{\partial \alpha}{\partial t} = L_0 \alpha + \kappa_{11} L_1 \alpha + \kappa_{12} L_2 \alpha + \kappa_{21} L_3 \alpha + \kappa_{33} L_4 \alpha$$

where  $L_r$ ,  $r = 1, \dots, 4$ , are linear operators independent of  $\boldsymbol{\kappa}$  defined by

$$L_r = -\mathcal{L}(\mathbf{I}_r) - \mathbf{I}_r : \mathbf{uu} \left( 3 - 2s \frac{1 + \eta}{1 - \eta} \right) - 2\mathbf{I}_r : \mathbf{uu}(1 + \eta) \frac{\partial}{\partial \eta}, \quad (4.36)$$

with the matrices  $\mathbf{I}_k$  of the form

$$\mathbf{I}_1 = \begin{pmatrix} 1 & 0 & 0 \\ 0 & -1 & 0 \\ 0 & 0 & 0 \end{pmatrix}, \quad \mathbf{I}_2 = \begin{pmatrix} 0 & 1 & 0 \\ 0 & 0 & 0 \\ 0 & 0 & 0 \end{pmatrix}, \quad (4.37)$$

$$\mathbf{I}_3 = \begin{pmatrix} 0 & 0 & 0 \\ 1 & 0 & 0 \\ 0 & 0 & 0 \end{pmatrix}, \quad \mathbf{I}_4 = \begin{pmatrix} 0 & 0 & 0 \\ 0 & -1 & 0 \\ 0 & 0 & 1 \end{pmatrix}. \quad (4.38)$$

### Discretization in configuration space

A discrete approximation of the unknown function  $\alpha(t, \eta, \theta, \varphi)$  may be written as

$$\alpha_N(t, \eta, \theta, \varphi) = \sum_{i=0}^1 \sum_{l=1}^{N_\eta} \sum_{n=0}^{N_u} \sum_{m=i}^n \alpha_{i,l,n,m}(t) \Phi_{2n,2m}^i(\theta, \varphi) h_l(\eta), \quad (4.39)$$

where  $\Phi_{n,m}^i(\theta, \varphi) = P_n^m(\cos \theta) \cos(m\varphi - i\frac{\pi}{2})$  are spherical harmonics and  $P_n^m$  are the associated Legendre polynomials. In (4.39), only the spherical harmonics of even order appear because  $\alpha$  is an even function of  $\mathbf{u}$ .  $h_l(\eta)$  are Lagrange interpolating polynomials of order  $N_\eta$  based on the Gauss-Jacobi points  $\eta_k$  with certain parameters  $J_\alpha, J_\beta > -1$  (see Section 2.1). In contrast with the 2D FENE case, we prefer to use here the more general Jacobi polynomials for reasons that will be explained below.

To discretize the operators  $L_0, \dots, L_4$  we insert (4.39) into (4.34) and (4.36), form the products with test functions  $\Phi_{2n,2m}^i(\theta, \varphi)h_l(\eta)$  multiplied by a weight function and integrate over the configuration space. In doing so, the integrals with respect to  $\theta$  and  $\varphi$  can be evaluated exactly since the spherical harmonics form the orthogonal basis in  $L_2$  space on the unit sphere. For the integrals with respect to  $\eta$ , we resort to the Gaussian quadrature rule (2.1).

We note also that the spherical harmonics are the eigenfunctions of the Laplace operator on the unit sphere, so we have

$$\Lambda \Phi_{n,m}^i = -n(n+1)\Phi_{n,m}^i.$$

We can thus write the discretization  $\mathbf{L}_0$  of the operator  $L_0$ :

$$\mathbf{L}_0 \alpha_N(t, \mathbf{x}, \eta, \theta, \varphi) = \sum_{i=0}^1 \sum_{l=1}^{N_\eta} \sum_{n=0}^{N_u} \sum_{m=i}^n (L_0 \alpha)_{i,l,n,m}(t, \mathbf{x}) \Phi_{2n,2m}^i(\theta, \varphi) h_l(\eta), \quad (4.40)$$

where

$$\begin{aligned} (L_0 \alpha)_{i,l,n,m} &= \left( -\frac{2n(2n+1)}{\lambda b(1+\eta_l)} + \frac{(5-\eta_l-2s(1+\eta_l))(b-2s)}{b\lambda(1-\eta_l)^2} \right) \alpha_{i,l,n,m} \\ &+ \frac{2}{b\lambda} \left( 3 + (b-4s)\frac{1+\eta_l}{1-\eta_l} \right) \sum_{p=0}^{N_\eta} h'_p(\eta_l) \alpha_{i,p,n,m} \\ &+ \frac{4(1+\eta_l)}{b\lambda} \sum_{p=0}^{N_\eta} h''_p(\eta_l) \alpha_{i,p,n,m}. \end{aligned} \quad (4.41)$$

In the case of operators  $L_1, \dots, L_4$  we need also the discretizations of operators  $\mathcal{L}(\boldsymbol{\kappa})$  and  $\boldsymbol{\kappa} : \mathbf{u}\mathbf{u}$  that are described in Appendix A (see formulas (A.6) and (A.9) there with the necessary coefficients supplied in Tables A.1–A.4). We can thus write the discretizations  $\mathbf{L}_r$  of the operators  $L_r$ ,  $r = 1, \dots, 4$ :

$$\begin{aligned} (L_r \alpha)_{i,l,n,m} &= - \sum_{k=m-1}^{m+1} \sum_{j=n-1}^{n+1} \left[ a_{2j,2n}^{2k,2m} (w_{2j}^{2k}(\mathbf{I}_r) \alpha_{i,l,j,k} + (-1)^i v_{2j}^{2k}(\mathbf{I}_r) \alpha_{1-i,l,j,k}) \right. \\ &+ \left( 3 - 2s \frac{1+\eta_l}{1-\eta_l} \right) b_{2j,2n}^{2k,2m} (w_{2j}^{2k}(\mathbf{I}_r) \alpha_{i,l,j,k} + (-1)^i v_{2j}^{2k}(\mathbf{I}_r) \alpha_{1-i,l,j,k}) \\ &+ \left. 2(1+\eta_l) \sum_{p=0}^{N_\eta} h'_p(\eta_l) b_{2j,2n}^{2k,2m} (w_{2j}^{2k}(\mathbf{I}_r) \alpha_{i,p,j,k} + (-1)^i v_{2j}^{2k}(\mathbf{I}_r) \alpha_{1-i,p,j,k}) \right]. \end{aligned} \quad (4.42)$$

Discretization in time can be done in exactly the same manner as for the 2D FENE model.

### Computation of the elastic extra-stress

The elastic extra-stress can be written as (see equation (3))

$$\boldsymbol{\tau} = \frac{\eta_p}{\lambda} \left( \frac{b+5}{b} \right) \left( -\mathbf{I} + \int_{|\mathbf{q}| < \sqrt{b}} \mathbf{q} \otimes \mathbf{F}(\mathbf{q}) \psi d\mathbf{q} \right). \quad (4.43)$$

We use the expression (4.22) for  $\mathbf{q} \otimes \mathbf{F}(\mathbf{q})$  and replace the pdf  $\psi$  by a function of  $\alpha$  to get

$$\begin{aligned} & \int_{|\mathbf{q}| < \sqrt{b}} \mathbf{q} \otimes \mathbf{F}(\mathbf{q}) \psi(t, \mathbf{x}, \mathbf{q}) d\mathbf{q} \\ &= \int_{-1}^1 \int_0^{2\pi} \int_0^\pi \frac{b^{5/2}}{2^{5/2+s}} (1+\eta)^{3/2} (1-\eta)^{s-1} \alpha(t, \mathbf{x}, \mathbf{q}) \mathbf{u} \otimes \mathbf{u} d\theta d\varphi d\eta. \end{aligned} \quad (4.44)$$

We then replace  $\alpha$  in the above integral by its discrete representation (4.39), evaluate the integrals with respect to  $\theta$  and  $\varphi$  analytically and the integral with respect to  $\eta$  numerically. Most of the terms vanish and we get the following expressions for the three components of the elastic extra-stress :

$$\begin{aligned} \tau_{xx} &= \frac{\eta_p b + 5}{\lambda b} \left( -1 + \frac{\pi b^{5/2}}{2^{s+1/2}} \sum_{l=0}^{N_\eta} \omega_l (1+\eta_l)^{3/2-J_\beta} (1-\eta_l)^{s-1-J_\alpha} \right. \\ &\quad \left. \left( \frac{1}{3} \alpha_{0,l,0,0} - \frac{1}{15} \alpha_{0,l,1,0} + \frac{2}{5} \alpha_{0,l,1,1} \right) \right), \\ \tau_{xy} &= \frac{\eta_p b + 5}{\lambda b} \frac{\pi b^{5/2}}{2^{s+1/2}} \frac{2}{5} \sum_{l=0}^{N_\eta} \omega_l (1+\eta_l)^{3/2-J_\beta} (1-\eta_l)^{s-1-J_\alpha} \alpha_{1,l,1,1}, \\ \tau_{yy} &= \frac{\eta_p b + 5}{\lambda b} \left( -1 + \frac{\pi b^{5/2}}{2^{s+1/2}} \sum_{l=0}^{N_\eta} \omega_l (1+\eta_l)^{3/2-J_\beta} (1-\eta_l)^{s-1-J_\alpha} \right. \\ &\quad \left. \left( \frac{1}{3} \alpha_{0,l,0,0} - \frac{1}{15} \alpha_{0,l,1,0} - \frac{2}{5} \alpha_{0,l,1,1} \right) \right), \\ \tau_{zz} &= \frac{\eta_p b + 5}{\lambda b} \left( -1 + \frac{\pi b^{5/2}}{2^{s+1/2}} \sum_{l=0}^{N_\eta} \omega_l (1+\eta_l)^{3/2-J_\beta} (1-\eta_l)^{s-1-J_\alpha} \right. \\ &\quad \left. \left( \frac{1}{3} \alpha_{0,l,0,0} + \frac{2}{15} \alpha_{0,l,1,0} \right) \right) \end{aligned}$$

where  $\omega_l$  are the the quadrature weights from (2.1).

Analogously, the formula for computing the integral of  $\psi$  over the whole configuration space may be written as

$$\int_{|\mathbf{q}| < \sqrt{b}} \psi d\mathbf{q} \approx \frac{\pi b^{3/2}}{2^{s+1/2}} \sum_{l=1}^{N_\eta} \omega_l (1-\eta_l)^{s-J_\alpha} (1+\eta_l)^{1/2-J_\beta}.$$



We see that the power of  $(1 + \eta_i)$  in all the sums above is  $1/2 - J_\beta$  or  $3/2 - J_\beta$  and that of  $(1 - \eta_i)$  is  $s - 1 - J_\alpha$  or  $s - J_\alpha$ . Therefore, these terms correspond to polynomials if  $1/2 - J_\beta$  and  $s - 1 - J_\alpha$  are non-negative integers, i.e. if we set  $J_\alpha = s - 1 - k$  and  $J_\beta = 1/2 - l$  for some non-negative integers  $k$  and  $l$ . Since the Gauss quadrature rule is exact for polynomials of degree up to  $2N_\eta - 1$  and the interpolating polynomial over  $N_\eta$  points has the degree  $N_\eta - 1$ , all the sums above will calculate the corresponding integrals exactly if  $3/2 - J_\beta + s - 1 - J_\alpha + N_\eta - 1 \leq 2N_\eta - 1$  or  $k + l \leq N_\eta - 1$  in terms of the integers  $k$  and  $l$ . This is why in the case of the 3D FENE model, we prefer to work with Jacobi polynomials with  $J_\alpha$  and  $J_\beta$  selected as described above, rather than with Legendre polynomials. We should recall the restrictions on the parameters  $J_\alpha, J_\beta > -1$  that give rise to the further restrictions on  $k$  and  $l$ :  $k < s$ ,  $l < 3/2$  i.e.  $l$  is 0 or 1.

## 4.2 Numerical results for simple flows

In our numerical experiments we have used the following parameters :  $s = 2$  for 2D FENE simulations and  $s = 2.5$ ,  $J_\alpha = J_\beta = 0.5$  for 3D FENE simulations. We have no rigorous justification for choosing those values; they have been found after some numerical experiments to give a good compromise between accuracy and stability.

### Shear flow

We first consider a homogeneous shear flow, for which the velocity field is given by  $(u_x, u_y) = (\dot{\gamma}y, 0)$  where  $\dot{\gamma}$  is the shear rate. In Fig. 4.1 we compare the steady-state values of the effective polymeric viscosity  $\eta_p(\dot{\gamma}) = \tau_{xy}/\dot{\gamma}$  computed using the 2D FENE algorithm on the mesh  $(N_F, N_R) = (15, 31)$  against the same quantity computed for 3D FENE dumbbells on the mesh  $(N_F, N_R) = (12, 24)$ . We see that the results for 2D and 3D dumbbells are close for non-dimensional shear rates  $\lambda\dot{\gamma}$  in the range  $(0, 10)$ . Moreover, the time-dependent behaviour is very similar in the same parameter range. We illustrate this in Fig. 4.2 by comparing 2D FENE and 3D FENE results for the evolution in time of the elastic extra-stress obtained at  $b = 100$  and  $\lambda\dot{\gamma} = 5$ . Since good agreement with the experimental data is reported in [43] only for  $\lambda\dot{\gamma} \approx 4$  or less, we suggest that the simplified 2D FENE model can be used to simulate planar flows of dilute polymeric solutions as well as the full 3D model.

We have observed severe stability restrictions at high shear rates, which are more pronounced for the 3D FENE simulations than for the 2D FENE ones. This is illustrated in Figs. 4.3 and 4.4, where the spectra of the discretized 2D FENE and 3D FENE FP operators (that is,  $\mathbf{L}_0 + \dot{\gamma}\mathbf{L}_2$ ) are plotted for three levels of discretization, the parameters of the model being set to  $b = 100$  and  $\lambda\dot{\gamma} = 10$ . We see that a large number of spurious eigenvalues with positive real parts is present in the 2D case for the meshes  $(N_F, N_R) = (10, 20)$  and  $(12, 24)$  but that the spurious eigenvalues disappear after refining the mesh to  $(N_F, N_R) = (14, 28)$ . In contrast, the spurious eigenvalues are present even with the finest mesh  $(12, 24)$  in the case of the 3D FENE model. Since the number of degrees of freedom in the representation of the pdf is  $N_R(N_F + 1)^2$  in this case, which is equal to 6300 for the finest mesh in Fig. 4.4, this can become a serious obstacle in using such a discretization in complex flow simulations. We hope that some filtering techniques can help to remove the spurious eigenfunctions, but this is yet to be verified.

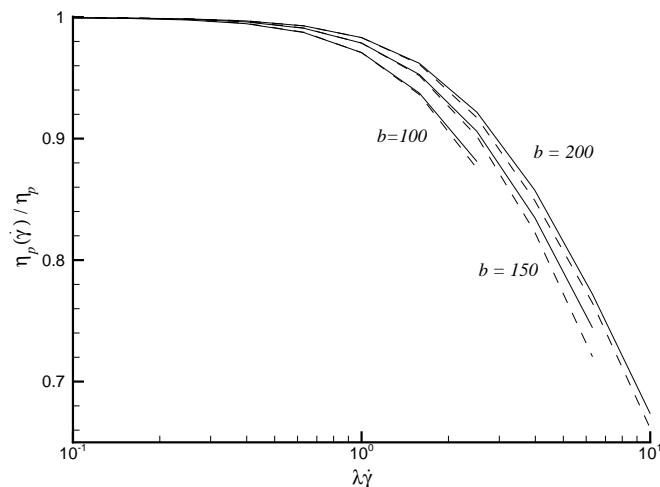


Figure 4.1: Steady-state polymeric viscosity for 2D (solid line) and 3D (dashed line) FENE models. The meshes are  $(N_F, N_R) = (15, 31)$  for the 2D FENE model and  $(N_F, N_R) = (12, 24)$  for the 3D FENE model.

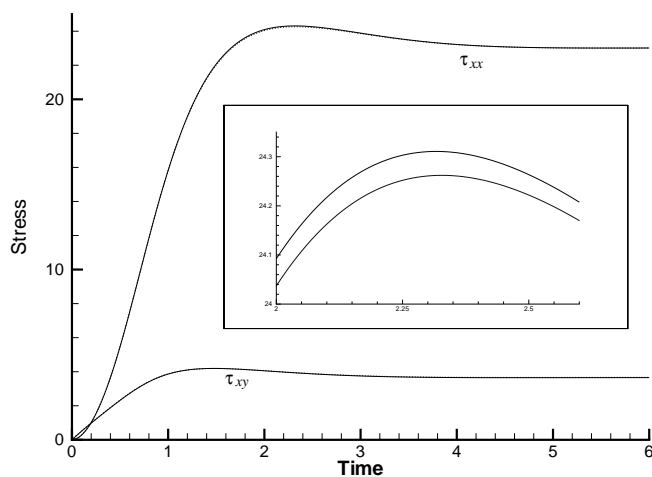


Figure 4.2: Stress vs. time; 2D (solid line) and 3D (dotted line) FENE models. The meshes are  $(N_F, N_R) = (15, 31)$  for the 2D FENE model and  $(N_F, N_R) = (12, 24)$  for the 3D FENE model.  $\Delta t = 0.01$ .

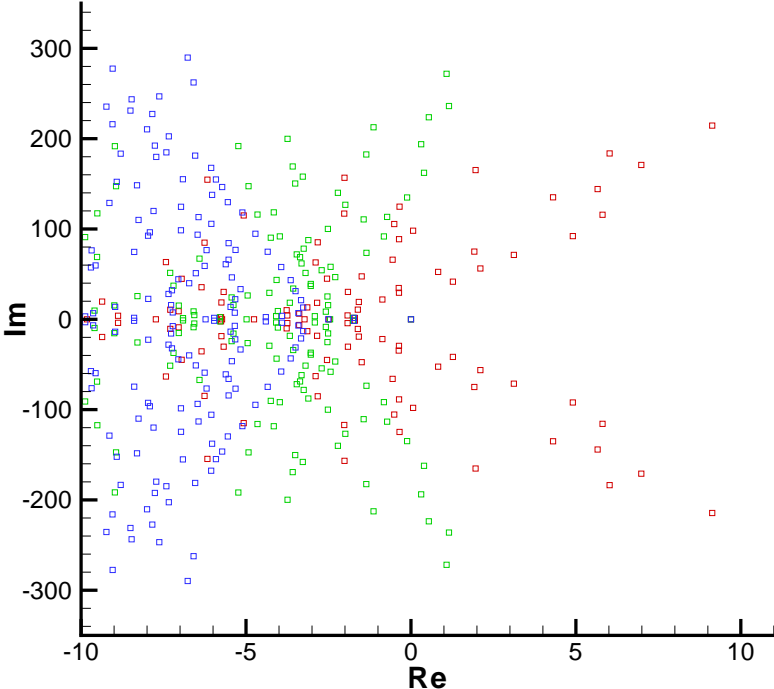


Figure 4.3: Spectrum of the discretized FP operator for the 2D FENE model at 3 levels of discretization: red  $(N_F, N_R) = (10, 20)$ , green  $(N_F, N_R) = (12, 24)$ , blue  $(N_F, N_R) = (14, 28)$ .

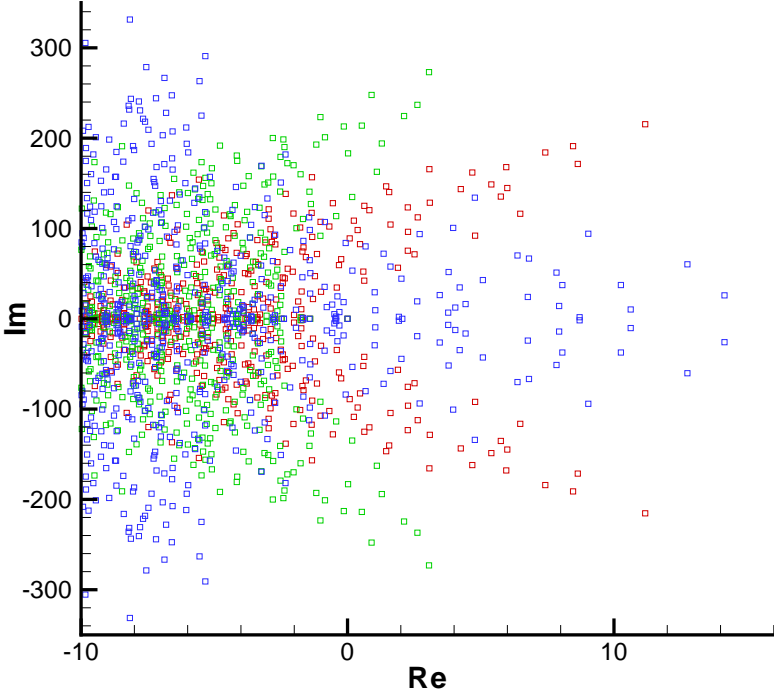


Figure 4.4: Spectrum of the discretized FP operator for the 3D FENE model at 3 levels of discretization: red  $(N_F, N_R) = (10, 20)$ , green  $(N_F, N_R) = (12, 24)$ , blue  $(N_F, N_R) = (14, 28)$ .

$N_R$	$N_F$	Computed	Relative error
11	5	9.37276961201	$3.7 \cdot 10^{-5}$
13	6	9.37240261618	$2.2 \cdot 10^{-6}$
15	7	9.37242377204	$1.1 \cdot 10^{-7}$
17	8	9.37242273550	$4.5 \cdot 10^{-9}$
19	9	9.37242277922	$1.6 \cdot 10^{-10}$
21	10	9.37242277768	$5.5 \cdot 10^{-12}$

Table 4.1: Numerical results for planar extensional flow at  $\dot{\varepsilon} = 1$  (the exact value of  $\tau_{xx}$  is 9.37242277773).

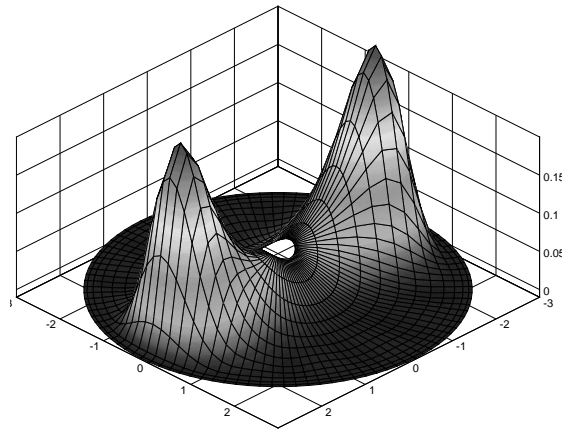


Figure 4.5: Plot of the pdf  $\psi$  for  $\dot{\varepsilon} = 1$  and  $(N_F, N_R) = (6, 13)$ .

$N_R$	$N_F$	Computed	Relative error
11	5	diverging	—
13	6	79.3936	0.35
21	10	119.819187	$2.0 \cdot 10^{-2}$
31	15	122.313126	$1.4 \cdot 10^{-4}$
41	20	122.295791	$2.1 \cdot 10^{-7}$

Table 4.2: Numerical results for planar extensional flow at  $\dot{\varepsilon} = 5$  (the exact value of  $\tau_{xx}$  is 122.295817)

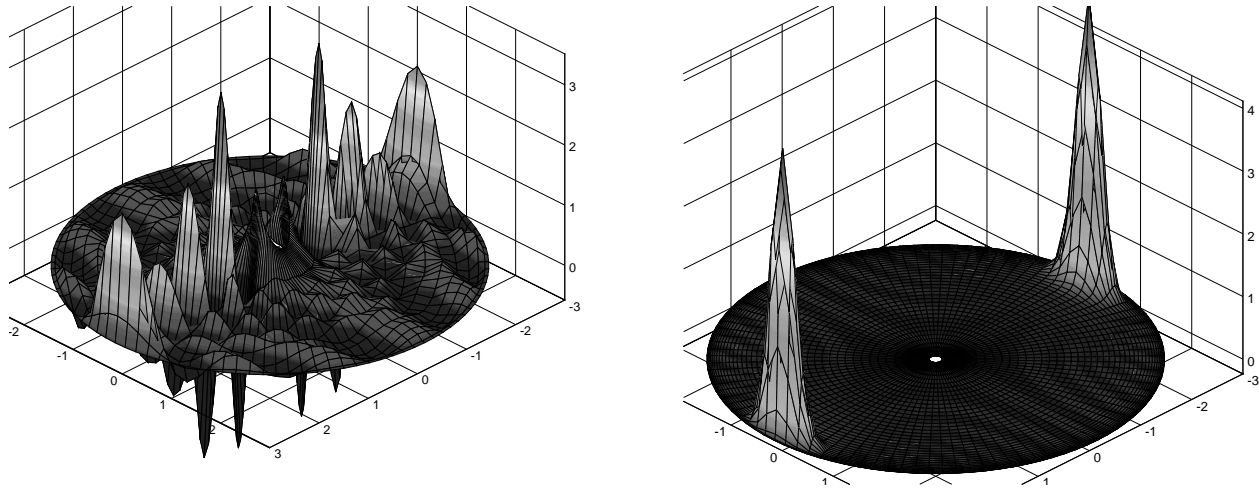


Figure 4.6: Plot of the pdf  $\psi$  for  $\dot{\varepsilon} = 5$  on two meshes: (a)  $(N_F, N_R) = (6, 13)$ ; (b)  $(N_F, N_R) = (20, 41)$ .

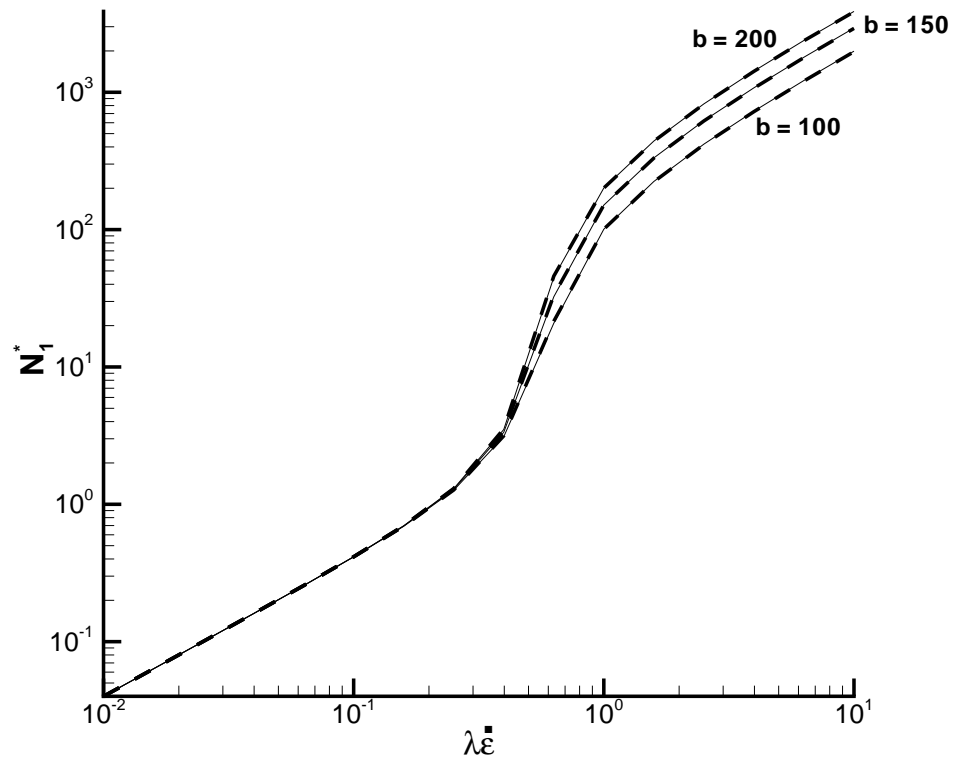


Figure 4.7: Normal stress difference in the extensional flow of 2D and 3D FENE models.

### Planar extensional flow

To study the convergence of our 2D FENE algorithm with mesh refinement, we consider a homogeneous planar extensional flow, for which the velocity gradient is given by (1.28). The analytical expression (1.30) of the steady-state pdf can be written in this case (see [18]) as

$$\psi = C \left(1 - \frac{|\mathbf{q}|^2}{b}\right)^{b/2} \exp(\lambda \dot{\varepsilon} \rho^2 \cos 2\varphi)$$

where  $C$  is some normalization constant.

We report the results of two computations for different values of the non-dimensional extension rate ( $\lambda \dot{\varepsilon} = 1$  and  $\lambda \dot{\varepsilon} = 5$ ) with the maximum extensibility parameter  $b = 10$ . Table 4.1 gives the computed values of the  $xx$ -component of the elastic extra-stress and the relative error for different resolutions in the case  $\dot{\varepsilon} = 1$ . We can see that the error is very small even for low resolutions. At this extension rate, the solution is very smooth (see Fig. 4.5, which represents the pdf for the computational mesh  $(N_F, N_R) = (6, 13)$ ) and only a few points are needed for our spectral method to properly capture the solution.

When the extension rate is increased up to  $\lambda \dot{\varepsilon} = 5$ , getting accurate numerical results requires much more refined meshes, as is shown in Table 4.2. This is because the exact solution at high extension rates possesses huge gradients which are very localized. Capturing such a solution requires highly refined meshes. Figure 4.6(a) shows the numerical oscillatory solution for a low level of discretization  $(N_F, N_R) = (6, 13)$  and Fig. 4.6(b) shows how the solution can be properly captured when the mesh is refined up to  $(N_F, N_R) = (20, 41)$ . It is clear from Fig. 4.6(b) that a stochastic simulation would outperform our FP-based algorithm at sufficiently large extension rates (or more generally at large velocity gradients) since the statistical variance in the solution is very small.

To compare the behaviour of the 2D FENE and 3D FENE models in steady-state extensional flow, we plot in Fig. 4.7 the non-dimensional normal stress difference  $N_1^* = (\tau_{xx} - \tau_{yy})\lambda/\eta_p$  computed using the exact solution (4.2) at three values of the maximum extensibility parameter and non-dimensional extension rates  $\lambda \dot{\varepsilon} \in (0, 10)$ . The difference between the two models is too small to be captured on such a graph. In fact, it is less than 1 per cent over the range of parameters presented in this figure.

## 4.3 Algorithms for complex flow simulations

We turn now to simulations of complex flows under local homogeneity assumption. We will give first some more details on the stochastic simulations (Brownian configuration fields (BCF) method) and then present two algorithms based on the FP equation.

### 4.3.1 Brownian configuration fields method for FENE dumbbells

The BCF method has been described in Section 3.1.2 for Hookean dumbbells, but in order to implement it for FENE dumbbells we need to introduce some small changes. Indeed, it would be prohibitively expensive to use the Brownian configuration field equations as they are written in (3.6) since this would require solving a large non-linear system at each time step. On the other hand, if we were to replace the implicit Euler method in (3.6) by an explicit Euler

method, we would have to use very small time steps. Moreover, it is preferable to treat the  $\mathbf{F}(\mathbf{q})$  term in an implicit way in order to prevent it from exceeding the maximum length  $\sqrt{b}$  (otherwise, a rejection technique should be used, see [9]). Therefore, we implement the BCF method using a time-splitting technique with implicit treatment at both stages of the splitting:

$$\frac{\tilde{\mathbf{q}}_m(t_i, \mathbf{x}) - \mathbf{q}_m(t_{i-1}, \mathbf{x})}{\Delta t} + \mathbf{u}(t_i, \mathbf{x}) \cdot \nabla \tilde{\mathbf{q}}_m(t_i, \mathbf{x}) = \mathbf{0}, \quad (4.45)$$

$$\frac{\mathbf{q}_m(t_i, \mathbf{x}) - \tilde{\mathbf{q}}_m(t_i, \mathbf{x})}{\Delta t} + \frac{1}{2\lambda} \mathbf{F}(\mathbf{q}_m(t_i, \mathbf{x})) = \kappa(t_i, \mathbf{x}) \tilde{\mathbf{q}}_m(t_i, \mathbf{x}) + \sqrt{\frac{1}{\lambda \Delta t}} \Phi_m(t_i). \quad (4.46)$$

The first equation should be solved using a numerical method appropriate for hyperbolic PDEs and (4.46) can be solved independently at every grid point. To see that this splitting prevents the norm of the vectors  $\mathbf{q}_m$  from exceeding  $\sqrt{b}$ , we rearrange (4.46) and use (1.21) to arrive at

$$\left( \frac{1}{\Delta t} + \frac{1}{2\lambda} \frac{1}{1 - \frac{|\mathbf{q}_m(t_i, \mathbf{x})|^2}{b}} \right) \mathbf{q}_m(t_i, \mathbf{x}) = \mathbf{s}_m(t_i, \mathbf{x}), \quad (4.47)$$

where

$$\mathbf{s}_m(t_i, \mathbf{x}) = \frac{\tilde{\mathbf{q}}_m(t_i, \mathbf{x})}{\Delta t} + \kappa(t_i, \mathbf{x}) \tilde{\mathbf{q}}_m(t_i, \mathbf{x}) + \sqrt{\frac{1}{\lambda \Delta t}} \Delta \mathbf{W}_m(t_i),$$

is a known vector since  $\tilde{\mathbf{q}}_m(t_i, \mathbf{x})$  has been computed from equation (4.45). We put  $s_m = |\mathbf{s}_m(t_i, \mathbf{x})|$  and  $q_m = |\mathbf{q}_m(t_i, \mathbf{x})|$  and derive from (4.47) the cubic polynomial equation for  $q_m$

$$q_m^3 - \Delta t s_m q_m^2 - b \left( \frac{\Delta t}{2\lambda} + 1 \right) q_m + \Delta t s_m b = 0. \quad (4.48)$$

This equation can be shown to possess one root that satisfies  $0 \leq q_m < \sqrt{b}$ . Having determined this root, the configuration vector  $\mathbf{q}_m(t_i, \mathbf{x})$  is simply

$$\mathbf{q}_m(t_i, \mathbf{x}) = \left( \frac{1}{\Delta t} + \frac{1}{2\lambda} \frac{1}{1 - \frac{q_m^2}{b}} \right)^{-1} \mathbf{s}_m(t_i, \mathbf{x}). \quad (4.49)$$

### 4.3.2 A “slow” FP solver

We recall that the FP equation takes the form (1.32) under the local homogeneity assumption, which differs formally from the FP equation for a homogeneous flow (4.1) only in that the partial derivative in time is replaced by the material derivative. The difficulty in a numerical simulation of (1.32) is that it has to be solved in a high dimensional space  $(t, \mathbf{x}, \mathbf{q})$ . We would like to solve (1.32) in an implicit manner in order to avoid severe restrictions on time steps. We introduce therefore a first-order time-splitting to decouple the computation in physical space  $\Omega$  from the computation in configuration space  $D = \{|\mathbf{q}|^2 < b\}$ . Using an implicit Euler method on each step of the splitting, combining it with the discretization in configuration space, which has been described for homogeneous flows in preceding sections, and coupling this with the solution of equations for velocity and pressure, we can write the following method to discretize (1.32) in the case of inertialess planar flows:

On the  $(n + 1)$ -st time step:

- Update velocity and pressure  $\mathbf{v}^n$  and  $p^n$  using a discretization of the Stokes system (1), (1.33) with  $\rho = 0$ , supplying on the right-hand side of the momentum equation the known approximation of the elastic extra-stress  $\boldsymbol{\tau}^n(\mathbf{x})$  at time  $t_n = n\Delta t$ .
- Perform a configuration step in updating the function  $\alpha$  which is related to the pdf  $\psi$  through (4.6) by calculating at each grid point  $\mathbf{x}$  of the physical domain  $\Omega$  the approximation  $\alpha_N^{n+1/2}(\mathbf{x})$ :

$$\alpha_N^{n+1/2}(\mathbf{x}) = (\mathbf{I} - \Delta t (\mathbf{L}_0 + \kappa_{11}(\mathbf{x})\mathbf{L}_1 + \kappa_{12}(\mathbf{x})\mathbf{L}_2 + \kappa_{21}(\mathbf{x})\mathbf{L}_3))^{-1} \alpha_N^n, \quad (4.50)$$

where the components of the velocity gradient  $\kappa_{kl} = \partial v_k^n / \partial x_l$  are calculated from the latest available velocity field at the grid point  $\mathbf{x}$ . The matrices  $\mathbf{L}_0 - \mathbf{L}_3$  are given by (4.15)-(4.18) for the 2D FENE model and by (4.41) and (4.42) for the 3D FENE model.

- Perform a configuration step in updating the function  $\alpha$  by solving the transport equation

$$\frac{\alpha^{n+1} - \alpha^{n+1/2}}{\Delta t} + \mathbf{v}^n \cdot \nabla \alpha^{n+1} = 0. \quad (4.51)$$

- Use  $\alpha^{n+1}$  to calculate the elastic extra-stress  $\boldsymbol{\tau}^{n+1}(\mathbf{x})$  at time  $t_{n+1}$  at each grid point  $\mathbf{x}$ .

The CPU-expensive part of this scheme is the solution of (4.50) rather than that of (4.51). This can be easily seen by noticing that implementing (4.50) results in a system of linear equations with the coefficients depending on the position in physical space and on time, while (4.51) is the same for all the components of  $\alpha$ . Therefore, a different linear system resulting from (4.50) should be solved at every grid point at each time step, which can lead to unacceptably long computing times. We call the procedure described above the slow FP solver.

### 4.3.3 A “fast” FP solver

Fortunately, the first step of the splitting (4.50)–(4.51) can be implemented in a much more efficient way. To construct this implementation we need to rewrite the homogeneous FP equation (4.1) in a slightly different form. We are going to present the derivation of this form in the case of the 3D FENE model, the 2D case being completely analogous.

We decompose the velocity gradient for a planar flow

$$\boldsymbol{\kappa} = \begin{pmatrix} \kappa_{11} & \kappa_{12} & 0 \\ \kappa_{21} & -\kappa_{11} & 0 \\ 0 & 0 & 0 \end{pmatrix}.$$

into symmetric and antisymmetric parts and rotate the coordinates to the principal axes of the symmetric part. We thus have

$$\boldsymbol{\kappa} = k\pi_\phi \mathbf{I}_1 \boldsymbol{\pi}_{-\phi} + k_a \mathbf{I}_a \quad (4.52)$$

where  $\mathbf{I}_a = \mathbf{I}_2 - \mathbf{I}_3$ ,  $\mathbf{I}_1$ ,  $\mathbf{I}_2$  and  $\mathbf{I}_3$  are defined by (4.37), (4.38) and  $\boldsymbol{\pi}_\phi$  is the matrix of the rotation by angle  $\phi$  in 12-plane

$$\boldsymbol{\pi}_\phi = \begin{pmatrix} \cos \phi & -\sin \phi & 0 \\ \sin \phi & \cos \phi & 0 \\ 0 & 0 & 1 \end{pmatrix}.$$



The scalars  $k$ ,  $\phi$  and  $k_a$  appearing in (4.52) are calculated from  $\boldsymbol{\kappa}$  via

$$k(\boldsymbol{\kappa}) = \sqrt{\kappa_{11}^2 + (\kappa_{12} + \kappa_{21})^2/4}, \quad (4.53)$$

$$\sin 2\phi = \frac{\kappa_{12} + \kappa_{21}}{2k}, \quad \cos 2\phi = \frac{\kappa_{11}}{k}, \quad (4.54)$$

and

$$k_a(\boldsymbol{\kappa}) = \frac{\kappa_{12} - \kappa_{21}}{2}. \quad (4.55)$$

Let  $\Pi_\phi$  be the operator defined for an arbitrary function on the unit sphere  $\Phi(\varphi, \theta)$  by

$$\Pi_\phi \Phi(\varphi, \theta) = \Phi(\varphi + \phi, \theta), \quad (4.56)$$

i.e. the result of the rotation of coordinates  $\boldsymbol{\pi}_{-\phi}$ . Substituting (4.52) into (4.33) and using the notation (4.56) and the fact that  $\mathcal{L}(\mathbf{I}_a) = -\partial/\partial\varphi$  (see Appendix A.1) and  $\mathbf{I}_a : \mathbf{u}\mathbf{u} = 0$ , we arrive at the desired form of the FP equation

$$\frac{D\alpha}{Dt} = k\Pi_{-\phi}L_1\Pi_\phi\alpha + k_a\frac{\partial\alpha}{\partial\varphi} + L_0\alpha \quad (4.57)$$

We see now that (4.50) is the first order approximation in time of the following equation

$$\frac{\partial\alpha}{\partial t} = k^n\Pi_{-\phi^n}L_1\Pi_{\phi^n}\alpha + k_a^n\frac{\partial\alpha}{\partial\theta} + L_0\alpha, \quad (4.58)$$

which is solved from  $t = t_n$  to  $t = t_{n+1}$ ,  $\alpha^{n+1/2}$  and  $\alpha^n$  being set to  $\alpha|_{t=t_{n+1}}$  and  $\alpha|_{t=t_n}$  respectively. The upper indices  $n$  have been added to  $k$ ,  $\varphi$  and  $k_a$  defined by (4.53)-(4.55) to emphasize the fact that those quantities are computed for the tensor  $\boldsymbol{\kappa}^n$  that is updated at time  $t = t_n$ . In what follows, we denote explicitly the dependence of  $\alpha$  on  $t$  and  $\theta$  alone but it should be kept in mind that  $\alpha$  is a function of  $\boldsymbol{\eta}$  as well and that all the quantities ( $\alpha$ ,  $k$ ,  $\varphi$  and  $k_a$ ) depend on the position in physical space as a parameter.

We set  $t_{n+1/2} = t_n + \Delta t/2$  and note (using a Taylor expansion) that

$$\alpha(t_{n+1/2}, \theta) = \frac{1}{2} \left( \alpha(t_{n+1}, \theta - \frac{1}{2}k_a^n\Delta t) + \alpha(t_n, \theta + \frac{1}{2}k_a^n\Delta t) \right) + O(\Delta t^2), \quad (4.59)$$

$$\frac{\partial\alpha}{\partial\theta}(t_{n+1/2}, \theta) = \frac{1}{2} \left( \frac{\partial\alpha}{\partial\theta}(t_{n+1}, \theta - \frac{1}{2}k_a^n\Delta t) + \frac{\partial\alpha}{\partial\theta}(t_n, \theta + \frac{1}{2}k_a^n\Delta t) \right) + O(\Delta t^2), \quad (4.60)$$

and

$$\frac{\partial\alpha}{\partial t}(t_{n+1/2}, \theta) - k_a^n\frac{\partial\alpha}{\partial\theta}(t_{n+1/2}, \theta) = \frac{\alpha(t_{n+1}, \theta - \frac{1}{2}k_a^n\Delta t) - \alpha(t_n, \theta + \frac{1}{2}k_a^n\Delta t)}{\Delta t} + O(\Delta t^2). \quad (4.61)$$

We now evaluate (4.58) at  $t = t_{n+1/2}$ , use (4.59)-(4.61), neglect the terms of order  $O(\Delta t^2)$  and denote similarly to (4.50)  $\alpha^{n+1/2}(\theta) = \alpha(t_{n+1}, \theta)$  and  $\alpha^n = \alpha(t_n, \theta)$  to get

$$\frac{\alpha^{n+1/2}(\theta - \frac{1}{2}k_a^n\Delta t) - \alpha^n(\theta + \frac{1}{2}k_a^n\Delta t)}{\Delta t} = RHS \quad (4.62)$$

where

$$\begin{aligned} RHS &= \frac{1}{2}k^n \Pi_{-\phi^n} L_1 \Pi_{\phi^n} \left( \alpha^{n+1/2} (\theta - \frac{1}{2}k_a^n \Delta t) + \alpha^n (\theta + \frac{1}{2}k_a^n \Delta t) \right) + \\ &\quad \frac{1}{2}L_0 \left( \alpha^{n+1/2} (\theta - \frac{1}{2}k_a^n \Delta t) + \alpha^n (\theta + \frac{1}{2}k_a^n \Delta t) \right). \end{aligned} \quad (4.63)$$

We have thus obtained a time discretization of (4.58) of Crank-Nicolson type. Of course, this does not mean that the global scheme formed by equations (4.62) and (4.51) will be second order accurate in time (a three-stage Strang splitting would be necessary for that). However, (4.62) has an important advantage over (4.50) since it can be implemented in an efficient way as will be explained in the remaining part of this subsection.

Applying  $\Pi_{\phi^n}$  to both sides of equation (4.62), noting that  $\Pi_{\phi^n}$  commutes with  $L_0$  and  $L_1$ , and introducing the discretizations  $\mathbf{L}_0$  and  $\mathbf{L}_1$  we get the discretized equations:

$$\frac{\Pi_{\phi^n - \frac{1}{2}k_a^n \Delta t} \alpha^{n+1/2} - \Pi_{\phi^n + \frac{1}{2}k_a^n \Delta t} \alpha^n}{\Delta t} = \frac{1}{2} \mathbf{L}_0 \left( \Pi_{\phi^n - \frac{1}{2}k_a^n \Delta t} \alpha^{n+1/2} + \Pi_{\phi^n + \frac{1}{2}k_a^n \Delta t} \alpha^n \right) + \frac{k^n}{2} \mathbf{L}_1 \left( \Pi_{\phi^n - \frac{1}{2}k_a^n \Delta t} \alpha^{n+1/2} + \Pi_{\phi^n + \frac{1}{2}k_a^n \Delta t} \alpha^n \right), \quad (4.64)$$

where we have denoted the unknowns discretized in configuration space by the same symbols as the non-discretized ones. By rearranging (4.64) we get

$$\left( \frac{1}{\Delta t} \mathbf{I} - \frac{1}{2} \mathbf{M}_0 - \frac{k^n}{2} \mathbf{L}_1 \right) \Pi_{\phi^n - \frac{1}{2}k_a^n \Delta t} \alpha^{n+1/2} = \left( \frac{1}{\Delta t} \mathbf{I} + \frac{1}{2} \mathbf{L}_0 + \frac{k^n}{2} \mathbf{L}_1 \right) \Pi_{\phi^n + \frac{1}{2}k_a^n \Delta t} \alpha^n,$$

or

$$\alpha^{n+1/2} = \Pi_{\frac{1}{2}k_a^n \Delta t - \phi^n} (\mathbf{I} - k^n \mathbf{L})^{-1} (\mathbf{R} + k^n \mathbf{M}) \Pi_{\phi^n + \frac{1}{2}k_a^n \Delta t} \alpha^n, \quad (4.65)$$

with the matrices  $\mathbf{M}$  and  $\mathbf{R}$  defined by

$$\begin{aligned} \mathbf{M} &= \frac{1}{2} \left( \frac{1}{\Delta t} \mathbf{I} - \frac{1}{2} \mathbf{L}_0 \right)^{-1} \mathbf{L}_1, \\ \mathbf{R} &= \left( \frac{1}{\Delta t} \mathbf{I} - \frac{1}{2} \mathbf{L}_0 \right)^{-1} \left( \frac{1}{\Delta t} \mathbf{I} + \frac{1}{2} \mathbf{L}_0 \right). \end{aligned} \quad (4.66)$$

Finally, let's call  $\mathbf{D}$  the diagonal matrix formed with the eigenvalues of  $\mathbf{M}$ . Then, there exists an invertible matrix  $\mathbf{P}$  (with columns formed by the eigenvectors of  $\mathbf{M}$ ) such that  $\mathbf{M} = \mathbf{PDP}^{-1}$ . Thus, we can express (4.65) in the form

$$\alpha^{n+1/2} = \Pi_{\frac{1}{2}k_a^n \Delta t - \phi^n} \mathbf{P} (\mathbf{I} - k^n \mathbf{D})^{-1} \mathbf{P}^{-1} (\mathbf{R} + k^n \mathbf{M}) \Pi_{\phi^n + \frac{1}{2}k_a^n \Delta t} \alpha^n. \quad (4.67)$$

In the above equation, the matrices  $\mathbf{D}$ ,  $\mathbf{P}$ ,  $\mathbf{P}^{-1}$ ,  $\mathbf{M}$  and  $\mathbf{R}$  do not change in space and time, so they can be computed once at a preprocessing step. Since  $(\mathbf{I} - k^n \mathbf{D})$  is a diagonal matrix it can be inverted and multiplied by a vector at a cost of  $O(N)$  where  $N$  is the dimension of the discrete configuration space for  $\alpha$ . Clearly, the rotation operations are inexpensive as well. Indeed, the rotation operator (4.56) is implemented by using the expression

$$\Pi_{\phi} \Phi_{il}(\theta) = \cos 2l\theta \Phi_{il}(\theta) - (-1)^n \sin 2l\theta \Phi_{il}(\theta). \quad (4.68)$$

Therefore, for a given grid point, the major cost for determining the solution of the pdf comes from the matrix-vector multiplication with  $\mathbf{M}$ ,  $\mathbf{R}$ ,  $\mathbf{P}^{-1}$  and  $\mathbf{P}$ .

The reason for using (4.67) rather than (4.50) as the first step in time splitting of the FP equation (4.3) should now be clear. Indeed, in the right-hand side of (4.50) we had three coefficients that were varying with a grid point (namely  $\kappa_{11}$ ,  $\kappa_{12}$  and  $\kappa_{21}$ ) whereas, after the transformations and rotations, in (4.67) we have only one coefficient varying with a grid point (namely  $k^n$ ). This enables us to use the diagonalization technique to solve (4.67) with the help of the formula (4.67) at a cost  $O(N^2)$  instead of a cost  $O(N^3)$  that the solution of (4.50) would have required .

Let us recapitulate the method. On the  $(n + 1)$ -st time step, we perform the following:

- Update velocity and pressure  $\mathbf{v}^n$  and  $p^n$  using a discretization of the Stokes system (1), (1.33) with  $\rho = 0$  supplying at the right-hand side of the momentum equation the known approximation of the elastic extra-stress  $\boldsymbol{\tau}^n(\mathbf{x})$  at time  $t_n = n\Delta t$ .
- Perform a configuration step in updating the function  $\alpha$  by calculating  $\alpha_N^{n+1/2}(\mathbf{x})$  at each grid point  $\mathbf{x}$  of the physical domain  $\Omega$  using the equation (4.67) where the components of the velocity gradient  $\kappa_{kl} = \partial v_k^n / \partial x_l$  are calculated from the latest available velocity field at the grid point  $\mathbf{x}$ .
- Perform a configuration step in updating the function  $\alpha$  by solving the transport equation (4.51).
- Use  $\alpha^{n+1}$  to calculate the elastic extra-stress  $\boldsymbol{\tau}^{n+1}(\mathbf{x})$  at time  $t_{n+1}$  at each grid point  $\mathbf{x}$ .

The method described in this section will be called the fast FP solver.

## 4.4 Numerical results for the flow past a confined cylinder

We test the algorithms described above on the benchmark problem of steady planar viscoelastic flow around a cylinder confined in a channel. We choose the aspect ratio  $\Lambda = R/H = 1/2$ , where  $H$  is the half-width of the channel and  $R$  is the radius of the cylinder (see Fig. 2.8). The ratio of the solvent viscosity  $\eta_s$  to the total zero shear-rate viscosity  $\eta = (\eta_p + \eta_s)$  was taken equal to 0.59 as is usually done by other authors. A global Weissenberg number for this problem may be defined by  $We = \lambda \bar{U}/R$ , where  $\bar{U}$  is the average velocity of the fluid in the channel at entry.

Periodic boundary conditions are used at the inflow and outflow of the channel for all quantities except the pressure which is periodic up to a linear function. The total length of the channel is 40 times the cylinder radius so that we can assume that the interaction of the cylinder with the other cylinders in the periodic array is negligible. We impose no-slip conditions on the cylinder surface and on the channel wall. In order to save in computational cost, we assume that the flow has  $y = 0$  as a plane of symmetry so that only half of the domain needs to be considered. The problem is solved by dividing the flow domain into 30 conforming spectral elements and polynomial degrees ranging from  $N = 8$  to  $N = 10$  are used in the two spatial directions. We use an SUPG spectral element-by-element method as described in Section 2.4 to solve the hyperbolic equations (4.45) and (4.51). The time step  $\Delta t$  is chosen

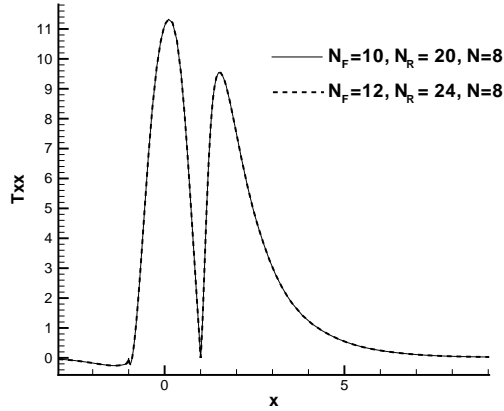


Figure 4.8:  $xx$  component of the elastic extra-stress along the axis of symmetry and on the cylinder surface for  $We = 1.2$  and two levels of discretization in configuration space.

equal to 0.01. For the deterministic simulations based on the FP equation the iterations are stopped when the following convergence criterion is fulfilled for all collocation points  $\mathbf{x} \in \Omega$  :

$$\frac{|\mathbf{u}^{i+1}(\mathbf{x}) - \mathbf{u}^i(\mathbf{x})|}{\Delta t} \leq 10^{-4}. \quad (4.69)$$

It would be impossible to satisfy the same criterion with the stochastic simulations because of the presence of the random noise. The stochastic simulations are arbitrarily stopped instead at  $t = 7$ .

The most popular quantity used for the comparison of numerical results is the drag factor  $F^*$  defined by (3.35). However, as noted in numerous papers ([6, 32, 47, 48], for example), such a quantity is not a good indicator of the quality or accuracy of the solution. Therefore, we will not only give the value of the drag factor in this section but we will also plot the tensile elastic normal stress in the wake of the cylinder, this being the most difficult flow region in which to resolve the solution convincingly.

#### 4.4.1 Numerical results for the 2D FENE model

##### Convergence with mesh refinement

We first demonstrate convergence with mesh refinement in both configuration and physical spaces for our highest Weissenberg number  $We = 1.2$  using the fast FP solve, as summarized at p. 87. The parameter  $b$  in (1.21) is taken equal to 20. We plot the  $xx$  component of the elastic extra-stress along the axis of symmetry ( $|x/R| > 1$ ) and on the cylinder surface ( $|x/R| \leq 1$ ) for the following two cases:

1. The polynomial degree for the representation of the variables in physical space is kept at  $N = 8$  and the resolution in configuration space is increased from  $(N_F, N_R) = (10, 20)$  to  $(N_F, N_R) = (12, 24)$ .
2. The resolution in configuration space is set at  $(N_F, N_R) = (10, 20)$  and the polynomial degree in physical space is increased from  $N = 8$  to  $N = 10$ .

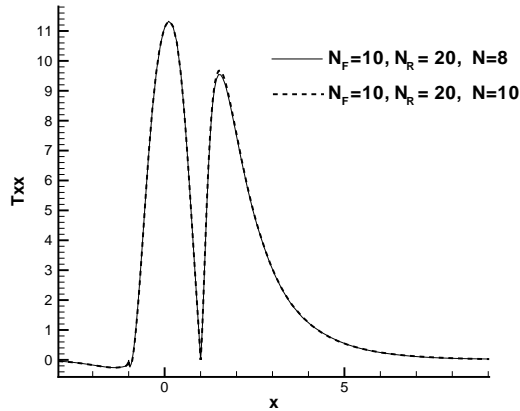


Figure 4.9:  $xx$  component of the elastic extra-stress along the axis of symmetry and on the cylinder surface for  $We = 1.2$  and two levels of discretization in physical space.

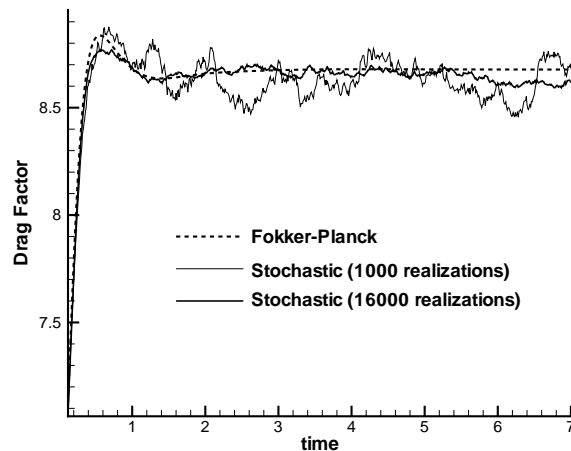


Figure 4.10: Comparison of the drag factor for stochastic and deterministic simulations at  $We = 0.8$ .

Figures 4.8 and 4.9 show that convergence with mesh refinement is achieved in both cases (1) and (2), respectively. Therefore, in the sequel we can restrict our numerical investigations by taking  $(N_F, N_R, N) = (10, 20, 8)$ .

### Comparison between deterministic simulations and stochastic simulations

We now compare the deterministic simulations with their stochastic counterparts in terms of accuracy and CPU cost. We first compare the drag factor as a function of time for the stochastic simulation when the number of pseudo-random realizations  $M$  is set to 1000 and then 16000. The results are shown in Fig. 4.10 for a Weissenberg number  $We = 0.8$  and clearly, the stochastic solution converges towards the solution of the deterministic approach as we increase the number of realizations. However for stochastic simulations, the rate of convergence is very low (typically  $O(1/\sqrt{M})$ ). Note that for the two approaches, we have used the same resolution in physical space ( $N = 8$ ). The same experiment is carried out in Fig. 4.11 but for a higher Weissenberg number ( $We = 1.2$ ) and the conclusions remains unchanged.

Figures 4.12 and 4.13 show the contour plots of the three components of the elastic extra-stress ( $\tau_{yy}$ ,  $\tau_{xy}$  and  $\tau_{xx}$  from top to bottom) for the stochastic simulation (with 16000 realizations) and the FP simulation, respectively, at a Weissenberg number  $We = 1.2$ . We can see

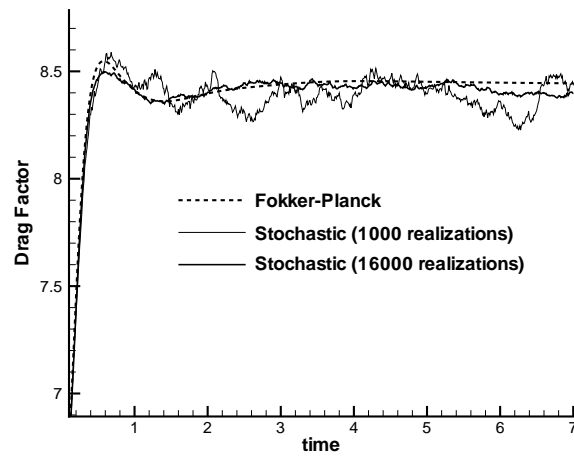


Figure 4.11: Comparison of the drag factor for stochastic and deterministic simulations at  $We = 1.2$ .

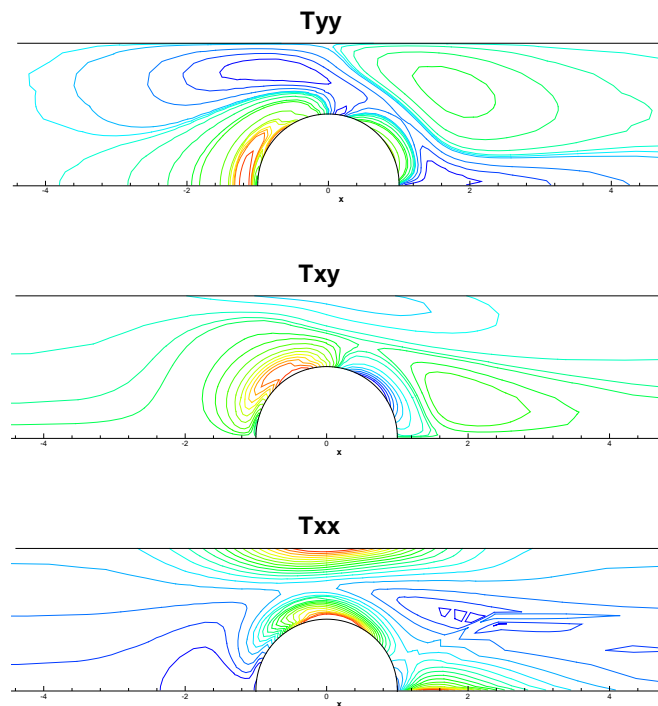


Figure 4.12: Contour plot of the three components of the elastic extra-stress. Stochastic simulation.

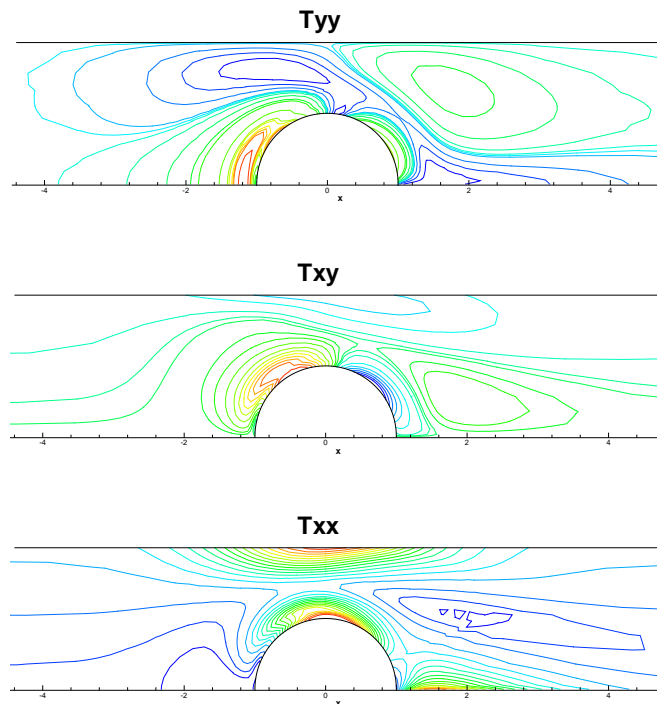


Figure 4.13: Contour plot of the three components of the elastic extra-stress. Deterministic simulation.

Table 4.3: Comparison of the CPU cost per time step for the deterministic approach and for the stochastic approach.

FP (fast solver)	FP (slow solver)	BCF-1000	BCF-16000
3.3	198.0	18.0	285.0

that for the FP case, the three plots are reasonably smooth whereas for the stochastic case, wiggles appear in the plot of the  $xx$ -component of the elastic extra-stress<sup>1</sup>.

We now turn our attention to the comparison of the CPU cost of the different approaches. Table 4.3 shows the average CPU time per time step for the solution of the FP equation by the fast solver summarized on p. 87 with  $(N_F, N_R, N) = (10, 20, 8)$ , for the slow solver summarized on p. 83 with the same  $N_F, N_R$  and  $N$  and for the stochastic simulations using 1000 and 16000 realizations. Results are reported in seconds and the test was made on a PC with a Pentium IV 1.5GHz processor. We see that the fast solver produces a speedup of a factor 60 compared to the slow solver. The deterministic simulations using the fast solver are about 5.5 times faster than the stochastic simulation with a low number of realizations and up to 86 times faster for the case with 16000 realizations. Because of the noise in the stochastic solution, in both cases, the deterministic approach is always more accurate.

Lastly we report in Table 4.4 the values of the drag factor on the cylinder as a function of the Weissenberg number for the deterministic simulation. To the author's knowledge, these values have not been available in the literature so far. The solutions of stochastic simulations

<sup>1</sup>The most important wiggles actually lie along a spectral element boundary in the wake region. Unfortunately, we have no explanation for this phenomenon.

Table 4.4: Drag factor  $F^*$  computed on uniform meshes ( $N = 8, N_f = 10, N_r = 12$ ) for different Weissenberg numbers. Fokker-Planck simulation.

We	0.6	0.7	0.8	0.9	1.0	1.1	1.2
<b>Drag Factor</b>	8.8941	8.7729	8.6776	8.6008	8.5384	8.4865	8.4429

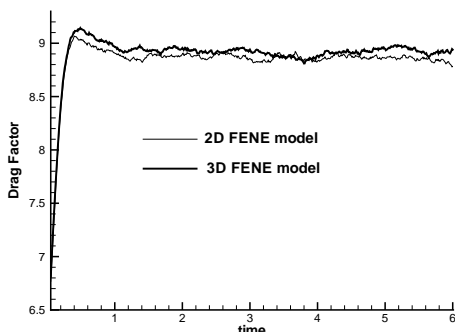


Figure 4.14: Drag factor as a function of time for the 2D and 3D FENE models with a stochastic simulation using 16000 realizations at  $We = 0.6$ .

are too noisy (see Figs. 4.10 and 4.11) to give an accurate average value of the drag factor.

#### 4.4.2 Numerical results for the 3D FENE model

For all the simulations involving the 3D FENE model, the maximum extensibility  $b$  is chosen equal to 10. The stochastic simulations are arbitrarily stopped instead at  $t = 6$ . We take  $N_u = 6$  and  $N_\eta = 12$  for the discretization in configuration space (see formula (4.39)).

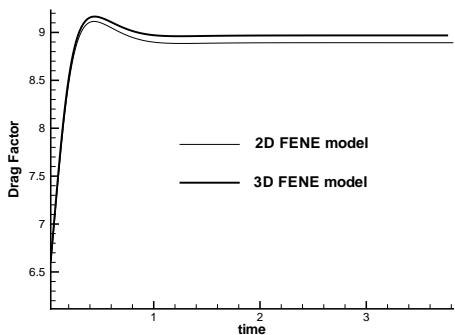


Figure 4.15: Drag factor as a function of time for the 2D and 3D FENE models using the Fokker-Planck equation at  $We = 0.6$ .



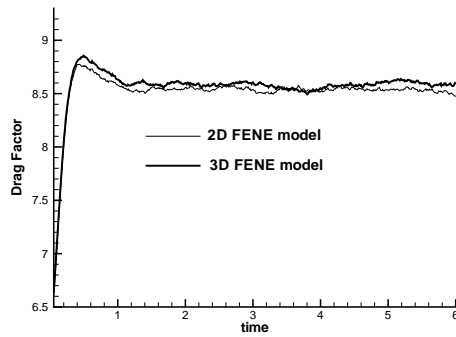


Figure 4.16: Drag factor as a function of time for the 2D and 3D FENE models with a stochastic simulation using 16000 realizations at  $We = 0.9$ .

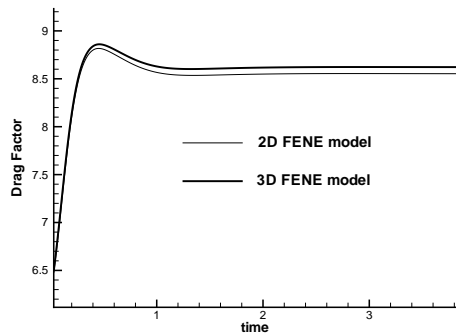


Figure 4.17: Drag factor as a function of time for the 2D and 3D FENE models using the Fokker-Planck equation at  $We = 0.9$ .

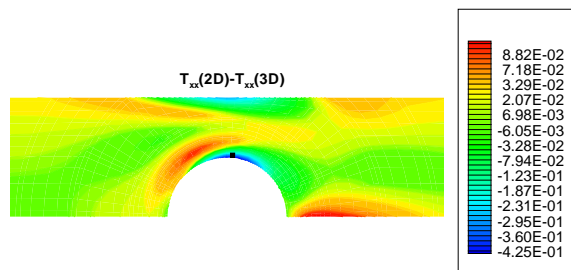


Figure 4.18: Difference of the  $xx$  component of the elastic extra-stress between the 2D and the 3D FENE model at  $We = 0.6$ .

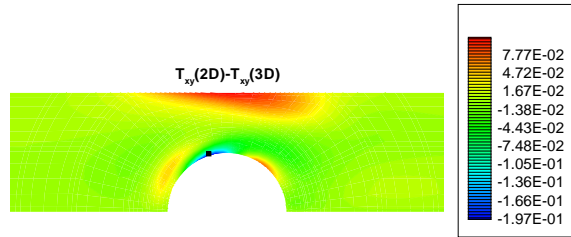


Figure 4.19: Difference of the  $xy$  component of the elastic extra-stress between the 2D and the 3D FENE model at  $We = 0.6$ .

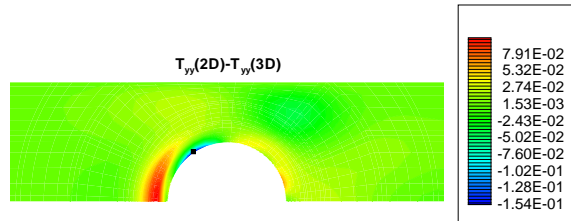


Figure 4.20: Difference of the  $yy$  component of the elastic extra-stress between the 2D and the 3D FENE model at  $We = 0.6$ .

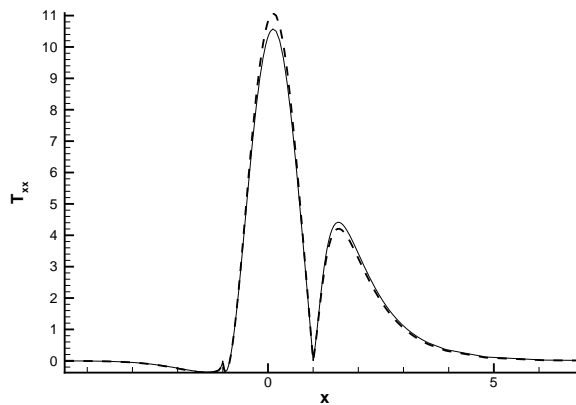


Figure 4.21: The  $xx$  component of the elastic extra-stress for the 2D (solid line) and the 3D (dashed line) FENE models at  $We = 0.9$ .

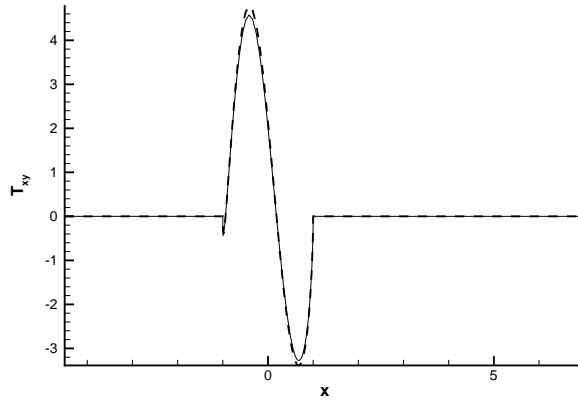


Figure 4.22: The  $xy$  component of the elastic extra-stress for the 2D (solid line) and the 3D (dashed line) FENE models at  $We = 0.9$ .

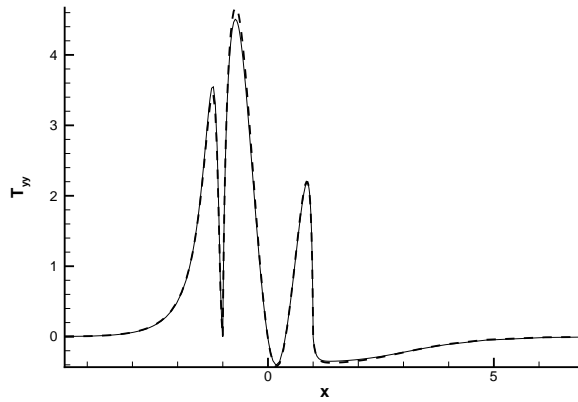


Figure 4.23: The  $yy$  component of the elastic extra-stress for the 2D (solid line) and the 3D (dashed line) FENE models at  $We = 0.9$ .

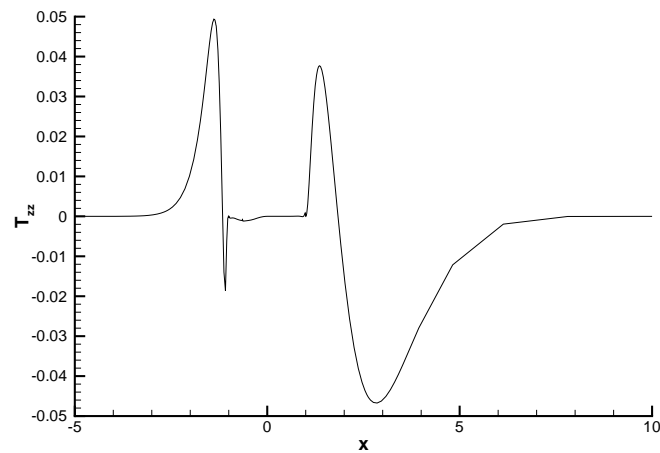


Figure 4.24: The  $zz$  component of the elastic extra-stress for the 3D FENE models at  $We = 0.9$ .

### Comparison between the stochastic approach and the deterministic approach

Figure 4.14 shows the value of the drag factor as a function of time for the stochastic simulation using 16000 realizations for the 2D and the 3D FENE models at a Weissenberg number of 0.6. For the stochastic simulation in Fig. 4.14, the magnitude of the noise is such that it is difficult to conclude which model (2D or 3D) gives the higher drag factor. On the other hand, the FP simulation is deterministic and for the same problem and same parameters, the results shown in Fig. 4.15 clearly indicate that the drag factor of the 3D FENE model is higher than the drag factor for the 2D FENE model. The same kind of results are reproduced in Fig. 4.16 and 4.17, but for a higher Weissenberg number ( $We = 0.9$ ) and the conclusions remain the same. Not only is the FP approach more accurate than its stochastic counterpart, but it is also more efficient in terms of CPU cost. This can be seen from Table 4.5 which gives the average CPU time per time step in seconds for a computation performed on a Pentium IV 1.5GHz processor. Solving the FP equation is about 1.8 times faster than solving the stochastic equation with 1000 realizations. Note that, as can be expected, the stochastic approach with 16000 realizations is about 16 times slower than the same computation with only 1000 samples.

Table 4.5: Comparison of the CPU cost per time step for the deterministic approach and for the stochastic approach (3D FENE model).

Fokker-Planck	Stochastic-1000	Stochastic-16000
7.1	12.6	202.0

### Comparison between 2D FENE and 3D FENE models

Based on the drag factor (see Fig. 4.15 or Fig. 4.17), it seems that the differences between the 2D FENE model and the 3D FENE model are small. Such a finding is confirmed in Figs. 4.18–4.20 which show respectively the differences in the  $xx$ ,  $xy$  and  $yy$  components of the elastic extra-stress between the 2D and 3D FENE models at  $We = 0.6$ . The small black square indicates the location of maximum absolute difference. As can be seen from the values of the contour levels, the differences between the two models are small for all components over all of the domain. In all cases, the maximum difference is located on the cylinder surface, where we have strong shear flow. Results at a higher Weissenberg number of 0.9 are presented in Figs. 4.21–4.24 where the components of the stress are plotted only on the cylinder surface and on the axis of the symmetry. We see from Figs. 4.21–4.23 that the differences between  $xx$ ,  $xy$  and  $yy$  components of the extra-stress computed by the 2D and the 3D FENE models are again small. Moreover, Fig. 4.24 indicates that the  $zz$ -component of the extra-stress, which is obviously absent from the 2D FENE model, remains very small in the 3D FENE model.

Such an investigation would not have been possible using a stochastic approach since the difference between the two models would have been of the order of magnitude of the noise. The fact that we can use the 2D FENE model instead of the 3D model without major changes in the solution is important from a computational point of view, since solving the FP equation in a 2D configuration space is one order of magnitude cheaper than solving it in a 3D configuration space. On the other hand, for the stochastic approach, going from 2D to 3D is not so critical since it only requires one extra equation to be solved for  $q_z$ .

### Maximum Weissenberg number achievable

The maximum Weissenberg number that could be achieved for the 3D FENE model using the FP equation was  $We = 1.1$ . However, convergence with mesh refinement (both in physical space and in configuration space) was only possible up to  $We = 0.9$  and this is why in the previous section we only present results up to this Weissenberg number. The difficulty, as we increase the Weissenberg number, comes from the fact that the flow may be strong in some areas of the domain, leading to a pdf with extremely localized features, which are very difficult to capture numerically. In contrast, the limiting Weissenberg numbers using the stochastic approach were found to be around  $We = 4.0$ . This situation is quite different from what we have observed in our 2D FENE simulations. The maximum Weissenberg number achievable in the latter case was about 1.2 both for stochastic and deterministic approaches.

## 4.5 A Fokker-Planck-based numerical method for modelling strongly non-homogeneous flows of dilute polymeric solutions

This section differs considerably from the previous sections of this chapter as well as from Chapter 3, since we here abandon the assumption of a linear variation in the configuration density function (cdf) over the length scale of a dumbbell. To simplify the numerical method, we keep still the analogous assumption concerning the solvent velocity field. Nevertheless, such an approach allows us to take into account at least qualitatively phenomena near the boundary and in strongly non-homogeneous regions. We choose the FENE dumbbell model<sup>2</sup> in its two-dimensional version. As is evidenced in the preceding sections, assumption of two-dimensional dumbbells does not corrupt significantly the results. Following [16] and [116], the boundary conditions for the cdf are derived from the assumption of elastic collisions between the beads of the dumbbells and the wall. We will present a deterministic numerical method based on the FP equation for a Poiseuille flow in a narrow channel using this model. Results collapse to those of the usual locally homogeneous flow FENE model for polymer dimensions sufficiently small compared to the channel wall separation distance.

Among other formulations for non-homogeneous flows of polymer solutions we may cite the body-tensor continuum formalism of Öttinger [98], the two-fluid Hamiltonian model of Mavrantzas and Beris [1, 90] and the kinetic theory of Bhave et al. [15] that has been recently corrected and expanded upon by Curtiss and Bird [34]. The theory of Bhave et al. starts from the FP equation for Hookean dumbbells. Then, a number of approximations are used to obtain constitutive equations for the polymer number density and the stress tensor. In an illuminating paper dating from 1994, Beris and Mavrantzas [12] performed a detailed comparison of the three approaches mentioned above. Although the body-tensor continuum formalism of Öttinger [98] and the two-fluid Hamiltonian model of Mavrantzas and Beris [1, 90] predicted the same equation for the polymer number density, the kinetic theory of Bhave et al. [15] led to the addition of an extra term in this equation. Beris and Mavrantzas identified the difficulty with the approach of Bhave et al. as being due to their retention only of the linear terms in a

---

<sup>2</sup>Whereas we admit that it would be desirable from a micro-mechanical point of view to work with full FENE chains within distances of several polymer lengths from a solid boundary, the present results should nevertheless be considered to have qualitative value.

Taylor series expansion of the cdf in their expression for the polymer species concentration. The damaging consequences of this inconsistent approximation could be avoided by rederiving the mass flux equation using the force balance equation and by using a Taylor expansion for the cdf up to and including second-order terms. The resulting equation for the polymer number density was now the same as in the analyses of Öttinger and Mavrantzas and Beris. Neglect of second and higher-order terms in the velocity gradient could be shown to lead to the same stress evolution equation under all three formulations. Note that no explicit equation for the polymer number density is required in this chapter since we work throughout with the cdf  $\psi$ . The polymer number density may be calculated, however, at any time by integrating  $\psi$  over configuration space (see (1.17)).

Previous simulations with non-homogeneous flow models have included the use of a two-fluid Hamiltonian [90] in investigations of instabilities in cone-and-plate and parallel plate rheometers [91] and of stress gradient-induced migration effects in the viscoelastic Taylor-Couette problem [1]. Rectilinear shear flows of Hookean dumbbells have been studied by, amongst others, Bhave et al. [15] using a finite difference method. Biller and Petruccione [16] used a Brownian dynamics simulation for simple shear flow of dumbbells having both a Hookean spring force law and a simple nonlinear modification to this force law, obtained from the FENE spring force law for small values of dumbbell extension  $R$ . The same technique was used by the authors to investigate non-homogeneous pressure-driven flows of the same dumbbell solutions [116]. The present work applies a new method (see Sections 4.5.1 and 4.5.2) to the planar Poiseuille flow of dumbbells having a FENE force law without the same restriction on the magnitude of the extension  $R$ . The results therefore generalize what has gone before.

### 4.5.1 Boundary conditions and weak problem statement

Let us recall the notation of Section 1.1.1 that will also be used here.  $\psi^{12}$  stands for the cdf in terms of the position of two beads  $\mathbf{r}_1$ ,  $\mathbf{r}_2$  and  $\psi^c$  stands for the cdf in terms of the position vector of the centre of mass  $\mathbf{x}$  and the end-to-end vector  $\mathbf{q}$ . We assume that the boundary  $\Gamma$  of the flow domain  $\Omega$  is an impenetrable wall. Following Biller and Petruccione [16, 116], a no flux condition  $\ll \dot{\mathbf{r}}_i \gg \cdot \mathbf{n} = 0$  on  $\Gamma$  with normal vector  $\mathbf{n}$  is applied to the averaged bead velocity  $\ll \dot{\mathbf{r}}_i \gg$  ( $i = 1, 2$ ). Assuming that  $\mathbf{v}(\mathbf{r}_i) \cdot \mathbf{n} = 0$ , Eqns. (1.8)- (1.10) lead to

$$\left( kT \frac{\partial \psi^{12}}{\partial \mathbf{r}_i} + \mathbf{F}(\mathbf{r}_i - \mathbf{r}_j) \psi \right) \cdot \mathbf{n} = 0 \text{ for } \mathbf{r}_i \in \Gamma. \quad (4.70)$$

To take into account the fact that the dumbbells cannot be extended to the maximum length  $R_{\max}$ , we also impose a homogeneous Dirichlet condition on  $\psi$ :

$$\psi = 0, \text{ for } |\mathbf{r}_1 - \mathbf{r}_2| = R_{\max}. \quad (4.71)$$

Conditions (4.70) and (4.71) enable us to write down the weak statement of the FP problem

(1.11) as

$$\begin{aligned}
\int \int_{\mathbf{r}_1, \mathbf{r}_2 \in \Omega} \frac{\partial \psi^{12}}{\partial t} \varphi \, d\mathbf{r}_1 d\mathbf{r}_2 &= \int \int_{\mathbf{r}_1, \mathbf{r}_2 \in \Omega} \left( \mathbf{v}(\mathbf{r}_1) \cdot \frac{\partial \varphi}{\partial \mathbf{r}_1} + \mathbf{v}(\mathbf{r}_2) \cdot \frac{\partial \varphi}{\partial \mathbf{r}_2} \right) \psi^{12} \, d\mathbf{r}_1 d\mathbf{r}_2 \\
&\quad - \frac{1}{\zeta} \int \int_{\mathbf{r}_1, \mathbf{r}_2 \in \Omega} \left( kT \frac{\partial \psi^{12}}{\partial \mathbf{r}_1} + \mathbf{F}(\mathbf{r}_1 - \mathbf{r}_2) \psi \right) \cdot \frac{\partial \varphi}{\partial \mathbf{r}_1} \, d\mathbf{r}_1 d\mathbf{r}_2 \\
&\quad - \frac{1}{\zeta} \int \int_{\mathbf{r}_1, \mathbf{r}_2 \in \Omega} \left( kT \frac{\partial \psi^{12}}{\partial \mathbf{r}_2} + \mathbf{F}(\mathbf{r}_2 - \mathbf{r}_1) \psi \right) \cdot \frac{\partial \varphi}{\partial \mathbf{r}_2} \, d\mathbf{r}_1 d\mathbf{r}_2, \quad (4.72)
\end{aligned}$$

where  $\varphi = \varphi(\mathbf{r}_1, \mathbf{r}_2)$  is a suitable test function such that  $\varphi = 0$  for  $|\mathbf{r}_1 - \mathbf{r}_2| = R_{\max}$ .

Although formally correct, the weak form (4.72) is difficult to discretize efficiently since proper account should be taken of the localization of  $\psi$  in the subdomain of small  $|\mathbf{r}_1 - \mathbf{r}_2|$ . We prefer therefore to work with  $\mathbf{x}$  and  $\mathbf{q}$  since this allows us to obviate the latter problem. In general, however, even simple flow geometries can become rather complicated in these variables. Indeed, the vector  $\mathbf{q}$  ‘‘lives’’ in configuration spaces dependent on  $\mathbf{x}$ :

$$D(\mathbf{x}) = \{\mathbf{q} : |\mathbf{q}| < R_{\max}\} \cap \{\mathbf{q} : \mathbf{x} \pm \mathbf{q}/2 \in \Omega\}.$$

Analogously, the domain for  $\mathbf{x}$  depends on  $\mathbf{q}$ .

In recasting the weak statement of the FP problem (4.72) into one in terms of  $\mathbf{x}$  and  $\mathbf{q}$  we reintroduce the assumption of a linear variation in the solvent velocity over the length scale of a dumbbell, i.e.  $(\mathbf{v}(\mathbf{r}_1) + \mathbf{v}(\mathbf{r}_2))/2 \approx \mathbf{v}(\mathbf{x})$  and  $\mathbf{v}(\mathbf{r}_2) - \mathbf{v}(\mathbf{r}_1) \approx \nabla \mathbf{v}(\mathbf{x}) \mathbf{q}$ . Although it is of course possible to simply rewrite all derivatives and inner products appearing in (4.72) directly in terms of  $\mathbf{x}$  and  $\mathbf{q}$  this does not yield an equation which will be useful to us in the sequel. Instead, we begin by observing that the boundary condition (4.70) may be re-expressed in the following form:

$$\left[ \frac{\partial \psi^c}{\partial \mathbf{x}} \pm 2 \left( \frac{\partial \psi^c}{\partial \mathbf{q}} + \frac{1}{kT} \mathbf{F}(\mathbf{q}) \psi^c \right) \right] \cdot \mathbf{n} = 0, \text{ for } \mathbf{x} \pm \frac{\mathbf{q}}{2} \in \Gamma. \quad (4.73)$$

Then, multiplying (1.12) throughout by a test function  $\varphi^c = \varphi^c(\mathbf{x}, \mathbf{q})$ , integrating over all  $(\mathbf{x}, \mathbf{q})$ -space such that  $\mathbf{x} \pm \mathbf{q}/2 \in \Omega$  and using integration by parts in configuration space, we have

$$\begin{aligned}
&\int_{\Omega} \int_{D(\mathbf{x})} \frac{D\psi^c}{Dt} \varphi^c \, d\mathbf{q} d\mathbf{x} + \int_{\Omega} \int_{D(\mathbf{x})} \nabla \mathbf{v}(\mathbf{x}) \mathbf{q} \cdot \frac{\partial \psi^c}{\partial \mathbf{q}} \varphi^c \, d\mathbf{q} d\mathbf{x} \\
&= \int_{\Omega} \int_{\Gamma^{\pm}(\mathbf{x})} \left[ \left( \frac{2kT}{\zeta} \frac{\partial \psi^c}{\partial \mathbf{q}} + \frac{2}{\zeta} \mathbf{F}(\mathbf{q}) \psi^c \right) \cdot \mathbf{n} \varphi^c \right] \, dS d\mathbf{x} \\
&\quad - \int_{\Omega} \int_{D(\mathbf{x})} \left( \frac{2kT}{\zeta} \frac{\partial \psi^c}{\partial \mathbf{q}} + \frac{2}{\zeta} \mathbf{F}(\mathbf{q}) \psi^c \right) \cdot \frac{\partial \varphi^c}{\partial \mathbf{q}} \, d\mathbf{q} d\mathbf{x} \\
&\quad + \frac{kT}{2\zeta} \int_{\Omega} \int_{D(\mathbf{x})} \frac{\partial^2 \psi^c}{\partial \mathbf{r}^2} \varphi^c \, d\mathbf{q} d\mathbf{x}, \quad (4.74)
\end{aligned}$$

where  $\Gamma^{\pm}(\mathbf{x})$  are the parts of the boundary of  $D(\mathbf{x})$ , on which  $\mathbf{x} \pm \mathbf{q}/2 \in \Gamma$ . In (4.74)  $\Gamma(\mathbf{x})$  denotes the boundary of  $D(\mathbf{x})$  and we have used the configuration boundary condition  $\psi^c =$

$\varphi^c = 0$  for  $|\mathbf{q}| = R_{\max}$ . Appealing to the boundary condition (4.73) we see that the weak form (4.74) may be further expressed as

$$\begin{aligned}
& \int_{\Omega} \int_{D(\mathbf{x})} \frac{D\psi^c}{Dt} \varphi^c d\mathbf{q}d\mathbf{x} + \int_{\Omega} \int_{D(\mathbf{x})} \nabla_{\mathbf{v}(\mathbf{x})} \mathbf{q} \cdot \frac{\partial \psi^c}{\partial \mathbf{q}} \varphi^c d\mathbf{q}d\mathbf{x} \\
&= \int_{\Omega} \int_{\Gamma^{\pm}(\mathbf{x})} \left[ \mp \frac{kT}{\zeta} \frac{\partial \psi^c}{\partial \mathbf{x}} \cdot \mathbf{n} \varphi^c \right] dS d\mathbf{x} \\
&- \int_{\Omega} \int_{D(\mathbf{x})} \left( \frac{2kT}{\zeta} \frac{\partial \psi^c}{\partial \mathbf{q}} + \frac{2}{\zeta} \mathbf{F}(\mathbf{q}) \psi^c \right) \cdot \frac{\partial \varphi^c}{\partial \mathbf{q}} d\mathbf{q}d\mathbf{x} \\
&+ \frac{kT}{2\zeta} \int_{\Omega} \int_{D(\mathbf{x})} \frac{\partial^2 \psi^c}{\partial \mathbf{r}^2} \varphi^c d\mathbf{q}d\mathbf{x}. \tag{4.75}
\end{aligned}$$

### 4.5.2 Discretization and solution algorithm

We are now going to describe a discretization of the weak form (4.75) applying it to non-homogeneous start-up plane Poiseuille flow of a 2D FENE fluid. The flow geometry is shown in Fig. 4.25(a) and consists of two plates  $y = \pm d$  between which a dilute polymer solution flows under a constant pressure gradient. We assume that stress and velocity depend only on  $y$ , so that the dependence on the position vector  $\mathbf{x}$  will be denoted in the sequel of the section by dependence on  $y$ .

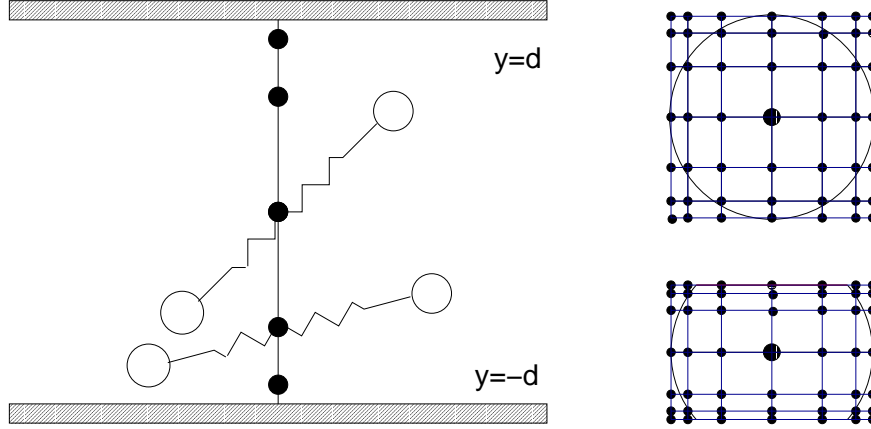


Figure 4.25: (a) Flow between two parallel walls and Gauss collocation grid, (b) configuration spaces  $D(y)$  for two different values  $y_k$  of  $y$  with superposed Gauss-Lobatto grids

As in the case of homogeneous and locally homogeneous flow simulations we introduce a new variable  $\alpha$  which is related to  $\psi$  by (cf. (4.6))

$$\psi^c(t, y, \mathbf{q}) = \psi_s(\mathbf{q}) \alpha(t, y, \mathbf{q}), \tag{4.76}$$

where  $\psi_s(\mathbf{q}) = \left(1 - \frac{R^2}{R_{\max}^2}\right)^s$  for some  $s \geq 1$ , and rewrite the problem (4.75) in terms of  $\alpha$ . We will discretize the weak problem (4.75) by collocating in physical space and employing a Galerkin spectral method in configuration space. What we do is formally equivalent to introducing a test function

$$\varphi^c = \varphi_k^c = \delta(y - y_k) \psi_s^{-1}(\mathbf{q}) \sigma_k(\mathbf{q}), \tag{4.77}$$



where  $\delta$  is a delta function,  $y_k$  is the position vector of the  $k$ -th point in some collocation grid covering the interior physical flow domain  $(-d, d)$  and  $\sigma_k$  an (as yet) arbitrary function whose support is  $D(y_k)$ . In each  $D(y_k)$ , a suitably defined set  $\Sigma_k$  of Lagrangian interpolants on a Gauss-Lobatto-Legendre (GLL) grid adapted to  $D(y_k)$  will be used for the test and trial functions in configuration space.

Allowing  $\Delta t$  to denote a time step and  $\alpha_k^n \in \Sigma_k$  an approximation to  $\alpha(n\Delta t, y_k, \mathbf{q})$ , where  $\alpha$  has been introduced in (4.76), we may use an Euler method for (4.75) with an implicit treatment of the operators in configuration space and an explicit treatment for those in physical space:

$$\begin{aligned} & \left( \frac{\alpha_k^{n+1} - \alpha_k^n}{\Delta t}, \sigma_k \right)_{D(y_k)} + A_k(\alpha_k^{n+1}, \sigma_k) \\ &= -\frac{kT}{\zeta} \left( n_y \left( \frac{\partial \alpha}{\partial y} \right)_k^n, \sigma_k \right)_{\Gamma(y_k)} + \frac{kT}{2\zeta} \left( \left( \frac{\partial^2 \alpha}{\partial y^2} \right)_k^n, \sigma_k \right)_{D(y_k)}, \quad \forall \sigma_k \in \Sigma_k, \end{aligned} \quad (4.78)$$

where  $(\cdot, \cdot)_{D(y_k)}$  denotes the  $L^2$  inner product over  $D(y_k)$ ,  $n_y = \text{sgn}(y)$  and

$$\begin{aligned} A_k(\alpha, \sigma) &= \left( \frac{2kT}{\zeta} \frac{\partial}{\partial \mathbf{q}} (\psi_s \alpha) + \frac{2}{\zeta} \mathbf{F}(\mathbf{q}) \psi_s \alpha, \frac{\partial}{\partial \mathbf{q}} (\psi_s^{-1} \sigma) \right)_{D(y_k)} \\ &+ \frac{\partial v_x}{\partial y}(y_k) \left( R_y \frac{\partial}{\partial R_x} (\psi_s \alpha), \psi_s^{-1} \sigma \right)_{D(y_k)}. \end{aligned} \quad (4.79)$$

where  $(\cdot)_k^n$  denotes a suitable approximation to the quantity in parentheses at  $t = n\Delta t$  and  $y = y_k$ . A Gauss-Lobatto quadrature formula is to be used in this paper for the evaluation of the integrals over  $D(y_k)$ . The computation of the partial derivatives of  $\alpha$  in physical space appearing on the right-hand side of (4.78) is normally performed by taking a weighted sum of physical nodal values of  $\alpha$ . Therefore a double sum - for the quadrature rule and the difference formulae required for the physical derivatives - is needed and care must be taken to ensure that each term in the double sum makes sense i.e. no attempt is made to evaluate a nodal value  $\alpha_p^n$  (say) of  $\alpha$  at a quadrature point in configuration space which is outside  $D(y_p)$ .

### Approximation of derivatives in physical space

Since the most interesting phenomena are near the boundaries  $y = \pm d$ , we choose the collocation points to be the Gauss-Legendre (GL) points  $y_k$  ( $k = 1, \dots, N_{GL}$ ) (for some choice of the parameter  $N_{GL}$ ) mapped onto the interval  $(-d, d)$ . Note that this set of collocation points does not include the end points  $\pm d$  since the cdf  $\psi^c(y, \mathbf{q}, t)$  has no meaning for  $y$  lying on the boundary (configuration space has zero two-dimensional measure there). Fig. 4.25(b) illustrates the configuration spaces  $D(y)$  for two different choices of  $y$ . We are now going to describe the approximation of partial derivatives in  $y$  contained in the scheme (4.78).

Using a first-order approximation for the derivative  $\frac{\partial \psi}{\partial y}$  in the boundary integral, we obtain from (4.78)

$$\begin{aligned} & \left( \frac{\alpha_k^{n+1} - \alpha_k^n}{\Delta t}, \sigma_k \right)_{D(y_k)} + A_k(\alpha_k^{n+1}, \sigma_k) \\ &= \frac{kT}{\zeta} \left( \frac{\alpha_{k+j}^n - \alpha_k^n}{h_k^+}, \sigma_k \right)_{\Gamma(y_k)} + \frac{kT}{2\zeta} \left( \left( \frac{\partial^2 \alpha}{\partial y^2} \right)_k^n, \sigma_k \right)_{D(y_k)}, \end{aligned} \quad (4.80)$$

where  $j$  is  $-n_{y_k}$  so that  $y_{k+j} \in (-|y_k|, |y_k|)$  and  $h_k^+ = |y_{k+j} - y_k|$ . In what follows below  $h_k^-$  will denote the step size  $|y_{k-j} - y_k|$ .

Equation (4.80) is the scheme we shall use for our simulations.  $\Lambda\psi_k^n$  needs still to be specified. This discrete operator in physical space depends upon the point of configuration space where it is applied. Indeed, if  $y_{k-j}$  is defined and  $\mathbf{q} \in D(y_{k-j})$ , then we can use the standard central difference approximation:

$$\left(\frac{\partial^2 \alpha}{\partial y^2}\right)_k^n(\mathbf{q}) = \frac{2}{h_k^+ + h_k^-} \left( \frac{\alpha_{k+j}^n(\mathbf{q}) - \alpha_k^n(\mathbf{q})}{h_k^+} + \frac{\alpha_{k-j}^n(\mathbf{q}) - \alpha_k^n(\mathbf{q})}{h_k^-} \right).$$

Otherwise,  $\alpha_{k-j}^n(\mathbf{q})$  is not defined and we construct instead a first-order approximation for  $\frac{\partial^2 \alpha}{\partial y^2}(y_k, \mathbf{q}, t_n)$  using the boundary condition (4.70).

Using the notation

$$\Psi = \psi_s^{-1} \left( \frac{1}{kT} F_y(\mathbf{q}) \psi_s \alpha + \frac{\partial(\psi_s \alpha)}{\partial R_y} \right) \text{sgn}(R_y),$$

the boundary condition (4.70) can be rewritten as

$$\frac{\partial \alpha}{\partial y} n_y = -2\Psi. \quad (4.81)$$

In this situation, the point  $y_b$ , such that  $y_b + R_y/2$  or  $y_b - R_y/2$  is on the boundary, lies in the interval between  $y_k$  and  $y_{k-j}$ . Let  $\delta = |y_b - y_k|$ ,  $\delta < h$ . Using the Taylor expansion we can write

$$\frac{\partial \alpha}{\partial y}(t_n, y_b, \mathbf{q}) = \frac{\partial \alpha}{\partial y}(t_n, y_k, \mathbf{q}) + n_{y_b} \delta \frac{\partial^2 \alpha}{\partial y^2}(t_n, y_k, \mathbf{q}) + O(h^2).$$

Denoting the value of  $\Psi$  at time  $t_n$  and point  $y_k$  by  $\Psi_k^n(\mathbf{q})$ , we can also write

$$\Psi(t_n, y_b, \mathbf{q}) = \Psi_k^n - \delta \frac{\Psi_{k+j}^n - \Psi_k^n}{h_k^+} + O(h^2).$$

Applying the boundary condition (4.81) at point  $y_b$  and using the last two formulas, we get

$$n_{y_b} \frac{\partial \alpha}{\partial y}(t_n, y_k, \mathbf{q}) + \delta \frac{\partial^2 \alpha}{\partial y^2}(t_n, y_k, \mathbf{q}) = -2\Psi_k^n + 2\delta \frac{\Psi_{k+j}^n - \Psi_k^n}{h_k^+} + O(h^2). \quad (4.82)$$

From a Taylor expansion, we have

$$\alpha_{k+j}^n = \alpha_k^n - n_{y_b} h_k^+ \frac{\partial \alpha}{\partial y}(t_n, y_k, \mathbf{q}) + \frac{(h_k^+)^2}{2} \frac{\partial^2 \alpha}{\partial y^2}(t_n, y_k, \mathbf{q}) + O(h^3),$$

which in combination with (4.82) gives

$$\alpha_{k+j}^n = \alpha_k^n + 2h_k^+ \Psi_k^n - 2\delta(\Psi_{k+j}^n - \Psi_k^n) + h_k^+ \left( \frac{h_k^+}{2} + \delta \right) \frac{\partial^2 \alpha}{\partial y^2}(t_n, y_k, \mathbf{q}) + O(h^3).$$

We see now that a first order approximation for  $\frac{\partial^2 \alpha}{\partial y^2}(y_k, \mathbf{q}, t_n)$  can be defined as

$$\left(\frac{\partial^2 \alpha}{\partial y^2}\right)_k^n(\mathbf{q}) = \frac{\alpha_{k+j}^n - \alpha_k^n - 2h_k^+ \Psi_k^n + 2\delta(\Psi_{k+j}^n - \Psi_k^n)}{h_k^+(\delta + h_k^+/2)}.$$

*Remark:* Although only first-order discretizations in physical space as described above have been used for the numerical results to be presented in Section 4.5.3 this is for the sake of illustration and simplicity only. Extension to second- and higher-order approximations to the first and second derivatives of  $\alpha$  with respect to  $y$  are entirely straightforward.

### Discretization in configuration space

For each  $y_k$  the corresponding configuration space is the intersection of the disc  $R < \sqrt{b}$  and the rectangle  $(R_x, R_y) \in (-\sqrt{b}, \sqrt{b}) \times (-d_k, d_k)$  where  $d_k = 2(d - |y_k|)$ . We introduce in this rectangle the GLL points  $(R_x^{k,i}, R_y^{k,j})$ ,  $i = 1, \dots, N_x^k$ ,  $j = 1, \dots, N_y^k$ , and then expand  $\alpha$  in terms of a tensorized basis consisting of Lagrange interpolating polynomials based upon these points. That is, we write

$$\alpha_k^n(\mathbf{q}) = \sum_{i=1}^{N_x^k} \sum_{j=1}^{N_y^k} \widehat{\alpha}_{ijk}^n H_i^k(R_x) H_j^k(R_y), \quad (4.83)$$

where the coefficients  $\widehat{\alpha}_{ijk}^n$  are set to zero for polynomials corresponding to grid points outside the disc, i.e. such that  $(R_x^{k,i})^2 + (R_y^{k,j})^2 \geq b$ . In other words, the discrete space  $\Sigma_k$  to which both trial and test functions in configuration space belong, is defined to consist of polynomials  $H_i^k(R_x) H_j^k(R_y)$  with  $i, j$  such that  $(R_x^{k,i})^2 + (R_y^{k,j})^2 < b$ . For the results presented in Section 4.5.3 we have chosen for simplicity the number of points  $N_x^k$  and  $N_y^k$  in the two directions equal to some constant  $N_{GLL}$  (say), independent of  $k$ .

We recall that the parameter  $s$  was set equal to 2 in our simulations of homogeneous and locally homogeneous flows of a 2D FENE fluid and that  $\alpha$  was only required to be bounded on  $R = \sqrt{b}$  there. However, in the present approach  $\alpha$  approximated by (4.83) is already approximately zero at  $R = \sqrt{b}$  so that the parameter  $s$  may be set equal to unity here.

We now give attention to explaining how the configuration step for a given  $y = y_k$  may be performed efficiently. The main idea follows that of Section 4.3.3 but in the present case is considerably simplified since there is only one non-zero component of  $\nabla \mathbf{v}$ . Denoting the solution velocity vector by  $\mathbf{v} = (v_x(y), 0)$  and gathering the coefficients  $\widehat{\alpha}_{ijk}^{n+1}$  of (4.83) into a vector  $\widehat{\boldsymbol{\alpha}}_k^{n+1}$ , the configuration step may be written in matrix-vector form for any given  $k$  as

$$\frac{\widehat{\boldsymbol{\alpha}}_k^{n+1} - \widehat{\boldsymbol{\alpha}}_k^n}{\Delta t} + \frac{\partial v_x}{\partial y} \mathbf{A} \widehat{\boldsymbol{\alpha}}_k^{n+1} + \mathbf{B} \widehat{\boldsymbol{\alpha}}_k^{n+1} = \boldsymbol{\beta}_k^n, \quad (4.84)$$

where  $\boldsymbol{\beta}_k^n$  is a vector known from the previous time step. Gathering terms together we may write (4.84) in the form

$$\left( (\mathbf{I} + \mathbf{B}\Delta t) + \Delta t \frac{\partial v_x}{\partial y} \mathbf{A} \right) \widehat{\boldsymbol{\alpha}}_k^{n+1} = \Delta t \boldsymbol{\beta}_k^n + \widehat{\boldsymbol{\alpha}}_k^n. \quad (4.85)$$

Since the matrix multiplying  $\widehat{\boldsymbol{\alpha}}_k^{n+1}$  on the left-hand side of (4.85) varies both with  $y$  and time and is non-trivial, computing its inverse could be expensive and moreover will have to be done for each real collocation point  $y_k$  and at each time step. As a first step towards a more efficient approach we write  $\widehat{\boldsymbol{\alpha}}_k^{n+1}$  in terms of  $\widehat{\boldsymbol{\alpha}}_k^n$  as

$$\widehat{\boldsymbol{\alpha}}_k^{n+1} = \left( (\mathbf{I} + \mathbf{B}\Delta t) \left[ \mathbf{I} + \Delta t \frac{\partial v_x}{\partial y} (\mathbf{I} + \mathbf{B}\Delta t)^{-1} \mathbf{A} \right] \right)^{-1} (\Delta t \boldsymbol{\beta}_k^n + \widehat{\boldsymbol{\alpha}}_k^n). \quad (4.86)$$

Now suppose that the matrix  $(\mathbf{I} + \mathbf{B}\Delta t)^{-1} \mathbf{A}$  is diagonalizable. Then there exists a matrix  $\mathbf{P}$  and a diagonal matrix  $\mathbf{D}$  (neither being dependent on  $t$ ) such that  $(\mathbf{I} + \mathbf{B}\Delta t)^{-1} \mathbf{A} = \mathbf{P} \mathbf{D} \mathbf{P}^{-1}$  and so

$$\widehat{\boldsymbol{\alpha}}_k^{n+1} = \mathbf{P} \left( \mathbf{I} + \Delta t \frac{\partial v_x}{\partial y} \mathbf{D} \right)^{-1} \mathbf{P}^{-1} (\mathbf{I} + \mathbf{B}\Delta t)^{-1} (\Delta t \boldsymbol{\beta}_k^n + \widehat{\boldsymbol{\alpha}}_k^n). \quad (4.87)$$

Now, although the matrix  $\left(\mathbf{I} + \Delta t \frac{\partial v_x}{\partial y} \mathbf{D}\right)$  depends upon  $y$  and  $t$ , its inversion is very cheap. All other matrices appearing on the right-hand side of (4.87) need only be computed for each collocation point  $y_k$  in real space once at the first time step.

### Computation of the polymer density $n$ and elastic stress $\sigma^C$

Direct computation of  $\sigma^C$  by a discrete variant of (1.15) would involve the interpolations of  $\alpha$  between different configuration spaces  $D(y_k)$ . We found in practice that better accuracy and stability could be achieved by an alternative way of computation of  $\sigma^C$  that does not involve such interpolations.

Instead of (1.15) we use its weak form:

$$\begin{aligned} & \int_{-d}^d \sigma^C(y, t) H(y) dy \\ &= \int_{-d}^d \int_R \int_{s=0}^1 \mathbf{qF}(\mathbf{q}) \psi^c(y + (s - 1/2)R_y, \mathbf{q}, t) H(y) ds d\mathbf{q} dy \\ &= \int_{-d}^d \int_R \mathbf{qF}(\mathbf{q}) \psi^c(y, \mathbf{q}, t) \left( \int_{s=0}^1 H(y - (s - 1/2)R_y) ds \right) d\mathbf{q} dy, \end{aligned} \quad (4.88)$$

the test function  $H(y)$  here being set to 0 outside the interval  $(-d, d)$ . We now set  $H(y)$  equal to the  $i$ -th interpolating Lagrangian polynomial  $h_i(y)$  based on the physical collocation points  $\{y_j\}$  ( $h_i(y_j) = \delta_{ij}$ ) and evaluate the integral in  $(-d, d)$  by using the Gauss-Legendre quadrature rule with weights  $\{\omega_k\}_{k=1}^{N_{GL}}$ . We thus obtain an approximation for  $\sigma^C$  at the grid points

$$\sigma^C(y_i, t_n) = \sum_{k=1}^{N_{GL}} \frac{\omega_k}{\omega_i} \int_{D(y_k)} \mathbf{qF}(\mathbf{q}) \psi_s(\mathbf{q}) \alpha_k^n \int_{s=0}^1 H(y_k - (s - 1/2)R_y) ds d\mathbf{q}. \quad (4.89)$$

The same idea can be applied to the computation of the number density:

$$n(y_i, t_n) = \sum_{k=1}^{N_{GL}} \frac{\omega_k}{\omega_i} \int_{D(y_k)} \psi_s(\mathbf{q}) \alpha_k^n H(y_k - R_y/2) d\mathbf{q}. \quad (4.90)$$

### Computation of the velocity

For our one-dimensional problem, the equation of motion can be written as

$$-\eta_s \frac{d^2 v_x}{dy^2} = P + \frac{d\sigma_{xy}^C}{dy}, \quad (4.91)$$

where  $P$  is the magnitude of the imposed pressure gradient.

After integration in  $y$ , (4.91) becomes

$$\eta_s \frac{dv_x}{dy} = -Py - \sigma_{xy}^C + C, \quad (4.92)$$

with unknown constant  $C$ .

We approximated the velocity  $v_x$  by using a basis consisting of interpolating polynomials based on a GLL grid of  $N_{GL} + 1$  points. The discrete system for determining the approximation of the velocity was then obtained by collocating (4.92) at the points  $\{y_k\}$ ,  $k = 1, \dots, N_{GL}$ , and setting  $v_x$  to zero at  $y = \pm d$ . We thus have  $N_{GL} + 2$  equations for the components of  $v_x$  and  $C$ .

### 4.5.3 Numerical results

The numerical results in this section will be presented in terms of the dimensionless ordinate  $y/d$ . A dimensionless streamwise velocity and polymer number density may be defined as  $v_x/V$  and  $n/n_{avg}$ , respectively, where the characteristic velocity  $V$  may be chosen as  $d/\lambda$  and where  $n_{avg}$  is the average polymer number density. Accordingly, the natural unit for stresses and pressure is  $n_{avg}kT$ , and for the viscosity  $n_{avg}kT\lambda$ . We chose the following parameter set:  $\sqrt{b} = 3$ ,  $\eta_s = 0.2n_{avg}kT\lambda$  and the dimensionless pressure gradient  $P^*$  was set equal to 2 or 10. The number  $N_{GL}$  of GL collocation points in real space was chosen equal to 24 or 34 and the number  $N_{GLL}$  of GLL points in each direction in configuration space varied between 20 and 30. The time step  $\Delta t$  was set equal to  $0.01\lambda$ .

In the presentation of the results we shall make frequent reference to the parameter ratio

$$\frac{l_0}{d} = \frac{1}{d} \sqrt{\frac{kT}{H}}, \quad (4.93)$$

which measures a characteristic equilibrium length scale for the dumbbell relative to the wall separation distance. Thus, the smaller the value of  $l_0/d$  the smaller the influence of the walls on the flow between them, except for an increasingly thin boundary layer. Indeed, for  $l_0/d = 0$  the usual FENE solution for plane Poiseuille flow is recaptured.

#### Equilibrium

We report first some numerical results at equilibrium, i.e.  $\mathbf{v} = \mathbf{0}$ . In Fig. 4.26 we plot the components of  $\boldsymbol{\sigma}^C$  in the case  $l_0/d = 0.1$ . We see that at equilibrium  $\sigma_{xx}^C$  is greater than or equal to  $\sigma_{yy}^C$  throughout the gap between the plates  $y = \pm d$ . This property is proved analytically in Appendix B. In Fig. 4.27 we plot  $\sigma_{yy}^C$  at equilibrium for values of  $l_0/d = 0.05, 0.1$  and  $0.2$ . Although  $\sigma_{yy}^C$  varies strongly with  $y$  in the boundary layers the lower plot shows that  $\sigma_{yy}^C + \sigma_{yy}^K$  is a constant in accordance with the momentum conservation equation (4.91). This is confirmed analytically in Appendix B: see (B.17).

#### Planar start-up non-homogeneous Poiseuille flow

In Figs. 4.28-4.29 the profiles of the steady dimensionless velocity  $v_x(y)$  and of the polymer number density  $n(y)$ , calculated with an applied dimensionless pressure gradient  $P^* = 2$  are shown for different values of  $l_0/d$ . For  $l_0/d = 0$  (equivalent to the locally homogeneous FENE model) the polymer number density is a constant. However, we observe that as  $l_0/d$  increases from 0 to 0.2 the wall effects become stronger and polymer migrates from the channel walls  $y/d = \pm 1$  towards the centre of the channel. As a consequence the velocity gradient steepens near the walls in order to maintain the total shear stress and the profile flattens near the channel centre since the total viscosity increases there. These effects are also evident as we increase the applied pressure gradient from  $P^* = 2$  to  $P^* = 10$  whilst fixing  $l_0/d = 0.1$ . As well as the obvious increase in mass flow rate (see Fig. 4.30) we see that by dividing each of the profile values by their maximum value (see Fig. 4.31) the rescaled profiles are typical of those at lower and higher shear rates in a shear-thinning fluid, the profile flattening near the centreline for the higher pressure gradient.

From Eqn. (1.15) it should be clear that the dimensionless spring tension contribution  $\boldsymbol{\sigma}^C$  to the total Cauchy stress vanishes at the boundaries  $y/d = \pm 1$  since configuration space

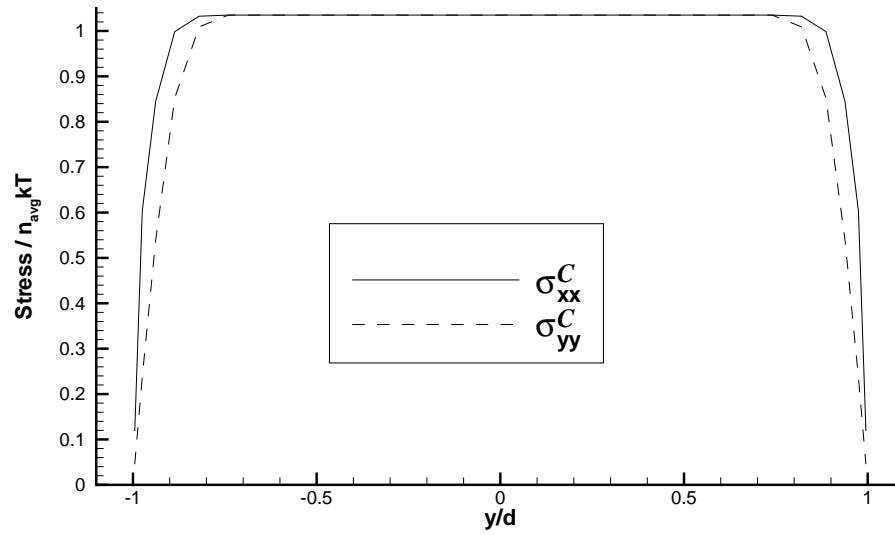


Figure 4.26: Normal components of  $\sigma^C$  at equilibrium;  $l_0/d = 0.1$ ,  $N_{GL} = 24$ ,  $N_{GLL} = 20$ .

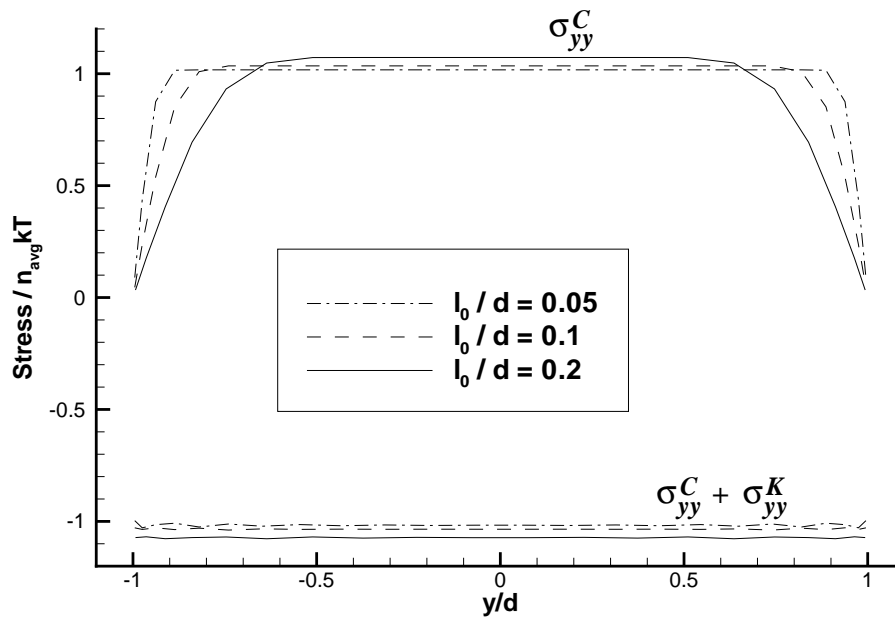


Figure 4.27:  $\sigma_{yy}^C$  and  $\sigma_{yy}^C + \sigma_{yy}^K$  at equilibrium;  $N_{GL} = 24$ ,  $N_{GLL} = 20$ .

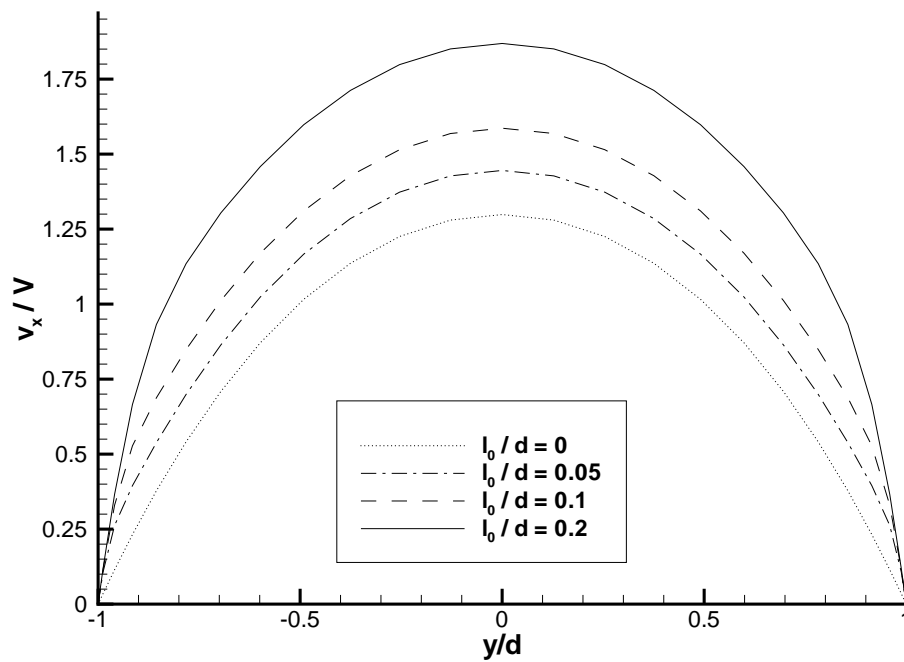


Figure 4.28: Velocity  $v_x$  for different ratios  $l_0/d$ ;  $N_{GL} = 24$ ,  $N_{GLL} = 20$ .

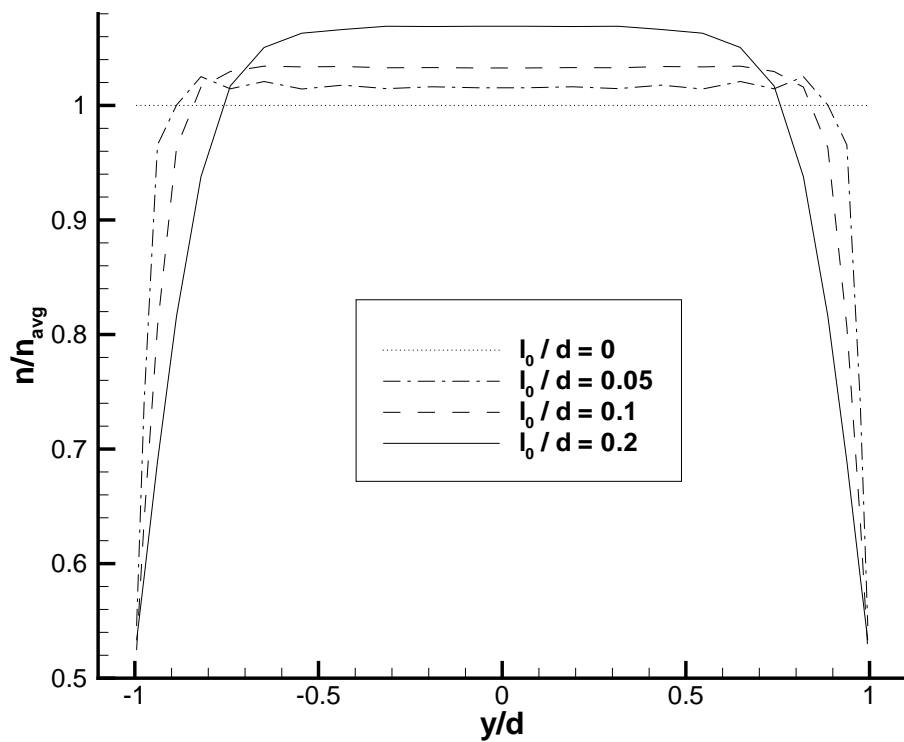


Figure 4.29: Polymer number density  $n$  for different ratios  $l_0/d$ ;  $N_{GL} = 24$ ,  $N_{GLL} = 20$ .

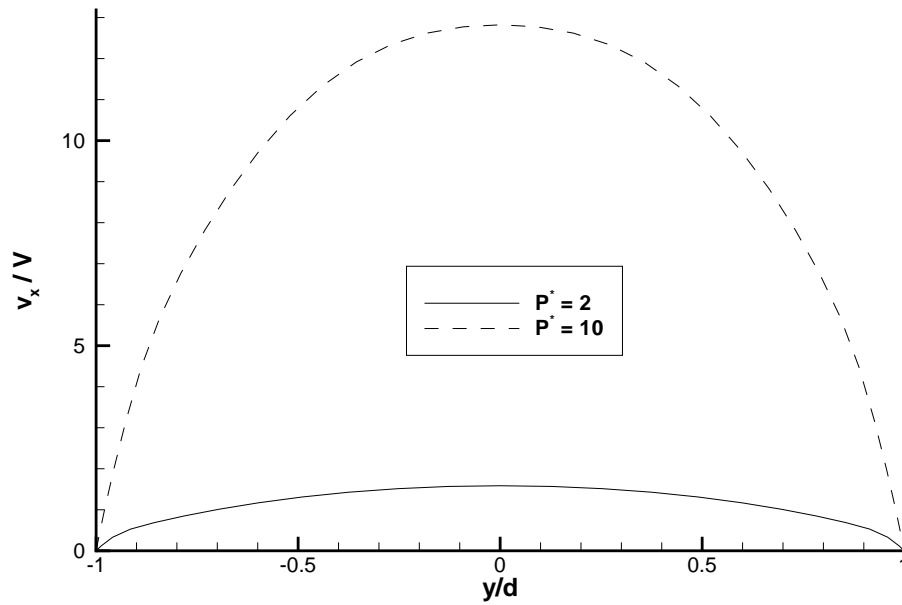


Figure 4.30: Velocity for  $P^* = 2$  and  $P^* = 10$ ;  $N_{GL} = 34$ ,  $N_{GLL} = 30$ .

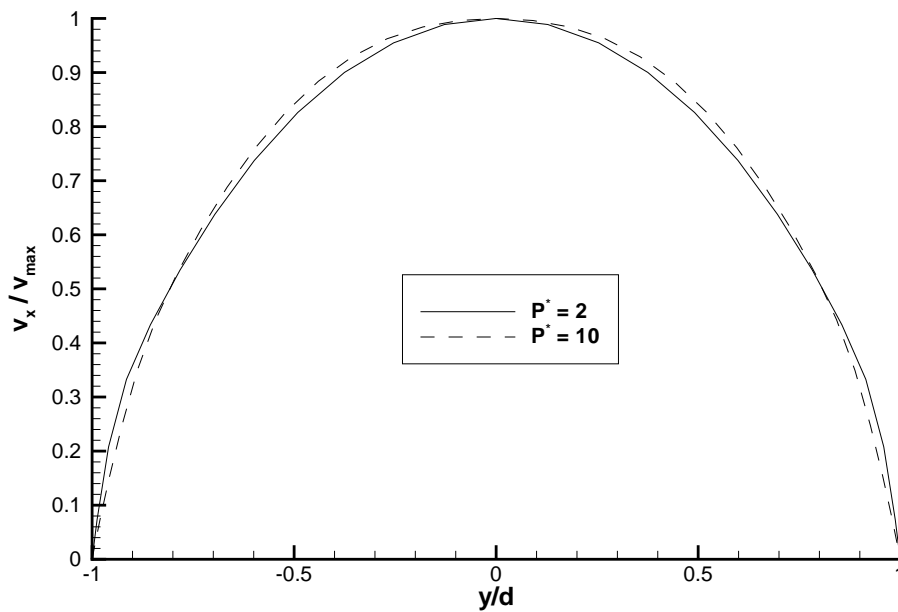


Figure 4.31: Normalized velocity for  $P^* = 2$  and  $P^* = 10$ ;  $N_{GL} = 34$ ,  $N_{GLL} = 30$ .



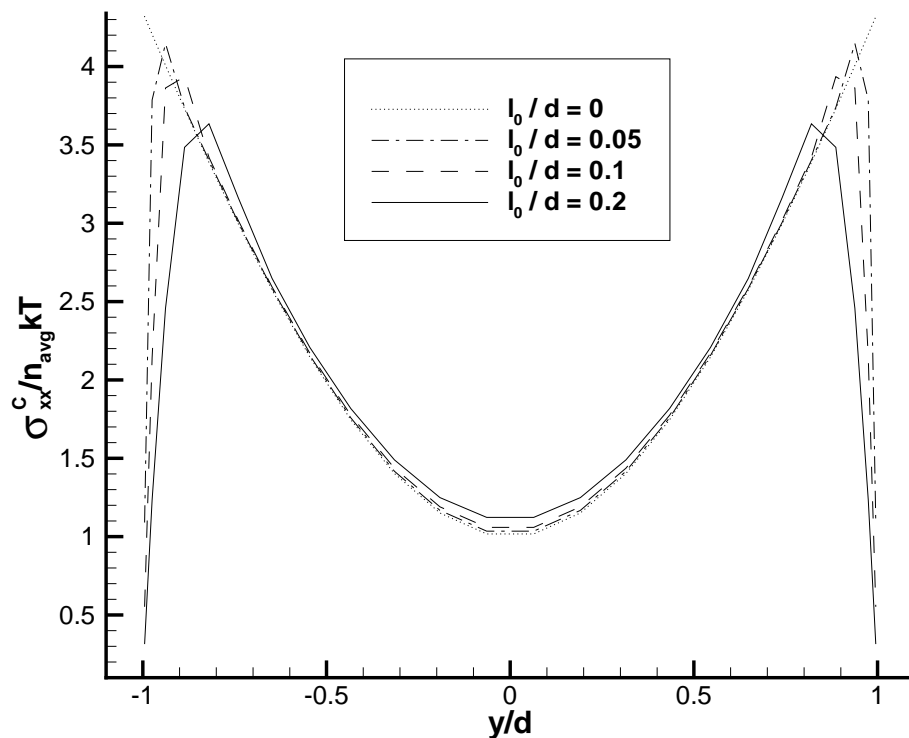


Figure 4.32: Stress component  $\sigma_{xx}^C$  for different ratios  $l_0/d$ ;  $N_{GL} = 24$ ,  $N_{GLL} = 20$ .

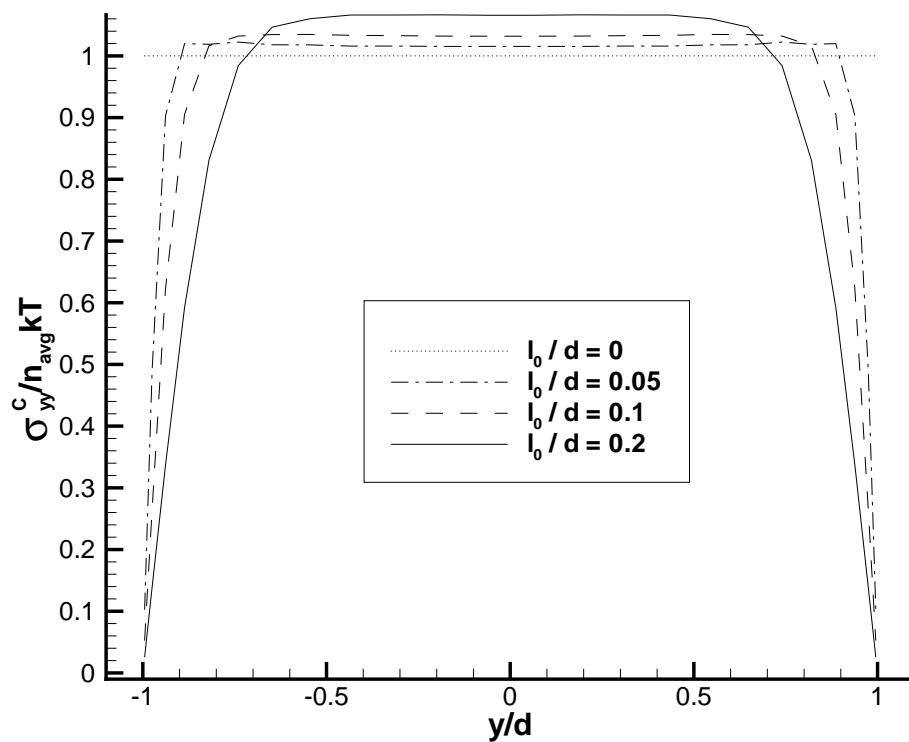


Figure 4.33: Stress component  $\sigma_{yy}^C$  for different ratios  $l_0/d$ ;  $N_{GL} = 24$ ,  $N_{GLL} = 20$ .

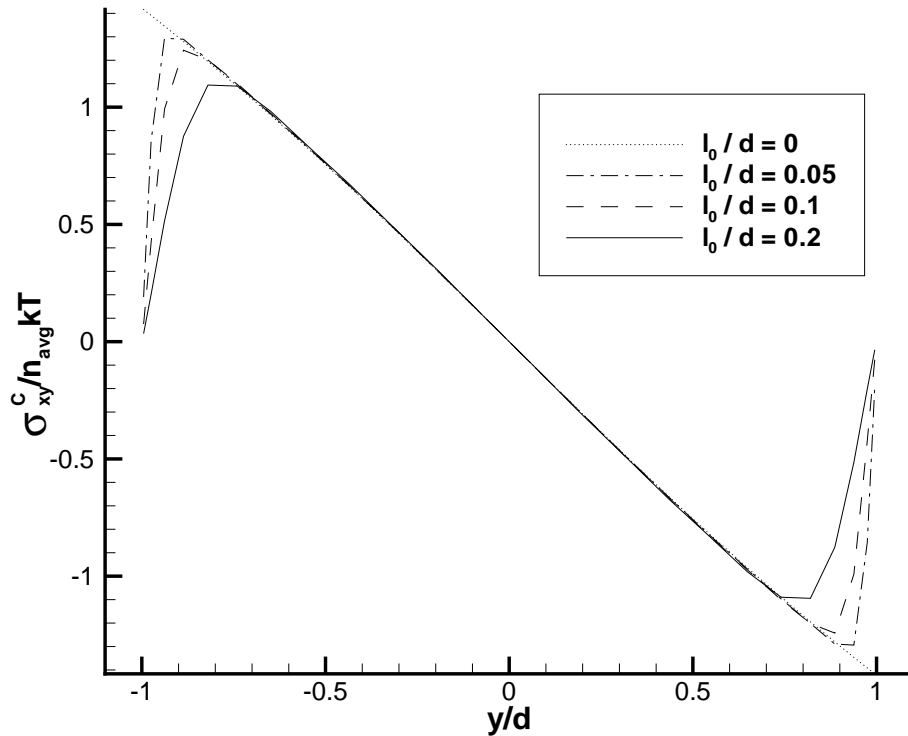


Figure 4.34: Stress component  $\sigma_{xy}^C$  for different ratios  $l_0/d$ ;  $N_{GL} = 24$ ,  $N_{GLL} = 20$ .

shrinks to a line (and therefore to a region in two-dimensional space of measure zero!) From a micro-mechanical point of view  $\sigma^C$  must be zero at a solid wall since no dumbbells can straddle this boundary. Thus, for  $l_0/d > 0$  boundary layers are to be seen in Figs. 4.32-4.34. As  $l_0/d$  increases from 0 to 0.2 the number density of polymers in the bulk flow also increases and leads to an increase in the magnitude of the stress there relative to the homogeneous flow (constant  $n$ ) case.

In Figs. 4.35 and 4.36 we test the convergence of our method with mesh refinement and compare our results with those obtained by stochastic simulations analogous to that of [6, 116]. For the stochastic simulations we implemented an Euler method with the implicit treatment of the spring force term using  $M$  pseudo-random realizations and an equispaced grid in  $(-d, d)$  with  $N_P$  points. The boundary conditions (4.70), which correspond to the reflection of the beads from the walls  $y = \pm d$  once they attempt to cross it, are modelled by the method described in Appendix C. The time step in the stochastic simulations was set to  $\Delta t = 0.001\lambda$ . The simulations were performed over the time interval  $(0, 6\lambda)$  and all the results were averaged over  $(4\lambda, 6\lambda)$ .

As can be seen from Figs. 4.35-4.36, excellent convergence is achieved for our Fokker-Planck-based method with the grid  $N_{GL} = 24$ ,  $N_{GLL} = 20$  for  $l_0/d = 0.1$  and there is a good agreement between the results obtained with our deterministic approach and the stochastic simulations. However, significant noise is present in the results of stochastic calculations (especially for the polymer number density, see Fig. 4.36), unless the number of pseudo-random realizations is big enough, so that stochastic simulations require comparable or even larger CPU times than the (converged) deterministic simulation.

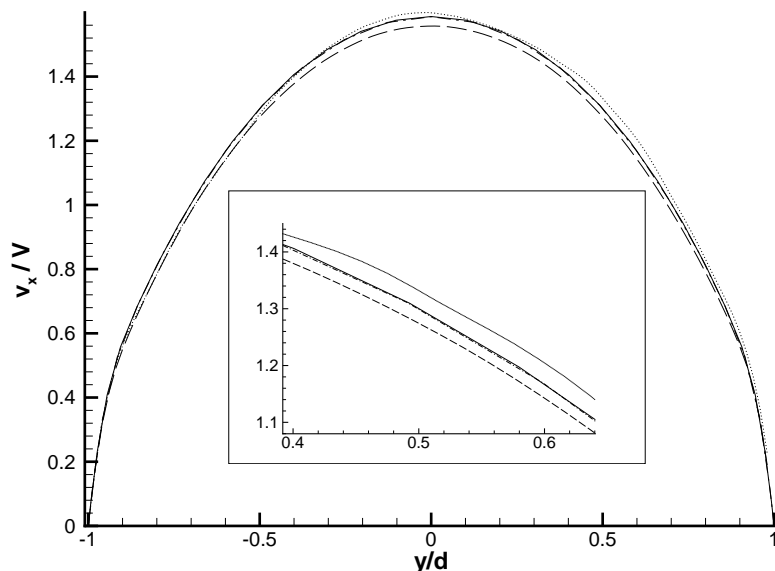


Figure 4.35: Velocity computed with the different methods,  $l_0/d = 0.1$ ; dots – stochastic with  $M = 5000$ ,  $N_P = 100$  (CPU time 4 sec), dashed – stochastic with  $M = 500000$ ,  $N_P = 100$  (CPU time 394 sec), dash-dot – deterministic with  $N_{GL} = 24$ ,  $N_{GLL} = 20$  (CPU time 51 sec), solid – deterministic with  $N_{GL} = 30$ ,  $N_{GLL} = 26$  (CPU time 230 sec).

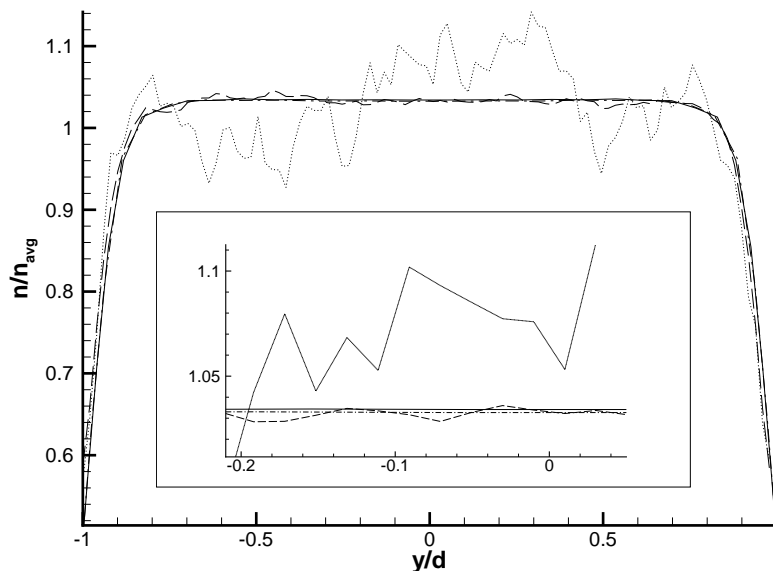


Figure 4.36: Polymer number density computed with the different methods,  $l_0/d = 0.1$ ; dots – stochastic with  $M = 5000$ ,  $N_P = 100$  (CPU time 4 sec), dashed – stochastic with  $M = 500000$ ,  $N_P = 100$  (CPU time 394 sec), dash-dot – deterministic with  $N_{GL} = 24$ ,  $N_{GLL} = 20$  (CPU time 51 sec), solid – deterministic with  $N_{GL} = 30$ ,  $N_{GLL} = 26$  (CPU time 230 sec).



# Chapter 5

## Fokker-Planck simulations of fast flows of melts and concentrated polymer solutions

### 5.1 Description of the models

In this section we state the equations of three reptation models mentioned in Section 1.2: the Doi-Edwards (DE) model [38, 39, 40], the Mead-Larson-Doi (MLD) model [92] and the simplified uniform (SU) version of the Öttinger model [100, 49]. Unlike the DE model, the reptation models of Mead et al. and Öttinger allow for tube stretching and both incorporate CCR. Additionally, the SU model has two features not present in the MLD model: double reptation (see (5.15) and the succeeding paragraph) and the possibility of incorporating anisotropy in the tube cross-sections. As in [49], however, we make no use in this paper of this last feature of Öttinger's model.

#### 5.1.1 Doi-Edwards model

The FP equation of the original DE model [38, 39, 40] has been already presented in Section 1.2 for homogeneous flows. Using the local homogeneity assumption, as was done for dumbbell models of dilute polymeric solutions, the same FP equation with the material derivative in place of the partial time derivative can be used in the situation of non-homogeneous flows. Thus, the FP equation for the pdf  $\psi(\mathbf{u}, s, \mathbf{x}, t)$  can be written as

$$\frac{D\psi}{Dt} = -\frac{\partial}{\partial \mathbf{u}} \cdot [(\mathbf{I} - \mathbf{u}\mathbf{u}) \cdot \boldsymbol{\kappa} \cdot \mathbf{u}\psi] + \frac{1}{\pi^2 \tau_d} \frac{\partial^2 \psi}{\partial s^2}, \quad (5.1)$$

where  $\boldsymbol{\kappa}$  denotes the velocity gradient tensor ( $\kappa_{ij} = \frac{\partial v_i}{\partial x_j}$ ) which is a function of position in physical space  $\mathbf{x}$ ,  $D/Dt$  is the material derivative, and  $\tau_d$  is the reptation time. The differential operator  $\partial/\partial \mathbf{u}$  in (5.1) includes only the derivatives tangent to the unit sphere. The boundary conditions at  $s = 0$  and  $s = 1$  supplementing the FP equation (5.1) are

$$\psi(\mathbf{u}, s, \mathbf{x}, t) = \frac{1}{4\pi} \delta(|\mathbf{u}| - 1), \quad s = 0, 1, \quad (5.2)$$

where  $\delta$  denotes the delta function. The elastic contribution  $\boldsymbol{\tau}$  to the Cauchy stress is then determined in the Doi-Edwards theory by

$$\boldsymbol{\tau} = 5G_N^0 \mathbf{S}, \quad (5.3)$$

where  $G_N^0$  is an elastic modulus,  $\mathbf{S} = \langle \mathbf{u}\mathbf{u} \rangle$  is the orientation tensor and  $\langle \cdot \rangle$  denotes an ensemble average.

We note that the DE model can be written in equivalent form as an integral equation for the orientation tensor  $\mathbf{S}(t)$

$$\mathbf{S}(t) = \int_{t'=-\infty}^t m(t, t') \mathbf{Q}(\mathbf{F}(t, t')) dt', \quad (5.4)$$

where  $m$  is the memory function, given for the DE model by

$$m(t, t') = m^{DE}(t, t') = \frac{8}{\pi^2 \tau_d} \sum_{k=0}^{\infty} \exp\left(-\frac{(2k+1)^2(t-t')}{\tau_d}\right), \quad (5.5)$$

and  $\mathbf{Q}$  is the deformation-dependent tensor defined in terms of the deformation gradient tensor  $\mathbf{F}(t, t')$  as follows:

$$\mathbf{Q}(t, t') = \langle \mathbf{u}\mathbf{u} \rangle_{t'} = \left\langle \frac{\mathbf{F}(t, t') \cdot \mathbf{u}(t') \mathbf{F}(t, t') \cdot \mathbf{u}(t')}{|\mathbf{F}(t, t') \cdot \mathbf{u}(t')|^2} \right\rangle_{t'}. \quad (5.6)$$

The subscript  $t'$  in (5.6) indicates that the orientation vector  $\mathbf{u}$  in the ensemble average was created at time  $t'$  according to the uniform distribution as in the boundary conditions (5.2). The integration in (5.4) is performed along the particle paths. The DE simulations of Peters et al. [114] using a deformation field method, the results of which are discussed in Section 5.3.3, were for a single-mode version of this model. In this case the memory function is given by

$$m^{DEsm}(t, t') = \frac{1}{\tau_d} \exp\left(-\frac{(t-t')}{\tau_d}\right), \quad (5.7)$$

and the corresponding FP equation by

$$\frac{D\psi}{Dt} = -\frac{\partial}{\partial \mathbf{u}} \cdot [(\mathbf{I} - \mathbf{u}\mathbf{u}) \cdot \boldsymbol{\kappa} \cdot \mathbf{u}\psi] - \frac{1}{\tau_d} \left( \psi - \frac{1}{4\pi} \right). \quad (5.8)$$

### 5.1.2 Mead-Larson-Doi (MLD) model

As mentioned already in Section 1.2, although the predictions of the DE model are in excellent agreement with experimental step-shear strain data, the model is severely shear-thinning in steady shear flow. Some more recent reptation models incorporate two important improvements to the original DE model: tube stretching for flows faster than the inverse of the Rouse time  $\tau_s$  for the relaxation of the polymer chain, and the CCR mechanism for flows faster than the inverse of the reptation time  $\tau_d$ . In this subsection we recapitulate the essential mathematics of the MLD model [92].

The MLD model is based on the model by Pearson et al. [110], which is a simplified form of the Marrucci-Grizzuti extension of the DE model [89]. The MLD model incorporates the effects of tube stretching and constraint release. Specifically, account is taken of tube stretching via a function  $\lambda = \lambda(\mathbf{x}, t)$  defined as

$$\lambda = \frac{L}{L_0},$$

where  $L$  is the contour length of a polymer chain and  $L_0$  its equilibrium contour length.  $\lambda$  is incorporated into the expression for  $\boldsymbol{\tau}$  as

$$\boldsymbol{\tau} = 5G_N^0 \lambda^2 \mathbf{S}, \quad (5.9)$$

where  $\mathbf{S} = \langle \mathbf{u}\mathbf{u} \rangle$  is the orientation tensor, which is calculated through the integral equation (5.4) with the memory function specified below. The time rate of change of  $\lambda$  is governed by the balance between stretch due to the flow field and relaxation of the chain within the tube. Constraint release effects are also taken into account, which gives the equation

$$\dot{\lambda} = \frac{D\lambda}{Dt} = \lambda \boldsymbol{\kappa} : \mathbf{S} - \frac{1}{\tau_s} (\lambda - 1) - \frac{1}{2} \left( \boldsymbol{\kappa} : \mathbf{S} - \frac{\dot{\lambda}}{\lambda} \right) (\lambda - 1), \quad (5.10)$$

where  $\tau_s$  is the longest Rouse time of the polymer chain.

In deriving the expression for the memory function, Mead et al. started from the memory function of the single-mode DE model (5.7). The latter may be seen to satisfy

$$\frac{Dm^{DEsm}}{Dt} = -\frac{1}{\tau_d} m^{DEsm}, \quad (5.11)$$

with an effective relaxation time  $\tau = \tau_d$ . By modifying  $\tau$  to take account of an extra relaxation of orientation due to CCR, Mead et al. proposed a memory function that satisfies

$$\frac{Dm^{MLD}}{Dt} = -\left( \frac{1}{\lambda^2 \tau_d} + \frac{1}{\lambda} \left( \boldsymbol{\kappa} : \mathbf{S} - \frac{\dot{\lambda}}{\lambda} \right) \right) m^{MLD}. \quad (5.12)$$

Here the reptation time  $\tau_d$  is multiplied by  $\lambda^2$  to take account of the increase in the reptation time produced as a result of the lengthening of the chain's primitive path by the flow.

### 5.1.3 Simplified Uniform (SU) model

We now briefly discuss the equations characterizing the SU model [100], as implemented by Fang et al. [49].

The model features a maximum allowable extension ratio  $\lambda_{max}$  and the evolution equation for the chain stretching ratio  $\lambda$  is

$$\dot{\lambda} = \frac{D\lambda}{Dt} = \lambda \boldsymbol{\kappa} : \mathbf{S} - \frac{1}{\tau_s} \frac{(\lambda^2 - 1) \lambda_{max}^2}{\lambda (\lambda_{max}^2 - \lambda^2)}. \quad (5.13)$$

The first term on the right-hand side of (5.13) corresponds to affine deformation and will be denoted in Section 5.2 by  $\dot{\lambda}_{con}$ . The second term is a dissipative contribution, denoted hereafter by  $\dot{\lambda}_{dissip}$ .

The FP equation for the configuration pdf assumes the form

$$\begin{aligned} \frac{D\psi}{Dt} = & -\frac{\partial}{\partial \mathbf{u}} \cdot [(\mathbf{I} - \mathbf{u}\mathbf{u}) \cdot \boldsymbol{\kappa} \cdot \mathbf{u}\psi] - \frac{\partial}{\partial s} (\dot{s}_{tot} \psi) - \frac{\dot{\lambda}_{dissip}}{\lambda} \psi \\ & + \frac{1}{\pi^2 \tau_d} \frac{\partial^2 \psi}{\partial s^2} + D \frac{\partial}{\partial \mathbf{u}} \cdot \frac{\partial \psi}{\partial \mathbf{u}}, \end{aligned} \quad (5.14)$$

where the drift velocity  $\dot{s}_{tot} = -\frac{1}{\lambda} \left(s - \frac{1}{2}\right) \dot{\lambda}_{dissip}$  and  $D$  is an orientational diffusion coefficient. The second term on the right-hand side of (5.14) is a creation/destruction term accounting for non-zero drift of configurations through the boundaries  $s = 0$  and  $s = 1$ . The boundary conditions for the FP equation (5.14) are the same as those in (5.2). The physical significance of the terms in (5.14) is discussed in [49, 100]. The orientational diffusion coefficient  $D$  in (5.14) may be defined as

$$D = \frac{1}{6} \left[ \delta_1 \frac{1}{\tau_d} - \delta_2 \frac{\dot{\lambda}_{dissip}}{\lambda} H \left( -\frac{\dot{\lambda}_{dissip}}{\lambda} \right) \right], \quad (5.15)$$

where  $H$  is a Heaviside function.  $\delta_1$  and  $\delta_2$  are positive  $\lambda$ -dependent parameters representing double reptation and the CCR mechanism, respectively. Double reptation is so called because with  $\delta_1 = 1$  there is an additional relaxation mechanism with the same reptation time as in the original DE model. Following [49] we have chosen  $\delta_1 = \delta_2 = 1/\lambda$ .

Finally, the elastic stress  $\boldsymbol{\tau}$  is related to the orientation tensor  $\mathbf{S} = \langle \mathbf{u}\mathbf{u} \rangle$  by

$$\boldsymbol{\tau} = 5G_N^0 \left[ 1 + \frac{\lambda^2 - 1}{1 - (\lambda/\lambda_{max})^2} \right] \mathbf{S}, \quad (5.16)$$

and is the sum of a DE contribution (first term in the square parentheses of (5.16)) and a contribution associated with chain stretching. We note in passing that as  $\lambda_{max} \rightarrow \infty$   $\boldsymbol{\tau} \rightarrow 5G_N^0 \lambda^2 \mathbf{S}$ , which is the same as (5.9).

### 5.1.4 Modified SU model

In this subsection we will introduce two modifications to the SU model, which are intended to improve the modelling of polymer chains at high velocity gradients and will be shown later to lead to better agreement with experimental data. The model includes all the features of the original SU model, with the addition of convective conformation renewal (CCR2) mechanism due to flow-induced lengthening of tube segments [7, 68].

The FP equation (5.14), the boundary conditions for it (5.16) and the expression for the elastic stress tensor (5.16) remain the same as for the SU model. We introduce, however, a modified expression for  $D$  in (5.14) as  $D = 1/6\tau_{eff}$  where

$$\tau_{eff} = \frac{1}{\frac{1}{\tau_d} + \beta_1 k H(k)} + \tau_R H(k), \quad (5.17)$$

where  $H = H(k)$  is the Heaviside step function with

$$k = \boldsymbol{\kappa} : \mathbf{S} - \frac{\dot{\lambda}}{\lambda}. \quad (5.18)$$

The diffusion coefficient  $D$ , defined in Eq. (5.17), accounts for double reptation (through  $\tau_d$ ) and CCR (through  $k$ ) in the same way as in the SU model. The factor  $\beta_1$  appearing in Eq. (5.17) allows CCR2 to be represented in the same manner as for CCR and  $\beta_1 k H(k)$  determines the effective orientation relaxation rate caused by constraint releases. We note that in addition to the double reptation and CCR terms in (5.17) there is a third term proportional to the Rouse time  $\tau_R$ . Without such a term the orientational relaxation time would tend to zero in the limit



of very fast flows. The additional term is an irreducible friction term expressing the fact that once the topological contribution to the chain friction is swept away the orientational relaxation time of the now unentangled chain drops to the Rouse time  $\tau_R$  (see Ianniruberto and Marrucci [68, 69]). Eq. (5.17) describes a monotonic variation of  $D$  from  $1/6\tau_d$  to  $1/6\tau_R$  due to CCR and the argument just mentioned.

In opposition to the point of view expressed by some in the literature [68, 69], we here argue that a similar physical mechanism also applies to chain length relaxation. That is,  $\tau_s$  should also vary with CCR from the value at equilibrium under constraint to the value corresponding to a somehow unconstrained Rouse chain, because of the fast removal of constraints. Hence we propose

$$\tau_s = \frac{1}{\frac{1}{\tau_{R0}} + \beta_2 k H(k)} + \tau_R H(k), \quad (5.19)$$

where  $\tau_{R0}$  is the primary Rouse time at equilibrium and the factor  $\beta_2$  has the same role as  $\beta_1$ , i.e.  $\beta_2 k H(k)$  is the effective stretching relaxation rate caused by constraint releases. We choose  $\tau_d/\tau_R = 3Z$  and  $\tau_d/\tau_{R0} = Z$  consistent with the fact that at equilibrium (entangled case) stretch relaxation is simply along the contour path of the chain and thus essentially one-dimensional, whereas the assumption underlying the choice of the pre-factor 3 in the original Doi-Edwards choice of  $3Z$  for the reptation to Rouse time ratio was that relaxation occurred in three dimensions [93]. Stretch relaxation therefore takes place over a longer time under equilibrium conditions than in a fast flow, as seems intuitively reasonable. Note that it has been usual in the literature (see, for example, [49]) to choose a fixed ratio  $\tau_d/\tau_s = 3Z$  for the characteristic reptation and stretching times.

## 5.2 Numerical method

One of the most efficient techniques that has been used up to now for numerical simulation of reptation models in complex flows is the deformation field method [113, 65]. It is applied to the DE model in [128] and to the MLD model in [114]. This method is based on the integral representation (5.4), (5.6) of the orientation tensor  $\mathbf{S}(t)$ . However, such a simple representation does not exist for the SU model due to the presence of the second and third terms on the right-hand side of its FP equation (5.14). This makes impossible the application of the deformation field method to the SU model.

An alternative is to use stochastic numerical methods. This approach was applied to the SU model by Fang et al. [49]. However, only homogeneous flows were considered by these authors.

Recently, Gigras and Khomami [56] have combined the Brownian configuration fields method and the deformation field method to allow the simulation of advanced reptation models such as the SU model. Their so-called adaptive configuration fields method was tested against the results of the Brownian dynamics simulations of [49] for several homogeneous flows and the results were found to be in excellent agreement.

In the present work we explore an alternative approach to simulate the SU and modified SU models: solving directly the FP equation (5.14) using high-order methods, similar to what was done in Chapter 4 for the FENE model of dilute polymeric solutions. We shall show that this can be much more efficient than stochastic methods in the case of homogeneous flows and moreover complex flows can also be investigated. The equations to solve in the SU

model are (1), (1.33), (5.13) and (5.14). This necessitates discretization in time and in both configuration and physical space. A Galerkin method is used in configuration space and a streamline-upwinded Petrov/Galerkin (SUPG) spectral element method in physical space, as will be elaborated on in the subsections to follow.

### 5.2.1 Time-splitting scheme

We denote the evaluation of a field variable  $(\mathbf{v}, p, \boldsymbol{\tau}, \lambda, \psi)$  at time  $t = j\Delta t$  with a superscript ‘ $j$ ’.

The initial conditions ( $j = 0$ ) are chosen as  $\boldsymbol{\tau}^0 = \mathbf{0}$ ,  $\lambda^0 = 1$  and  $\psi^0 = 1/4\pi$ . For simplicity, we decouple the solution of the Stokes system (1)-(1.33) from the elastic extra-stress calculation (5.13), (5.14) and (5.16). Thus,  $\boldsymbol{\tau}^j$  appears as a source term evaluated at time  $j\Delta t$  in (1.33) and we solve the continuity-momentum pair for velocity  $\mathbf{v}^j$  and pressure  $p^j$ .

As in the case of the FENE model in Chapter 4, we propose splitting every time step into two half time steps, the first one accounting for configuration space and the second one for physical space. The physical step can be done implicitly, but it is difficult to do so for the configuration one. Indeed, the fast FP solver, introduced in Chapter 4 for the FENE model, cannot be applied here, because the FP equation now contains several non-constant coefficients. We treat therefore the configuration step explicitly, splitting it into  $N_\alpha$  smaller time steps to meet possible restrictions of CFL type.  $N_\alpha$  was set equal to 10 for all the results presented in Section 5.3. All this leads to the following time marching scheme:

- *First half time step*

Set  $\lambda^{j(0)} = \lambda^j$  and  $\psi^{j(0)} = \psi^j$  and calculate  $\psi^{j(\alpha)}$  for  $\alpha = 0, \dots, N_\alpha - 1$  via the formulas

$$\frac{\lambda^{j(\alpha+1)} - \lambda^{j(\alpha)}}{\Delta t/N_\alpha} = \dot{\lambda}_{con}(\lambda^{j(\alpha)}, \mathbf{S}^{j(\alpha)}) + \dot{\lambda}_{dissip}(\lambda^{j(\alpha)}), \quad (5.20)$$

$$\frac{\psi^{j(\alpha+1)} - \psi^{j(\alpha)}}{\Delta t/N_\alpha} = \mathcal{L}_{FP}(\psi^{j(\alpha)}, \lambda^{j(\alpha)}), \quad (5.21)$$

where  $\mathcal{L}_{FP}$  refers to the Fokker-Planck operator appearing on the right-hand side of (5.14). In the calculations according to both (5.20) and (5.21) we use the latest available velocity field, i.e.  $\mathbf{v}^j$ , to compute the velocity gradient that is present implicitly in these formulas. The orientation tensor  $\mathbf{S}^{j(\alpha)}$  may be calculated from

$$\mathbf{S}^{j(\alpha)}(\mathbf{x}, t) = \int_{s=0}^1 \int_{\theta=0}^\pi \int_{\varphi=0}^{2\pi} \psi^{j(\alpha)}(\mathbf{x}, t, \mathbf{u}(\theta, \varphi), s) \mathbf{u}(\theta, \varphi) \mathbf{u}(\theta, \varphi) \sin \theta \, d\varphi d\theta ds, \quad (5.22)$$

where  $\mathbf{u} = \sin \theta \cos \varphi \mathbf{e}_x + \sin \theta \sin \varphi \mathbf{e}_y + \cos \theta \mathbf{e}_z$ .

We set then  $\lambda^{j+1/2} = \lambda^{j(N_\alpha)}$  and  $\psi^{j+1/2} = \psi^{j(N_\alpha)}$ .

- *Second half time step*

$$\frac{\lambda^{j+1} - \lambda^{j+1/2}}{\Delta t} + (\mathbf{v}^j \cdot \nabla) \lambda^{j+1} = 0, \quad (5.23)$$

$$\frac{\psi^{j+1} - \psi^{j+1/2}}{\Delta t} + (\mathbf{v}^j \cdot \nabla) \psi^{j+1} = 0. \quad (5.24)$$

We compute then  $\boldsymbol{\tau}^{j+1}$  using (5.16) and the algorithm increments  $j$  by 1 and returns to the Stokes system (1)-(1.33).

### 5.2.2 Discretization in configuration space

A discrete approximation to the configuration pdf  $\psi$ , expressing dependence on  $s$  and on a generic point on the unit sphere in configuration space, may be written in the form

$$\psi(\mathbf{u}, s, \mathbf{x}, t) \approx \sum_{i=0}^1 \sum_{l=0}^{N_s} \sum_{n=0}^{N_u} \sum_{m=i}^n \psi_{i,\ell,n,m}(\mathbf{x}, t) \Phi_{2n,2m}^i(\theta, \varphi) L_\ell(s). \quad (5.25)$$

In (5.25)  $\Phi_{n,m}^i = P_n^m(\cos \theta)((1-i)\cos m\varphi + i\sin m\varphi)$  ( $i = 0, 1$ ) are spherical harmonics<sup>1</sup> defined in terms of the associated Legendre polynomials  $P_n^m$  and the spherical polar coordinates  $\theta$  and  $\varphi$ .  $L_\ell(s)$  is a degree  $N_s$  polynomial, defined on  $[0, 1]$  by

$$L_\ell(s) = h_\ell(\xi), \quad (5.26)$$

where  $\xi = 2s - 1$  and

$$h_\ell(\xi) = -\frac{1}{N_s(N_s+1)P_{N_s}(\xi_\ell)} \frac{(1-\xi^2)P'_{N_s}(\xi)}{(\xi-\xi_\ell)}. \quad (5.27)$$

Here  $P_{N_s}(\xi)$  is the degree  $N_s$  Legendre polynomial and the  $\{\xi_\ell\}_{\ell=0}^{N_s}$  are the Gauss-Lobatto-Legendre (GLL) points.  $h_\ell$  is the  $\ell$ th Lagrange interpolating polynomial based on the GLL points and has the property that  $h_\ell(\xi_j) = \delta_{\ell j}$   $j, \ell = 0, \dots, N_s$ .

Inserting (5.25) into the FP equation (5.14) for  $\psi$  we simplify the terms in the square parentheses appearing on the right-hand side of (5.14), by using the formula (see Appendix A)

$$\frac{\partial}{\partial \mathbf{u}} \cdot [(\mathbf{I} - \mathbf{u}\mathbf{u}) \cdot \boldsymbol{\kappa} \cdot \mathbf{u} \Phi_{n,m}^i] = \sum_{k=m-2}^{m+2} \sum_{j=n-2}^{n+2} a_{n,j}^{m,k} (w_j^k(\boldsymbol{\kappa}) \Phi_{j,k}^i + (-1)^{1-i} v_j^k(\boldsymbol{\kappa}) \Phi_{j,k}^{1-i}). \quad (5.28)$$

The diffusion term is much easier. The spherical harmonics are the eigenfunctions of the Laplace operator on the unit sphere; specifically,

$$\frac{\partial}{\partial \mathbf{u}} \cdot \frac{\partial \Phi_{n,m}}{\partial \mathbf{u}} = -n(n+1) \Phi_{n,m}^i. \quad (5.29)$$

Using (5.25) and (5.28)-(5.29) we form the product of (5.14) with a test function  $\Phi_{2p,2q}^i(\theta, \varphi) L_k(s)$  ( $i = 0, 1; p = 0, \dots, N_u; q = i, \dots, p; k = 0, \dots, N_s$ ) and integrate over configuration space  $B(0, 1) \times [0, 1]$ . The integral with respect to  $s$  is evaluated using a Gauss-Lobatto quadrature rule, and orthogonality of the spherical harmonics over  $B(0, 1)$  is exploited. The time- and configuration space-discretized equations corresponding to (5.21) and (5.24) now therefore

<sup>1</sup>We note that only the spherical harmonics of even order appear in (5.25). This is because  $\psi$  is an even function of  $\mathbf{u}$ .

become

$$\begin{aligned} \frac{\omega_k}{\Delta t/N_\alpha} \left( \psi_{i,k,p,q}^{j(\alpha+1)}(\mathbf{x}) - \psi_{i,k,p,q}^{j(\alpha)}(\mathbf{x}) \right) &= -\omega_k \sum_{n=p-1}^{p+1} \sum_{m=q-1}^{q+1} a_{2p,2n}^{2q,2m} \left( w_{2n}^{2m} \psi_{i,k,n,m}^{j(\alpha)}(\mathbf{x}) + (-1)^i v_{2n}^{2m} \psi_{1-i,k,n,m}^{j(\alpha)}(\mathbf{x}) \right) \\ &- \sum_{\ell=0}^{N_s} \psi_{i,\ell,p,q}^{j(\alpha)}(\mathbf{x}) \left( (\dot{s}_{tot} L_\ell(s))', L_k(s) \right)_{N_s} - \frac{\dot{\lambda}_{dissip}}{\lambda} \omega_k \psi_{i,k,p,q}^{j(\alpha)}(\mathbf{x}) \\ &+ \frac{1}{\pi^2 \tau_d} \sum_{\ell=0}^{N_s} \psi_{i,\ell,p,q}^{j(\alpha)}(L_\ell''(s), L_k(s))_{N_s} - 2p(2p+1) \omega_k D \psi_{i,k,p,q}^{j(\alpha)}, \end{aligned}$$

and

$$\begin{aligned} \frac{1}{\Delta t} \left( \psi_{i,k,p,q}^{j+1}(\mathbf{x}) - \psi_{i,k,p,q}^{j+1/2}(\mathbf{x}) \right) + (\mathbf{v}^j \cdot \nabla) \psi_{i,k,p,q}^{j+1}(\mathbf{x}) &= 0, \\ i = 0, 1; p = 0, \dots, N_u; q = i, \dots, p; k = 1, \dots, N_s - 1. \end{aligned}$$

$(\cdot, \cdot)_{N_s}$  denotes the  $(N_s + 1)$  point GLL quadrature evaluation of the  $L^2$  inner product over  $[0, 1]$  (see (2.2)).

Once we have the pdf in the form (5.25), the components of the orientation tensor  $\mathbf{S} = \langle \mathbf{u}\mathbf{u} \rangle$  may be computed from the formulas

$$\begin{aligned} S_{xx} &= 4\pi \sum_{l=0}^{N_s} \omega_l \left( \frac{1}{3} \psi_{0,\ell,0,0} - \frac{1}{15} \psi_{0,\ell,1,0} + \frac{2}{5} \psi_{0,\ell,1,1} \right), \\ S_{yy} &= 4\pi \sum_{l=0}^{N_s} \omega_l \left( \frac{1}{3} \psi_{0,\ell,0,0} - \frac{1}{15} \psi_{0,\ell,1,0} - \frac{2}{5} \psi_{0,\ell,1,1} \right), \\ S_{zz} &= 4\pi \sum_{l=0}^{N_s} \omega_l \left( \frac{1}{3} \psi_{0,\ell,0,0} + \frac{2}{15} \psi_{0,\ell,1,0} \right), \\ S_{xy} &= \frac{8\pi}{5} \sum_{l=0}^{N_s} \omega_l \psi_{1,\ell,1,1}, \end{aligned}$$

the other components being zero in a flow parallel to the  $xy$ -plane.

### 5.2.3 Discretization in physical space

Finally, we discretize equations (1), (5.20) and (5.23)-(5.24) in physical space using a spectral element method. This is done by choosing tensorized bases in real space for all dependent variables - with the exception of the pressure - consisting of polynomials of degree  $N$  in each spatial variable. The pressure basis polynomials are chosen to be of degree 2 less in each direction so as to ensure that the discrete problem is well posed [14]. A discrete system of equations is set up using a Galerkin method for (1), (1.33) and an Uzawa algorithm (block Gaussian elimination) is used to construct a discrete Poisson-type problem for the pressure from (1) and (1.33).

Equations (5.20) and (5.21) are solved separately at each collocation point. An SUPG element-by-element spectral element method with constant upwinding factor, as detailed in Section 2.4, is used to treat the convection equations (5.23) and (5.24).

Table 5.1: Convergence of our FP method for the simple shear flow (5.31) at  $\dot{\gamma}\tau_d = 3$ . Final time  $100/\dot{\gamma}$ .

$N_u$	$N_s$	$\dot{\gamma}\Delta t$	$\tau_{xy}$	$ \Delta\tau_{xy}/\tau_{xy} $	CPU time (sec)
4	4	0.02	0.509716873089292	$3.6 \times 10^{-3}$	0.16
8	8	0.02	0.511583481828495	$6.0 \times 10^{-10}$	0.75
12	12	0.01	0.511583481521587	$6.5 \times 10^{-13}$	5.4
16	16	0.005	0.511583481521068	$3.6 \times 10^{-13}$	27
20	20	0.0025	0.511583481521067	$3.6 \times 10^{-13}$	113
24	24	0.00125	0.511583481521072	$3.5 \times 10^{-13}$	527
28	28	0.000625	0.511583481521099	$3.0 \times 10^{-13}$	2535
40	40	$1.5625 \times 10^{-4}$	0.511583481521253	-	34161

Table 5.2: Convergence of the stochastic simulations [49] for the simple shear flow (5.31) at  $\dot{\gamma}\tau_d = 3$ . Final time  $100/\dot{\gamma}$ .

$N_{\text{sample}}$	$N_{\text{block}}$	$\dot{\gamma}\Delta t$	$\tau_{xy}$	$\delta\tau_{xy}$	$ \Delta\tau_{xy}/\tau_{xy} $	CPU time (seconds)
10000	10	0.04	0.5073	$2.7 \times 10^{-3}$	$8.4 \times 10^{-3}$	604
10000	10	0.02	0.5097	$4.3 \times 10^{-3}$	$3.6 \times 10^{-3}$	1166
10000	10	0.01	0.5103	$3.6 \times 10^{-3}$	$2.4 \times 10^{-3}$	2320
10000	100	0.04	0.5074	$8.7 \times 10^{-4}$	$8.1 \times 10^{-3}$	6054
10000	100	0.02	0.5091	$1.4 \times 10^{-3}$	$4.8 \times 10^{-3}$	11672
10000	100	0.01	0.5104	$1.2 \times 10^{-3}$	$2.3 \times 10^{-3}$	23225

## 5.3 Results

In the presentation of the results in Section 5.3 we work with dimensionless variables, here denoted with an asterisk, and defined by

$$\mathbf{x}^* = \mathbf{x}/L, \quad t^* = t/\tau_d, \quad \mathbf{v}^* = \mathbf{v}\tau_d/L, \quad p^* = p/G_N^0 \quad \text{and} \quad \boldsymbol{\tau}^* = \boldsymbol{\tau}/G_N^0, \quad (5.30)$$

where  $L$  represents a suitably chosen length scale.

In rewriting equations (1), (1.33), (5.13)-(5.14) and (5.16) in terms of these dimensionless variables it may be shown easily that the only parameters that require prescription are the maximum extension ratio  $\lambda_{max}$ , the ratio of the reptation time to the Rouse time  $\tau_d/\tau_s$  and the dimensionless solvent viscosity  $\eta_s^* = \eta_s/G_N^0\tau_d$ .

### 5.3.1 Homogeneous flows of the SU model: Stochastic simulations [49] vs. the Fokker-Planck method

The predictions of the SU model for homogeneous shear and extensional flows are described in detail in [49]. Here we want to validate our numerical method by comparing the results with those from the stochastic simulations [49]. We also want to investigate the efficiency of the two approaches. All CPU times quoted in Section 5.3.1 are for a Pentium III 800 MHz machine and the parameters of the SU model are taken to be  $\lambda_{max} = 21$  and  $\tau_d/\tau_s = 50$ .

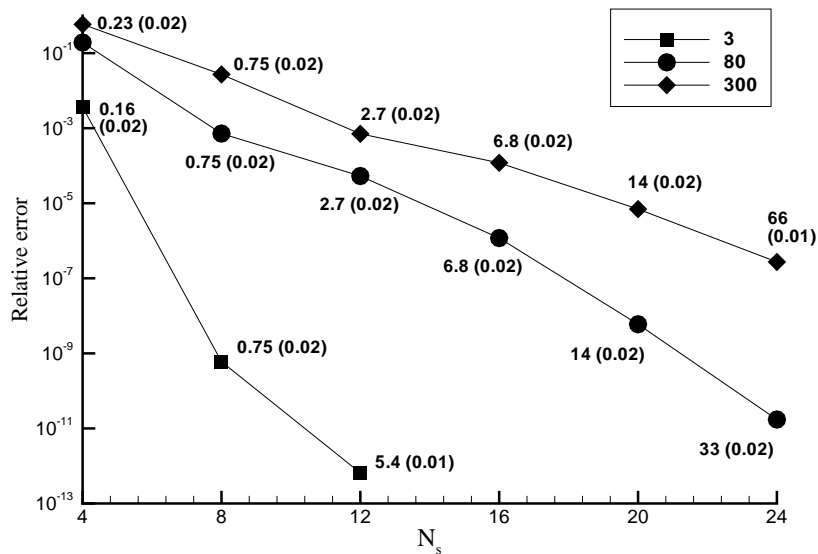


Figure 5.1: Relative error for  $\tau_{xy}$  for the simple shear flow (5.31) at three values of  $\dot{\gamma}\tau_d$  using  $N_u = N_s = 4, 8, 12, 16, 20$  and  $24$ . Each data point is labelled with the total CPU time in seconds and, in parentheses, the value of  $\dot{\gamma}\Delta t$  used. Final time =  $100/\dot{\gamma}$ .

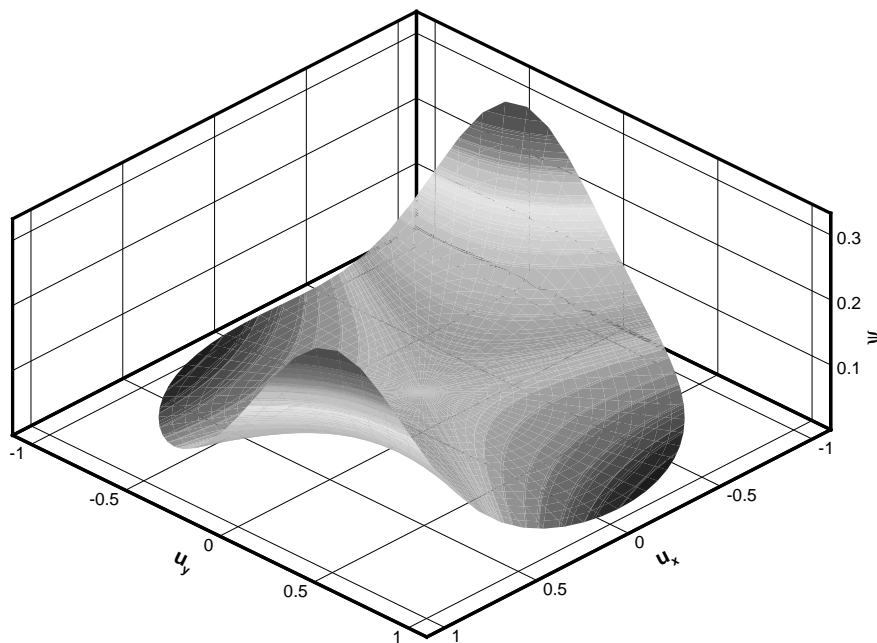


Figure 5.2: The pdf  $\psi$  as a function of  $u_x$  and  $u_y$  at  $s = 0.5$  for the simple shear flow (5.31) at  $\dot{\gamma}\tau_d = 3$  computed with  $N_u = N_s = 12$ .

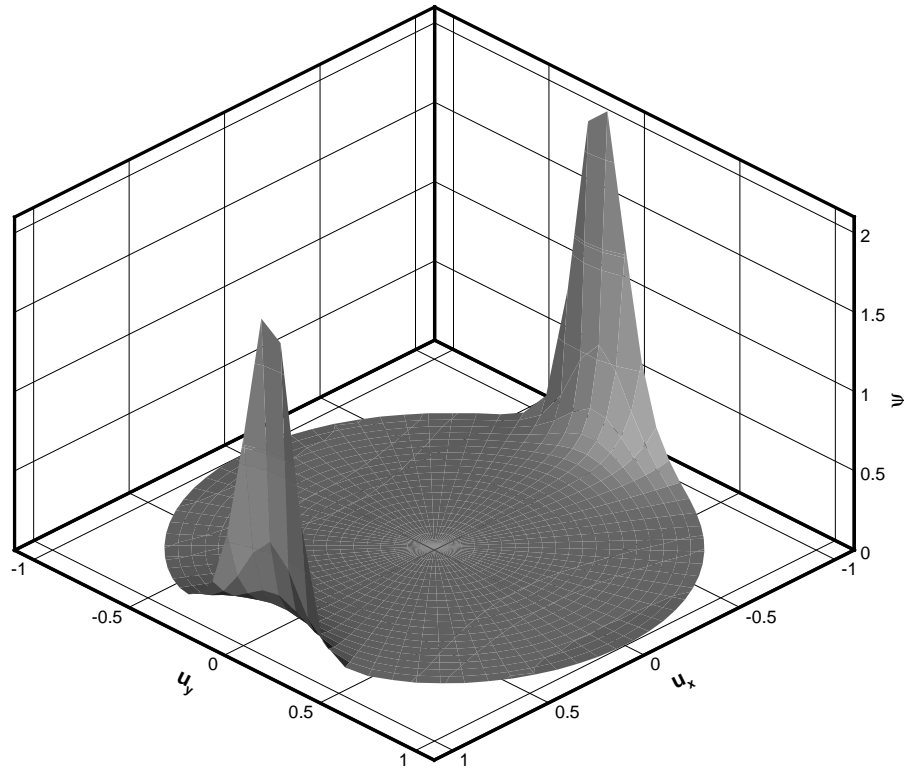


Figure 5.3: The pdf  $\psi$  as a function of  $u_x$  and  $u_y$  at  $s = 0.5$  for the simple shear flow (5.31) at  $\dot{\gamma}\tau_d = 800$  computed with  $N_u = N_s = 16$ .

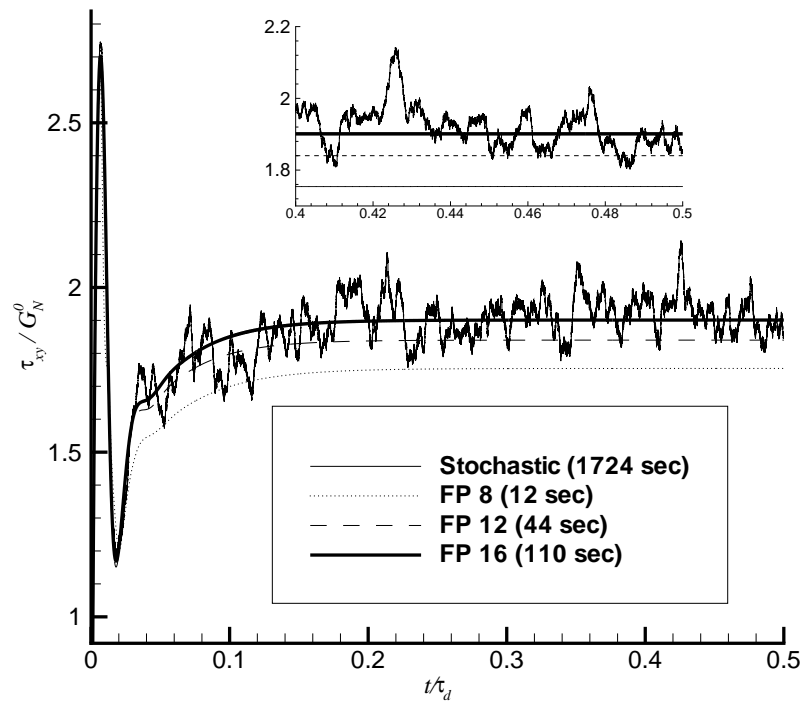


Figure 5.4: Evolution of  $\tau_{xy}$  for the start-up simple shear flow (5.31) at  $\dot{\gamma}\tau_d = 800$ . FP  $M$  stands for the FP-based numerical method with  $N_u = N_s = M$  and  $\Delta t = 0.005/\dot{\gamma}$ . The stochastic simulation was implemented with  $N_{\text{sample}} = 10000$ ,  $N_{\text{block}} = 2$ ,  $\Delta t = 0.01/\dot{\gamma}$ . The CPU times on a Pentium III 800 MHz machine are also indicated.

### Start-up shear flow.

We report here the results for homogeneous start-up shear flow. That is, we solve the FP equation (5.14) coupled with (5.13) with the steady velocity field

$$\mathbf{v} = (v_x, v_y, v_z) = (\dot{\gamma}y, 0, 0). \quad (5.31)$$

Fig. 5.1 shows the relative errors for  $\tau_{xy}$  after reaching the steady state with the FP-based method described in Section 5.2 for three different values of the dimensionless shear rate  $\dot{\gamma}\tau_d = \{3, 80, 300\}$ , taking the value computed on a finer grid ( $N_u = N_s = 40$ ) as the exact one. Each data point in the figure is labelled first with the CPU time required to reach a final time of  $100/\dot{\gamma}$  and secondly, in parentheses, we indicate the dimensionless time step  $\dot{\gamma}\Delta t$  chosen. The choice of the time step was made by performing a run at  $\dot{\gamma}\Delta t = 0.02$  and (if necessary) dividing this successively by 2, 4,  $\dots$ , etc. until convergence was achieved. We see that the approximation provided by the scheme is exponentially convergent. However, as is to be expected, the rate of convergence gets lower with increasing  $\dot{\gamma}\tau_d$ .

The reason for this becomes clear if we compare the solutions for the pdf  $\psi$  at the shear rates  $\dot{\gamma}\tau_d = 3$  and 800 shown in Figs. 5.2 and 5.3 respectively, where  $\psi$  is plotted as a function of  $u_x$  and  $u_y$  at  $s = 0.5$  for the steady state i.e.,  $\psi$  evaluated at  $s = 0.5$  on the upper hemisphere pointed to by  $\mathbf{u}$  is projected onto the unit disc. We see that the solution in Fig. 5.2 is very smooth, but that in Fig. 5.3 has two spikes that can be captured accurately only on a sufficiently refined mesh.

Not surprisingly, our FP method is particularly advantageous in comparison with the stochastic simulations in [49] at low shear rates. We compare the respective CPU times at  $\dot{\gamma}\tau_d = 3$  in Tables 5.1 and 5.2 (note that the simulations were performed in [49] in  $N_{block}$  independent blocks, in each of which  $N_{sample}$  trajectories of the stochastic processes  $\mathbf{u}$  and  $s$  were allowed to propagate). In Table 5.1 we show the computed values of  $\tau_{xy}$ , the absolute relative errors  $|\Delta\tau_{xy}/\tau_{xy}|$  (assuming the solution computed with  $N_u = N_s = 40$  to be exact) and the CPU times for our method. In Table 5.2 we supply the values of  $\tau_{xy}$  computed with the method of [49] and averaged over the final 200 time steps, the standard deviations  $\delta\tau_{xy}$  over the same time interval, the absolute relative errors  $|\Delta\tau_{xy}/\tau_{xy}|$  (again, assuming that our FP solution computed with  $N_u = N_s = 40$  is exact) and the CPU times. We see that both methods give approximately the same results, but that our FP method can be thousands of times faster for the same level of accuracy. As an example, in the FP shear flow calculation with  $N_u = N_s = 4$  detailed in Table 5.1, only 0.16 CPU seconds were taken to compute a solution having a relative error in the shear stress  $\tau_{xy}$  of  $3.6 \times 10^{-3}$ . The vast majority of this time (99.9%) was consumed performing the iterations (5.20)-(5.21) and the remaining time mainly with the construction of the coefficient matrix for the FP operator in (5.21). For the same level of accuracy it may be seen from Table 5.2 that 1166 CPU seconds were required by Fang et al.'s stochastic algorithm to reach the same final time of  $100/\dot{\gamma}$ . The reason for the significant difference in CPU time between the two methods is that reduction of the variance requires that  $N_{sample} \times N_{block}$  be chosen sufficiently large and accuracy demands that  $\Delta t$  be chosen sufficiently small.

What is less evident is that our method can be more efficient than the stochastic simulation technique even at the high shear rate  $\dot{\gamma}\tau_d = 800$ , as may be seen from Fig. 5.4. Although relatively high values for  $N_u$  and  $N_s$  are needed in order to match the ‘‘deterministic’’ solution with the stochastic one, our method gives about a 15-fold gain in CPU time.



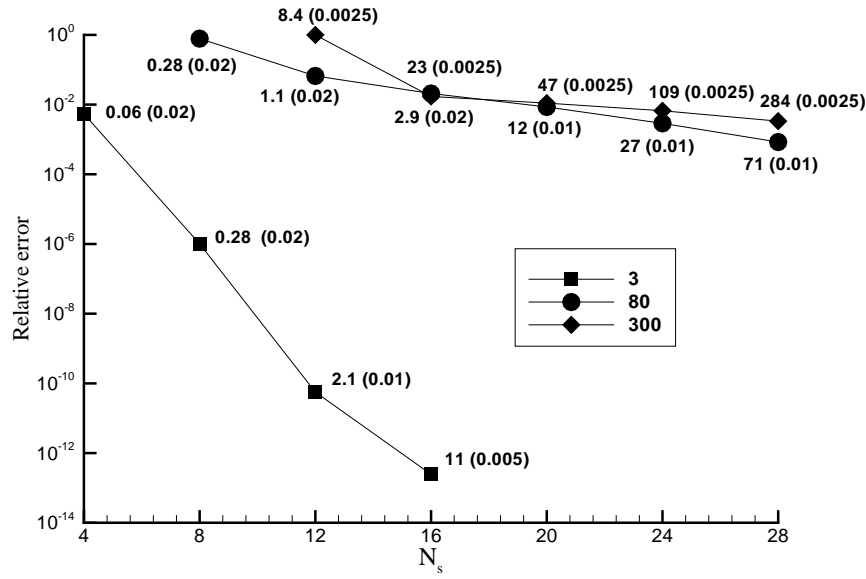


Figure 5.5: Relative error for  $N_1$  for the uniaxial extensional flow (1.29) at three values of  $\dot{\epsilon}\tau_d$  using  $N_u = N_s = 4, 8, 12, 16, 20, 24$  and  $28$ . Each data point is labelled with the total CPU time in seconds and, in parentheses, the value of  $\dot{\epsilon}\Delta t$  used. Final time =  $50/\dot{\epsilon}$ .

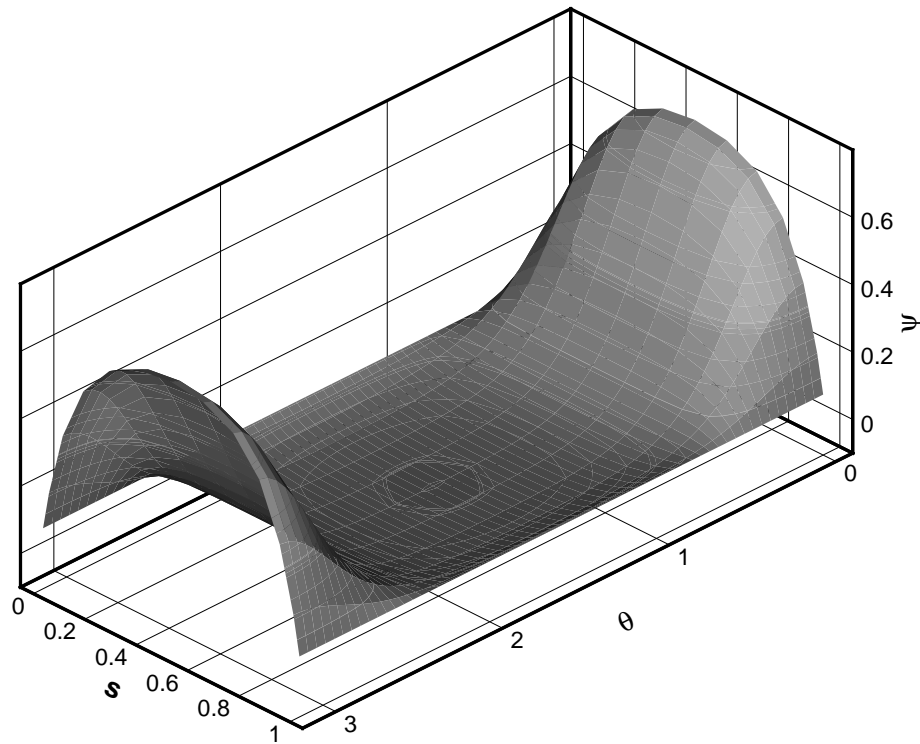


Figure 5.6: The pdf  $\psi$  for the uniaxial extensional flow (1.29) at  $\dot{\epsilon}\tau_d = 3$  computed with  $N_u = N_s = 12$ .

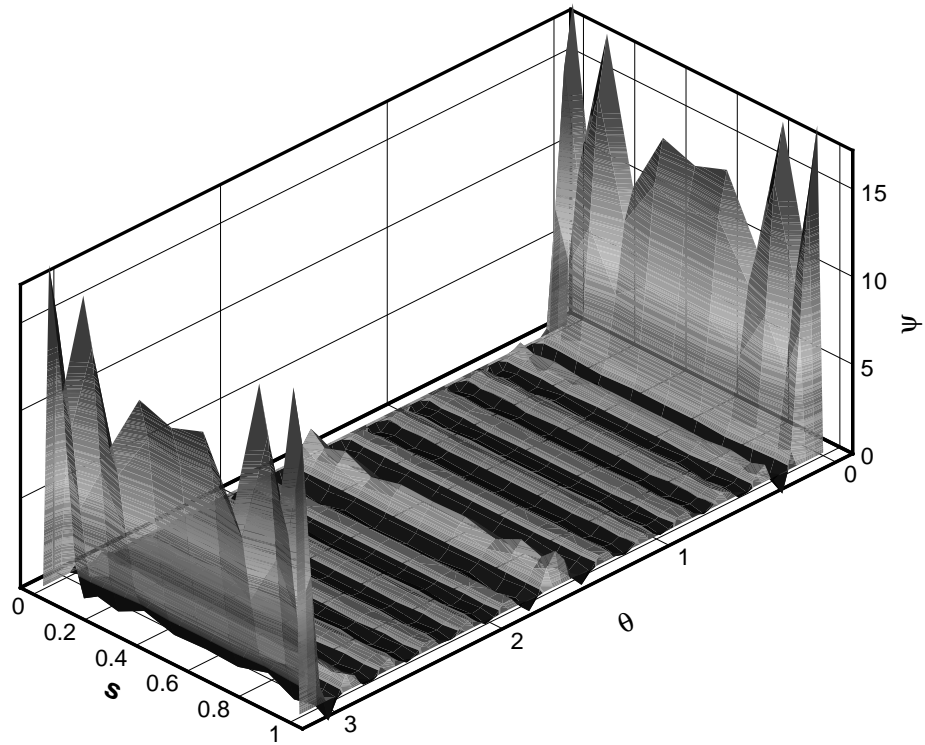


Figure 5.7: The pdf  $\psi$  for the uniaxial extensional flow (1.29) at  $\dot{\varepsilon}\tau_d = 300$  computed with  $N_u = N_s = 12$ .

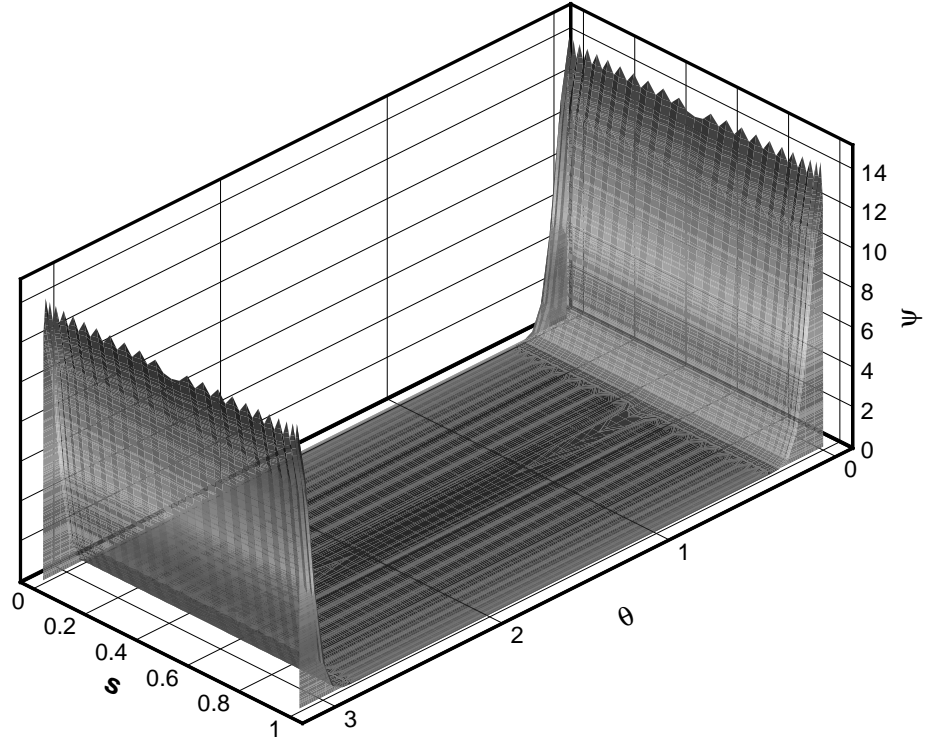


Figure 5.8: The pdf  $\psi$  for the uniaxial extensional flow (1.29) at  $\dot{\varepsilon}\tau_d = 300$  computed with  $N_u = N_s = 50$ .

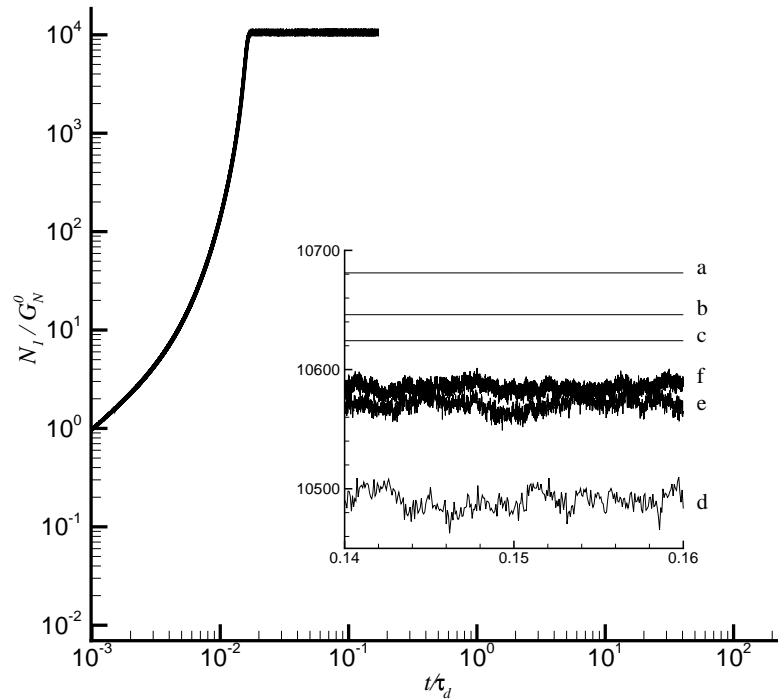


Figure 5.9: Evolution of  $N_1$  for the start-up uniaxial extensional flow (1.29) at  $\dot{\epsilon}\tau_d = 300$  with a zoom on steady state regime. a) FP-based simulation with  $N_u = N_s = 24$ ,  $\Delta t = 0.0025/\dot{\epsilon}$ , CPU time 109 seconds; b) the same with  $N_u = N_s = 28$ , CPU time 284 seconds; c) the same with  $N_u = N_s = 32$ , CPU time 437 seconds; d) stochastic simulation with  $N_{\text{sample}} = 10000$ ,  $N_{\text{block}} = 2$ ,  $\Delta t = 0.02/\dot{\epsilon}$ , CPU time 107 seconds; e) the same with  $\Delta t = 0.002/\dot{\epsilon}$ , CPU time 1063 seconds; f) the same with  $\Delta t = 0.0002/\dot{\epsilon}$ , CPU time 10609 seconds. All CPU times quoted are for a Pentium III 800 MHz machine.

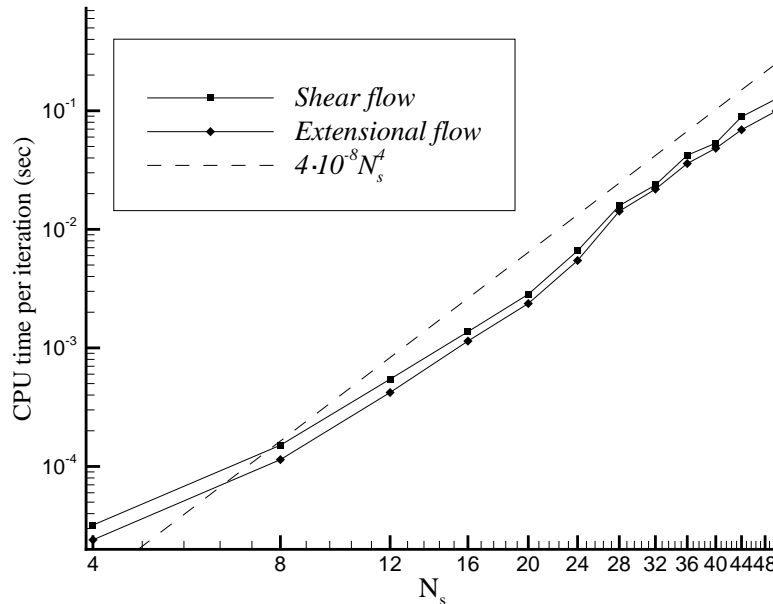


Figure 5.10: CPU time (seconds) per time step for the simple shear flow (5.31) and the start-up uniaxial extensional flow (1.29) vs. the configuration resolution  $N_s$ .

### Uniaxial extensional flow.

We report here the results for homogeneous start-up uniaxial extensional flow, for which the velocity gradient is given by (1.29).

Fig. 5.5 shows the relative errors for the normal stress difference  $N_1 = \tau_{zz} - \tau_{xx}$  after reaching the steady state (final time  $50/\dot{\epsilon}$ ) with the FP-based numerical method for three different values of the dimensionless extensional rate  $\dot{\epsilon}\tau_d = \{3, 80, 300\}$ . “Exact” solutions for these three extensional rates were calculated with  $N_u = N_s = 40$ . In a similar manner to Fig. 5.1, each data point in Fig. 5.5 is labelled first with the CPU time required to reach a final time of  $50/\dot{\epsilon}$  and then, in parentheses, the dimensionless time step  $\dot{\epsilon}\Delta t$  chosen.

The scheme again converges exponentially fast but, of course, the convergence rate decreases with increasing  $\dot{\epsilon}\tau_d$ . We are able to demonstrate even more clearly than in the previous subsection why this should be so.  $\psi$  is plotted in Figs. 5.6 and 5.7 for  $\dot{\epsilon}\tau_d = 3$  and 300 as a function of  $\theta$  and  $s$  (the solution for  $\psi$  does not depend on  $\varphi$  in this extensional flow since the velocity field is invariant to rotation about the  $z$ -axis). We see that the solution at  $\dot{\epsilon}\tau_d = 300$  has sharp boundary layers at  $s = 0$  and 1, which a mesh of  $N_u = N_s = 12$  is unable to resolve adequately; numerical oscillations being the result. Increasing the resolution in configuration space to  $N_u = N_s = 50$  captures the boundary layers satisfactorily, as shown in Fig. 5.8. However, our method is at least as efficient as the stochastic simulation for the same accuracy level as may be seen from Fig. 5.9. Reasonable agreement is found in the steady state values of  $N_1$  at  $\dot{\epsilon}\tau_d = 300$  predicted by run “c” of the FP method and run “f” of the stochastic method of [49]. Having said this, whereas run “c” required just 437 CPU seconds, the stochastic calculation took 10609 seconds using the same hardware. Although the convergence of both the FP and stochastic approaches is rather slow in the case of large extensional rates, the CPU time is always less for our method than for the stochastic one.

To facilitate comparisons of the computational cost for different levels of configuration mesh resolution for both the start-up shear flow (5.31) and the uniaxial extensional flow (1.29), we have computed the CPU time per time step for each of the values of  $N_u = N_s$  selected in Figs. 5.1 and 5.5. These results are presented in graphical form in Fig. 5.10 on a log-log scale and indicate that the CPU requirement increases in both cases no more rapidly than  $O(N_s^4)$ .

### 5.3.2 SU and modified SU models: comparison with experimental data

The results of comparing the predictions of the SU model and the modified SU model with experimental data for steady simple shear flow are presented in Fig. 5.11. In this figure the steady-state values of the shear stress  $\tau_{xy}$  and the first normal stress difference  $N_1$  are plotted as functions of the shear rate  $\dot{\gamma}$ . The experimental data used for comparison are taken from the thesis of Kahvand [72]. The test fluid is a solution in tricresyl phosphate of nearly monodisperse polystyrene with a molecular weight  $M_w$  of  $1.9 \times 10^6$  (polydispersity index of 1.2) and a polymer density of  $0.135 \text{ g/cm}^3$ . The average number of entanglements ( $Z$ ) of the fluid is estimated to be 10. The maximum chain stretching ratio ( $\lambda_{\max}$ ) of the fluid is equal to the square root of the number of Kuhn steps per entanglement according to the theory in [49] and is thus estimated to be 17.6. The parameters  $\tau_d$  and  $G_N^0$  are chosen in such a way that the cross-over point of the steady shear stress and first normal stress difference curves is predicted correctly.

For the two models, we then obtain  $\tau_d = 15$  s and  $G_N^0 = 1160$  Pa. With a value of  $\lambda_{max} = 17.6$  both the predictions of the original SU model and those of the modified SU model leave something to be desired. Firstly, the SU model predicts a slight decrease in the shear stress over a range of shear rates that extends from roughly  $\dot{\gamma} \approx 0.2s^{-1}$  to  $\dot{\gamma} \approx 2s^{-1}$ , which is inconsistent with the data and indicates an instability. Then, although good for low shear rates, the modified SU model predicts a sharp increase in the shear stress and first normal stress difference for  $\dot{\gamma} > 10s^{-1}$ , way above what has been measured experimentally. However, we found that a much smaller value (1.75) of  $\lambda_{max}$  gives more realistic predictions at high shear rates. The predictions of the shear stress by the modified SU model with the smaller value of  $\lambda_{max}$  are now in excellent agreement with the experimental data over the whole range of shear rates and the first normal stress difference increases gradually with shear rate, consistent with the experimental data. We note in passing that a similar reduction in  $\lambda_{max}$  brought about only a marginal improvement in the predictions of the original SU model. The same need for  $\lambda_{max}$  smaller than the theoretically determined value was documented by Ianniruberto and Marrucci [68] in their comparisons of shear data with the experimental results of Bercea et al. [9] for a semi-dilute solution of PMMA in toluene. The authors conjectured that the small value of  $\lambda_{max}$  that had to be taken in the simulations could be attributed to the crudeness of their single-relaxation-time model and that more realistic values could be used in multi-mode simulations: something that was shown to be true, at least partially, in a subsequent paper [69].

For all the fact that we have registered an improvement in the predictive capacities of the modified SU model by taking  $\lambda_{max} = 1.75$ , this situation is far from ideal. Numerical evidence that the need for an unphysically small value of  $\lambda_{max}$  finds its origin in the decoupling of Eqn. (5.13) for the chain stretch  $\lambda$  from Eqn. (5.1) is presented in [50].

### 5.3.3 Two-dimensional flow past a confined cylinder.

Having validated our numerical method for start-up shear flow and extensional flow in Sections 5.3.1 and 5.3.1 we now wish to evaluate, for the first time, the SU model in a complex flow. For this we choose the benchmark problem of flow past a confined cylinder (see Fig. 2.8) with a cylinder radius to half-channel ratio of  $R/H = 0.5$ . The cylinder radius  $R$  is chosen as the characteristic length scale with respect to which the spatial variables are non-dimensionalized (see (5.30)) and a Weissenberg number  $We$  for this flow is defined as

$$We = \bar{U}^* \equiv \frac{\bar{U}\tau_d}{R}, \quad (5.32)$$

where  $\bar{U}$  is the mean velocity in the inflow/outflow section of the channel. For all the calculations presented here we have chosen  $\lambda_{max} = 21$  and  $\tau_d/\tau_s = 50$ . Unless otherwise indicated in a figure caption, the discretization in configuration space was chosen as  $N_u = N_s = 14$ . The flow domain was decomposed into 30 spectral elements and, unless indicated otherwise, degree  $N = 10$  polynomials in both spatial directions were used for the representation of all dependent variables with the exception of the pressure. Upstream and downstream channel lengths of 50 cylinder radii were chosen and periodic boundary conditions for all the field variables except the pressure were applied (the pressure is periodic up to addition by a linear function).

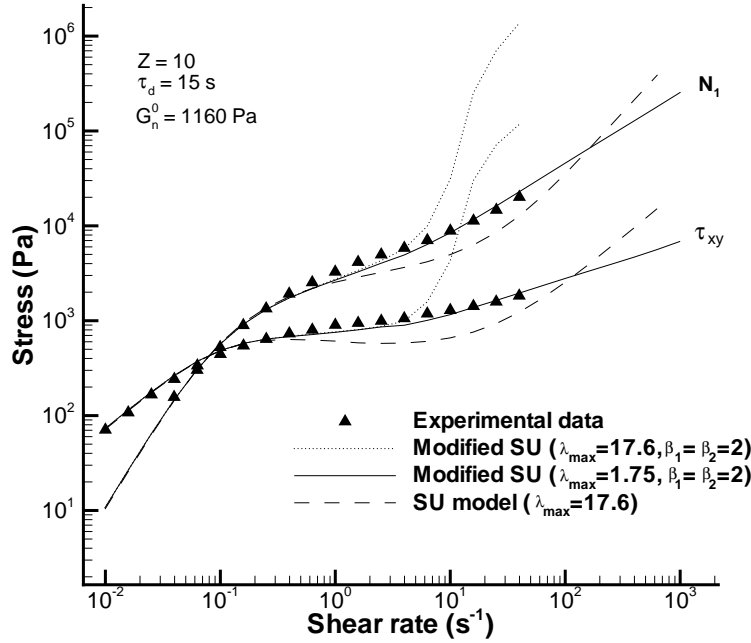


Figure 5.11: Steady-state values of shear stress  $\tau_{xy}$  and first normal stress difference  $N_1$  as functions of shear rate  $\dot{\gamma}$ . Shown are the predictions of the SU model, the modified SU model and experimental data [72].

### Comparison of SU model with DE and MLD models [114] at low Weissenberg numbers.

Direct comparisons of the SU results with those obtained for the single-mode DE model and the MLD model over long time intervals are not possible using our FP method - in neither case is there a diffusion term in  $\mathbf{u}$  in the FP equation, provoking numerical instabilities at modest Weissenberg numbers. However, we are able to compare our results at  $We = 0.3$  and  $0.6$  with those obtained for these two models by Peters et al. [114], who used a deformation field method [113] and the same value as above for  $\tau_d/\tau_s$ .

Throughout this subsection, for both our results and those of Peters et al., the dimensionless solvent viscosity  $\eta_s^*$  is set equal to  $0.05$ . At a Weissenberg number of  $0.6$ , the viscous stresses play an important but not yet dominant role, as may be seen from Fig. 5.12 where both the elastic and viscous contributions to the  $xx$ -component of the Cauchy stress are plotted along the axis of symmetry and on the cylinder surface. Fig. 5.13 shows that at Weissenberg numbers of  $0.3$  and  $0.6$  the departure from unity of the stretch parameter  $\lambda$  for the SU and MLD models on the cylinder surface is very small (less than  $5\%$  difference between the maximum and equilibrium values for the MLD model) with the stretch in the SU model even smaller than that of the MLD model. The extra contribution to the elastic stress due to chain stretching is therefore expected to be comparatively small and the stress-orientation tensor relations (5.9) and (5.16) essentially collapse to that of the DE model (5.3). This does not mean that the drags on the cylinder computed with the three models will be even approximately the same, however. Certainly, and the same was observed in [114], low Weissenberg numbers and a solvent viscosity  $\eta_s = 0.05G_N^0\tau_d$  tend to mask the difference between the single-mode DE model and the MLD model. However, as may be observed from Figs. 5.14 and 5.15 a slightly higher steady-state

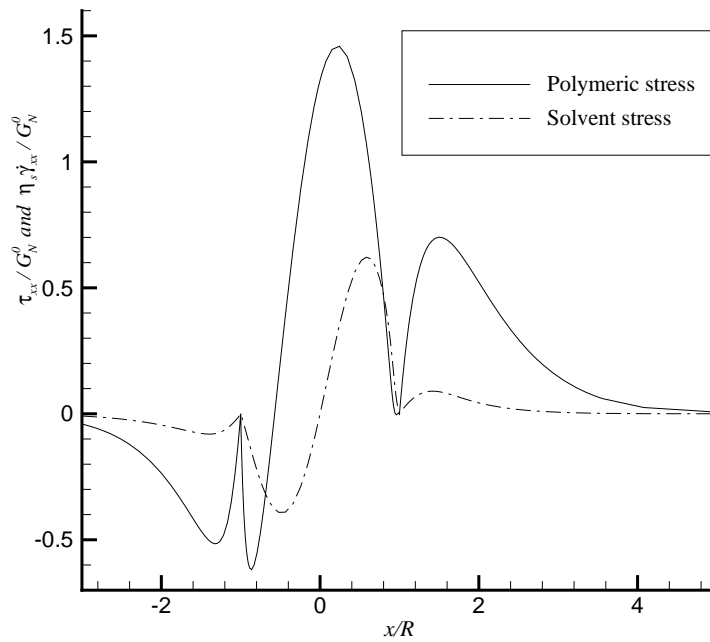


Figure 5.12: Flow past a confined cylinder: Non-dimensionalized solvent ( $\eta_s \dot{\gamma}_{xx}/G_N^0$ ) and elastic ( $\tau_{xx}/G_N^0$ ) contributions to the  $xx$ -component of the Cauchy stress tensor along the axis of symmetry and on the cylinder surface ( $-1 \leq x/R \leq 1$ ) for SU model at  $We = 0.6$ .  $\eta_s/G_N^0 \tau_d = 0.05$ ,  $\beta = 0$ ,  $N_u = N_s = 14$ ,  $N = 10$ .

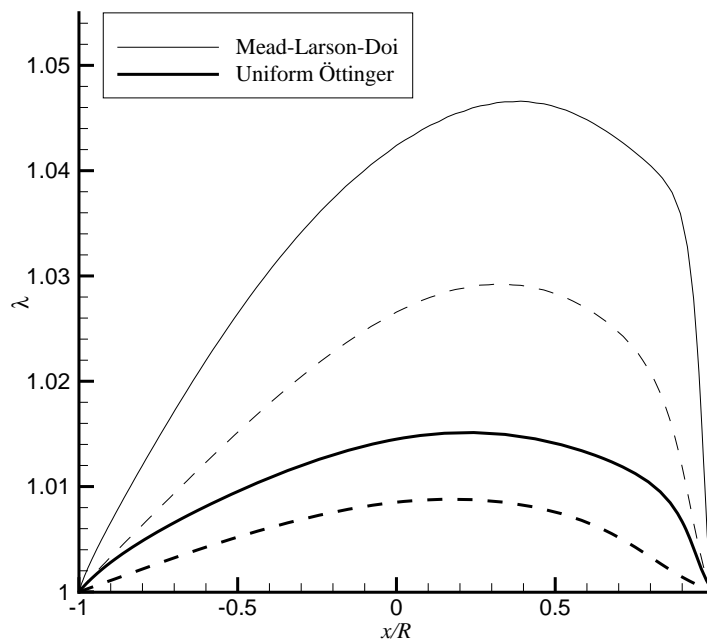


Figure 5.13: Flow past a confined cylinder: Comparison of stretch parameter  $\lambda$  along the cylinder wall for MLD model [114] and SU model. Dashed curves:  $We=0.3$ . Solid curves:  $We=0.6$ .

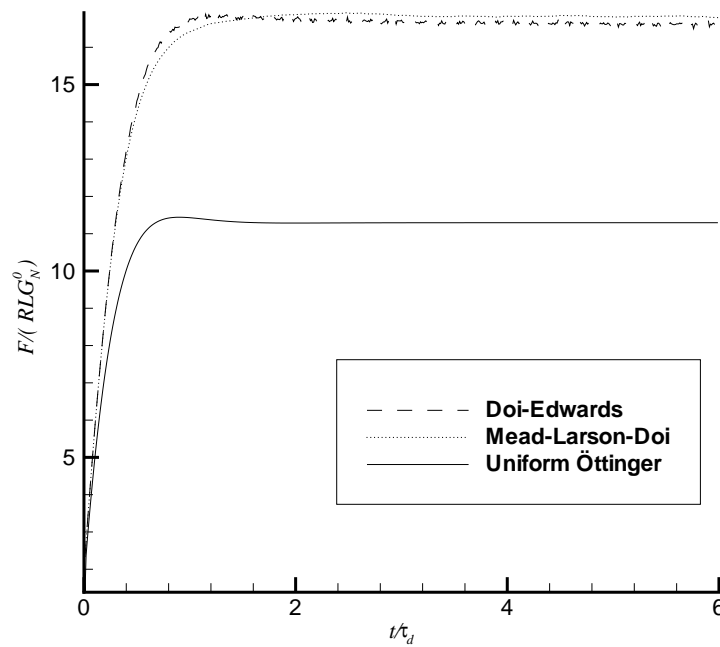


Figure 5.14: Flow past a confined cylinder: Comparison of dimensionless drag force for DE and MLD models [114] and SU model at  $We = 0.3$ .  $L$  denotes the length of the cylinder.

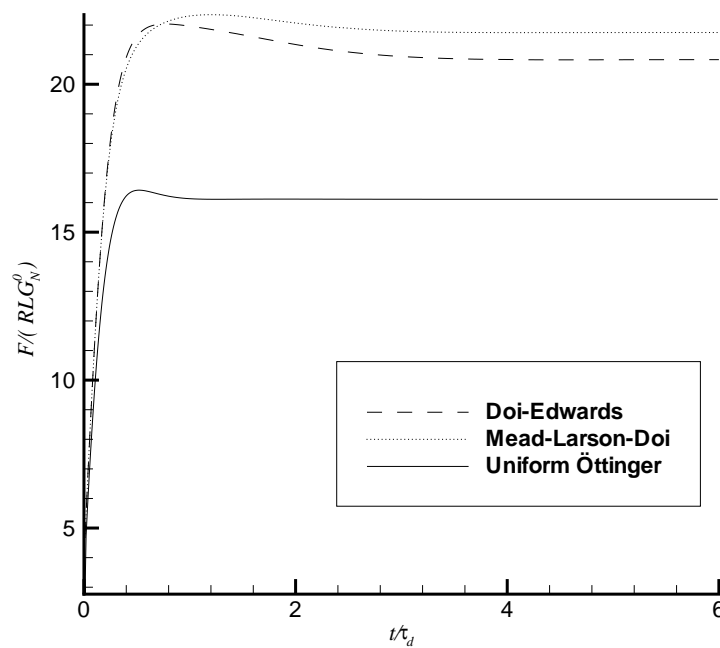


Figure 5.15: Flow past a confined cylinder: Comparison of dimensionless drag force for DE and MLD models [114] and SU model at  $We = 0.6$ .  $L$  denotes the length of the cylinder.



drag is found at  $We = 0.3$  and  $0.6$  with the MLD model than for the single-mode DE model, due to the small amount of tube stretching<sup>2</sup>.

Clearly, the explanation for the significant difference visible in Figs. 5.14 and 5.15 between the computed steady-state drag values for the SU model and the other two models must lie other than in the amount of tube stretch present. The key to the explanation lies in a comparison of the FP equations (5.8) and (5.14) for the single-mode DE and SU models. With  $\lambda \approx 1$ ,  $\lambda_{dissip} \approx 0$  and a noteworthy difference in this case between the two FP equations is seen to be the presence of the diffusion term  $(\delta_1/6\tau_d)\partial/\partial\mathbf{u} \cdot \partial\psi/\partial\mathbf{u}$  in (5.14). This double reptation term in the SU model introduces an additional relaxation mechanism for the polymer chains and results in a primitive relaxation time a half that of the DE model. Chains in the SU model have the possibility of escaping their tubes more quickly than those in the single-mode DE model. Hence they may escape high orientation with the flow field and as a consequence normal stresses are lower and so is the drag. As the flow rate is increased (going from Fig. 5.14 to Fig. 5.15) with  $\tau_d$  unaltered, both sets of drag values increase in magnitude but those for the DE and MLD models remain larger than that for the SU model.

### Computation for zero solvent viscosity: flow of a melt

Simulations of the SU fluid in the case of a zero solvent viscosity necessitates modification of the numerical treatment of the linear momentum equation (1.33). As a generalization of the approach adopted in the previous subsection we now introduce a variant of the DEVSS-G scheme [79] in the form

$$\nabla p^j - (\eta_s + \beta)\nabla^2 \mathbf{v}^j = \nabla \cdot \left( \boldsymbol{\tau}^j - \beta \left( \mathbf{G}^{j-1} + \mathbf{G}^{j-1T} \right) \right), \quad (5.33)$$

where  $\beta$  is a viscosity term.  $\mathbf{G}$  is a continuous second-order tensor which is obtained by filtering the velocity gradient tensor  $\nabla \mathbf{v}$  in each spectral element using an exponential filter [86] and then replacing the component values on elemental interfaces by the average values computed there from the adjoining elements. We note that the addition of the elliptic stabilization terms on the both sides of equation (5.33) does not modify the continuous linear momentum equations and furthermore that in the limit  $\beta \rightarrow 0$  we recapture our original scheme (1.33).

In validation of our numerical method for zero solvent viscosity we present in Figs. 5.16 and 5.17 some results of convergence studies at  $We = 0.6$ . In Fig. 5.16 profiles of  $\tau_{xx}$  (the most sensitive component of the elastic stress) along the axis of symmetry and on the cylinder surface are shown. We see that choosing two different values of  $\beta$  has little effect on the computed elastic stress, with only a small discrepancy visible near the peak value on the cylinder surface. Convergence with spatial mesh refinement ( $N = 8, 10$  and  $12$ ) is evident from Fig. 5.17 and convergence with refinement in configuration space may be deduced by comparing the  $N = 10$  plots from Figs. 5.16 and 5.17. The non-dimensionalized drag, being an integrated quantity (and therefore averaged and smoothed, in some sense) is considerably less sensitive than the components of the elastic stress to changes in the resolution in configuration and real space and this is apparent from Fig. 5.18 where for  $\eta_s = 0$  very close agreement at all times is seen between simulations on a coarse ( $N_u = N_s = N = 10$ ) and a fine ( $N_u = N_s = 14, N = 12$ ) mesh.

<sup>2</sup>We remark here that the drags computed in [114], and presented in Figs. 4 and 6 of this paper, were for only half a cylinder [115]. Accordingly, we have doubled all their drag values in our discussion of the results.

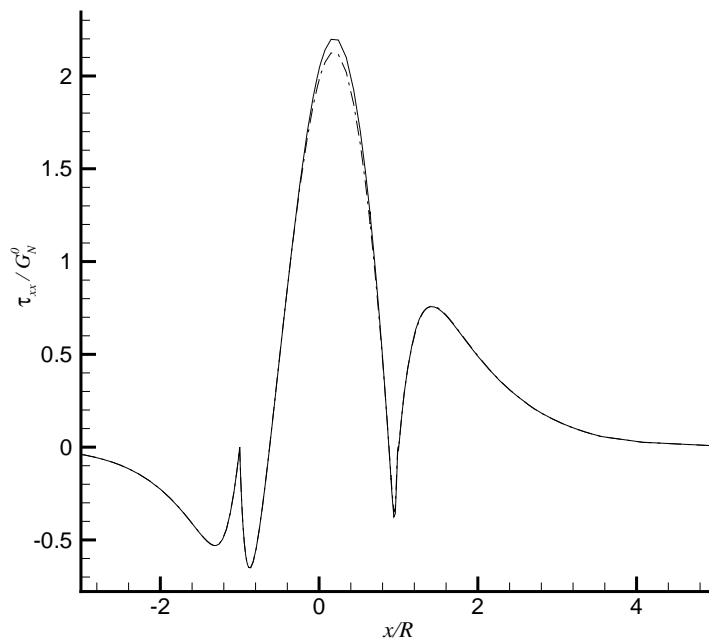


Figure 5.16: Flow past a confined cylinder: Non-dimensionalized stress  $\tau_{xx}/G_N^0$  along the axis of symmetry and on the cylinder surface ( $-1 \leq x/R \leq 1$ ) for SU model at  $We = 0.6$ .  $\eta_s = 0$ ,  $N_u = N_s = 10$ . Solid curve:  $\beta/G_N^0\tau_d = 0.5$ ,  $\Delta t/\tau_d = 0.005$ ,  $N_\alpha = 25$ . Dashed and dotted curve:  $\beta/G_N^0\tau_d = 1$ ,  $\Delta t/\tau_d = 0.01$ ,  $N_\alpha = 50$ .

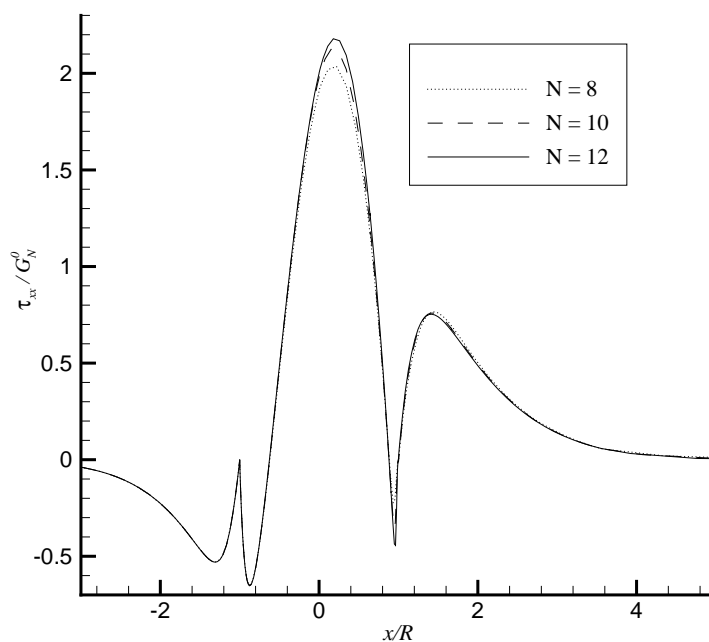


Figure 5.17: Flow past a confined cylinder: Non-dimensionalized stress  $\tau_{xx}/G_N^0$  along the axis of symmetry and on the cylinder surface ( $-1 \leq x/R \leq 1$ ) for SU model at  $We = 0.6$ .  $\eta_s = 0$ ,  $N_u = N_s = 14$ .

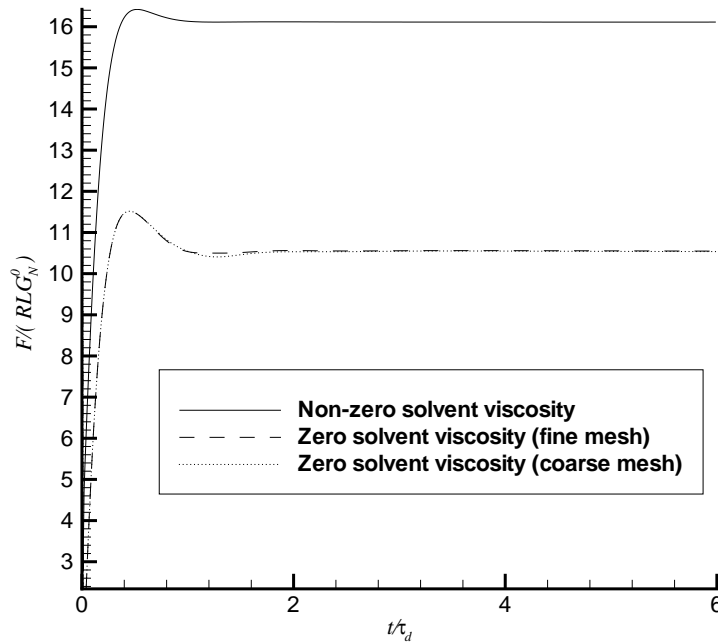


Figure 5.18: Flow past a confined cylinder: Dimensionless drag force for SU model at  $We = 0.6$ . Solid curve:  $\eta_s/G_N^0\tau_d = 0.05$ ,  $\beta = 0$ . Dashed and dotted curves:  $\eta_s = 0$ ,  $\beta/G_N^0\tau_d = 1$ . For the non-zero solvent viscosity results and the  $\eta_s = 0$  fine mesh computation  $N_u = N_s = 14$  and  $N = 12$ . For the  $\eta_s = 0$  coarse mesh computation  $N_u = N_s = N = 10$ .  $L$  denotes the length of the cylinder.

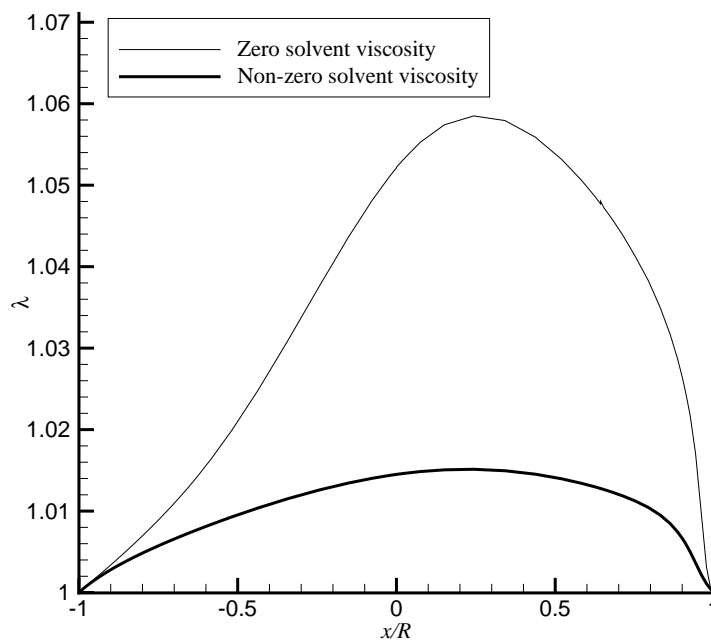


Figure 5.19: Flow past a confined cylinder: Stretch parameter  $\lambda$  on the cylinder surface for SU model at  $We = 0.6$ .  $N_u = N_s = 14$ ,  $N = 10$ . Thick curve:  $\eta_s/G_N^0\tau_d = 0.05$ ,  $\beta = 0$ . Fine curve:  $\eta_s = 0$ ,  $\beta/G_N^0\tau_d = 1$ .

Having established the reliability of our DEVSS-G scheme we now proceed to consider the effects on the drag, chain stretch and Cauchy stress of selecting  $\eta_s$  to be zero (melt) or non-zero (concentrated polymer solution). Consistent with our observations from Figs. 5.13-5.15 that chain stretching effects on the elastic stress are comparatively small, we note from Fig. 5.18 that a non-zero solvent viscosity results in a higher drag on the cylinder than in the zero solvent viscosity case but that this must be due to the viscous stresses rather than to chain contour stretching. This assertion is substantiated in Fig. 5.19 where for both zero and non-zero solvent viscosities the maximum stretch on the cylinder is less than 6% of the equilibrium value.

# Chapter 6

## Conclusions and future perspectives

This thesis describes the fruit of three years of work during which we have tried to construct more efficient and more robust methods for the simulations of viscoelastic flows.

From the viewpoint of robustness, some progress has been made in deriving new numerical methods for discretizing the Oldroyd B model, as is described in Chapter 3. Our efforts were inspired by the observation that the most challenging difficulty in the numerical solution of this model was the proper treatment of the non-linear terms in the constitutive equation (see Section 2.3) whereas most attention was paid in the past to stabilizing the transport term. That is why we have constructed new methods for the Oldroyd B model (taking its kinetic theory interpretation as a departure point) that respect certain properties of the system of differential equations in the hope of enhancing the robustness of simulations. As is evidenced in Chapter 3, our methods permit slightly higher Weissenberg numbers to be reached than via their conventional counterparts. However, convergence is obtained only at sufficiently low Weissenberg numbers and we are not in a position yet to decide with certainty whether their divergence should be attributed to the deficiency of the numerical approach or to that of the model. Much greater effort is needed on the levels of the underlying physics, mathematical analysis and numerical analysis.

Here are some tracks that may be followed in the future:

- A diffusion term [15, 42] and some terms describing the breaking of polymer chains [42] can be added to the Oldroyd B equation. In principle, this should help to increase the stability of numerical methods, since it will smooth the steep gradients in the stress field, that are present in the solutions of Oldroyd B (and other) models. El Kareh and Leal [42] were even able to prove the existence of solution at all Weissenberg numbers for a constitutive equation featuring a diffusion term and a term that keeps the stress bounded to model the breaking of polymers under tensions that exceed some bound. However, the diffusion coefficient is usually very small so that the proper inclusion of such a diffusion term will be problematic on the numerical level. On the level of modelling, the problem lies in formulating boundary conditions. Moreover, the appropriateness of modelling the polymeric solutions using suspensions of dumbbells is arguable near the wall and in regions where the flow is strongly non-homogeneous. Well established models for polymer chains breaking are not yet available either.
- On a purely numerical-analytical level, one could try to generalize the results of Keiller [73, 74]. Indeed, he showed that the stability of a finite difference scheme for the time-

dependent Couette and Poiseuille flows of an Oldroyd B fluid is determined by the ratio of resolution scales in the streamwise and cross-stream directions. It is probable that for more complex geometries a proper local assignment of this ratio in different points of the flow domain would also increase the stability of numerical methods.

All the above remarks concerning the stability of numerical methods also apply to kinetic theory models that do not possess closed-form constitutive equations. An additional problem here is the huge CPU and memory requirements of numerical simulations using such models. That was our motivation in constructing the deterministic methods based on the Fokker-Planck equation for the FENE dumbbell model (Chapter 4) and Öttinger SU reptation model (Chapter 5). We have showed that significant savings can be achieved by using such methods compared with stochastic simulation techniques. Stability properties of our methods in complex flow simulations are more or less the same as that of the stochastic simulations with the exception of the 3D FENE model, where higher Weissenberg numbers could be reached with the stochastic simulations.

Unfortunately, the Fokker-Planck methods are restricted to the models with low dimensional configuration space (essentially with dimension up to 3). The efficient implementation of deterministic methods for more complex models, such as bead-spring chains, would require much more work. The ideas presented in [111], for example, look promising.

# Appendix A

## Expression of some operators through spherical harmonics

The purpose of this appendix is to compute the expansion coefficients of the operators  $\mathcal{L}(\boldsymbol{\kappa})$  and  $\boldsymbol{\kappa} : \mathbf{u}\mathbf{u}$  with respect to the spherical harmonics  $\Phi_{n,m}^i$ . These coefficients are needed to construct the discretizations of the FP equations for the 3D FENE model and reptation models. The coefficients for the operator  $\mathcal{L}(\boldsymbol{\kappa})$  are borrowed from [45].

### A.1 Discretization of the operator $\mathcal{L}(\boldsymbol{\kappa})$

Let us define the operator  $\mathcal{L}(\boldsymbol{\kappa})$  by

$$\mathcal{L}(\boldsymbol{\kappa})\psi = \frac{\partial}{\partial \mathbf{u}} \cdot [(\mathbf{I} - \mathbf{u}\mathbf{u}) \cdot \boldsymbol{\kappa} \cdot \mathbf{u}\psi],$$

with a  $3 \times 3$  matrix  $\boldsymbol{\kappa}$ . We restrict our attention to matrices with  $\kappa_{13} = \kappa_{23} = \kappa_{31} = \kappa_{32} = 0$  and  $\text{tr}\boldsymbol{\kappa} = 0$ .

The operator  $\mathcal{L}(\boldsymbol{\kappa})$  can be written in spherical coordinates as

$$\begin{aligned} \mathcal{L}(\boldsymbol{\kappa})\psi &= \left( \mathbf{e}_\varphi \frac{1}{\sin \theta} \frac{\partial}{\partial \varphi} + \mathbf{e}_\theta \frac{\partial}{\partial \theta} \right) \cdot (A_\varphi \psi \mathbf{e}_\varphi + A_\theta \psi \mathbf{e}_\theta) \\ &= \frac{1}{\sin \theta} \left[ \frac{\partial}{\partial \varphi} (A_\varphi \psi) + \frac{\partial}{\partial \theta} (\sin \theta A_\theta \psi) \right], \end{aligned} \quad (\text{A.1})$$

where

$$A_\varphi = \boldsymbol{\kappa} \mathbf{u} \cdot \mathbf{e}_\varphi = \left( -\frac{\kappa_{11} - \kappa_{22}}{2} \sin 2\varphi + \frac{\kappa_{21} + \kappa_{12}}{2} \cos 2\varphi + \frac{\kappa_{21} - \kappa_{12}}{2} \right) \sin \theta,$$

and

$$A_\theta = \boldsymbol{\kappa} \mathbf{u} \cdot \mathbf{e}_\theta = \left( \frac{\kappa_{11} - \kappa_{22}}{2} \cos 2\varphi + \frac{\kappa_{21} + \kappa_{12}}{2} \sin 2\varphi - \frac{3\kappa_{33}}{2} \right) \sin \theta \cos \theta.$$

Plugging the above expression for  $A_\theta$  and  $A_\varphi$  into (A.1), we get after simplifications

$$\begin{aligned} \mathcal{L}(\boldsymbol{\kappa})\psi &= \left( -\frac{\kappa_{11} - \kappa_{22}}{2} \sin 2\varphi + \frac{\kappa_{21} + \kappa_{12}}{2} \cos 2\varphi + \frac{\kappa_{21} - \kappa_{12}}{2} \right) \frac{\partial\psi}{\partial\varphi} \\ &+ \left( \frac{\kappa_{11} - \kappa_{22}}{2} \cos 2\varphi + \frac{\kappa_{21} + \kappa_{12}}{2} \sin 2\varphi \right) \left( -3 \sin^2 \theta \psi + \sin \theta \cos \theta \frac{\partial\psi}{\partial\theta} \right) \\ &+ \left( \frac{\kappa_{11} + \kappa_{22}}{2} - \kappa_{33} \right) \left( (3 \cos^2 \theta - 1) \psi + \sin \theta \cos \theta \frac{\partial\psi}{\partial\theta} \right) \end{aligned} \quad (\text{A.2})$$

Let's put  $\psi = \Phi_{n,m}^i = P_n^m(\cos \theta) \cos(m\varphi - i\frac{\pi}{2})$  into (A.2), then we get, denoting  $\cos \theta$  by  $x$ ,

$$\begin{aligned} \mathcal{L}(\boldsymbol{\kappa})\Phi_{n,m}^i &= -m \left( -\frac{\kappa_{11} - \kappa_{22}}{2} \sin 2\varphi + \frac{\kappa_{21} + \kappa_{12}}{2} \cos 2\varphi + \frac{\kappa_{21} - \kappa_{12}}{2} \right) \sin \left( m\varphi - i\frac{\pi}{2} \right) \cdot P_n^m(x) \\ &+ \left( \frac{\kappa_{11} - \kappa_{22}}{2} \cos 2\varphi + \frac{\kappa_{21} + \kappa_{12}}{2} \sin 2\varphi \right) \cos \left( m\varphi - i\frac{\pi}{2} \right) \cdot S_n^m(x) \\ &- \frac{3\kappa_{33}}{2} \cos \left( m\varphi - i\frac{\pi}{2} \right) \cdot (S_n^m(x) + 2P_n^m(x)), \end{aligned} \quad (\text{A.3})$$

where

$$S_n^m(x) = (x^2 - 1) \left( 3P_n^m(x) + x \frac{d}{dx} P_n^m(x) \right).$$

Noting that for  $i = 0, 1$

$$\sin \left( \varphi - i\frac{\pi}{2} \right) = (-1)^i \cos \left( \varphi - (1-i)\frac{\pi}{2} \right), \quad (\text{A.4})$$

we can rewrite (A.3) as

$$\begin{aligned} \mathcal{L}(\boldsymbol{\kappa})\Phi_{n,m}^i &= \frac{\kappa_{11} - \kappa_{22}}{4} \left[ \cos \left( (m+2)\varphi - i\frac{\pi}{2} \right) \bar{S}_n^m(x) + \cos \left( (m-2)\varphi - i\frac{\pi}{2} \right) S_n^m \right] \\ &+ (-1)^i \frac{\kappa_{12} + \kappa_{21}}{4} \left[ \cos \left( (m+2)\varphi - (1-i)\frac{\pi}{2} \right) \bar{S}_n^m - \cos \left( (m-2)\varphi - (1-i)\frac{\pi}{2} \right) S_n^m \right] \\ &- \frac{3}{2} \kappa_{33} \cos \left( m\varphi - i\frac{\pi}{2} \right) \cdot S_n^m - (-1)^i m \frac{\kappa_{21} - \kappa_{12}}{2} \cos \left( m\varphi - (1-i)\frac{\pi}{2} \right) \cdot P_n^m(x) \end{aligned} \quad (\text{A.5})$$

where

$$S_n^\pm(x) = S_n^m(x) \pm mP_n^m(x) \text{ and } S_n^0(x) = S_n^m(x) + 2P_n^m(x).$$

The following identities hold for the spherical harmonics (the first and second ones are valid for all  $m \geq 0$  and the third one for all  $m \geq 2$ ):

$$\begin{aligned} \bar{S}_n^m(x) &= \frac{(n-2)}{(2n+1)(2n-1)} P_{n-2}^{m+2}(x) \\ &+ \frac{3}{(2n+3)(2n-1)} P_n^{m+2}(x) \\ &- \frac{(n+3)}{(2n+1)(2n+3)} P_{n+2}^{m+2}(x), \end{aligned}$$



Table A.1: Coefficients  $a_{n,j}^{m,k}$  from formula ( A.6).

$a_{n,n-2}^{m,m-2}$	$\frac{(n-2)(n+m)(n+m-1)(n+m-2)(n+m-3)(1-\delta_{m0})}{4(2n+1)(2n-1)}$
$a_{n,n}^{m,m-2}$	$\frac{3(n+m)(n+m-1)(n-m+1)(n-m+2)(1-\delta_{m0})}{4(2n+1)(2n+3)}$
$a_{n,n+2}^{m,m-2}$	$\frac{(n+3)(n-m+1)(n-m+2)(n-m+3)(n-m+4)(1-\delta_{m0})}{4(2n+1)(2n+3)}$
$a_{n,n-2}^{m,m}$	$\frac{(n-2)(n+m)(n+m-1)}{2(2n+1)(2n-1)}$
$a_{n,n}^{m,m}$	$\frac{3(n+m)(n-m)-n(2n-1)}{2(2n+1)(2n+3)}$ for $w_j^k$ or $\frac{m}{2}$ for $v_j^k$
$a_{n,n+2}^{m,m}$	$\frac{(n+3)(n-m+1)(n-m+2)}{2(2n+1)(2n+3)}$
$a_{n,n-2}^{m,m+2}$	$\frac{(n-2)(1+\delta_{m0})}{4(2n+1)(2n-1)}$
$a_{n,n}^{m,m+2}$	$\frac{3(1+\delta_{m0})}{4(2n+1)(2n+3)}$
$a_{n,n+2}^{m,m+2}$	$\frac{(n+3)(1+\delta_{m0})}{4(2n+1)(2n+3)}$

Table A.2: Coefficients  $w_j^k(\boldsymbol{\kappa})$  from formulas ( A.6) and ( A.9).

$w_{n-2}^{m-2}$	$w_n^{m-2}$	$w_{n+2}^{m-2}$	$w_{n-2}^m$	$w_n^m$	$w_{n+2}^m$	$w_{n-2}^{m+2}$	$w_n^{m+2}$	$w_{n+2}^{m+2}$
$\kappa_{11} - \kappa_{22}$	$\kappa_{11} - \kappa_{22}$	$\kappa_{22} - \kappa_{11}$	$3\kappa_{33}$	$-3\kappa_{33}$	$-3\kappa_{33}$	$\kappa_{11} - \kappa_{22}$	$\kappa_{11} - \kappa_{22}$	$\kappa_{22} - \kappa_{11}$

Table A.3: Coefficients  $v_j^k(\boldsymbol{\kappa})$  from formulas ( A.6) and ( A.9).

$v_{n-2}^{m-2}$	$v_n^{m-2}$	$v_{n+2}^{m-2}$	$v_{n-2}^m$	$v_n^m$	$v_{n+2}^m$	$v_{n-2}^{m+2}$	$v_n^{m+2}$	$v_{n+2}^{m+2}$
$\kappa_{12} + \kappa_{21}$	$\kappa_{12} + \kappa_{21}$	$-\kappa_{12} - \kappa_{21}$	0	$\kappa_{21} - \kappa_{12}$	0	$-\kappa_{12} - \kappa_{21}$	$-\kappa_{12} - \kappa_{21}$	$\kappa_{12} + \kappa_{21}$

$$\begin{aligned}
S_n^0(x) &= -\frac{(n-2)(n+m)(n+m-1)}{(2n+1)(2n-1)}P_{n-2}^m(x) \\
&+ \frac{3(n+m)(n-m) - n(2n-1)}{(2n+3)(2n-1)}P_n^m(x) \\
&+ \frac{(n+3)(n-m+1)(n-m+2)}{(2n+1)(2n+3)}P_{n+2}^m(x),
\end{aligned}$$

and

$$\begin{aligned}
S_n^+(x) &= \frac{(n-2)(n+m)(n+m-1)(n+m-2)(n+m-3)}{(2n+1)(2n-1)}P_{n-2}^{m-2}(x) \\
&+ \frac{3(n+m)(n+m-1)(n-m+1)(n-m+2)}{(2n+3)(2n-1)}P_n^{m-2}(x) \\
&- \frac{(n+3)(n-m+1)(n-m+2)(n-m+3)(n-m+4)}{(2n+1)(2n+3)}P_{n+2}^{m-2}(x).
\end{aligned}$$

Replacing  $S_n^\pm(x)$  and  $S_n^0(x)$  by their expressions given above we obtain

$$\mathcal{L}(\boldsymbol{\kappa})\Phi_{n,m}^i = \sum_{k=m-2}^{m+2} \sum_{j=n-2}^{n+2} a_{n,j}^{m,k} (w_j^k(\boldsymbol{\kappa})\Phi_{j,k}^i + (-1)^{1-i}v_j^k(\boldsymbol{\kappa})\Phi_{j,k}^{1-i}). \quad (\text{A.6})$$

All the non-zero coefficients  $a_{n,j}^{m,k}$ ,  $w_j^k(\boldsymbol{\kappa})$  and  $v_j^k(\boldsymbol{\kappa})$  are collected in the Tables A.1, A.2 and A.3, respectively.

## A.2 Discretization of the operator $\boldsymbol{\kappa} : \mathbf{uu}$

We now turn our attention to the operator  $\boldsymbol{\kappa} : \mathbf{uu}$ . We note that

$$\boldsymbol{\kappa} : \mathbf{uu} = \frac{\kappa_{11} + \kappa_{22}}{2} \sin^2 \theta + \frac{\kappa_{11} - \kappa_{22}}{2} \sin^2 \theta \cos 2\varphi + \frac{\kappa_{12} + \kappa_{21}}{2} \sin^2 \theta \sin 2\varphi + \kappa_{33} \cos^2 \theta.$$

Denoting  $x = \cos \theta$ , we have thus

$$\boldsymbol{\kappa} : \mathbf{uu} = \frac{\kappa_{11} - \kappa_{22}}{2} (1 - x^2) \cos 2\varphi + \frac{\kappa_{12} + \kappa_{21}}{2} (1 - x^2) \sin 2\varphi + \frac{\kappa_{33}}{2} (3x^2 - 1). \quad (\text{A.7})$$

Multiplying (A.7) by  $\Phi_{nm}^i = P_n^m(\cos \theta) \cos(m\varphi - i\frac{\pi}{2})$  and using (A.4), we obtain

$$\begin{aligned}
\boldsymbol{\kappa} : \mathbf{uu}\Phi_{nm}^i &= \frac{\kappa_{11} - \kappa_{22}}{4} (1 - x^2) P_n^m(x) \left[ \cos\left((m+2)\varphi - i\frac{\pi}{2}\right) + \cos\left((m-2)\varphi - i\frac{\pi}{2}\right) \right] \\
&+ (-1)^i \frac{\kappa_{12} + \kappa_{21}}{4} (1 - x^2) P_n^m(x) \left[ \cos\left((m+2)\varphi - (1-i)\frac{\pi}{2}\right) - \cos\left((m-2)\varphi - (1-i)\frac{\pi}{2}\right) \right] \\
&+ \frac{\kappa_{33}}{2} (3x^2 - 1) P_n^m(x) \cos\left(m\varphi - i\frac{\pi}{2}\right). \quad (\text{A.8})
\end{aligned}$$

Table A.4: Coefficients  $b_{n,j}^{m,k}$  from formula (A.9).

$b_{n,n-2}^{m,m-2}$	$\frac{(n+m)(n+m-1)(n+m-2)(n+m-3)(1-\delta_{m0})}{4(2n+1)(2n-1)}$
$b_{n,n}^{m,m-2}$	$\frac{(n-m+2)(n+m-1)(m(m-1)-n(n+1))}{2(2n+1)(2n+3)}$
$b_{n,n+2}^{m,m-2}$	$-\frac{(n-m+1)(n-m+2)(n-m+3)(n-m+4)(1-\delta_{m0})}{4(2n+1)(2n+3)}$
$b_{n,n-2}^{m,m}$	$\frac{(n+m)(n+m-1)}{2(2n+1)(2n-1)}$
$b_{n,n}^{m,m}$	$-\frac{3(n+m)(n-m)-n(2n-1)}{3(2n+1)(2n+3)}$ for $w_j^k$ or 0 for $v_j^k$
$b_{n,n+2}^{m,m}$	$-\frac{(n-m+1)(n-m+2)}{2(2n+1)(2n+3)}$
$b_{n,n-2}^{m,m+2}$	$\frac{1+\delta_{m0}}{4(2n+1)(2n-1)}$
$b_{n,n}^{m,m+2}$	$-\frac{1+\delta_{m0}}{2(2n+1)(2n+3)}$
$b_{n,n+2}^{m,m+2}$	$-\frac{1+\delta_{m0}}{4(2n+1)(2n+3)}$

As for the operator  $\mathcal{L}(\kappa)$ , we note the identities (the first and second ones are valid for all  $m \geq 0$  and the third one for all  $m \geq 2$ ):

$$\begin{aligned}
(1-x^2)P_n^m(x) &= \frac{(n+m-3)(n+m-2)(n+m-1)(n+m)}{(2n-1)(2n+1)}P_{n-2}^{m-2}(x) \\
&+ 2\frac{(n-m+2)(n+m-1)[m(m-1)-n(n+1)]}{(2n-1)(2n+3)}P_n^{m-2}(x) \\
&+ \frac{(n-m+1)(n-m+2)(n-m+3)(n-m+4)}{(2n+1)(2n+3)}P_{n+2}^{m-2}(x),
\end{aligned}$$

$$\begin{aligned}
(1-x^2)P_n^m(x) &= -\frac{(n+m-1)(n+m)}{(2n-1)(2n+1)}P_{n-2}^m(x) \\
&- 2\frac{n^2-m^2-(2n-1)(n+1)}{(2n-1)(2n+3)}P_n^m(x) \\
&- \frac{(n-m+1)(n-m+2)}{(2n+1)(2n+3)}P_{n+2}^m(x),
\end{aligned}$$

and

$$\begin{aligned}
 (1-x^2)P_n^m(x) &= \frac{1}{(2n-1)(2n+1)}P_{n-2}^{m+2}(x) \\
 &\quad - \frac{2}{(2n-1)(2n+3)}P_n^{m+2}(x) \\
 &\quad + \frac{1}{(2n+1)(2n+3)}P_{n+2}^{m+2}(x).
 \end{aligned}$$

We plug these identities into (A.8) and obtain

$$\boldsymbol{\kappa} : \mathbf{u}\mathbf{u}\Phi_{n,m}^i = \sum_{k=m-2}^{m+2} \sum_{j=n-2}^{n+2} b_{n,j}^{m,k} (w_j^k(\boldsymbol{\kappa})\Phi_{j,k}^i + (-1)^{1-i}v_j^k(\boldsymbol{\kappa})\Phi_{j,k}^{1-i}). \quad (\text{A.9})$$

All the non-zero coefficients  $w_j^k(\boldsymbol{\kappa})$ ,  $v_j^k(\boldsymbol{\kappa})$  and  $b_{n,j}^{m,k}$  are collected in the Tables A.2, A.3 and A.4, respectively.

# Appendix B

## Equilibrium solution for a FENE fluid in a tube with the account of non-homogeneous effects

In this appendix we study the kinetic theory of a FENE dumbbell solution under equilibrium conditions in the channel shown in Fig. 4.25(a) without assuming a linear variation in the configuration density function (cdf) over the length scale of a dumbbell. The results presented here generalize those of Brunn and Grisafi [25] who considered Hookean dumbbells in equilibrium.

Beginning with (4.74) in a no-flow situation, we see that the cdf  $\psi_{eq}^c$  satisfies

$$\begin{aligned}
 0 &= \int_{\mathbf{x}} \int_{\Gamma^{\pm}(\mathbf{x})} \left[ \left( \frac{2kT}{\zeta} \frac{\partial \psi_{eq}^c}{\partial \mathbf{q}} + \frac{2}{\zeta} \mathbf{F}(\mathbf{q}) \psi_{eq}^c \right) \cdot \mathbf{n} \varphi^c \right] dS d\mathbf{x} \\
 &\quad - \int_{\mathbf{x}} \int_{D(\mathbf{x})} \left( \frac{2kT}{\zeta} \frac{\partial \psi_{eq}^c}{\partial \mathbf{q}} + \frac{2}{\zeta} \mathbf{F}(\mathbf{q}) \psi_{eq}^c \right) \cdot \frac{\partial \varphi^c}{\partial \mathbf{q}} d\mathbf{q} d\mathbf{x} \\
 &\quad + \frac{kT}{2\zeta} \int_{\mathbf{x}} \int_{D(\mathbf{x})} \frac{\partial^2 \psi_{eq}^c}{\partial \mathbf{r}^2} \varphi^c d\mathbf{q} d\mathbf{x}.
 \end{aligned} \tag{B.1}$$

This has solution

$$\psi_{eq}^c(\mathbf{x}, \mathbf{q}) = \begin{cases} \psi_0(\mathbf{q}), & \text{if } \mathbf{x} \pm \mathbf{q}/2 \in \Omega = (-\infty, \infty) \times [-d, d], \\ 0, & \text{otherwise,} \end{cases} \tag{B.2}$$

where

$$\psi_0(\mathbf{q}) = C \left( 1 - \frac{|\mathbf{q}|^2}{R_{\max}^2} \right)^{b/2}, \tag{B.3}$$

is the equilibrium cdf for the homogeneous-flow FENE model and which satisfies

$$\mathbf{F}(\mathbf{q}) \psi_0(\mathbf{q}) + kT \frac{\partial \psi_0(\mathbf{q})}{\partial \mathbf{q}} = \mathbf{0}. \tag{B.4}$$

From (1.15) and (B.2) we may write the spring force contribution to the equilibrium stress tensor as

$$\begin{aligned}
 \boldsymbol{\sigma}_{eq}^C(\mathbf{r}) &= \int_{|\mathbf{q}| < R_{\max}} \int_{s=\alpha(y, R_y)}^{\beta(y, R_y)} \mathbf{F}(\mathbf{q}) \mathbf{q} \psi_0(\mathbf{q}) ds d\mathbf{q}, \\
 &= \int_{|\mathbf{q}| < R_{\max}} (\beta(y, R_y) - \alpha(y, R_y)) \mathbf{F}(\mathbf{q}) \mathbf{q} \psi_0(\mathbf{q}) d\mathbf{q},
 \end{aligned} \tag{B.5}$$

where  $\mathbf{r} = (x, y)^T$  and limits  $\alpha$  and  $\beta$  on  $s$  have been chosen to ensure that  $\mathbf{r} + (s - 1/2)\mathbf{q} \in \Omega$ , i.e.  $|y + (s - 1/2)R_y| < d$ . It is straightforward to show that

$$\beta(y, R_y) - \alpha(y, R_y) = \min \left( 1, \left( \frac{d - |y|}{|R_y|} \right) \right). \quad (\text{B.6})$$

We appeal to (B.4) to rewrite (B.5) as

$$\boldsymbol{\sigma}_{eq}^C = -kT \int_{|\mathbf{q}| < R_{\max}} (\beta(y, R_y) - \alpha(y, R_y)) \mathbf{q} \frac{\partial \psi_0(\mathbf{q})}{\partial \mathbf{q}} d\mathbf{q}, \quad (\text{B.7})$$

and, using integration by parts,

$$\boldsymbol{\sigma}_{eq}^C = kT \int_{|\mathbf{q}| < R_{\max}} \frac{\partial}{\partial \mathbf{q}} ((\beta(y, R_y) - \alpha(y, R_y)) \mathbf{R}) \psi_0(\mathbf{q}) d\mathbf{q}. \quad (\text{B.8})$$

Hence,

$$\begin{aligned} \sigma_{eq,xx}^C(y) &= kT \int_{|\mathbf{q}| < R_{\max}} \frac{\partial}{\partial R_x} ((\beta(y, R_y) - \alpha(y, R_y)) R_x) \psi_0(\mathbf{q}) d\mathbf{q}, \\ &= kT \int_{|\mathbf{q}| < R_{\max}} (\beta(y, R_y) - \alpha(y, R_y)) \psi_0(\mathbf{q}) d\mathbf{q}, \end{aligned} \quad (\text{B.9})$$

and

$$\sigma_{eq,yy}^C(y) = kT \int_{|\mathbf{q}| < R_{\max}} \frac{\partial}{\partial R_y} ((\beta(y, R_y) - \alpha(y, R_y)) R_y) \psi_0(\mathbf{q}) d\mathbf{q}. \quad (\text{B.10})$$

Note that

$$\frac{\partial}{\partial R_y} ((\beta(y, R_y) - \alpha(y, R_y)) R_y) = \begin{cases} \frac{\partial R_y}{\partial R_y} = 1, & \text{if } d - |y| > |R_y| \\ \frac{\partial}{\partial R_y} \left( \frac{d - |y|}{|R_y|} R_y \right) = 0, & \text{if } d - |y| < |R_y| \end{cases}$$

Hence, from (B.10)

$$\sigma_{eq,yy}^C(y) = kT \int_{\{|\mathbf{q}| < R_{\max}\} \cap \{|R_y| < d - |y|\}} \psi_0(\mathbf{q}) d\mathbf{q}, \quad (\text{B.11})$$

and from (B.9) and (B.11) we see that

$$\sigma_{eq,xx}^C - \sigma_{eq,yy}^C = kT \int_{\{|\mathbf{q}| < R_{\max}\} \cap \{|R_y| \geq d - |y|\}} \left( \frac{d - |y|}{|R_y|} \right) \psi_0(\mathbf{q}) d\mathbf{q} \geq 0 \quad (\text{B.12})$$

with the inequality strict provided  $|y| \in (d - R_{\max}, d)$ . Hence the equilibrium stress field is anisotropic, as observed by Brunn and Grisafi [25] for Hookean dumbbells.

Troubling as an anisotropic stress field at equilibrium may appear at first sight, there is in fact no inconsistency between this and equilibrium conditions since

$$\nabla \cdot (\boldsymbol{\sigma}_{eq}^C + \boldsymbol{\sigma}_{eq}^K) = \mathbf{0}.$$

There are two results that need to be shown in order to substantiate this. First, and rather obviously,

$$\sigma_{eq,xy}^C(y) = kT \int_{|\mathbf{q}| < R_{\max}} \frac{\partial}{\partial R_x} ((\beta(y, R_y) - \alpha(y, R_y)) R_y) \psi_0(\mathbf{q}) d\mathbf{q} = 0. \quad (\text{B.13})$$

Secondly, the  $yy$ -component of the total equilibrium Cauchy stress is independent of  $y$ . To see this, we introduce the integrals

$$I_1 = \int_{|\mathbf{q}| < R_{\max}} \psi_0(\mathbf{q}) d\mathbf{q}, \quad (\text{B.14})$$

and

$$I_2 = \int_{\{|\mathbf{q}| < R_{\max}\} \cap \{|R_y| \geq d - |\mathbf{q}|\}} \psi_0(\mathbf{q}) d\mathbf{q}. \quad (\text{B.15})$$

Then, we note that the integrand in (1.17) is non-zero only for  $\mathbf{q}$  such that  $\mathbf{r} + \mathbf{q} \in \Omega$ , i.e.  $y + R_y \in (-d, d)$ . Hence, we obtain in the case  $y > 0$ , for example, that

$$\sigma_{eq,yy}^K = -2kTn(y) = -2kT \int_{\{|\mathbf{q}| < R_{\max}\} \cap \{R_y < d - y\}} \psi_0(\mathbf{q}) d\mathbf{q}. \quad (\text{B.16})$$

or, by the symmetry of  $\psi_0(\mathbf{q})$

$$\sigma_{eq,yy}^K = -2kT(I_1 - I_2/2).$$

Thus, we can use (B.11) to obtain

$$\begin{aligned} \sigma_{yy}^C + \sigma_{yy}^K &= kT(I_1 - I_2) - 2kT(I_1 - I_2/2) \\ &= -kTI_1, \end{aligned} \quad (\text{B.17})$$

and this is independent of  $y$ .





# Appendix C

## Weak approximation of stochastic differential equations with reflecting boundary conditions

In this appendix we present a scheme of weak order 1.0 for an Itô stochastic differential equation (SDE) with reflecting boundary condition. This scheme is used in the stochastic simulations of the strongly non-homogeneous Poiseuille flow described in Section 4.5.

Consider the SDE of the form

$$dX_t = A(X_t)dt + BdW_t \quad (\text{C.1})$$

with a constant coefficient  $B$ . We restrict  $X_t$  to be  $> 0$  for all  $t$  and impose the reflecting boundary condition at  $x = 0$ . The pdf  $p(t, x)$  of the stochastic process  $X_t$  satisfies the FP equation

$$\frac{\partial p}{\partial t}(t, x) = -\frac{\partial}{\partial x}(A(x)p(t, x)) + \frac{1}{2}B^2\frac{\partial^2 p}{\partial x^2}(t, x) \quad (\text{C.2})$$

with a boundary condition at  $x = 0$  of the form

$$-A(0)p(t, 0) + \frac{1}{2}B^2\frac{\partial p}{\partial x}(t, 0) = 0. \quad (\text{C.3})$$

Let us consider a semi-implicit Euler discretization of the SDE (C.1)

$$X_{n+1} - A(X_{n+1})\Delta t = X_n + B\Delta W_n + Y_n \quad (\text{C.4})$$

where  $X_n$  is an approximation of  $X_t$  at the discrete time  $t_n = n\Delta t$ ,  $\Delta W_n$  is an approximation of  $W(t_{n+1}) - W(t_n)$  and  $Y_n$  is a random variable representing a possible reflection at  $x = 0$ .  $Y_n$  should be chosen so that  $X_n + B\Delta W_n + Y_n$  is always  $> 0$ . The function  $A(x)$  is supposed to be such that the equation  $x - A(x)\Delta t = f$  has a unique solution  $x > 0$  provided  $f > 0$ . Hence the equation (C.4) is solvable for  $X_{n+1}$ .

Such a scheme (with an explicit treatment of the drift term and  $Y_n$  making the process  $X_n$  reflect with respect to 0 once it crosses it) is known to be of weak order 1 if the increments  $\Delta W_n$  are Gaussian variables with the mean 1 and the variance 1 (see [22] for a proof in a very general setting). It is also known that in numerical simulations of SDE on the whole line (without boundary conditions)  $\Delta W_n$  can be chosen arbitrarily, as long as it has the correct mean and

variance, without losing the order of weak convergence. In this note we are interested in the question whether the same is true for an SDE with reflections, i.e. we want to construct a scheme with weak order 1 when a distribution other than Gaussian is used for  $\Delta W_n$ . In view of the analysis below, we choose for  $\Delta W_n$  the two-point distribution:

$$P(\Delta W_n = \pm\sqrt{\Delta t}) = \frac{1}{2}.$$

We see now that a numerical reflection ( $X_n + B\Delta W_n < 0$ ) can occur only if  $X_n \in (0, B\sqrt{\Delta t})$  and  $\Delta W_n = -\sqrt{\Delta t}$ . Therefore the most natural choice for the random variable  $Y_n$  seems to be

$$Y_n = \begin{cases} 2(B\sqrt{\Delta t} - X_n), & \text{if } X_n \in (0, B\sqrt{\Delta t}) \text{ and } \Delta W_n = -\sqrt{\Delta t}, \\ 0, & \text{otherwise.} \end{cases} \quad (\text{C.5})$$

It turns out, however, that the scheme (C.4) with (C.5) converges weakly only with order 0.5.

Consider arbitrary sufficiently smooth function  $g(x)$ . We apply  $g$  to both sides of (C.4) and take the expectation to arrive at

$$\int_0^\infty g(x - A(x)\Delta t)p_{n+1}(x)dx = \int_0^\infty \langle g(x + B\Delta W_n + Y_n) \rangle_x p_n(x)dx \quad (\text{C.6})$$

where  $p_n(x)$  is the pdf of  $X_n$  and  $\langle \cdot \rangle_x$  denotes the conditional expectation of the quantity in parentheses under the hypothesis  $X_n = x$ . Taking into account that  $\Delta W_n$  and  $Y_n$  are of order  $\sqrt{\Delta t}$  and that  $Y_n$  vanishes for  $X_n \geq B\sqrt{\Delta t}$ , we can deduce from (C.6) that

$$\begin{aligned} \int_0^\infty (g(x) - g'(x)A(x)\Delta t)p_{n+1}(x)dx &= \int_0^\infty \left( g(x) + \frac{1}{2}g''(x)B^2\Delta t \right) p_n(x)dx \\ &+ \int_0^{B\sqrt{\Delta t}} \left( g'(x)\langle Y_n \rangle_x + \frac{1}{2}g''(x)(\langle Y_n^2 \rangle_x + 2B\langle \Delta W_n Y_n \rangle_x) \right) p_n(x)dx + O(\Delta t^2) \end{aligned}$$

or

$$\begin{aligned} \int_0^\infty (g(x) - g'(x)A(x)\Delta t)p_{n+1}(x)dx &= \int_0^\infty \left( g(x) + \frac{1}{2}g''(x)B^2\Delta t \right) p_n(x)dx \\ &+ g'(0)p_n(0) \int_0^{B\sqrt{\Delta t}} \langle Y_n \rangle_x dx + (g''(0)p_n(0) + g'(0)p'_n(0)) \int_0^{B\sqrt{\Delta t}} x \langle Y_n \rangle_x dx \\ &+ \frac{1}{2}g''(0)p_n(0) \int_0^{B\sqrt{\Delta t}} (\langle Y_n^2 \rangle_x + 2B\langle \Delta W_n Y_n \rangle_x) dx + O(\Delta t^2) \end{aligned} \quad (\text{C.7})$$

We can evaluate the integrals as

$$\int_0^{B\sqrt{\Delta t}} \langle Y_n \rangle_x dx = \int_0^{B\sqrt{\Delta t}} (B\sqrt{\Delta t} - x)dx = \frac{B^2\Delta t}{2}, \quad (\text{C.8})$$

$$\int_0^{B\sqrt{\Delta t}} x \langle Y_n \rangle_x dx = \int_0^{B\sqrt{\Delta t}} x(B\sqrt{\Delta t} - x)dx = \frac{B^3\Delta t^{3/2}}{6}, \quad (\text{C.9})$$

$$\begin{aligned}
\int_0^{B\sqrt{\Delta t}} (\langle Y_n^2 \rangle_x + 2B \langle \Delta W_n Y_n \rangle_x) dx &= \int_0^{B\sqrt{\Delta t}} [2(B\sqrt{\Delta t} - x)^2 - 2B\sqrt{\Delta t}(B\sqrt{\Delta t} - x)] dx \\
&= -\frac{B^3 \Delta t^{3/2}}{3}.
\end{aligned} \tag{C.10}$$

Substituting (C.8)-(C.10) into (C.7), we see that

$$\begin{aligned}
\int_0^\infty (g(x) - g'(x)A(x)\Delta t)p_{n+1}(x)dx &= \int_0^\infty \left( g(x) + \frac{1}{2}g''(x)B^2\Delta t \right) p_n(x)dx \\
&+ g'(0)p_n(0)\frac{B^2\Delta t}{2} + g'(0)p'_n(0)\frac{B^3\Delta t^{3/2}}{6} + O(\Delta t^2),
\end{aligned}$$

or, after two integrations by parts and dividing by  $\Delta t$

$$\begin{aligned}
\int_0^\infty g(x)\frac{p_{n+1}(x) - p_n(x)}{\Delta t} dx &= \int_0^\infty g(x) \left( -(A(x)p_{n+1}(x))' + \frac{1}{2}B^2p''_n(x) \right) dx \\
&+ g(0) \left( -A(0)p_{n+1}(0) + \frac{1}{2}B^2p'_n(0) \right) + g'(0)p'_n(0)\frac{B^3\sqrt{\Delta t}}{6} + O(\Delta t). \tag{C.11}
\end{aligned}$$

We see that (C.11) approximates the FP equation (C.2) with boundary conditions (C.3) only with order 0.5. The reason for this is the presence of terms of order  $(\Delta t)^{3/2}$  in (C.7), i.e. of non-zero integrals (C.9) and (C.10).

To increase the order of the convergence, we can modify the definition of  $Y_n$  so that the integrals (C.9) and (C.10) would be identically 0 while maintaining the value of the integral (C.8). A simple choice of such a definition is provided by

$$Y_n = \begin{cases} 3(B\sqrt{\Delta t} - X_n), & \text{if } X_n \in (0, B\sqrt{\Delta t}) \text{ and } \Delta W_n = -\sqrt{\Delta t}, \\ B\sqrt{\Delta t} - 3X_n, & \text{if } X_n \in (0, B\sqrt{\Delta t}) \text{ and } \Delta W_n = \sqrt{\Delta t}, \\ 0, & \text{if } X_n \geq B\sqrt{\Delta t}. \end{cases} \tag{C.12}$$

To see that this choice of  $Y_n$  is a good one we note, first of all, that it ensures the positivity of  $X_n$  for all  $n$ . Indeed

$$X_n + B\Delta W_n + Y_n = \begin{cases} 2(B\sqrt{\Delta t} - X_n), & \text{if } X_n \in (0, B\sqrt{\Delta t}), \\ X_n + B\Delta W_n, & \text{if } X_n \geq B\sqrt{\Delta t}. \end{cases} \tag{C.13}$$

Secondly, we note that the expansion (C.7) is still valid for the new  $Y_n$  and the integrals (C.8)-(C.10) can now be evaluated as

$$\begin{aligned}
\int_0^{B\sqrt{\Delta t}} \langle Y_n \rangle_x dx &= \int_0^{B\sqrt{\Delta t}} \left[ \frac{3}{2}(B\sqrt{\Delta t} - x) + \frac{1}{2}(B\sqrt{\Delta t} - 3x) \right] dx = \frac{B^2\Delta t}{2}, \\
\int_0^{B\sqrt{\Delta t}} x \langle Y_n \rangle_x dx &= \int_0^{B\sqrt{\Delta t}} \left[ \frac{3}{2}x(B\sqrt{\Delta t} - x) + \frac{1}{2}x(B\sqrt{\Delta t} - 3x) \right] dx = 0, \\
\int_0^{B\sqrt{\Delta t}} (\langle Y_n^2 \rangle_x + 2B \langle \Delta W_n Y_n \rangle_x) dx &= \int_0^{B\sqrt{\Delta t}} \left[ \frac{9}{2}(B\sqrt{\Delta t} - x)^2 + \frac{1}{2}(B\sqrt{\Delta t} - 3x)^2 \right] dx \\
&+ 2B\sqrt{\Delta t} \int_0^{B\sqrt{\Delta t}} \left[ -\frac{3}{2}(B\sqrt{\Delta t} - x) + \frac{1}{2}(B\sqrt{\Delta t} - 3x) \right] dx = 0.
\end{aligned}$$

Substituting these integrals into (C.7), we see now that the terms of order  $\Delta t^{3/2}$  are absent from it so that the the pdf of  $X_n$  satisfies

$$\begin{aligned} \int_0^\infty g(x) \frac{p_{n+1}(x) - p_n(x)}{\Delta t} dx &= \int_0^\infty g(x) \left( -(A(x)p_{n+1}(x))' + \frac{1}{2}B^2 p_n''(x) \right) dx \\ &+ g(0)(-A(0)p_{n+1}(0) + \frac{1}{2}B^2 p_n'(0)) + O(\Delta t), \end{aligned}$$

which is a first order approximation of the FP equation (C.2) with boundary conditions (C.3).

# Bibliography

- [1] M. V. Apostolakis, V. G. Mavrantzas and A. N. Beris, *Stress gradient-induced migration effects in the Taylor-Couette flow of a dilute polymer solution*, J. Non-Newtonian Fluid Mech. **102** (2002) 409-445.
- [2] R. C. Armstrong, R. Nayak and R. A. Brown, *The use of kinetic theory and microstructural models in the analysis of complex flows of viscoelastic liquids* in: Aït-Kadi, J.M. Dealy, D.F. James and M.C. Williams. *Proceedings of the 12th International Congress on Rheology*, Laval university, Québec, Aug. 18-23, 1996.
- [3] K. Atalık and R. Keunings, *Non-linear temporal stability analysis of viscoelastic plane channel flows using a fully-spectral method*, J. Non-Newtonian Fluid Mech. **102** (2002) 299–319.
- [4] M. Avgousti and A. N. Beris, *Non-axisymmetrical modes in viscoelastic Taylor-Couette flow*, J. Non-Newtonian Fluid Mech. **50** (1993) 225-251.
- [5] M. Avgousti, B. C. Liu and A. N. Beris, *Spectral methods for the viscoelastic time-dependent flow equations with applications to Taylor-Couette flow* Int. J. Numer. Meth. Fluids **17** (1993) 49-74.
- [6] F. P. T. Baaijens, S. H. A. Selen, H. P. W. Baaijens, G. W. M. Peters and H. E. H. Meijer, *Viscoelastic flow past a confined cylinder of a low density polyethylene melt* J. Non-Newtonian Fluid Mech. **68** (1997) 173-203.
- [7] J. Baranger, C. Guillopé and J.-C. Saut, *Mathematical analysis of differential models for viscoelastic fluids*, in: J.M. Piau and J.F. Agassant, eds., *Rheology of Polymer Melt Processing*, Elsevier Science, Amsterdam (1996) 199-236.
- [8] J. Baranger and D. Sandri, *A formulation of Stokes's problem and the linear elasticity equations suggested by the Oldroyd model for viscoelastic flow* Math. Model. Num. Anal. **26** (1992) 331-345.
- [9] M. Bercea, C. Peiti, B. Simionescu and P. Navard, *Shear rheology of semidilute poly(methyl methacrylate) solutions*, Macromolecules **26** (1993) 7095-7096.
- [10] A. Beris, R. C. Armstrong and R. A. Brown, *Spectral/Finite-element calculation of flow of a Maxwell fluid between eccentric rotating cylinders* J. Non-Newtonian Fluid Mech. **22** (1987) 129-167.

- [11] A. N. Beris, M. Avgousti and A. Souvaliotis, *Spectral calculations of viscoelastic flows – evaluation of the Giesekus constitutive equation in model flow problems* J. Non-Newtonian Fluid Mech. **44** (1992) 197-228.
- [12] A. N. Beris and V. G. Mavrantzas, *On the compatibility between various macroscopic formalisms for the concentration and flow of dilute polymer solutions* J. Rheol. **38** (1994) 1235-1250.
- [13] A. N. Beris and R. Sureshkumar, *Simulation of time-dependent viscoelastic channel Poiseuille flow at high Reynolds numbers*, Chem. Eng. Sci. **51** (1996) 1451- 1471.
- [14] C. Bernardi and Y. Maday, *Spectral methods*, in: P.G. Ciarlet and J.L. Lions, eds., *Handbook of numerical analysis, Vol. V, Techniques of scientific computing (part 2)* Elsevier science.
- [15] A. V. Bhave, R. C. Armstrong and R. A. Brown, *Kinetic theory and rheology of dilute, nonhomogeneous polymer solutions*, J. Chem. Phys. **95** (1991) 2988-3000.
- [16] P. Biller and F. Petruccione, *The flow of dilute polymer solutions in confined geometries: A consistent numerical approach*, J. Non-Newtonian Fluid Mech. **25** (1987) 347-364.
- [17] R. B. Bird, R. C. Armstrong and O. Hassager, *Dynamics of Polymeric Liquids, vol. 1*, 2nd ed. Wiley-Interscience, New York, Chichester, Brisbane, Toronto, Singapore (1987).
- [18] R. B. Bird, C. F. Curtiss, R. C. Armstrong and O. Hassager *Dynamics of polymeric liquids, vol. 2, Kinetic theory*, 2nd ed. Wiley-Interscience, New York, Chichester, Brisbane, Toronto, Singapore (1987).
- [19] R. B. Bird and J. R. Deaguiar, *An encapsulated dumbbell model for concentrated polymer solutions and melts I. Theoretical developments and constitutive equation* J. Non-Newtonian Fluid Mech. **13** (1983) 149-160.
- [20] J. Bonvin, *Numerical simulation of viscoelastic fluids with mesoscopic models* PhD thesis, Department of Mathematics, Ecole Polytechnique Fédérale de Lausanne (2000).
- [21] J. Bonvin and M. Picasso, *Variance reduction methods for CONNFFESSIT-like simulations*, J. Non-Newtonian Fluid Mech. **84** (1999) 191-215.
- [22] M. Bossy, E. Gobet and D. Talay, *Symmetrized Euler scheme for an efficient approximation of reflected diffusions*, Rapport interne 504 du CMAP (2003).
- [23] A. N. Brooks and T. J. R. Hughes, *Streamline upwind/Petrov-Galerkin formulations for convection dominated flows with particular emphasis on the incompressible Navier-Stokes equations*, Comput. Meth. Appl. Mech. Engrg. **32** (1982) 199-259.
- [24] R. A. Brown, M. J. Szady, P. J. Northey and R. C. Armstrong, *On the numerical stability of mixed finite-element methods for viscoelastic flows governed by differential constitutive equations*, Theoret. Comput. Fluid Dynamics **5** (1993) 77-106.
- [25] P. O. Brunn and S. Grisafi, *Kinetic theory of a dilute polymer solution in a small channel: equilibrium results*, Chem. Eng. Commun. **36** (1985) 367-383.

- [26] C. Canuto, M. Y. Hussaini, A. Quarteroni and T. A. Zang, *Spectral Methods in Fluid Dynamics*, Springer Verlag, Berlin, Heidelberg (1988).
- [27] A. E. Caola, Y. L. Joo, R. C. Armstrong and R. A. Brown, *Highly parallel time integration of viscoelastic flows*, J. Non-Newtonian Fluid Mech. **100** (2001) 191-216.
- [28] C. Chauvière, *A new method for micro-macro simulations of viscoelastic flows*, SIAM J. Sci. Comput. **23** (2002) 2123-2140.
- [29] C. Chauvière and A. Lozinski, *An efficient technique for simulations of viscoelastic flows, derived from the Brownian configuration field method*, SIAM J. Sci. Comput. **24** (2003) 1823-1837.
- [30] C. Chauvière and A. Lozinski, *Simulation of dilute polymer solutions using a Fokker-Planck equation*, Computers and Fluids, to appear (2003).
- [31] C. Chauvière and A. Lozinski, *Simulation of complex viscoelastic flows using Fokker-Planck equation: 3D FENE model*, J. Non-Newtonian Fluid Mech., submitted (2003).
- [32] C. Chauvière and R. G. Owens, *How accurate is your solution? Error indicators for viscoelastic flow calculations*, J. Non-Newtonian Fluid Mech. **95** (2000) 1-33.
- [33] C. Chauvière and R. G. Owens, *A new spectral element method for the reliable computation of viscoelastic flow*, Comput. Methods Appl. Mech. Engrg. **90** (2001) 3999-4018.
- [34] C. F. Curtiss and R. B. Bird, *Diffusion-stress relations in polymer mixtures*, J. Chem. Phys., **111** (1999) 10362-10370.
- [35] A. R. Davies and X. K. Li, *Numerical modelling of pressure and temperature effects in viscoelastic flow between eccentrically rotating cylinders*, J. Non-Newtonian Fluid Mech. **54** (1994) 331-350.
- [36] P. G. de Gennes, *Reptation of a polymer chain in the presence of fixed obstacles*, J. Chem. Phys. **55** (1971) 572-579.
- [37] J. des Cloizeaux, *Double reptation vs. simple reptation in polymer melts*, Europhys. Lett. **5** (1988) 437-442.
- [38] M. Doi and S. F. Edwards, *Dynamics of concentrated polymer systems: Brownian motion in the equilibrium state*, J. Chem. Soc. Faraday Trans. **74** (1978) 1789-1801 .
- [39] M. Doi and S. F. Edwards, *Dynamics of concentrated polymer systems: Molecular motion under flow*, J. Chem. Soc. Faraday Trans. **74** (1978) 1802-1817.
- [40] M. Doi and S. F. Edwards, *Dynamics of concentrated polymer systems: The constitutive equation*, J. Chem. Soc. Faraday Trans. **74** (1978) 1818-1832.
- [41] H. S. Dou and N. Phan-Thien, *The flow of an Oldroyd-B fluid past a cylinder in a channel: adaptive viscosity vorticity (DAVSS $\omega$ ) formulation*, J. Non-Newtonian Fluid Mech. **87** (1999) 47-73.

- [42] A. W. El-Kareh and L. G. Leal, *Existence of solutions for all Deborah numbers for a non-Newtonian model modified to include diffusion*, J. Non-Newtonian Fluid Mech. **33** (1989) 257-287.
- [43] X. J. Fan, *Viscosity, first normal-stress coefficient, and molecular stretching in dilute polymer solutions*, J. Non-Newtonian Fluid Mech. **17** (1985) 125-144.
- [44] X. J. Fan, *Viscosity, first normal-stress coefficients, and molecular stretching in concentrated solutions and melts*, J. Non-Newtonian Fluid Mech. **17** (1985) 251-265.
- [45] X. J. Fan, *Molecular models and flow calculation: I. The numerical solutions to multibead-rod models in inhomogeneous flows*, Acta Mech. Sin. **5** (1989) 49-59.
- [46] X. J. Fan, *Molecular models and flow calculations: II. Simulation of steady planar flow* Acta Mech. Sin. **5** (1989) 216-226.
- [47] Y. R. Fan, *A comparative study of the discontinuous Galerkin and continuous SUPG finite element methods for computation of viscoelastic flows*, Comput. Methods Appl. Mech. Engrg. **141** (1997) 47-65.
- [48] Y. R. Fan, R. I. Tanner and N. Phan-Thien, *Galerkin/least-squares finite-element methods for steady viscoelastic flows*, J. Non-Newtonian Fluid Mech. **84** (1999) 233-256.
- [49] J. Fang, M. Kröger and H. C. Öttinger, *A thermodynamically admissible reptation model for fast flows of entangled polymers. II. Model predictions for shear and extensional flows* J. Rheol. **44** (2000) 1293-1317.
- [50] J. Fang, A. Lozinski and R. G. Owens, *Towards more realistic kinetic models for concentrated solutions and melts*, J. Non-Newtonian Fluid Mech., submitted (2003).
- [51] N. Fiétier, *Numerical Simulation of Viscoelastic Fluid Flows by Spectral Element Methods and Time-Dependent Algorithms*, PhD. thesis, Section of Mechanical Engineering, Ecole Polytechnique Fédérale de Lausanne (2002).
- [52] N. Fiétier and M. O. Deville, *Time-dependent algorithms for the simulation of viscoelastic flows with spectral element methods: applications and stability* J. Comput. Phys. **186** (2003) 93-121.
- [53] M. I. Gerritsma and T. N. Phillips, *Discontinuous spectral element approximations for the velocity-pressure-stress formulation of the Stokes problem*, Int. J. Numer. Mech. Engrg. **43** (1998) 1401-1419.
- [54] M. I. Gerritsma and T. N. Phillips, *Compatible spectral approximations for the velocity-pressure-stress formulation of the Stokes problem*, SIAM J. Sci. Comput. **20** (1999) 1530-1550.
- [55] B. Gervang, A. R. Davies and T. N. Phillips, *On the simulation of viscoelastic flow past a sphere using spectral methods*, J. Non-Newtonian Fluid Mech. **44** (1992) 281-306.



- [56] P. G. Gigras and B. Khomami, *Adaptive configuration fields: a new multiscale simulation technique for reptation-based models with a stochastic strain measure and local variations of life span distribution*, J. Non-Newtonian Fluid Mech. **108** (2003) 99-122.
- [57] D. Gottlieb and J.S. Hesthaven, *Spectral methods for hyperbolic problems*, J. Comput. Appl. Math. **128** (2001) 83-131.
- [58] W. J. Gordon and C. A. Hall, *Transfinite element methods: blending function interpolation over arbitrary curved element domains*, Numer. Math. **21** (1973) 109-129.
- [59] P. Halin, G. Lielens, R. Keunings and V. Legat, *The Lagrangian particle method for macroscopic and micro-macro viscoelastic flow computations*, J. Non-Newtonian Fluid Mech. **79** (1998) 387-403.
- [60] M. Herrchen and H.C. Öttinger, *A detailed comparison of various FENE dumbbell models*, J. Non-Newtonian Fluid Mech. **68** (1997) 17-42.
- [61] C. C. Hua and J. D. Schieber, *Segment connectivity, chain-length breathing, segmental stretch, and constraint release in reptation models. I. Theory and single-step strain predictions*, J. Chem. Phys. **109** (1998) 10018-10027.
- [62] C. C. Hua, J. D. Schieber and D. C. Venerus, *Segment connectivity, chain-length breathing, segmental stretch, and constraint release in reptation models. II. Double-step strain predictions*, J. Chem. Phys. **109** (1998) 10028-10032.
- [63] C. C. Hua, J. D. Schieber and D. C. Venerus, *Segment connectivity, chain-length breathing, segmental stretch, and constraint release in reptation models. III. Shear flows*, J. Rheol. **43** (1999) 701-717.
- [64] M. A. Hulsen, A. P. G. van Heel, B. H. A. A. van den Brule, *Simulation of viscoelastic flows using Brownian configuration fields*, J. Non-Newtonian Fluid Mech. **70** (1997) 79-101.
- [65] M. A. Hulsen, E. A. J. F. Peters and B. H. A. A. van den Brule, *The deformation fields method for solving complex flows using integral constitutive equations*, J. Non-Newtonian Fluid Mech. **98** (2001) 201-221.
- [66] G. Ianniruberto and G. Marrucci, *On compatibility of the Cox-Merz rule with the model of Doi and Edwards*, J. Non-Newtonian Fluid Mech. **65** (1996) 241-246.
- [67] G. Ianniruberto and G. Marrucci, *Convective orientational renewal in entangled polymers*, J. Non-Newtonian Fluid Mech. **95** (2000) 363-374.
- [68] G. Ianniruberto and G. Marrucci, *A simple constitutive equation for entangled polymers with chain stretch*, J. Rheol. **45** (2001) 1305-1318.
- [69] G. Ianniruberto and G. Marrucci, *A multi-mode CCR model for entangled polymers with chain stretch*, J. Non-Newtonian Fluid Mech. **102** (2002) 383-395.
- [70] D.D. Joseph, *Fluid dynamics of viscoelastic liquids*, Springer-Verlag, New York (1990).

- [71] B. Jourdain, T. Lelièvre and C. Le Bris, *Numerical analysis of micro-macro simulations of polymeric fluid flows: a simple case*, Math. Model. Meth. Appl. Sci. **12** (2002) 1205-1243.
- [72] H. Kahvand, *Strain Coupling Effects in Polymer Rheology*, PhD thesis, Illinois Institute of Technology (1995).
- [73] R. A. Keiller, *Numerical instability of time-dependent flows*, J. Non-Newtonian Fluid Mech. **43** (1992) 229-246.
- [74] R. A. Keiller, *Spatial decay of steady perturbations of plane Poiseuille flow for the Oldroyd-B equation*, J. Non-Newtonian Fluid Mech. **46** (1993) 129-142.
- [75] M. Laso and H. C. Öttinger, *Calculation of viscoelastic flow using molecular models: the CONNFFESSIT approach*, J. Non-Newtonian Fluid Mech. **47** (1993) 1-20.
- [76] P. Lesaint and P. A. Raviart, On a finite element method for solving the neutron transport equation, in: C. de Boor, ed., *Mathematical Aspects of Finite Elements in Partial Differential Equations*, Academic Press, New York (1974) 89-123.
- [77] G. Lielens, R. Keunings and V. Legat, *The FENE-L and FENE-LS closure approximations to the kinetic theory of finitely extensible dumbbells*, J. Non-Newtonian Fluid Mech. **87** (1999) 176-196.
- [78] B. Liu and A. N. Beris, *The stability of numerical approximations to nonlinear hyperbolic equations*, Comput. Meth. Appl. Mech. Engrg. **76** (1989) 179-204.
- [79] A. W. Liu, D. E. Bornside, R. C. Armstrong and R. A. Brown, *Viscoelastic flow of polymer solutions around a periodic, linear array of cylinders: comparisons of predictions for microstructure and flow fields*, J. Non-Newtonian Fluid Mech. **77** (1998) 153-190.
- [80] A. Lozinski and C. Chauvière, *A fast solver for Fokker-Planck equation applied to viscoelastic flows calculations: 2D FENE model*, J. Comp. Phys. **189** (2003) 607-625.
- [81] A. Lozinski, C. Chauvière, J. Fang and R. G. Owens, *A Fokker-Planck simulation of fast flows of melts and concentrated polymer solutions in complex geometries*, J. Rheol. **47** (2003) 535-561.
- [82] A. Lozinski and R. G. Owens, *An energy estimate for the Oldroyd B model: Theory and applications*, J. Non-Newtonian Fluid Mech. **112** (2003) 161-176.
- [83] A. Lozinski and R. G. Owens, *A Fokker-Planck-based numerical method for modelling non-homogeneous flows of dilute polymeric solutions*, J. Non-Newtonian Fluid Mech., submitted (2003).
- [84] A. Lozinski, R. G. Owens and A. Quarteroni, *On the simulation of unsteady flow of an Oldroyd-B fluid by spectral methods*, J. Sci. Comput. **17** (2002) 375-383.
- [85] Y. Maday and A. T. Patera, *Spectral element methods for the incompressible Navier-Stokes equations*, State of the Art Surveys in Computational Mechanics, ASME, New York (1989) 71-143.

- [86] A. Majda, J. McDonough and S. Osher, *The Fourier method for nonsmooth initial data*, Math. Comp. **32** (1974) 1041–1081.
- [87] J. M. Marchal and M. J. Crochet, *A new mixed finite element for calculating viscoelastic flow*, J. Non-Newtonian Fluid Mech. **26** (1987) 77–114.
- [88] G. Marrucci, *Dynamics of entanglements: A nonlinear model consistent with the Cox-Merz rule*, J. Non-Newtonian Fluid Mech. **62** (1996) 279–289.
- [89] G. Marrucci and N. Grizzuti, *Fast flows of concentrated polymers - predictions of the tube model on chain stretching* Gazz. Chim. Ital. **118** (1988) 179–185.
- [90] V. G. Mavrantzas and A. N. Beris, *Modeling the rheology and flow-induced concentration changes in polymer solutions*, Phys. Rev. Lett. **69** (1992) 273–276; **70** (1993) 2659.
- [91] V. G. Mavrantzas, A. Souvaliotis and A. N. Beris, *Pseudo-spectral calculations of stress-induced concentration changes in viscometric flows of polymer solutions*, Theor. Comp. Fluid Dynam. **5** (1993) 3–31.
- [92] D. W. Mead, R. G. Larson and M. Doi, *A molecular theory for fast flows of entangled polymers*, Macromolecules **31** (1998) 7895–7914.
- [93] J. van Meerveld, Private communication (2002).
- [94] M. Melchior and H.C. Öttinger, *Variance reduced simulations of stochastic differential equations*, J.Chem. Phys. **103** (1995) 9506–9509.
- [95] M. Melchior and H.C. Öttinger, *Variance reduced simulations of polymer dynamics*, J.Chem. Phys. **105** (1996) 3316–3331.
- [96] R. Nayak, *Molecular simulation of liquid crystal polymer flow: a wavelet-finite element analysis*, PhD thesis, MIT, Cambridge, MA (1998).
- [97] J. G. Oldroyd, *On the formulation of rheological equations of state*, Proc. Roy. Soc. London **A200** (1950) 523–541.
- [98] H. C. Öttinger, *Incorporation of polymer diffusivity and migration into constitutive equations*, Rheol. Acta **31** (1992) 14–21.
- [99] H. C. Öttinger, *Stochastic Processes in Polymeric Fluids*, Springer Verlag, Berlin (1996).
- [100] H. C. Öttinger, *A thermodynamically admissible reptation model for fast flows of entangled polymers*, J. Rheol. **43** (1999) 1461–1493.
- [101] H. C. Öttinger, B. H. A. Van Den Brule and M. A. Hulsen, *Brownian configuration fields and variance reduced CONNFFESSIT*, J. Non-Newtonian Fluid Mech. **70** (1997) 255–261.
- [102] R. G. Owens, *A posteriori error estimates for spectral element solutions to viscoelastic flow problems*, Comput. Methods Appl. Mech. Engrg. **164** (1998) 375–395.

- [103] R. G. Owens, C. Chauvière and T. N. Phillips, *A locally upwinded spectral technique (LUST) for viscoelastic flows*, J. Non-Newtonian Fluid Mech. **108** (2002) 49-72.
- [104] R. G. Owens and T. N. Phillips, *A spectral domain decomposition method for the planar non-Newtonian stick-slip problem*, J. Non-Newtonian Fluid Mech. **41** (1991) 43-79.
- [105] R. G. Owens and T. N. Phillips, *Compatible pseudospectral approximations for incompressible flow in an undulating tube*, J. Rheol. **37** (1993) 1181-1199.
- [106] R. G. Owens and T. N. Phillips, *Decoupled spectral element methods for steady viscoelastic flow past a sphere*, in: A. V. Ilin and L. R. Scott eds., *Proceedings of ICOSAHOM.95*, Houston J. Math. (1996) 287-294.
- [107] R. G. Owens and T. N. Phillips, *Steady viscoelastic flow past a sphere using spectral elements*, Int. J. Numer. Meth. Engrg. **39** (1996) 1517-1534.
- [108] R. G. Owens and T. N. Phillips, *Computational Rheology*, Imperial College Press/World Scientific, London (2002).
- [109] A. T. Patera, *A spectral element method for fluid dynamics: laminar flow in a channel expansion*, J. Comp. Phys. **54** (1984) 468-488.
- [110] D. S. Pearson, A. D. Kiss, L. J. Fetters and M. Doi, *Flow-induced birefringence of concentrated polyisoprene solutions*, J. Rheol. **33** (1989) 517-535.
- [111] I. Peschel, X. Wang and M. Kaulke, eds., *Density-Matrix Renormalization: A New Numerical Method Inphysics*, Springer Verlag, Berlin (1999).
- [112] A. Peterlin, *Hydrodynamics of macromolecules in a velocity field with longitudinal gradient*, J. Polym. Sci. B **4** (1966) 287-291.
- [113] E. A. J. F. Peters, M. A. Hulsen and B. H. A. A. van den Brule, *Instationary Eulerian viscoelastic flow simulations using time separable Rivlin-Sawyers constitutive equations* J. Non-Newtonian Fluid Mech. **89** (2000) 209-228.
- [114] E. A. J. F. Peters, A. P. G. van Heel, M. A. Hulsen and B. H. A. A. van den Brule, *Generalization of the deformation field method to simulate advanced reptation models in complex flow*, J. Rheol. **44** (2000) 811-829.
- [115] E. A. J. F. Peters, Private communication (2002).
- [116] F. Petruccione and P. Biller, *A consistent numerical analysis of the tube flow of dilute polymer solutions*, J. Rheol., **32** (1988) 1-21.
- [117] S. Pilitsis and A. N. Beris, *Calculations of steady-state viscoelastic flow in an undulating tube*, J. Non-Newtonian Fluid Mech. **31** (1989) 231-287.
- [118] S. Pilitsis and A. N. Beris, *Viscoelastic flow in an undulating tube. Part II. Effects of high elasticity, large amplitude of undulation and inertia*, J. Non-Newtonian Fluid Mech. **39** (1991) 375-405.

- [119] S. Pilitsis and A. N. Beris, *Pseudospectral calculations of viscoelastic flow in periodically constricted tube*, Comput. Methods Appl. Mech. Engrg. **98** (1992) 307-328.
- [120] T. N. Phillips, R. E. Need, A. R. Davies, B. P. Williamson and L. E. Scales, *The effect of viscoelasticity on the performance of dynamically loaded journal bearings*, SAE Technical Paper Series 982639 (1998).
- [121] T. N. Phillips and G. W. Roberts, *The treatment of spurious modes in spectral incompressible flow calculations*, J. Comput. Phys. **105** (1993) 150-164.
- [122] G. W. Roberts and K. Walters, *On viscoelastic effects in journal-bearing lubrication*, Rheol. Acta **31** (1992) 55-62.
- [123] T. Sato and S. M. Richardson, *Explicit numerical simulation of time-dependent viscoelastic flow problems by a finite element/finite volume method*, J. Non-Newtonian Fluid Mech. **51** (1994) 249-275.
- [124] R. Sizaire, G. Lielens, I. Jaumain, R. Keunings and V. Legat, *On the hysteretic behaviour of dilute polymer solutions in relaxation following extensional flow* J. Non-Newtonian Fluid Mech. **82** (1999) 233-253.
- [125] J. K. C. Suen, Y. L. Joo and R. C. Armstrong, *Molecular orientation effects in viscoelasticity*, Annu. Rev. Fluid Mech. **34** (2002) 417-444.
- [126] J. Sun, M. D. Smith, R. C. Armstrong and R. A. Brown, *Finite element method for viscoelastic flows based on the discrete adaptive viscoelastic stress splitting and the discontinuous Galerkin method: DAVSS-G/DG*, J. Non-Newtonian Fluid Mech. **86** (1999) 281-307.
- [127] R. Sureshkumar and A. N. Beris, *Effect of artificial stress diffusivity on the stability of numerical calculations and the flow dynamics of time-dependent viscoelastic flows* J. Non-Newtonian Fluid Mech. **60** (1995) 53-80.
- [128] A. P. G. van Heel, M. A. Hulsen and B. H. A. A. van den Brule, *Simulation of the Doi-Edwards model in complex flow* J. Rheol. **43** (1999) 1239-1260.
- [129] V. van Kemenade and M. O. Deville, *Application of spectral elements to viscoelastic creeping flows*, J. Non-Newtonian Fluid Mech. **51** (1994) 277-308.
- [130] V. van Kemenade and M. O. Deville, *Spectral elements for viscoelastic flows with change of type*, J. Rheol. **38** (1994) 291-307.
- [131] P. Wapperom, R. Keunings and V. Legat, *The backward-tracking Lagrangian particle method for transient viscoelastic flows*, J. Non-Newtonian Fluid Mech. **91** (2000) 273-295.
- [132] H. R. Warner, *Kinetic theory and rheology of dilute suspensions of finitely extensible dumbbells*, Ind. Eng. Chem. Fundam. **11** (1972) 379-387.
- [133] N. D. Waters and M. J. King, *Unsteady flow of an elastico-viscous liquid*, Rheol. Acta **9** (1970) 345-355.

- [134] H. J. Wilson, M. Renardy and Y. Renardy, *Structure of the spectrum in zero Reynolds number shear flow of the UCM and Oldroyd-B liquids*, J. Non-Newtonian Fluid Mech. **80** (1999) 251–268.

# Curriculum Vitae

I was born on September 29, 1975 in the town of Bryansk, Russia. In September 1992, after finishing 10 years at secondary school in my native town I entered the Moscow Institute of Physics and Technology (Department of Management and Applied Mathematics). There I studied mathematics and physics and graduated as an Engineer-Mathematician in June 1998. During the last two years of my study and another two years after my graduation I took part in research projects on developing iterative methods with splitting of boundary conditions for the Stokes problem and implementing numerical methods for some problems in non-linear optics. This work was done under the supervision of Profs. B.V. Pal'tsev (Computing Centre of Russian Academy of Sciences, Moscow) and A.A. Maier (Institute of General Physics of Russian Academy of Sciences, Moscow). Since October 2000 I have been a PhD student (under the supervision of Profs. Robert G. Owens and Alfio Quarteroni) in the Laboratory of Fluid Mechanics at the EPFL. I have been working on developing numerical methods for simulations of flows of viscoelastic fluids. I've been married to Alla since April 2000.